

AD-A110 785

YALE UNIV NEW HAVEN CT DEPT OF ENGINEERING AND APPL--ETC F/6 20/12  
RF PLASMA ANNEALING ON MOS STRUCTURES.(U)  
DEC 81 M CHIN

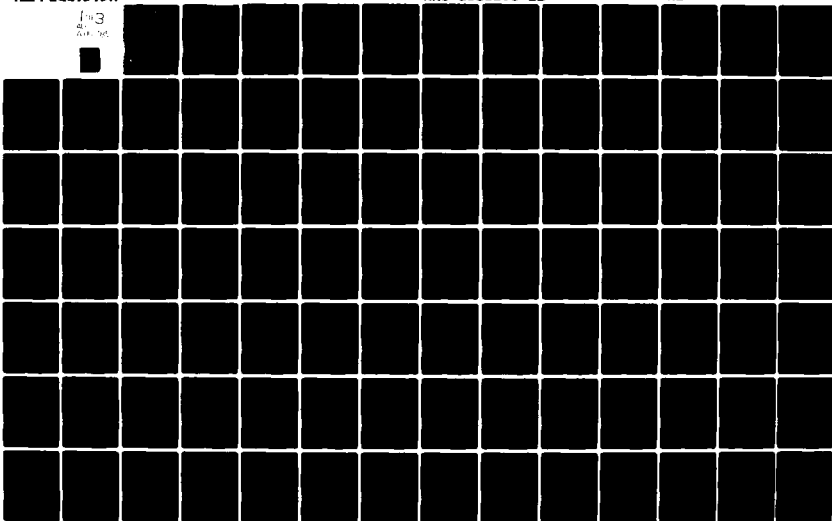
DAA629-79-C-0021

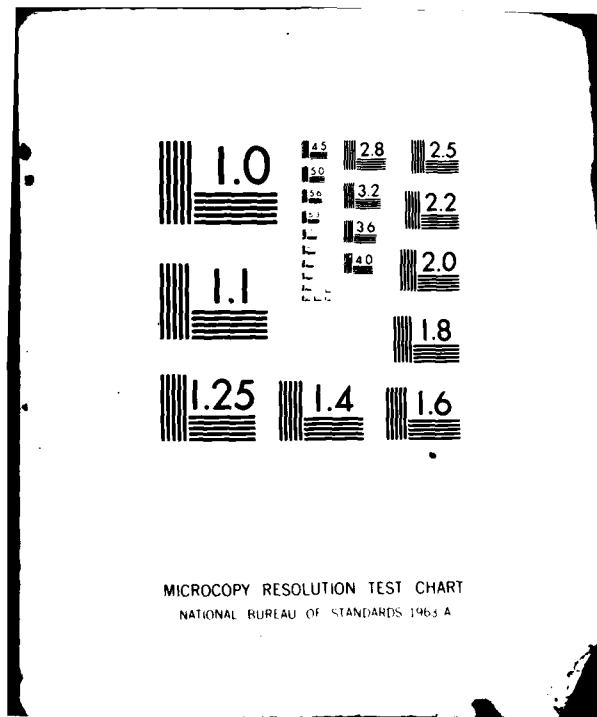
(MM) ACCTYED

ARO-15835.6-EL

NL

103  
201 30





ARO 15835.6-EL

LEVEL II

12



AD A110785

RF PLASMA ANNEALING ON MOS STRUCTURES

FINAL REPORT

Maw-Rong Chin

December, 1981

U.S. Army Research Office

Contract No. DAAG29-79-C-0021

DTIC  
ELECTRONIC  
S FEB 11 1982  
E

APPROVED FOR PUBLIC RELEASE;

DISTRIBUTION UNLIMITED

DTIC FILE COPY

DEPARTMENT OF ENGINEERING  
AND APPLIED SCIENCE

YALE UNIVERSITY

THE VIEW, OPINIONS, AND/OR FINDINGS CONTAINED IN  
THIS REPORT ARE THOSE OF THE AUTHOR AND SHOULD  
NOT BE CONSTRUED AS AN OFFICIAL DEPARTMENT OF  
THE ARMY POSITION, POLICY, OR DECISION, UNLESS  
SO DESIGNATED BY OTHER DOCUMENTATION.

UNCLASSIFIED

SECURITY CLASSIFICATION OF THIS PAGE (When Data Entered)

REPORT DOCUMENTATION PAGE		READ INSTRUCTIONS BEFORE COMPLETING FORM
1. REPORT NUMBER	2. GOVT ACCESSION NO.	3. RECIPIENT'S CATALOG NUMBER
4. TITLE (and Subtitle)  RF PLASMA ANNEALING ON MOS STRUCTURES		5. TYPE OF REPORT & PERIOD COVERED FINAL REPORT 2/1/79 - 1/31/82
7. AUTHOR(s)  Maw-Rong Chin		6. PERFORMING ORG. REPORT NUMBER
9. PERFORMING ORGANIZATION NAME AND ADDRESS Yale University Section of Electrical Engineering New Haven, Conn. 06520		8. CONTRACT OR GRANT NUMBER(s)  DAAG29-79-C-0021
11. CONTROLLING OFFICE NAME AND ADDRESS U. S. Army Research Office Post Office Box 12211 Research Triangle Park, NC 27709		10. PROGRAM ELEMENT, PROJECT, TASK AREA & WORK UNIT NUMBERS
14. MONITORING AGENCY NAME & ADDRESS (if different from Controlling Office)		12. REPORT DATE January 5, 1982
		13. NUMBER OF PAGES 219
		15. SECURITY CLASS. (of this report)  Unclassified
		15a. DECLASSIFICATION/DOWNGRADING SCHEDULE
16. DISTRIBUTION STATEMENT (of this Report)  Approved for public release; distribution unlimited.		
17. DISTRIBUTION STATEMENT (of the abstract entered in Block 20, if different from Report)  NA		
18. SUPPLEMENTARY NOTES The view, opinions, and/or findings contained in this report are those of the author(s) and should not be construed as an official department of the Army position, policy, or decision unless so designated by other documents.		
19. KEY WORDS (Continue on reverse side if necessary and identify by block number)  Radiation Effects in MOS Devices, MOS Interface Properties, Charges and Traps in SiO <sub>2</sub> , Low Pressure RF Plasma, Defect Annealing Process and Mechanism, Recombination-Enhanced Defect Reactions, X-ray Induced Photocurrent, Current Transport and Trapping Kinetics.		
20. ABSTRACT (Continue on reverse side if necessary and identify by block number) This work has been concerned with the study of the RF plasma annealing process, a technique which holds great promise of being able to remove the process-induced radiation effects in MOS device structures. The emphasis has been on the fundamental understanding of the complicated annealing mechanisms with a goal toward future development of a practical annealing tool. This report is a reproduction of the dissertation submitted by its author in partial fulfillment of the Ph.D. degree requirements.		

DD FORM 1473 1 JAN 73 EDITION OF 1 NOV 65 IS OBSOLETE

SECURITY CLASSIFICATION OF THIS PAGE (When Data Entered)

400787

## PREFACE

Very Large Scale Integrated Circuits (VLSI) require advanced processing techniques to achieve the necessary pattern resolution. Some of these techniques, including E-beam or X-ray lithography, plasma or reactive ion etching (RIE), and ion implantation, use energetic particles or photons to overcome the resolution limitations associated with the more conventional processes. As a result, varying degree of radiation damage is frequently introduced in the Metal-SiO<sub>2</sub>-Si (MOS) device structure, which causes severe degradation of the circuit performance and reliability.

Ever since the radiation effect was recognized as a potential problem for the development of VLSI technology, it has stimulated substantial research interest in many laboratories, in an effort to achieve sufficient level of scientific understanding, and to develop techniques that can best solve this problem.

This work, supported by the Army Research Office, has been concerned with the study of the RF plasma annealing process, a technique that holds great promise of being able to remove the process-induced radiation effects very effectively. The emphasis has been on the fundamental understanding of the complicated annealing mechanisms with a goal toward future development of a practical annealing tool.


This report is a reproduction of the dissertation submitted by its author to the faculty of the Department of Engineering and Applied Science in partial fulfillment of the requirements for the degree of Doctor of Philosophy in December 1981.

Tso-ping Ma  
Principal Investigator

ABSTRACT  
RF PLASMA ANNEALING ON MOS STRUCTURES

Maw-Rong Chin  
Yale University

1981

Accession No.	
NTIS	X
DTIC	
Unann	
Justif	
By _____	
Distribution _____	
Availability _____	
Dist	Spec
	

VLSI technology demands high density integrated circuits with ever smaller device dimensions, and advanced processing techniques, such as E-beam or X-ray lithography, reactive ion etching, and ion implantation are required for this purpose. As a result, process-induced radiation effects are frequently observed, which cause severe degradation of the MOS device performance. In the context of VLSI technology, the process-induced radiation effects must be removed to ensure proper operation of the fabricated IC's. A promising solution to this problem is RF plasma annealing.

Substantial experimental evidence has shown that the radiation-induced oxide charge, surface states and neutral traps can be readily removed by the use of this process. The primary advantage of RF plasma annealing is that it is a relatively low temperature process when compared with the conventional thermal annealing, and it is capable of removing certain significant electronic defects which are not removable by the thermal annealing. Examples in the latter category include the radiation-induced charge centers in MNOS structures, and the neutral traps in MOS structures.

The mechanisms of RF plasma annealing have been studied using an

experimental simulation, in which the three essential ingredients in the annealing process -- the RF field, the ionizing radiation source, and the wafer temperature can be independently controlled. The results have confirmed the importance of the simultaneous presence of all three components, whose cooperative effect leads to the effective annihilation of the oxide defects. The results of the experimental simulation show a substantial reduction of the activation energy of the annealing process with the presence of the X-ray excitation and the RF voltage, which is consistent with a mechanism based on Recombination Enhanced Defect Reaction (REDR) model.

The REDR theory and its applicability in the RF plasma annealing process have been examined. The analysis of our experimental data indicates that the observed temperature dependence of the RF annealing rate can be explained by two possible REDR processes.

In addition to the wafer temperature and the X-ray flux, the annealing rate has been found to depend on the amplitude and frequency of the RF voltage. A theoretical analysis suggests that the observed voltage dependence of the annealing behavior arises from the voltage dependence of the recombination rate, as predicted by the REDR model. The frequency dependence is not completely understood. Based on the frequency dependence of the hole transport in  $\text{SiO}_2$ , we have proposed a model which takes into account the hole-trapping kinetics, and this model seems to be in reasonable agreement with the experimental observations.

The above theoretical analyses require sufficient knowledge of the



X-ray induced carrier transport and recombination processes in thermal SiO<sub>2</sub>, for which we have designed and conducted a systematic experiment. We have found that, under the X-ray irradiation, both the contact photoinjection current and the bulk generation current contribute significantly to the total current, and the former contribution increases with decreasing oxide thickness. The voltage dependence of each current component has been analyzed, and their theoretical foundation has been established. These results contribute significantly to our overall understanding of the RF plasma annealing mechanisms.

## TABLE OF CONTENTS

	<u>Page Number</u>
Abstract	1
Title Page	ii
Acknowledgments	iv
Table of Contents	viii
List of Tables	ix
List of Illustrations	1
I. INTRODUCTION	3
1.1 Ionizing Radiation Effects in Thermal SiO <sub>2</sub>	6
1.2 Qualitative Models for Radiation Effects	6
1.2.1 Positive Oxide Charge	7
1.2.2 Surface States	11
1.2.3 Neutral Traps	12
1.2.4 Mobile Ion	13
1.3 Limitations of Thermal Annealing	14
1.4 RF Plasma Annealing	17
II. RF PLASMA ANNEALING : EXPERIMENTAL DETAILS AND ANNEALING RESULTS	17
2.1 Introduction	19
2.2 Annealing Apparatus	22
2.3 Operation of Annealing System and Annealing Parameters	24
2.4 Experimental Details	24
2.4.1 Sample Preparation and Irradiation	26
2.4.2 Sample Measurements and Analysis	

	<u>Page Number</u>
2.5 Annealing Results and Discussions	36
2.5.1 Oxide Charge and Surface States	37
2.5.2 Oxide Traps	41
2.6 Concluding Remarks : Qualitative Annealing Model	47
III. INTERACTION BETWEEN RF PLASMA AND MOS SAMPLE	51
3.1 Introduction	51
3.2 The Nature of The RF Plasma : Ions, Electrons, Neutrals and Photons	52
3.3 Absorption of VUV and X-ray in SiO <sub>2</sub>	54
3.4 Wafer Temperature Induced in The RF Plasma	59
3.5 RF Voltage across MOS Sample	60
3.6 Conclusions	73
IV. EXPERIMENTAL SIMULATION OF RF PLASMA ANNEALING	75
4.1 Introduction	75
4.2 Experimental Details	77
4.2.1 Sample Preparation	77
4.2.2 Setup and Procedure for Experimental Simulation	77
4.3 Results and Related Discussions	84
4.4 Frequency and Voltage Dependence of RF Annealing	98
4.4.1 Annealing Results	98
4.4.2 Theoretical Considerations and Data Analysis	104
4.5 Conclusion	116
V. MECHANISMS OF THERMAL ANNEALING AND RF ANNEALING	119
5.1 Introduction	119

	<u>Page Number</u>
5.2 Qualitative Model for Thermal Annealing Mechanism	120
5.3 Quantitative Rate Equation for Thermal Annealing	122
5.3.1 Single Activation Energy	122
5.3.2 Distributed Activation Energies	126
5.4 Mechanisms of RF Annealing	129
5.4.1 Possible Electronic Enhancement Processes in SiO <sub>2</sub>	129
5.4.2 REDR Theory and Its Mathematical Model	133
5.5 Conclusion	140
VI. PHOTOCURRENT IN THERMAL SiO <sub>2</sub> UNDER X-RAY IRRADIATION :	
SIGNIFICANCE OF CONTACT INJECTION	142
6.1 Introduction	142
6.2 Theoretical Considerations	144
6.2.1 Photoinjection	144
6.2.2 Generation Current in Oxide Bulk	147
6.2.3 Geminate Recombination	148
6.2.4 Total Collected Current	151
6.3 Experimental Details	152
6.3.1 Sample Preparation	152
6.3.2 Experimental Setup	152
6.4 Results and Discussions	154
6.4.1 Contact Photoinjection	154
6.4.2 Generation in SiO <sub>2</sub>	160
6.4.3 Geminate Recombination	162
6.5 Conclusions	167

	<u>Page Number</u>
VII. CONCLUSION	169
APPENDIX A: Contamination Problems in RF Plasma Chambers	176
APPENDIX B: Induction Coil Design and Matching Network	178
APPENDIX C: Other Applications of RF Plasma Annealing	183
APPENDIX C.1: Radiation Hardening of MOS Devices by RF Plasma Annealing	188
APPENDIX C.2: RF Plasma Annealing on MOS Capacitors with InSb Substrate	193
APPENDIX D: X-Ray Luminescence Spectra (XLS)	199
REFERENCES	208

LIST OF TABLES

		<u>Page Number</u>
TABLE 2.1	Trap parameters obtained from Fig. 2.7.	43
TABLE 3.1	Total available X-ray flux calculated using Eq. (3.1) for RF powers in the range of 100-600W.	57
TABLE 3.2	Procedure to calculate the total photon flux absorbed by the SiO <sub>2</sub> layer in an MOS sample with the data of TABLE 3.1.	58
TABLE 4.1	Trap parameters obtained from Fig. 4.6.	92
TABLE 4.2	Values of the various parameters used in the numerical fitting procedure for the voltage dependence of RF annealing rate.	111
TABLE 4.3	Trap capture cross-sections at room temperature obtained from Eq. (4.7.1).	111
TABLE 5.1	Possible E <sub>M</sub> , mean thermal activation energy for two different ν <sub>a</sub> 's.	127
TABLE 5.2	Calculated (E <sub>T</sub> -E <sub>R</sub> ), mean enhanced activation energy.	138
TABLE C	Effects of RF plasma annealing on radiation-induced shifts.	190

## LIST OF ILLUSTRATIONS

Page Number

- Fig. 2.1 (a) Schematic cross-sectional view of the original RF plasma annealing apparatus used at IBM. 18
- Fig. 2.1 (b) Schematic diagram of the parallel-plate RF plasma annealing system currently being used at Yale. 20
- Fig. 2.2 Avalanche hot electron injection circuit with a flatband voltage monitor. Output is  $V_{FB}$  vs  $t$ . 32
- Fig. 2.3 An example showing the analysis of Eq. (2.17). The slopes of the straight line segments give rise to  $\sigma$ 's, while the intercepts at  $t = 0$  give rise to  $N_{eff}$ 's. 35
- Fig. 2.4 1 MHz and quasi-static C-V curves of an MOS capacitor after radiation damage (curve 1) and after RF plasma annealing (curves 2 and 3). 38
- Fig. 2.5 Flatband voltage,  $V_{FB}$ , and surface-state density,  $N_{FS}$ , of an irradiated MOS capacitor as a function of annealing time at three different RF power levels. 39
- Fig. 2.6 High frequency and quasi-static C-V curves for an MNOS capacitor (300 Å/300 Å  $Si_3N_4/SiO_2$  dielectrics). Curve 1: after irradiation. Curve 2: after irradiation and then 400W RF annealed for 15 min. Curve 3: after irradiation and then 400W RF annealed for 25 min. Curve 4: after irradiation and then forming-gas annealed at 400°C for 60 min. 40
- Fig. 2.7 MOS C-V shifts as a function of the number of electrons/cm<sup>2</sup> avalanche injected from the silicon substrate. Curve 1: control sample; Curve 2:  $\gamma$ -ray irradiated sample; Curve 3: thermally annealed (425°C in dry  $N_2$  for 30 min) after irradiation; Curves 4 and 5: RF annealed at 400W and 600W after irradiation. 42
- Fig. 2.8 (a) Threshold voltage shifts,  $\Delta V_T$ , as a function of avalanche injection time for an MOSFET before and after irradiation, and after RF plasma annealing. 45
- Fig. 2.8 (b) Shifts in transfer characteristics for an irradiated MOSFET after hot-electron injection for 0', 10', and 100', respectively. 46

Fig. 2.9	Proposed RF plasma annealing mechanisms based on the plasma-wafer interaction, electron-hole generation, charge neutralization, and recombination-enhanced defect reactions.	49
Fig. 3.1	Photon absorption coefficient as a function of photon energy. Solid curve corresponds to aluminum film, dashed curve corresponds to silicon film, and dash-dotted curve corresponds to SiO <sub>2</sub> film.	55
Fig. 3.2	Wafer temperature as a function of RF power density. Shaded area: Logan's data (1970) for different types of substrates under 2μ pressure. Dash-dotted curve: Kurylo's data (1978) for pressures of 16-23μ.	61
Fig. 3.3	Voltage distribution in a dc plasma system. Variations of the electrical potential are depicted in the vicinity of a floating sample.	64
Fig. 3.4 (a)	Schematic diagram showing the voltage distribution in a symmetrical RF plasma system.	
(b)	Possible waveforms of sheath voltages near electrodes and sample.	65
Fig. 3.5 (a)	Equivalent circuit representation of an RF plasma annealing system with an MOS sample in it.	
(b)	Equivalent RC parallel network of load impedance Z <sub>L</sub> .	
(c)	Equivalent circuit of the plasma conductive branch with appropriate sample impedance and its associated sheaths.	67
Fig. 4.1	Experimental setup for the simulated RF annealing process.	78
Fig. 4.1.1	Circuit diagram of the automatic flatband and midgap voltage monitor.	82
Fig. 4.2	High frequency C-V curves of an MOS capacitor showing the effects of X-ray irradiation and RF field at several time intervals. Solid curve corresponds to the initial state of the sample. Curves X <sub>1</sub> and X <sub>2</sub> correspond to X-ray irradiation only. Curves RX <sub>1</sub> and RX <sub>2</sub> correspond to X-ray irradiation coupled with an applied RF field. All experiments are done at room temperature.	85



Fig. 4.3	C-V shift, measured at midgap, as a function of time under several different conditions. Solid curves correspond to the cases where X-ray irradiation and RF voltage are simultaneously applied. Dashed curve is taken with X-ray irradiation only. The X-ray and RF parameters are as specified in Fig. 4.2.	86
Fig. 4.4	Contribution of X-ray in the RF annealing process is exemplified. Curves correspond to C-V shifts, measured at midgap, as a function of time in a simulated RF annealing experiment at 65°C. Upper curve corresponds to the case where an RF voltage is applied in the absence of X-ray. Lower curve corresponds to the case where both X-ray and RF voltage are applied.	88
Fig. 4.5	Dependence of annealing on the X-ray flux at two different temperatures. Solid curves are taken with an X-ray flux of $7.2 \times 10^{17}$ eV/cm <sup>2</sup> -sec. Dashed curves are taken with an X-ray flux of $1.8 \times 10^{17}$ eV/cm <sup>2</sup> -sec.	89
Fig. 4.6	Results of the avalanche injection measurement indicate that the radiation-induced neutral traps are completely removed by the(X-ray + RF field) annealing at 300°C.	91
Fig. 4.7	Arrhenius plots of the oxide-charge annealing rate for pure thermal and recombination-enhanced processes. The X-ray fluxes are given in Fig. 4.5. The activation energies are 0.375 eV (pure thermal) and 0.128 eV (recombination-enhanced).	94
Fig. 4.8	Arrhenius plots for the annealing of surface states. The surface states correspond to the integrated number over the energy band between midgap and flatband. The X-ray fluxes are given in Fig. 4.5.	96
Fig. 4.9	Annealing of the positive oxide charge as a function of the ac voltage at 100°C for a wide range of frequencies.	99
Fig. 4.10	Annealing of the slow surface states as a function of the ac voltage for a wide range of frequencies.	101
Fig. 4.9.1	Annealing of the positive oxide charge as a function of frequency using the ac voltage as a parameter. These curves are redrawn from Fig. 4.9.	102
Fig. 4.10.1	Annealing of the slow surface states as a function of frequency using the ac voltage as a parameter. These curves are redrawn from Fig. 4.10.	103

Page Number

- Fig. 4.11 Voltage dependence of the RF annealing behavior at 1 KHz. Solid triangles: experimental data obtained from Fig. 4.9. Solid curve: theoretical fit using Eq. (4.2.3). 110
- Fig. 4.12 Frequency dependence of the RF annealing behavior at a peak ac voltage of 0.4 V. Solid dots: experimental data obtained from Fig. 4.9.1. Solid curve: theoretical fit using Eq. (4.11) with  $\alpha = 0.12$ ,  $\beta = 10984$ . 117
- Fig. 5.1 (a) Electronic energies vs lattice coordinate  $Q$ . The equilibrium positions of the lattice coordinates and the energy levels, before and after electron capture, are indicated by the dash-dotted lines. The short arrows represent the amplitudes of the thermal vibration. The long arrows represent the amplitude of the lattice vibrations about the new equilibrium position, immediately after capture.
- (b) The corresponding configuration coordinate diagram (electronic + elastic energies vs  $Q$ ). The optical excitation threshold  $E_p$  at lattice equilibrium and thermal excitation  $E_T$  are indicated. 121
- Fig. 5.2 Arrhenius plots of the annealing rate (Eq. (5.4)) for pure thermal and recombination-enhanced processes. Four X-ray fluxes are used where  $\phi = 1.8 \times 10^{16}$  eV/cm<sup>2</sup>-sec. The activation energies are <sup>c</sup>0.413 eV (pure thermal) and 0.143 eV (recombination-enhanced). 124
- Fig. 5.3 The annealing of oxide charge at three different temperatures with and without RF field is compared. 131
- Fig. 5.4 (a) Schematic diagram showing the indirect recombination process followed by nonradiative multiphonon emission.
- (b) Schematic diagram showing the recombination enhancement of defect reaction. 132

	<u>Page Number</u>
Fig. 6.1 Experimental setup for X-ray induced photocurrent measurement.	153
Fig. 6.2 Experimental X-ray induced photocurrent as a function of negative oxide field with oxide thickness as a parameter.	155
Fig. 6.3 Experimental X-ray induced photocurrent as a function of oxide thickness using negative oxide field as a parameter.	157
Fig. 6.4 Experimental X-ray induced photocurrent as a function of oxide thickness using positive oxide field as a parameter.	158
Fig. 6.5 Photoinjected currents as a function of oxide field. Solid circles : experimental data under negative bias obtained from Fig. 6.3 Dash-dot curve : theoretical fit using equation(6.1) with $A = 7.02 \times 10^{-9}$ and $p = 4.07$ . Open circles : experimental data under positive bias obtained from Fig. 6.4. Dashed curve : theoretical fit using equation (6.1) with $A = 6.84 \times 10^{-8}$ and $p = 7.42$ .	159
Fig. 6.6 Experimental photogeneration current in $\text{SiO}_2$ as a function of oxide field. Currents under negative bias are shown for four different oxide thicknesses (solid curves). Current under positive bias is shown for the $500 \text{ \AA}$ oxide (dashed curve).	161
Fig. 6.7 Net pair generation rate in $\text{SiO}_2$ as a function of oxide field. Solid circles : experimental data under negative bias obtained from Fig. 6.6. Open circles : experimental data under positive bias obtained from Fig. 6.6. Dash-dot curve : theoretical fit using Onsager's geminate recombination with $r_0 = 35 \text{ \AA}$ .	163
Fig. 6.8 Relative generation rate as a function of oxide field. Results from several different authors are compared. Data are normalized at a field of $2 \times 10^6 \text{ V/cm}$ where generation rate is taken to be 0.8.	165

		<u>Page Number</u>
Fig. B.1	Equivalent circuit diagram for an RF system. The RF generator, directional coupler and matching network are included to show the condition for the maximum power transfer.	179
Fig. B.2	Under optimal (maximum power transfer) condition the tunable load impedance range obtained from Eqs. (B.1) and (B.2) by varying $C_1$ and $C_2$ . The small area is for $L = 1 \mu\text{H}$ and the large area is for $L = 5 \mu\text{H}$ .	181
Fig. B.3	Coil dimensions used in the inductance formula. The wire diameter does not enter into the formula.	180
Fig. C	Current-voltage characteristics of Schottky diode: (1) before RF plasma annealing (ohmic contact), and (2) after 400W RF plasma annealing for 10 min. (rectifying behavior).	186
Fig. C.1	Radiation hardening results on surface state distribution after RF annealing. For high-dosage irradiation, a broad peak develops in the upper half of the silicon bandgap.	191
Fig. C.2	RF plasma annealing results of InSb MOS capacitors. The upper high frequency C-V curves show $V_{\text{FB}}$ shifts from -2V to 0V, and the lower ones show from +2V to 0V.	196
Fig. D.1	Experimental setup for X-ray luminescence measurement.	201
Fig. D.2	X-ray luminescence spectra for a typical optical fiber at room temperature.	203
Fig. D.3	X-ray luminescence at $4500 \text{ \AA}$ as a function of ambient temperature for a No. 1 coverglass.	204
Fig. D.4	X-ray luminescence spectra for a No. 1 coverglass: (1) after heavy irradiation, (2) RF annealed at $50^\circ\text{C}$ after irradiation and (3) RF annealed at $100^\circ\text{C}$ after irradiation.	204
Fig. D.5	Arrhenius plot of the annealing rate for pure thermal and enhanced processes. The experiment is done by examining the X-ray luminescence peak at $4500 \text{ \AA}$ from a No. 1 coverglass.	206

## CHAPTER I

### INTRODUCTION

It is well-known that the practical MOS devices contain various charge centers in the thermally grown  $\text{SiO}_2$  layer (Deal 1974). The charge centers that have been identified include fixed charges, surface states, mobile ions, and oxide traps for electrons or holes. Their presence in excess amounts can cause severe degradation of the MOS device performance, which includes the threshold voltage shift (due to fixed charges, mobile ions, and surface states), the reduction of transconductance (surface states), surface leakage current (surface states and fixed charge), threshold instability (mobile ions, slow surface states, and oxide traps) and long term reliability problems (oxide traps).

Even though the exact origins of these various charge centers are not entirely understood, it has been suggested that they may be closely related to the short-range structural defects (e.g., trivalent silicon, nonbridging oxygen, oxygen vacancies, interstitial oxygen, hydrogen related bonding sites, impurity centers, and strained bonds), and disordered bonds in the thermal  $\text{SiO}_2$  (Revesz 1965, 1967, Sah 1976). However, the detailed microscopic correlations between the various charge centers and the structural defects are still unclear. Some recent theoretical work in this area seems promising. For example, Lucousky (1979, 1980) has proposed a model for the intrinsic bonding defect in

$\text{SiO}_2$  based on the so-called intimate valence-alternation pairs (Mott 1978), which might eventually lead to the understanding of the chemical nature of the oxide traps and fixed charge (Lucousky 1979, 1980).

Whatever the chemical origins are, it has been found that these excess charge centers may arise due to improperly performed conventional processing steps (e.g., oxidation, diffusion, metallization, various heat treatments), and from radiation effects. As a result of more than a decade's research and development, the former has been successfully controlled, and MOS devices with minimal levels of charge centers can be manufactured routinely without much difficulty. The radiation effects, however, are still a major problem as reflected in the vast amount of literature dealing with this subject (Zaininger 1967).

To produce advanced devices with micron or submicron dimensions, one must use new fabrication techniques to overcome the fundamental and practical limitations associated with conventional technologies. The more promising new technologies on the scene include electron-beam lithography, X-ray lithography, reactive ion etching, plasma sputtering and deposition, ion-beam milling and ion implantation. The common feature of these technologies is that highly energetic particles or photons are used in the processes, and radiation effects are often observed to some extent.

In the following sections, ionizing radiation effects in thermal  $\text{SiO}_2$  will be reviewed. The physical phenomena pertinent to such effects will be presented in the context of MOS device properties. Several

models to account for the experimental observations will be described.

### 1.1 IONIZATION RADIATION EFFECTS IN THERMAL $\text{SiO}_2$

Radiation effects have been of both practical and fundamental interest for many years. The driving force for the research in this subject has originated from two major sources. On the one hand, there has been great need for radiation-hardened MOS devices which could tolerate certain radiation exposure and function properly in a radiation-rich environment. On the other hand, the quest for higher density, higher performance IC chips demands advanced processing techniques that often employ radiation sources such as electron beam, X-ray or plasma, etc. and frequently some resulting radiation damage is introduced during device processing. These process-induced radiation damage must be annealed out to ensure that the devices function properly after they are fabricated.

The most commonly observed radiation effects in thermal  $\text{SiO}_2$ , as revealed from the measurements of the electronic properties of MOS devices are the following :

#### (a) A Buildup of Positive Charge in The Oxide.

The amount of radiation-induced positive charge depends strongly on the accumulated total radiation dose absorbed in  $\text{SiO}_2$  (Zaininger 1967). This is in general true as long as the energy of the radiation exceeds the bandgap of  $\text{SiO}_2$  (~9 eV), and the exact nature of the radiation source

(e.g., whether it is e-beam, X-ray, or  $\gamma$ -ray) is unimportant. For a given electric field in  $\text{SiO}_2$ , the charge buildup is characterized by a monotonic increase with the radiation dose until saturation is reached. The saturation level increases with the field in the oxide during irradiation. A minimum occurs when a zero oxide field is maintained. The spatial distribution of the radiation-induced positive charge is strongly influenced by the polarity of the field. More charge tends to buildup near the  $\text{SiO}_2$ -Si interface under a positive field (in the direction Metal  $\rightarrow$  Silicon) than a negative field, resulting in a large C-V shift in the MOS measurement. This positive charge buildup gives rise to a negative shift in the threshold voltage of a MOS device, regardless whether it is n-channel or p-channel.

(b) An Increase in The Surface States.

The buildup of surface states follow qualitatively the same dose dependence as the radiation-induced positive charge. For low doses of radiation, the energy distribution of the radiation-induced surface states tends to track that of the initial (pre-irradiation) distribution (Ma et al. 1975). For high doses, a broad peak develops in the upper half of the silicon bandgap (see Appendix C, Fig. C). The magnitude and the shape of this surface-state distribution are independent of the dopant type and concentration of the silicon substrate. For a given radiation dose, the radiation-induced surface states increase with oxide thickness (Ma 1975). In the limiting case where  $\text{SiO}_2$  is of tunneling thickness ( $\leq 50 \text{ \AA}$ ), no radiation-induced surface states have been detected (Ma and Barker 1974,



Dressendorfer 1978). There is also strong evidence that the surface states above the midgap are acceptor type and those below are donor type (Scoggan and Ma 1977, Lai 1980). As a result of the buildup of surface states, the transconductance of an MOSFET device is degraded after irradiation. The charging of these states also causes a shift in the threshold voltage,  $\Delta V_T$ . The charged donor states contribute to a negative shift and the charged acceptor states a positive shift.

(c) An Increase in The Neutral Traps.

These are electronic trapping sites in  $\text{SiO}_2$  which are electrically neutral before an electron (or a hole) is trapped, and thus are not revealed by the usual steady-state C-V measurements. The effect of these traps, however, can be seen by pumping hot electrons (holes) into the oxide either by avalanche injection (Nicollian and Berglund 1971) or by photoinjection (Williams 1965). The general properties of these traps have been reviewed in an article by DiMaria (1978), and the radiation-induced neutral traps have been reported in several papers (Aitken et al. 1978, Gdula 1979, Aitken 1979). In general, the number of radiation-induced neutral traps depends on the quality of the oxide, and for a given oxide, it increases with the radiation dose as in the case of oxide charge and surface states. The spatial distribution of these traps has been found to extend throughout the  $\text{SiO}_2$  layer (Aitken 1979).

In addition to the effects noted above, occasionally an increase in the mobile charge level has been observed in certain radiation environments. In particular, this effect becomes significant when the thermal  $\text{SiO}_2$  is

directly exposed to a gas plasma typical of RF sputtering or dry etching (McCaughan et al. 1973, 1974).

## 1.2 QUALITATIVE MODELS FOR RADIATION EFFECTS

Qualitatively, the ionizing radiation effects arise from the energy transfer to the Si-O network, causing bond breakage, bond deformation, and generation of electrons and holes. The resulting deformed or broken bonds and the trapping of charge manifest themselves in the change of the electronic properties.

Several models have been proposed to account for the experimental observations, and their essential features are presented below.

### 1.2.1 Positive Oxide Charge

With high enough incident energy, electron-hole pairs are generated in SiO<sub>2</sub> following absorption. Many of the electrons and holes recombine, but some are separated. Since the electrons have relatively high mobility (20 - 40 cm<sup>2</sup>/V-sec) in the SiO<sub>2</sub> conduction band (R. Hughes 1973), they diffuse or drift out of SiO<sub>2</sub> very rapidly, leaving behind the excess holes. The holes are believed to have orders of magnitude lower mobility (~10<sup>-5</sup> cm<sup>2</sup>/V-sec) than the electrons (R. Hughes 1975), eventually some of them are trapped in the hole traps, giving rise to the radiation-induced positive oxide charge. This model was first proposed by Zaininger and Holmes-Siedle in 1967, and is still widely accepted.

A high concentration of hole traps has been found to exist near the  $\text{SiO}_2$ -Si interface (at a distance of  $\leq 50 \text{ \AA}$ ) (DiMaria et al. 1977, Stivers and Sah 1980), perhaps related to the non-stoichiometry of the thin transition zone in that region. Consequently, the radiation-induced positive charge tends to gather near that interface. The presence of an electric field in the oxide serves to separate the electron-hole pairs, which in effect reduces the geminate or columnar recombination rate (Curtis et al. 1974) and increases the net trapping of the holes. This effect is enhanced as the field increases. The polarity of the oxide field influences the spatial distribution of the trapped holes and results in the observed asymmetrical field dependence of the C-V shift.

This model is phenomenologically consistent with most of the experimental observations. The questions concerning the nature of the hole traps, the electron and hole transport mechanisms, and the trapping kinetics, however, remain to be answered, and have drawn significant attention in recent years (DiMaria 1978).

### 1.2.2 Surface States

At least three models have been proposed to explain the buildup of surface states due to ionizing radiation. These are designated as (a) Si-H, Si-OH model, (b) the strained bond model, and (c) the hole transport model. In all three models it is assumed that the surface states arise either from the broken bonds or the microscopic strain fields localized in the interface region. A theoretical calculation has shown that

broken bonds tend to result in a peaked structure in the energy distribution, while the strain fields result in a U-shape distribution (Laughlin et al. 1978), and both types have been observed experimentally.

(a) Si-H, Si-OH Model

The key feature in this model is the existence of Si-H or Si-OH bonds in  $\text{SiO}_2$  near the  $\text{SiO}_2$ -Si interface. These hydrogen related bonds may arise from the presence of moisture during thermal oxidation, or from subsequent processing steps such as metallization and forming gas annealing. The ionizing radiation breaks such bonds, permitting the H or the OH to drift away, and an unsaturated trivalent silicon bond is left behind. Such a trivalent Si bond at the  $\text{SiO}_2$ -Si interface could act as a surface state. Although both Si-H and Si-OH bonds are possible candidates for such a mechanism, Sah (1976) suggests that the latter is more consistent with the bias-dependence of the radiation-induced surface states.

While the above model is supported by some experimental evidence, it is not adequate to account for many other observations. For example, the oxide thickness dependence effect (Ma 1975), and in particular the fact that no radiation-induced surface states have been detected for  $\text{SiO}_2$  of tunneling thickness ( $\leq 50 \text{ \AA}$ ) (Ma and Barker 1974), seems to be inconsistent with the model. In addition, the radiation sensitivity of an MOS structure has been found to be a sensitive function of oxidation temperature and post-oxidation high temperature anneal in the  $900^\circ - 1000^\circ\text{C}$  range (Sah 1976), which also suggests that some other mechanism

without invoking hydrogen is required.

(b) Strained Bond Model

This model is based on the strained Si-O bonds in the amorphous thermal SiO<sub>2</sub> layer. The strained bonds may arise from the rapid thermal growth processes, the lattice mismatch at the SiO<sub>2</sub>-Si interface, and/or the presence of impurities. During the irradiation, many bonds (including the normal bonds and the strained bonds) are temporarily broken, resulting in electron-hole generation. Those broken bonds which are initially strained would relax and form trivalent silicon and nonbridging oxygen centers, giving rise to localized energy levels in the forbidden energy band (Gwyn 1969). If these broken bonds reside at the SiO<sub>2</sub>-Si interface, they can trap electrons or holes from the silicon surface and act as surface states.

In addition, the strained bonds in the bulk of SiO<sub>2</sub> can also contribute to the buildup of surface states upon radiation indirectly, due to the radiation-induced compaction of amorphous SiO<sub>2</sub> which has been observed in fused silica (Norris and EerNisse 1974) and thermal SiO<sub>2</sub> (H. Hughes 1969 and Sigsbee et al. 1973). This effect is a consequence of the relaxation of the broken bonds, which causes a structural modification leading to a shrinkage of the SiO<sub>2</sub> film. In the process of this structural rearrangement of the bulk SiO<sub>2</sub>, more strained bonds are generated at the SiO<sub>2</sub>-Si interface, which may be broken by continued radiation, and eventually more surface states are created.

This model suggests that the density of radiation-induced surface states depends on the total number of the strained bonds both at the interface and in the bulk of  $\text{SiO}_2$ . For a given thermal oxidation process, it is expected that the total number of strained bonds integrated over the  $\text{SiO}_2$  thickness increases with the thickness, which is consistent with the oxide thickness dependence results (Ma 1975). The dependence of the radiation sensitivity on the post oxidation high temperature treatments can be explained by the changes in the number of strained bonds. Such changes may arise from the viscous shear flow of thermal  $\text{SiO}_2$  at elevated temperatures, as proposed by EerNisse and Derbenwick (1976).

(c) Hole Transport Model

When the radiation-generated holes are swept across the  $\text{SiO}_2$ -Si interface under an electric field, some of them are trapped there, and a buildup of surface states begins to evolve as a function of time (Winokur et al. 1976, 1979, Hu and Johnson 1980). This time dependent surface-state buildup has been found to occur even for nonpenetrating radiation (Winokur and Sokoloski 1976, Weinberg et al. 1979, 1980), and only occurs after the holes have been transported across the interface. The saturation time for this process can be as long as thousands of seconds at room temperature (Winokur et al. 1976, 1979), which far exceeds the hole transit time.

To explain this result, a trapped hole model was proposed, in which it was suggested that the inhomogeneous hole distribution can lead to

fluctuations in the silicon surface potential and thus an increase in the surface-state density, whose energy distribution is in accordance with the model of Goetzberger et al. (1968). The observed long time constant was attributed to the time it takes for the trapped holes at the interface to form clusters. Some recent results obtained from the field-switching experiment (Winokur et al 1980), however, have prompted them to take a new look at the mechanisms involved, and they now favor a model involving a two-stage process as follows (McLean 1980). During the first stage, positive ions (probably  $H^+$ ) are released in the bulk of  $SiO_2$  due to the energy transfer through hole trapping and transport, and it is the interaction of the ions with the interface that produces the surface states in the second stage of the process. An empirical model has been developed which gives the mathematical dependences of the buildup on time, field, temperature, and dose (McLean 1980).

All three models presented above receive some experimental support, but none can fully explain all the results. Perhaps a combination of all these mechanisms is involved during radiation, with one or more of them dominating under particular sets of conditions.

### 1.2.3 Neutral Traps

Although the radiation-induced neutral traps have been observed and reported by several authors (Aitken et al. 1978, Gdula 1979, and Aitken 1979), the corresponding mechanisms are not clearly understood. From the relatively small capture cross sections of these traps and their

thermal annealing behavior, Aitken et al. (1978) proposed an atomic model which attributes the neutral traps to a dipole-like defect center associated with a broken bond. It is also possible that a strained bond itself, without being broken, may act as a neutral trap. These radiation-induced strained bonds are a consequence of the structural modifications arising from the broken bonds as described previously. Thus, both models invoke the process of bond breaking, and hence, in this respect are similar to the first two surface-state models discussed in the previous section; the major difference being that the location of the neutral traps is not confined to the  $\text{SiO}_2$ -Si interface.

#### 1.2.4 Mobile Ion

The introduction of mobile charge in  $\text{SiO}_2$  during plasma processes has been reported by McCaughan and Kushner (1974), and a model involving ion-insulator interactions has been proposed (McCaughan et al. 1973). It was assumed that, initially, electrically neutral or coulombically bonded immobile impurities may exist on the  $\text{SiO}_2$  surface. As positive plasma ions approach the  $\text{SiO}_2$  interface, they may be neutralized by electrons from the insulator surface through Auger or resonance transitions. Either holes in the valence band of  $\text{SiO}_2$  or positive ions from the surface impurities are produced as a result of this neutralization process. In the case positive ions such as  $\text{N}_a^+$  are produced, some of them could diffuse to the bulk of  $\text{SiO}_2$  and cause device instability. Experimental evidence in support of this model has also been reported (McCaughan et al. 1973).



### 1.3 LIMITATIONS OF THERMAL ANNEALING

Thermal annealing has been widely used to remove the defects caused by ionizing radiation, in which thermal energy serves to promote the recovery of the deformed bonds. If forming gas ( $H_2 + O_2$  mixture) is used, additional chemical reactions involving hydrogen may take place, which convert the electrically active broken bonds to neutral Si-H or Si-OH centers, and the annealing temperature can be reduced. It is believed that in MOS structures having Al-gate, a sufficient amount of hydrogen species could evolve from the Al-SiO<sub>2</sub> interface without external supply (Balk 1965).

The radiation-induced surface states and oxide charge in SiO<sub>2</sub> usually can be completely annealed out in forming gas at a temperature between 300° and 450°C. The latter is required for Si-gate MOS (Aitken 1979) and MNOS (Metal-Si<sub>3</sub>N<sub>4</sub>-SiO<sub>2</sub>-Si) structures (Deal 1974), presumably because it is more difficult for the hydrogen to diffuse into SiO<sub>2</sub> in such structures.

The radiation-induced neutral traps in SiO<sub>2</sub>, however, are much more difficult to anneal out, and a temperature range between 550°C to 700°C is required (Gdula 1979, Aitken 1979). Such high temperature requirement for the annealing of neutral traps suggests that a structural reordering is necessary (Aitken et al. 1978), which is consistent with the strained bond model discussed previously.

A serious limitation of thermal annealing arises after the aluminum metallization step, because significant Si and Al interdiffusion may take

place above 400°C (Best and McCaldin 1975). With the temperature limitation, not all of the radiation effects in SiO<sub>2</sub> can be removed by thermal annealing if the damage is introduced during or after the Al-metallization. An example of this is the E-beam or X-ray lithography step used to define the Al patterns.

Given the practical limitations of the conventional thermal annealing, there is a need for developing an alternative technique which can effectively anneal out the radiation effects without resorting to high temperatures. The RF plasma annealing technique, first introduced by Ma and Ma (1978), is just such a technique.

#### 1.4 RF PLASMA ANNEALING

This technique employs a low pressure RF plasma and is conceptually different from the conventional thermal annealing. It has been shown that, while the wafer temperature is typically much below that required for thermal annealing, RF plasma annealing is much more effective in removing the radiation effects in a wide variety of MOS and MNOS device structures (Ma and Ma 1978, 1979). Prior to this thesis work, although a significant amount of experimental results has been reported (Ma and Ma 1978), no systematic study has been made to investigate the detailed mechanisms involved in the annealing process. Therefore, it is the principal objective of this thesis research to address the more fundamental aspects of the RF plasma annealing process, and to advance the understanding of its mechanisms.

In Chapter II, we will describe the experimental annealing apparatus used in this work, which is an improved version of the original design reported by Ma and Ma (1978). The operation of the annealing system, its annealing performance, and the effective ranges of the annealing parameters will also be presented. In Chapter III, the nature of the RF plasma will be discussed, and the relevant plasma-wafer interactions will be examined. It will be shown that the X-ray flux in the RF plasma, its penetration and absorption in  $\text{SiO}_2$ , the RF voltage across the MOS wafer, and the induced wafer temperature can be obtained either theoretically or experimentally, and such information is essential to the subsequent modelling of the annealing mechanisms. In Chapter IV, we introduce an experimental simulation in which the RF plasma environment is simulated by the independently controlled RF voltage, X-ray irradiation, and wafer temperature. This experiment thus allows us to study the individual contribution of each of the above three parameters, and their cooperative effects. The results are qualitatively consistent with an annealing mechanism based on the REDR model. In Chapter V, we will review the theories of both the conventional thermal annealing and the REDR process, not only because of their similarity in the rate equations, but also because of their similarity in the physical mechanisms. It will be pointed out that much more work needs to be done in order to fully understand either process in a quantitative manner. In Chapter VI, the photocurrent in an MOS structure under X-ray irradiation will be studied. This study is relevant here because the modelling of the voltage and frequency dependences of the RF annealing rate requires such information.

It will be shown that the contact photoinjection component is a significant part of the total current, and its voltage dependence follows the internal photoemission theory developed previously for UV excitations. Finally, in Chapter VII, we will present the conclusion along with many comments and suggestions that might be useful for the future research in this field.

## CHAPTER II

### RF PLASMA ANNEALING : EXPERIMENTAL DETAILS AND ANNEALING RESULTS

#### 2.1 INTRODUCTION :

As mentioned previously, radiation sources such as electron beam, X-ray, and plasma can produce positive oxide charge, surface states, and electronic traps in thermal  $\text{SiO}_2$ . The radiation-induced surface states and oxide charge in  $\text{SiO}_2$  usually may be completely annealed out in forming gas at a temperature between  $300^\circ\text{C}$  -  $450^\circ\text{C}$  for 30 min. (Balk 1965). The radiation-induced neutral traps in  $\text{SiO}_2$ , however, are much more difficult to anneal out, and some of these traps cannot be removed by thermal annealing at temperatures as high as  $550^\circ\text{C}$  (Aitken et al. 1978, Gdula 1979, Aitken 1979). Although thermal annealing at higher temperature may be effective, it is not compatible with silicon IC processing with aluminum in place (Best and McCaldin 1975).

It is therefore desirable to develop an alternative annealing technique which is more effective than the conventional thermal annealing, but without involving as high a temperature. The RF plasma annealing seems to be just such a technique (Ma and Ma 1978, Ma and Chin 1980).

The original annealing apparatus, shown in Fig. 2.1(a) consists

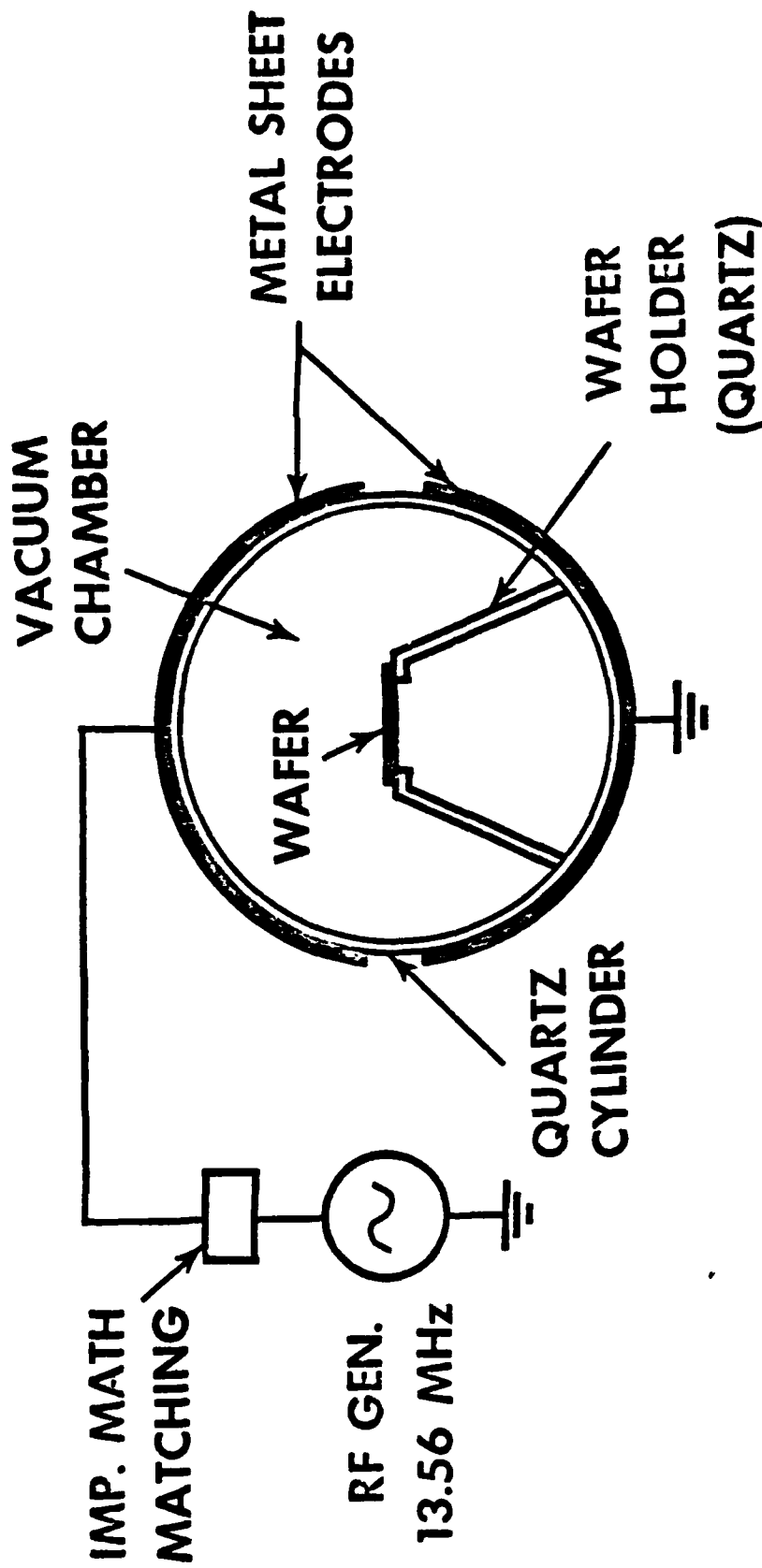


Fig. 2.1 (a) Schematic cross-sectional view of the original RF plasma annealing apparatus used at IBM.

of a cylindrical chamber and two sheet-metal electrodes surrounding it. This system was originally developed for plasma etching, and was adopted as an annealing tool for convenience. With this design, the electric field distribution is rather complicated, and certainly is not uniform across the wafer surface. Since the annealing rate depends on the electric field (see section 4.4), this design not only complicates the understanding of the annealing process, but also has the disadvantage that non-uniform annealing across a large-diameter wafer occurs.

In this Chapter, a newly-designed system with several improved features will be described. The operating conditions and experimental parameters for effective annealing will be presented. Sample preparation, measurements, and irradiation procedure will be detailed. The effectiveness of RF plasma annealing on the radiation-induced oxide charge, surface states and in particular, neutral traps will be reported. Besides MOS and MNOS capacitors, MOSFET's are also used in this study. Finally, a qualitative model is proposed for the mechanisms of RF plasma annealing.

## 2.2 ANNEALING APPARATUS

As shown schematically in Fig. 2.1(b), the newly-designed RF plasma annealing system consists of a pair of parallel-plate RF electrodes in a double-chamber low pressure plasma reactor, and a 13.56 MHz RF generator (1KW power rating) with appropriate impedance matching network is used to generate and sustain the RF plasma.

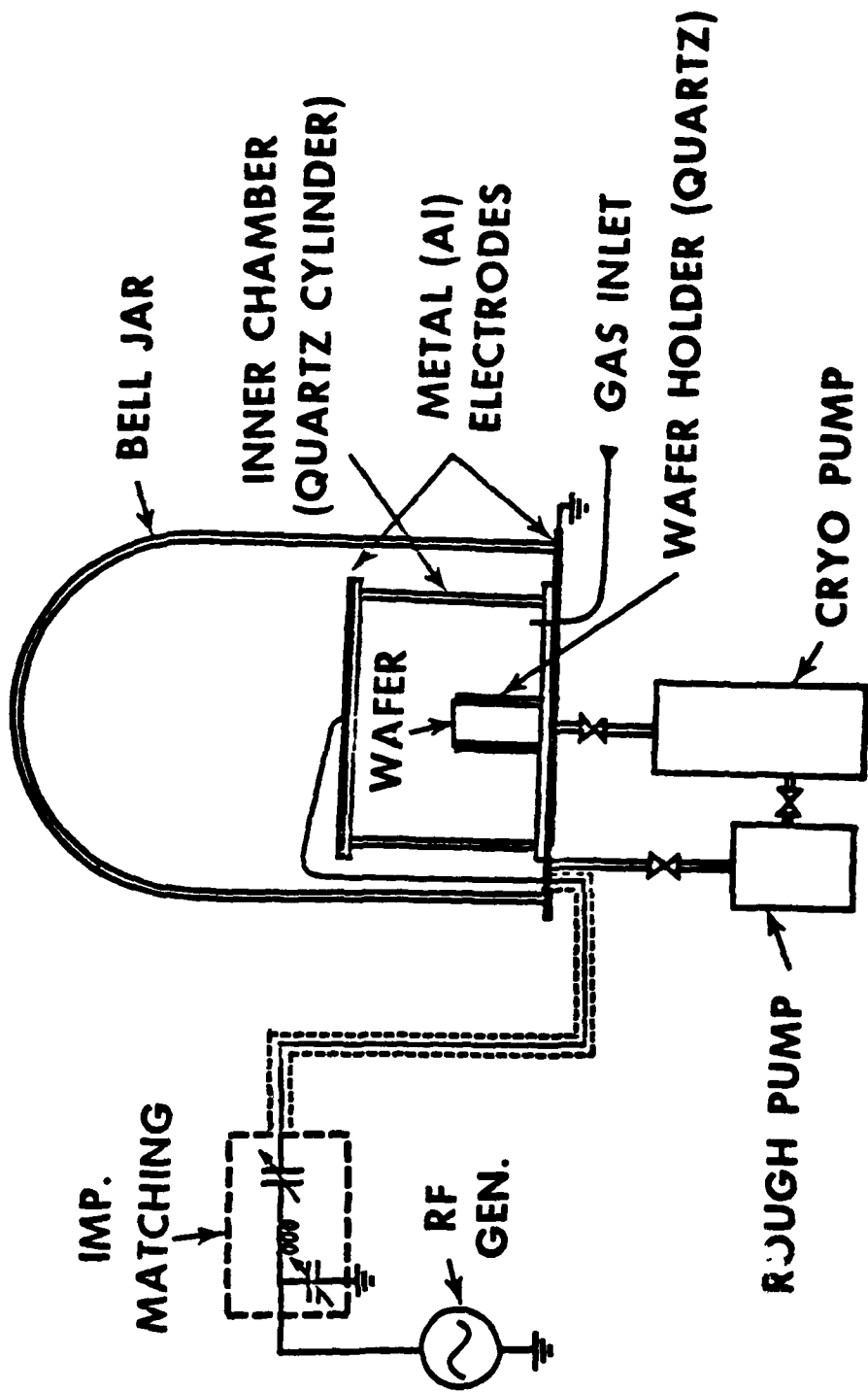


Fig. 2.1 (b) Schematic diagram of the parallel-plate RF plasma annealing system currently being used at Yale.



The pressure in the inner chamber (made of quartz) is maintained in the range between 1 and 10 microns. A differential pumping scheme is used to keep a lower pressure (approximately  $10^{-5}$  torr) in the outer chamber, and no plasma is sustained in there during an experiment. Confinement of the plasma inside the inner chamber is necessary to avoid back-sputtering and other contaminations due to plasma interactions with the pyrex Bell Jar, RF cable, and viton gasket in the outer chamber (see Appendix A for details).

Experimentally we have found that the level of contamination due to the pump oil vapor could significantly affect the annealing performance (see Appendix A), and it must be considered in the design of the annealing apparatus. For this reason, we use an oil-free cryo-pump instead of an oil diffusion pump for this system. A rotary rough pump, however, is used for initial pump-down to achieve a pressure of  $\sim 100\mu$  before the cryo-pump takes over, so as not to overly strain the cryo-pump. A molecular-sieve trap helps to minimize the back-streaming of the rough pump oil, and during annealing the rough pump is isolated from the chamber.

The spacing between the two parallel-plate electrodes is another important design parameter. Intuitively, it would seem that more efficient annealing could be achieved with smaller spacings. Empirically, however, it has been found that the minimum spacing for an effective annealing is approximately 7 inches. A smaller spacing tends to produce inconsistent results; sometimes radiation effect is observed for spacings less than 5 inches. At the present time, this spacing dependence is

not completely understood, but it is possible that the space-charge regions near the two electrodes extend well beyond the dark spaces, thus exerting a dc influence on the wafer (see Chapter III).

The wafer holder, made of quartz rods, is placed in the middle of the inner chamber. Four quartz rods, each forming an edge of a square, are joined together to form the top of the wafer holder which is supported by four legs. The wafer is resting on the top of the wafer holder so that both sides of the wafer are exposed to the plasma. The importance of this particular geometry is to avoid asymmetrical field effect on the sample, which has been discussed previously (Ma and Ma 1978).

The impedance-match tuning network serves to provide maximum power transfer to the plasma chamber. Because the load impedance of our system is quite different from those of most commercial plasma reactors, we found it necessary to modify our original LC tuning network which we obtained from Plasma Therm. Co. The design and construction of this modification is described in Appendix B.

### 2.3 OPERATION OF ANNEALING SYSTEM AND ANNEALING PARAMETERS

In a typical experiment, the rotary rough pump is used to initially pump down the whole system to a pressure of  $\sim 100\mu$  (this is in the viscous flow range and the back streaming is relatively light). Then, the rough pump is valved off and the high vacuum valve is open to pump the chamber down to a pressure below  $10^{-5}$  torr. Finally, the inner chamber

is backfilled with purified air (80% N<sub>2</sub> + 20% O<sub>2</sub>) to an operating pressure between 1 and 10 $\mu$ . At this point, one can turn on the RF power to initiate a plasma, and adjust the power state and the impedance-match tuning network until maximum transfer of RF power into the plasma chamber is achieved at the desired power level.

During the course of this annealing experiment, it has been found that the RF field orientation with respect to the wafer surface plane is a very important parameter which strongly affects the annealing performance. For best results, the wafer plane must be perpendicular to the RF field, as shown in Fig. 2.1(b). If the wafer is tilted substantially, sometimes radiation damage, rather than annealing, is observed.

It is also important that both sides of the wafer are exposed to the plasma during the annealing. For example, if the top of the wafer holder is made of a solid piece of quartz plate so that the bottom side of the wafer is not exposed to the plasma, then the effectiveness of the anneal is greatly reduced; in some cases additional damage to the wafer is observed.

The pressure range for the most effective RF plasma annealing has been experimentally determined to be 1 - 10 $\mu$ . For pressures below 1 $\mu$ , a stable plasma cannot be easily sustained, due to the long mean free path (~5 inches) of the electrons in the low pressure gas environment. For pressures above 10 $\mu$ , the plasma radiation damage rate starts to exceed the annealing rate, due to the increased ionizing

radiation flux generated at higher pressures.

The RF power used in our experiment ranges from 100 W to 600 W. The upper power level is limited by the present feedthrough design for the RF power cable. Due to the resistive heating and arc discharge, an electrical short could develop at the RF power feedthrough if more than 600 W is applied. The installation of proper cooling system for the RF power feedthrough is recommended for higher power operations. The lower RF power limit is determined by the desired annealing rate, which is a strong function of the RF power.

The annealing time typically ranges from 5 min to 30 min, depending on the sample structure, the type of defects to be annealed, and the history of damage. For example, radiation-damaged MNOS (Metal-Si<sub>3</sub>N<sub>4</sub>-SiO<sub>2</sub>-Semiconductor) structure is more difficult to anneal than MOS (section 2.5.1), and the electron-trapped centers after avalanche injection are more difficult to anneal than radiation-induced positive charge (Chin and Ma 1981).

## 2.4 EXPERIMENTAL DETAILS

### 2.4.1 Sample Preparation and Irradiation

The samples used in this study include MOS capacitors (with two different silicon doping concentrations), MNOS capacitors, and n-channel MOSFET's.

The MOS capacitors with higher doping concentration have square

Al-gate areas ranging from  $10 \times 10 \text{ mil}^2$  to  $40 \times 40 \text{ mil}^2$ . The starting silicon wafers are of (100) orientation and boron doped to a resistivity of  $1 \Omega\text{-cm}$ . The gate oxide, approximately  $500 \text{ \AA}$  in thickness, is grown in dry oxygen with HCl ( $98\% \text{ O}_2 + 2\% \text{ HCl}$ ) at  $1000^\circ\text{C}$ , followed by a dry  $\text{N}_2$  annealing at the growth temperature for 30 min. Following the gate oxide growth, the silicon surface is doped to  $1 \times 10^{17} \text{ cm}^{-3}$  by boron implantation through the oxide. The depth of implant is approximately 0.5 micron. A subsequent annealing step is done at  $1000^\circ\text{C}$  in He to activate the implanted boron and to remove the radiation damage. The gate aluminum is deposited in a magnetron sputtering apparatus, and gate area defined photolithographically. A post-metallization annealing is done at  $450^\circ\text{C}$  for 30 min in forming gas ( $15\% \text{ H}_2 + 85\% \text{ N}_2$ ).

The MOS capacitors with lower doping concentration and the MNOS capacitors have circular Al-gate areas with diameters ranging from 10 mil to 60 mil. These Si wafers are of (100) orientation, and are p-type boron doped to a resistivity of  $1 - 3 \Omega\text{-cm}$ . The thermal  $\text{SiO}_2$  is grown in dry  $\text{O}_2$  at  $970^\circ\text{C}$  to the desired thickness ( $300 \text{ \AA}$  for MNOS capacitors and  $\sim 600 \text{ \AA}$  for MOS capacitors), and subsequently annealed in dry  $\text{N}_2$  for 30 min. at the growth temperature. The  $\text{Si}_3\text{N}_4$  layer on the top of  $300 \text{ \AA}$   $\text{SiO}_2$  is CVD deposited to a thickness of approximately  $300 \text{ \AA}$  using  $\text{NH}_3$  and  $\text{SiH}_4$  (500 : 1) gases at a temperature of  $900^\circ\text{C}$ . The aluminum gate is evaporated from a resistance heated tantalum boat. A stainless steel mask is used to define the circular

gate areas. The post-metallization annealing is performed at 400 - 450°C for 30 min in forming gas (95% N<sub>2</sub> + 5% H<sub>2</sub>).

The MOSFET's are n-channel devices in a radiation-hardened CMOS test wafer supplied by Sandia Laboratory. The starting material is 1.2 - 1.5 Ω-cm, (100) oriented n-type silicon wafer, and the average p-well (boron doped) surface concentration is approximately  $5 \times 10^{16}$  cm<sup>-3</sup>. The gate oxide, approximately 700 Å in thickness, is grown in dry O<sub>2</sub> at 1000°C, followed by an annealing at 875°C in dry N<sub>2</sub>. After the gate-aluminum evaporation, the wafer is sintered at 450°C in dry N<sub>2</sub>. The channel length of the MOSFET's is approximately 7.5 microns.

Sample irradiation is done either in a Co<sup>60</sup> γ-ray chamber or by a moderate energy (≤35 KeV) X-ray beam; no external voltage bias is applied during the irradiation, and the accumulated radiation doses range from  $1 \times 10^5$  rad (Si) to  $1 \times 10^7$  rad (Si). No significant difference, both in radiation effects and in annealing behavior, has been observed between the two different radiation sources, and the results to be discussed are assumed to be representative for all ionizing radiation sources.

#### 2.4.2 Sample Measurements and Analysis

Information on oxide charge and surface states is obtained from high frequency (1MHz) and quasi-static C-V measurements on the MOS capacitors. Bias-temperature stress tests are used to determine the

extent of mobile ion charge in the oxide. Only those samples which exhibit low densities ( $< 1 \times 10^{11} \text{ cm}^{-2}$ ) of mobile ions are used in this study. Oxide traps are studied by the use of an avalanche injection circuit. The principles of these various measurements are discussed below.

#### A. Oxide Charge and Surface States

Oxide charge can be measured directly from the flatband voltage shift of the high frequency C-V curves. This voltage shift  $\Delta V_{\text{FB}}$  is related to the oxide charge, Q, by (Grove 1967, Sze 1969)

$$\Delta V_{\text{FB}} = - \frac{\bar{x}Q}{\epsilon_{\text{ox}}} = - \frac{\bar{x}}{d_{\text{ox}}} \frac{Q}{C_{\text{ox}}} \quad (2.1)$$

where  $\epsilon_{\text{ox}}$  is the permittivity of  $\text{SiO}_2$ ,  $\bar{x}$  is the centroid of the oxide charge distribution measured from the metal- $\text{SiO}_2$  interface,  $C_{\text{ox}}$  is the oxide capacitance and  $d_{\text{ox}}$  is the oxide thickness. Thus the flatband voltage not only depends on the density of the oxide charge, but also on its location within the oxide. When the oxide charge is located next to the  $\text{SiO}_2$ -Si interface, it will exert its maximum influence, and lead to

$$\Delta V_{\text{FB}} = - \frac{Q}{C_{\text{ox}}} \quad (2.1.1)$$

The surface states are measured by analyzing the high frequency C-V curves, the principle of which is discussed below.

Under a sufficiently low measurement frequency, the MOS capacitor,  $C(V_G)$ , at some applied gate voltage,  $V_G$ , is related to the equivalent circuit capacitances by the relation,

$$\frac{1}{C(V_G)} = \frac{1}{C_{ox}} + \frac{1}{C_{sc} + C_{ss}} \quad (2.2)$$

where  $C_{ss}$  is the capacitance due to surface states and  $C_{sc}$  is the semiconductor capacitance.

The total applied voltage across the device can be expressed as

$$V_G = \psi_s + V_{ox} \quad (2.3)$$

where  $\psi_s$  is the semiconductor surface potential, and  $V_{ox}$  is the potential across the oxide. We may write  $V_{ox}$  in terms of the space charge and surface state charge so that

$$V_G = \psi_s + (Q_{sc} + Q_{ss})/C_{ox} \quad (2.4)$$

consequently, from equations (2.2) and (2.4), and with the capacitance

definitions  $C_{sc} = \frac{dQ_{sc}}{d\psi_s}$  and  $C_{ss} = \frac{dQ_{ss}}{d\psi_s}$ ,

$$\begin{aligned} \frac{dV_G}{d\psi_s} &= 1 + \left( \frac{C_{sc} + C_{ss}}{C_{ox}} \right) \\ &= 1 + \left( \frac{C_{ox}}{C(V_G)} - 1 \right)^{-1} \end{aligned}$$

Hence, the variation of surface potential with applied voltage can be



simply determined from the low frequency (quasi-static) capacitance as

$$\frac{d\psi_s}{dV_G} = 1 - \frac{C(V_G)}{C_{ox}} \quad (2.5)$$

Integrating equation (2.5), the change in surface potential due to a change in applied MOS voltage from  $V_1$  to  $V_2$  is

$$\psi_s(V_1) - \psi_s(V_2) = \int_{V_1}^{V_2} \left[ 1 - \frac{C(V_G)}{C_{ox}} \right] dV_G \quad (2.6)$$

In particular, the integrated number of fast surface states between flatband ( $\psi_s = 0$ ) and inversion ( $\psi_s = 2\phi_B$ ) is of interest. From equation (2.6), we can write

$$2\phi_B = \int_{V_{FB}}^{V_I} \left[ \frac{C_{ox} - C(V_G)}{C_{ox}} \right] dV_G \quad (2.7)$$

where  $V_I$  is the inversion voltage, and  $V_{FB}$  is the flatband voltage ( $V_{FB}$ ,  $\phi_B$ , and  $Q_{sc}$  can be calculated from a high-frequency C-V trace).  $V_I$  can be determined using equation (2.7) by trial-and-error integration with a planimeter (Shine 1975). Thus equation (2.4) becomes

$$V_I = 2\phi_B + \frac{1}{C_{ox}} (Q_{sc} + Q_{ss}) \quad (2.8)$$

$$\text{and } N_{FS} = \frac{Q_{ss}}{q} = \frac{C_{ox}}{q} (V_I - 2\phi_B) - Q_{sc} \quad (2.9)$$

the integrated number of fast surface state per unit area can thus be obtained.

#### B. Oxide Traps (Neutral Traps)

The steady-state C-V measurements (high frequency and quasi-static) do not reveal the electronic traps in  $\text{SiO}_2$ . The presence of these traps, however, can be detected from the change in Si surface potential which results when electrons or holes are captured by these trapping centers. In our laboratory, the electron injection and trapping are provided by avalanche injection from the substrate of an MOS capacitor, or from the source (drain) junction of an MOSFET.

##### B.1 MOS Capacitor

In the substrate avalanche injection technique, first reported by Nicollian et al. (1970), the Si substrate is driven into deep depletion by means of an ac voltage. If the voltage amplitude is sufficiently large, avalanche breakdown in the Si substrate is induced during a portion of each cycle, giving rise to a hot electron distribution in the Si, some of which are injected into the  $\text{SiO}_2$  layer.

In the circuit described by Nicollian et al. (1971), a constant injection current is maintained by a feedback loop which applies a bias voltage on the sample to keep the field in the silicon constant. This bias voltage changes as some of the injected electrons are trapped in the  $\text{SiO}_2$ , and the amount of change corresponds to the flatband voltage shift. Thus this experimental setup provides

information about the device flatband shift as a function of time at a given injection current. The circuit we use, shown in Fig. 2.2, is similar to Nicollian's but with some slight modifications. In this circuit, a high frequency high voltage amplifier is used in place of the LC resonant branch originally used by Nicollian. Following a mathematical analysis to be briefly derived next, the effective density and the capture cross section of the electronic traps in the  $\text{SiO}_2$  layer may be obtained from such a measurement.

The trapping kinetics can be described by a first order rate equation given by (Ning and Yu 1974)

$$\frac{dn_t}{dt} = n_c V_t \sigma (N - n_t) \quad (2.10)$$

where

- $n_t$  = the trapped charge density.
- $N$  = the total trap density.
- $n_c$  = the conduction band electron density in  $\text{SiO}_2$ .
- $V_t$  = the thermal velocity.
- $\sigma$  = the capture cross section.

In order to relate this equation to the macroscopic current  $J$  measured in the external circuit, it is usually assumed that the thermal velocity of the electrons equals the drift velocity so that

$$J = qn_c V_d = qn_c V_t$$

This assumption is valid when the oxide field exceeds 1 MV/cm which

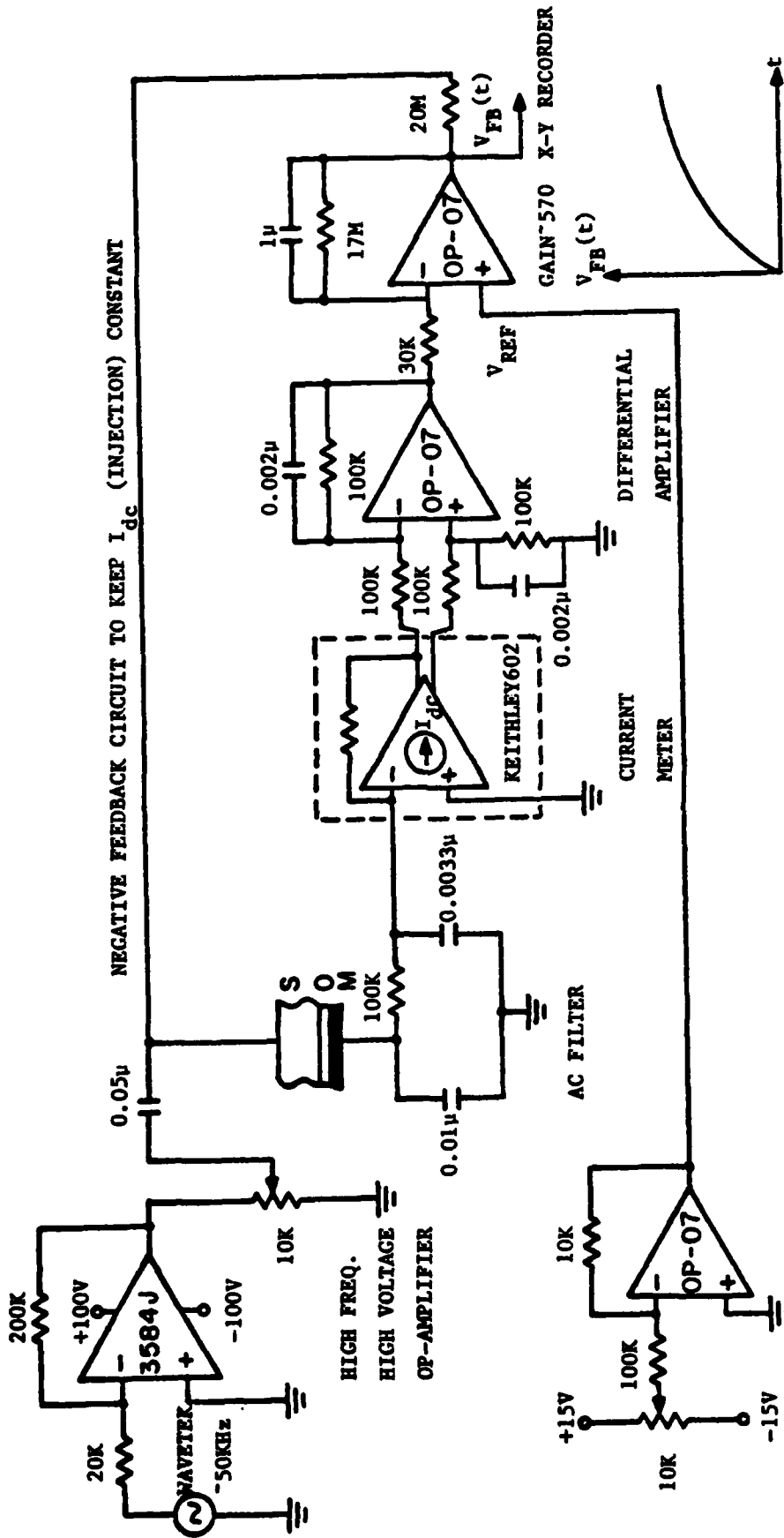


Fig. 2.2 Avalanche hot electron injection circuit with a flatband voltage monitor. Output is  $V_{FB}$  vs  $t$ .

is in general the case in an avalanche injection experiment. Thus equation (2.10) can be rewritten as

$$\frac{dn_t}{dt} = J \sigma (N - n_t) \quad (2.11)$$

Integrating the equation over the thickness of the  $\text{SiO}_2$ , one obtains

$$\frac{dQ}{dt} = \frac{J\sigma}{q} (qN_t - Q) \quad (2.12)$$

where  $Q = \int_0^d n_t dx$ , and  $N_t = \int_0^d N dx$ .

Equation (2.12) has the solution for a constant J

$$Q(t) = qN_t \left[ 1 - \exp\left(-\frac{\sigma J t}{q}\right) \right] \quad (2.13)$$

The trapped charge Q may be related to the flatband voltage shift by

$$\Delta V_{FB}(t) = -\frac{\bar{x}Q(t)}{\epsilon_{ox}} \quad (2.14)$$

where  $\bar{x}$  is the centroid of the trapped charge, and  $\epsilon_{ox}$  is the permittivity of the oxide.

Defining the effective trap density as

$$N_{eff} = \frac{\bar{x}N_t}{d_{ox}} \quad (2.15)$$

one can combine equations (2.13), (2.14) and (2.15) to yield

$$\Delta V_{FB}(t) = -\frac{qN_{eff}}{C_{ox}} \left[ 1 - \exp\left(-\frac{\sigma J t}{q}\right) \right] \quad (2.16)$$

where  $C_{ox} = \frac{\epsilon_{ox}}{d_{ox}}$  is the oxide capacitance per unit area. Equation (2.16)

then describes the time dependent flatband voltage shift that one measures during the constant current avalanche injection experiment.

If one takes the time derivative of equation (2.16), one finds

$$\frac{d}{dt} \Delta V_{FB}(t) = \frac{\sigma J N_{eff}}{C_{ox}} \exp\left(-\frac{\sigma J t}{q}\right) \quad (2.17)$$

The microscopic trapping parameters  $N_{eff}$  and  $\sigma$  are then obtainable from a plot of the natural logarithm of equation (2.17) against elapsed injection time as shown in Fig. 2.3. The slope of this line gives

$\frac{\sigma J}{q}$ , while the intercept at  $t = 0$  yields  $\frac{\sigma J N_{eff}}{C_{ox}}$ .

If more than one type of traps exist with different capture cross sections, more than one straight line segments will arise in this plot, and equation (2.17) can be modified as :

$$\frac{d}{dt} \Delta V_{FB}(t) = \sum_i \frac{J \sigma_i N_{effi}}{C_{ox}} \exp\left(-\frac{\sigma_i J t}{q}\right) \quad (2.18)$$

In order to obtain a uniform injection current and to reduce the edge effect of avalanche breakdown, a relatively large gate area is necessary for this measurement. The higher the Si doping concentration, the lower the applied voltage is required to reach avalanche condition.

In a typical experiment, the injection current density ranges from  $1 \times 10^{-8}$  A/cm<sup>2</sup> to  $5 \times 10^{-5}$  A/cm<sup>2</sup>, and is adjusted to reveal a wide range of traps. The flatband shifts, as measured by the feedback

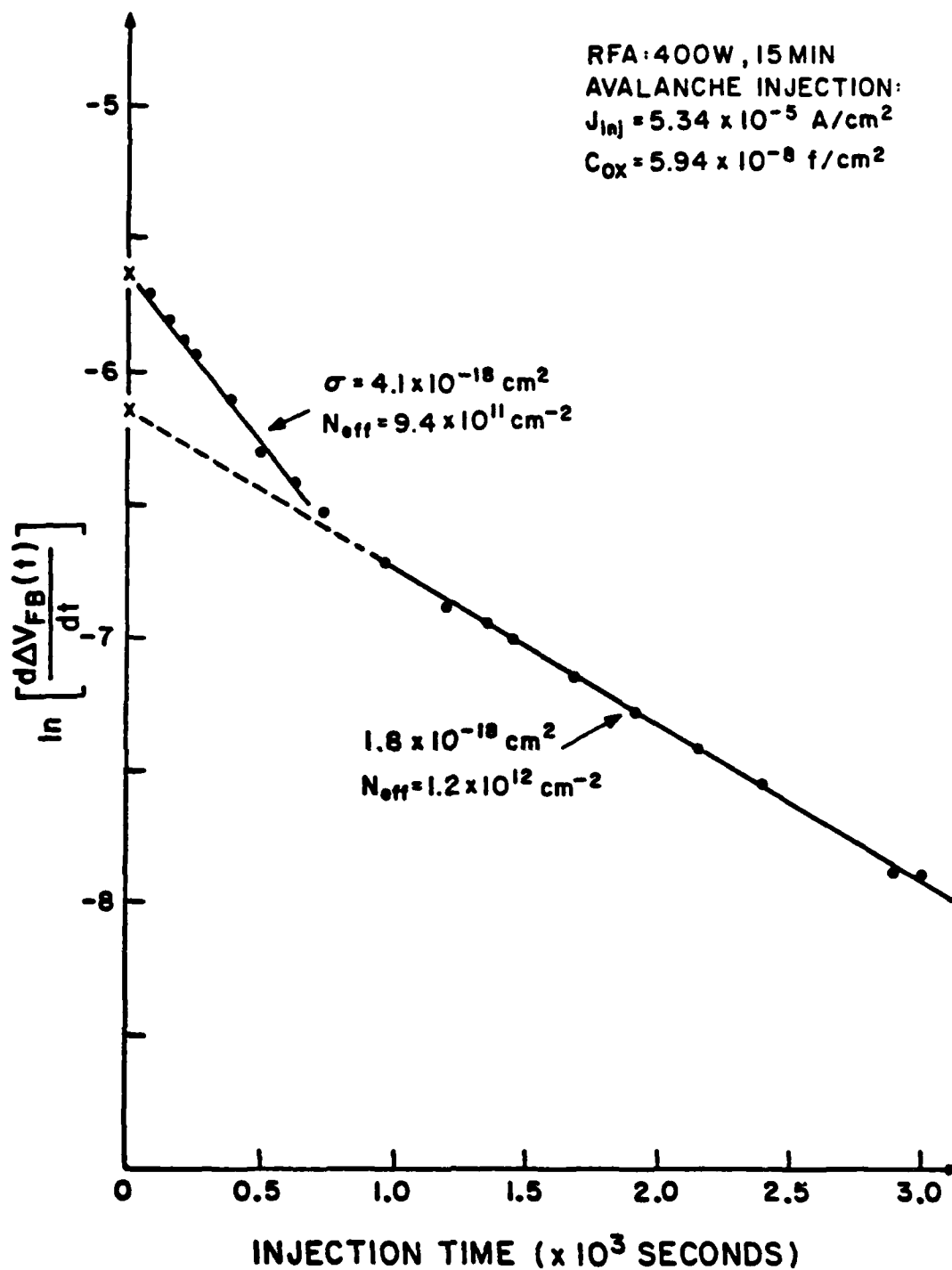


Fig. 2.3

An example showing the analysis of Eq. (2.17). The slopes of the straight line segments give rise to  $\sigma$ 's, while the intercepts at  $t = 0$  give rise to  $N_{eff}$ 's.

circuit, are frequently verified by an independent C-V measurement, and the agreement is typically within 0.1 V.

## B.2 MOSFET

In the MOSFET samples, the hot-electron injection is done by avalanching the source and drain junctions while keeping a positive bias on the gate. This bias creates an electric field in the gate oxide which enhances hot-electron injection from the substrate into the gate area. The trapping of the injected electrons in the gate oxide causes a shift in the threshold voltage, which is measured as a function of time under a constant stress condition. Notice that the principle of hot-electron injection in the MOSFET experiment is similar to that of FAMOS devices (Frohman-Bentchkowsky 1974), except that here constant voltages are applied instead of pulses. In our experiment, the junction breakdown current is maintained at 30 mA, and the gate voltage is 20 volts.

Unlike the experiment on the MOS capacitors, no quantitative information about the electron traps is obtained from the MOSFET experiment. The MOSFET experiment, however, does provide a qualitative comparison among the control, the irradiated, and the RF annealed samples. It also serves to verify that the RF annealing is effective on real device structures.

## 2.5 ANNEALING RESULTS AND DISCUSSIONS :



### 2.5.1 Oxide Charge and Surface States

The effectiveness of the RF plasma annealing is best illustrated in Fig. 2.4 where the high frequency (1 MHz) and quasi-static C-V curves of an MOS capacitor are plotted after X-ray radiation damage (curve 1), and after annealing for several minutes (curves 2 and 3). Since curve 3 coincides with the pre-irradiated curve, it is apparent that the radiation-induced oxide charge and surface states are completely removed in 5 min for this sample.

Fig. 2.5 shows the effect of RF power as an annealing parameter and the residual oxide charge and surface states are plotted as a function of annealing time. Within the power range of 300 - 500 W, most of the anneal is completed in the first 10 min.

Similar annealing behavior is observed for an MNOS capacitor consisting of a dielectric of  $300 \text{ \AA} \text{ Si}_3\text{N}_4$  on  $300 \text{ \AA} \text{ SiO}_2$  which is shown in Fig. 2.6. The conventional thermal annealing result is presented in the same figure for comparison. The annealing conditions are as specified in the figure. One can clearly see that, after the thermal anneal, there is still a substantial amount of charge centers and surface states remaining in the device, which is consistent with what has been reported, (Deal 1974 and Ma et al. 1976) and RF plasma annealing is far superior to thermal annealing in this case. The time for a complete anneal, however, is longer for the MNOS capacitor (25 min for this sample) than it is for an MOS capacitor.

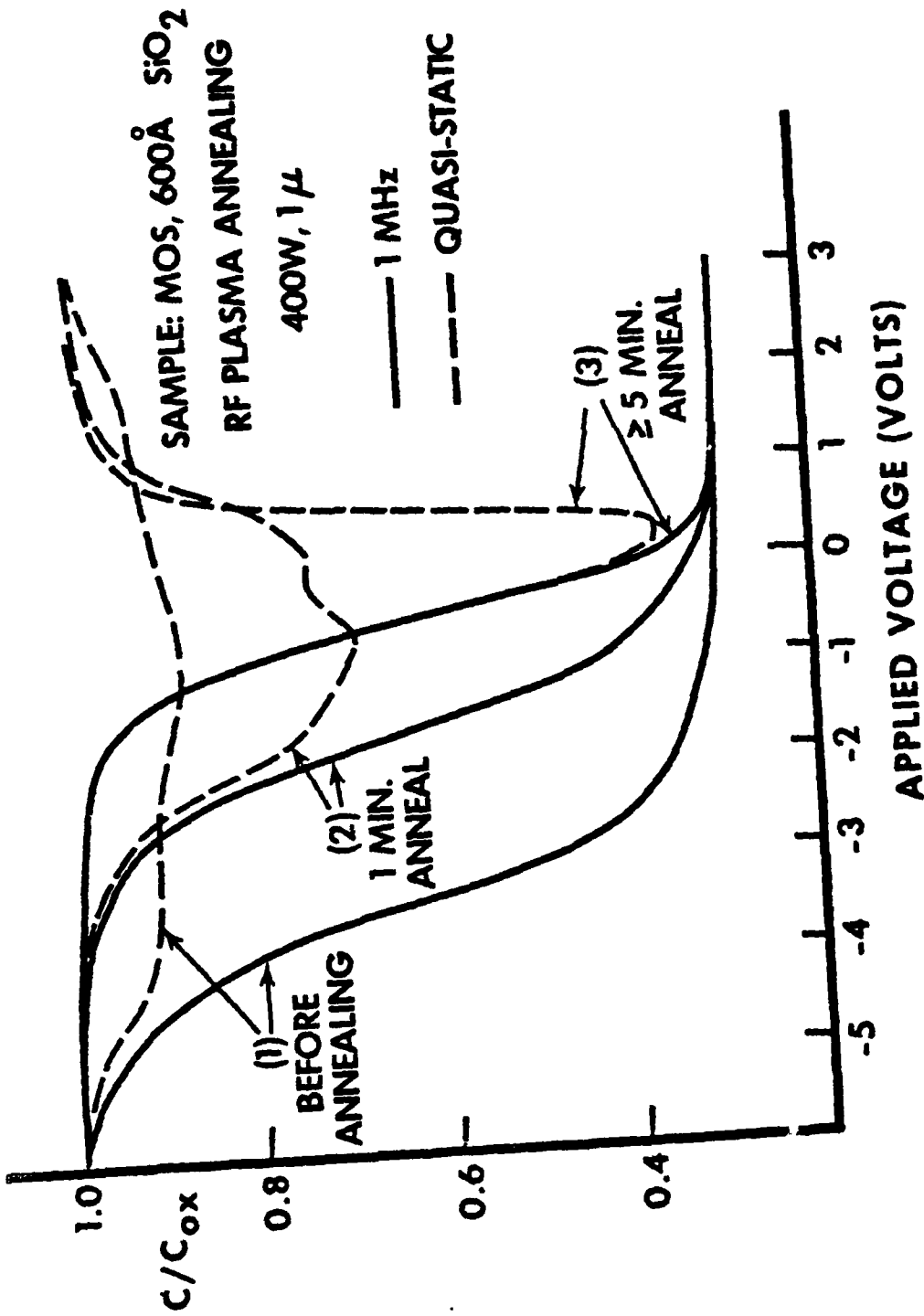


Fig. 2.4 1 MHz and quasi-static C-V curves of an MOS capacitor after radiation damage (curve 1) and after RF plasma annealing (curves 2 and 3).

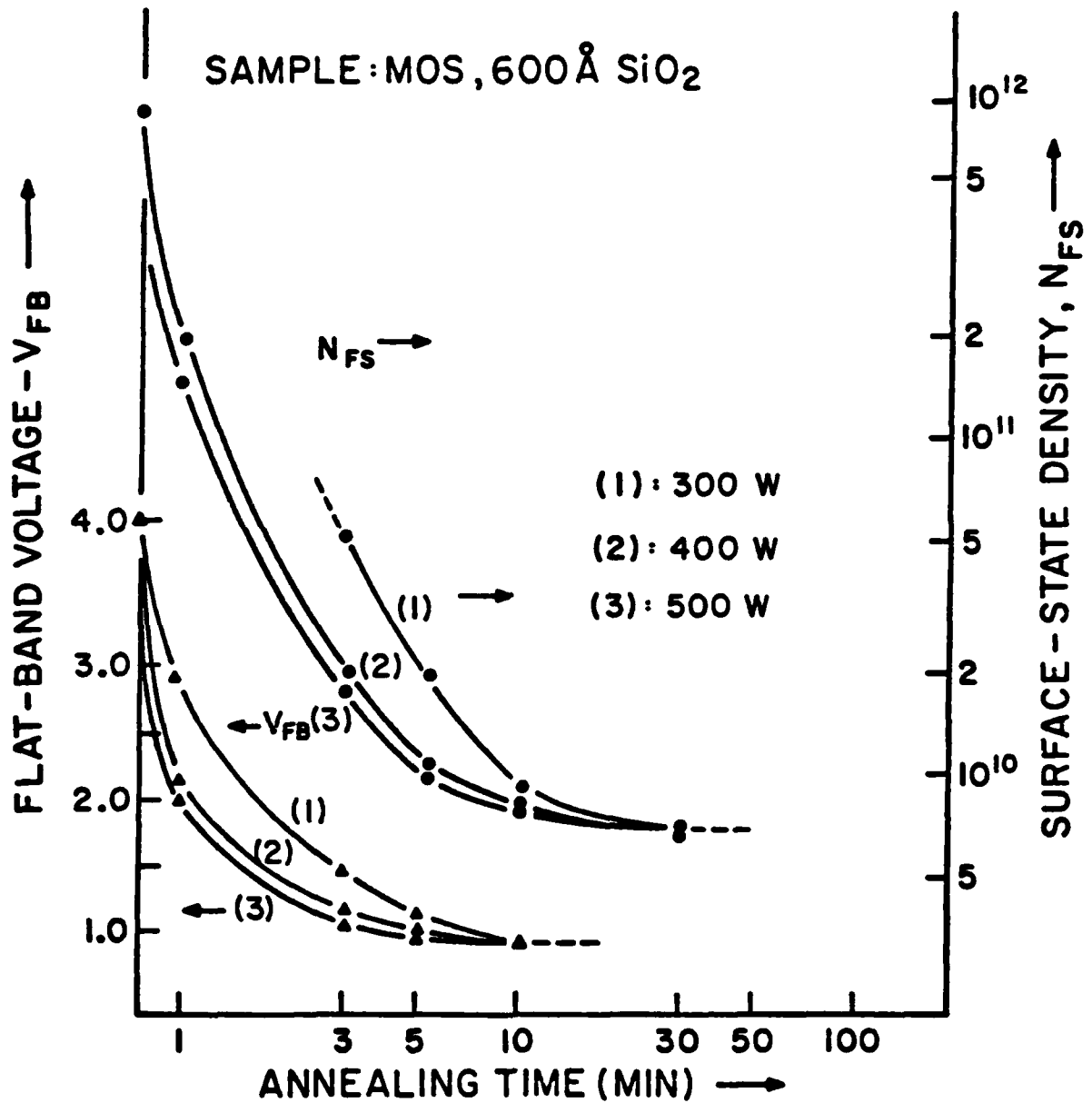
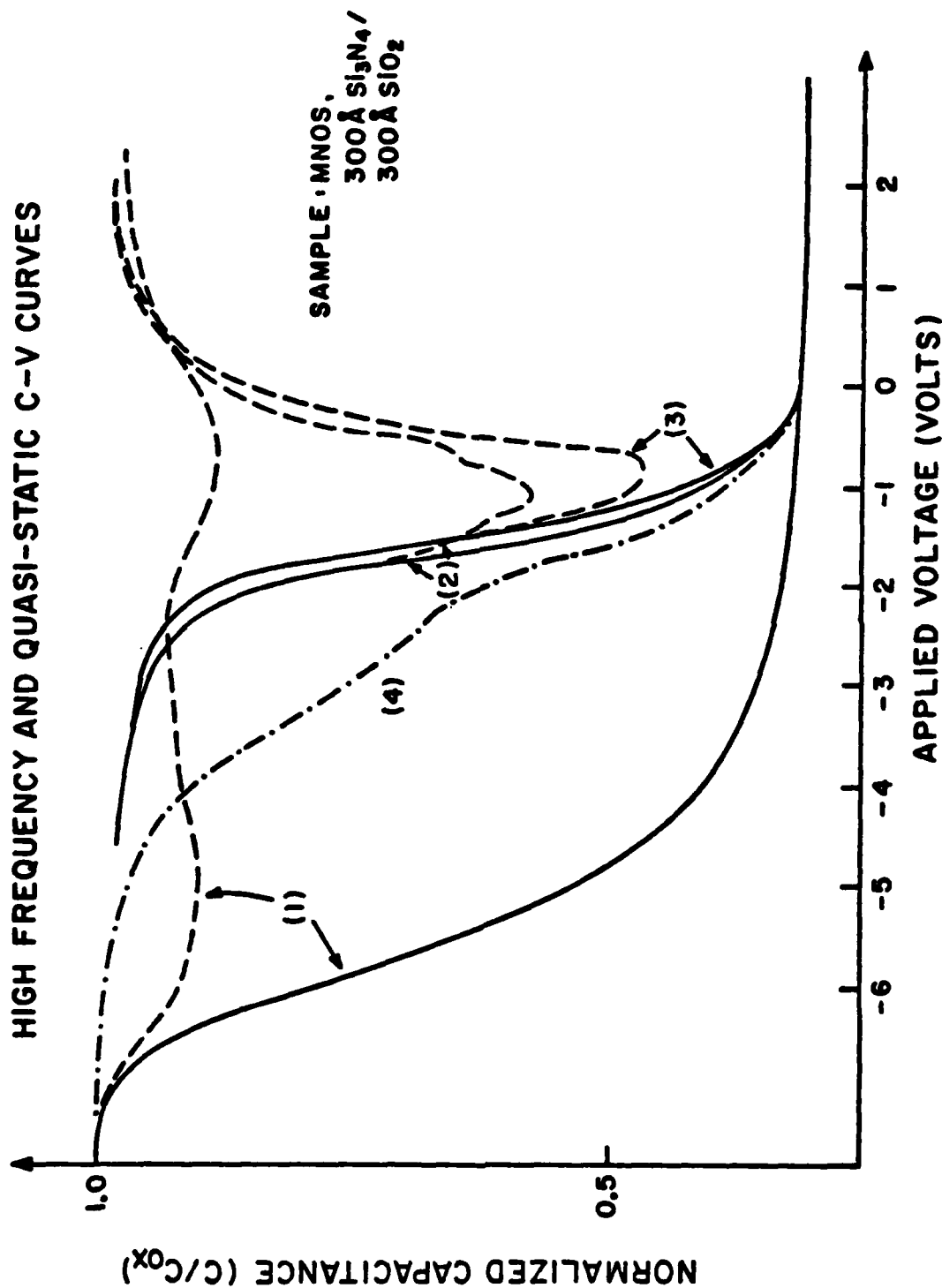


Fig. 2.5

Flatband voltage,  $V_{FB}$ , and surface-state density,  $N_{FS}$ , of an irradiated MOS capacitor as a function of annealing time at three different RF power levels.



**Fig. 2.6** High frequency and quasi-static C-V curves for an MNOS capacitor (300 Å/300 Å  $\text{Si}_3\text{N}_4$  / $\text{SiO}_2$  dielectrics). Curve 1: after irradiation. Curve 2: after irradiation and then 400W RF annealed for 15 min. Curve 3: after irradiation and then 400W RF annealed for 25 min. Curve 4: after irradiation and then forming-gas annealed at 400°C for 60 min.

## 2.5.2 Oxide Traps

### A. MOS Capacitors

Figure 2.7 shows the flatband shifts as a function of the number of injected electrons for the control (curve 1), irradiated (curve 2), post-irradiation thermally annealed (curve 3), and post-irradiation RF annealed (curves 4 and 5) samples. Right after the irradiation, the sample exhibited a radiation-induced flatband shift of -3 volts, corresponding to an increase of positive oxide charge of  $1.1 \times 10^{12} \text{ cm}^{-2}$ . A thermal annealing at  $425^\circ\text{C}$  for 30 min in  $\text{N}_2$  was found to have completely removed the radiation-induced shift from the C-V measurement. The data in Fig. 2.5, however, indicate that a substantial number of neutral traps, which are not detectable by the usual C-V measurement, have been generated by irradiation, and are not completely removed by the thermal anneal. This is in qualitative agreement with the findings of Aitken (1979) and Gdula (1979). RF plasma annealing on irradiated samples, however, shows improved trapping characteristics even when compared with the control.

The quantitative trap parameters have been analyzed from these curves, and are presented in Table 2.1. It is seen that the control sample exhibits three traps, all with relatively small capture cross-sections ( $\sigma$ ) and may be characterized as neutral traps (DiMaria, 1978). The irradiated sample shows three more traps ( $\sigma \sim 3.3 \times 10^{-16}$ ,  $3.5 \times 10^{-15}$ ,  $2.6 \times 10^{-14} \text{ cm}^2$ ) in addition to a substantial increase of the original traps. Some of the newly generated traps are undoubtedly Coulombic

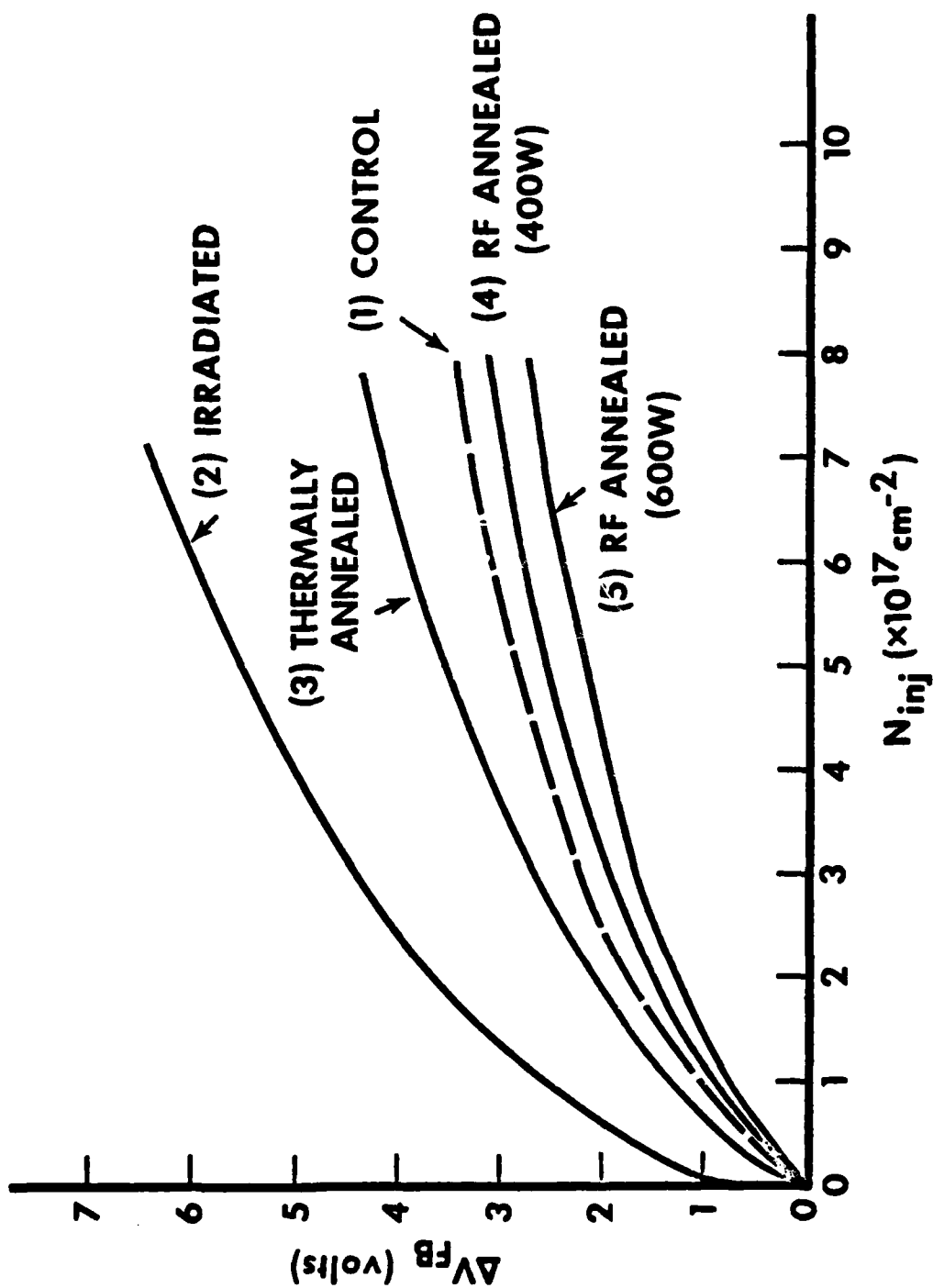


Fig. 2.7 MOS C-V shifts as a function of the number of electrons/cm<sup>2</sup> avalanche injected from the silicon substrate. Curve 1: control sample; Curve 2:  $\gamma$ -ray irradiated sample; Curve 3: thermally annealed (425°C in dry N<sub>2</sub> for 30 min) after irradiation; Curves 4 and 5: RF annealed at 400W and 600W after irradiation.

TABLE 2.1 Trap parameters obtained from Fig. 2.7.  $\sigma$  : Capture cross section,  
 $N_{\text{eff}}$  : Effective trap density.

TRAP PARAMETER		$\sigma$ (cm <sup>2</sup> )	$N_{\text{eff}}$ (cm <sup>-2</sup> )
SAMPLE			
CONTROL		$2.1 \times 10^{-18}$	$1.3 \times 10^{12}$
		$4.2 \times 10^{-18}$	$1.1 \times 10^{12}$
		$3.0 \times 10^{-17}$	$1.9 \times 10^{11}$
IRRADIATED		$1.8 \times 10^{-18}$	$1.7 \times 10^{12}$
		$4.4 \times 10^{-18}$	$1.1 \times 10^{12}$
		$2.8 \times 10^{-17}$	$6.7 \times 10^{11}$
		$3.3 \times 10^{-16}$	$7.9 \times 10^{11}$
		$3.5 \times 10^{-15}$	$5.4 \times 10^{11}$
		$2.6 \times 10^{-14}$	$1.2 \times 10^{12}$
THERMALLY ANNEALED AFTER IRRADIATION		$1.8 \times 10^{-18}$	$1.7 \times 10^{12}$
		$4.4 \times 10^{-18}$	$1.1 \times 10^{12}$
		$2.1 \times 10^{-17}$	$4.5 \times 10^{11}$
		$2.3 \times 10^{-16}$	$1.1 \times 10^{11}$
RF ANNEALED AFTER IRRADIATION	400W	$1.8 \times 10^{-18}$	$1.2 \times 10^{12}$
	600W	$4.1 \times 10^{-18}$	$9.4 \times 10^{11}$
		$1.9 \times 10^{-18}$	$1.2 \times 10^{12}$
		$4.2 \times 10^{-18}$	$8.4 \times 10^{11}$

centers with relatively large capture cross-sections. Thermal annealing has removed the two Coulombic traps, but one of the radiation-induced traps ( $\sigma \sim 3.3 \times 10^{-16} \text{ cm}^2$ ) remains.

The RF plasma annealing for this particular experiment is performed at a power level of 400 and 600 watts (the volume of the inner chamber is  $6400 \text{ cm}^3$ ) in a chamber pressure of approximately 5 microns. The annealing time is 15 minutes. The effects of lower and higher RF powers have also been studied, and preliminary results show that more than 250 watts is necessary to achieve complete anneal within 15 minutes.

One salient feature of the RF plasma annealing is that it not only has completely removed the radiation-induced electron traps ( $\sigma \sim 3.3 \times 10^{-16}$ ,  $3.5 \times 10^{-15}$ ,  $2.6 \times 10^{-14} \text{ cm}^2$ ), but also has removed one of the original traps that existed prior to irradiation ( $\sigma \sim 3 \times 10^{-17} \text{ cm}^2$ ) and reduced the densities of two other original traps.

#### B. MOSFET's

Fig. 2.8(a) shows the threshold voltage shifts,  $\Delta V_T$ , as a function of the avalanche injection time for an MOSFET before and after irradiation, and after RF plasma annealing. An example of the shifts in the transfer characteristics during hot-electron injection is shown in Fig. 2.8(b) for an irradiated sample. These results clearly indicate that the trapping probability in the gate oxide is significantly increased after irradiation, and has completely recovered after RF plasma annealing. Although no quantitative information about the trap parameters is obtained from this experiment, the results in Fig. 2.8(a) are consistent



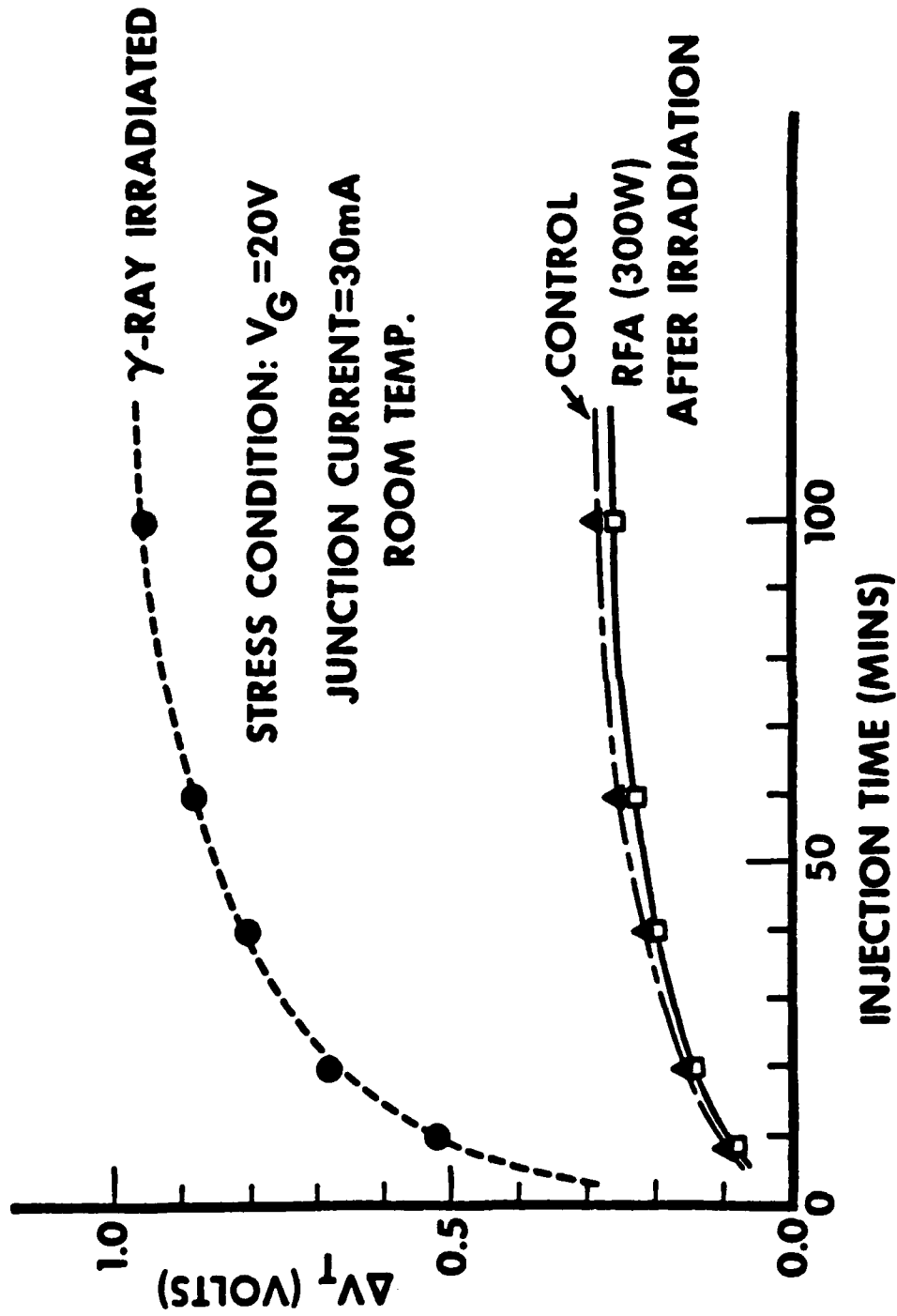


Fig. 2.8 (a) Threshold voltage shifts,  $\Delta V_T$ , as a function of avalanche injection time for an MOSFET before and after irradiation, and after RF plasma annealing.

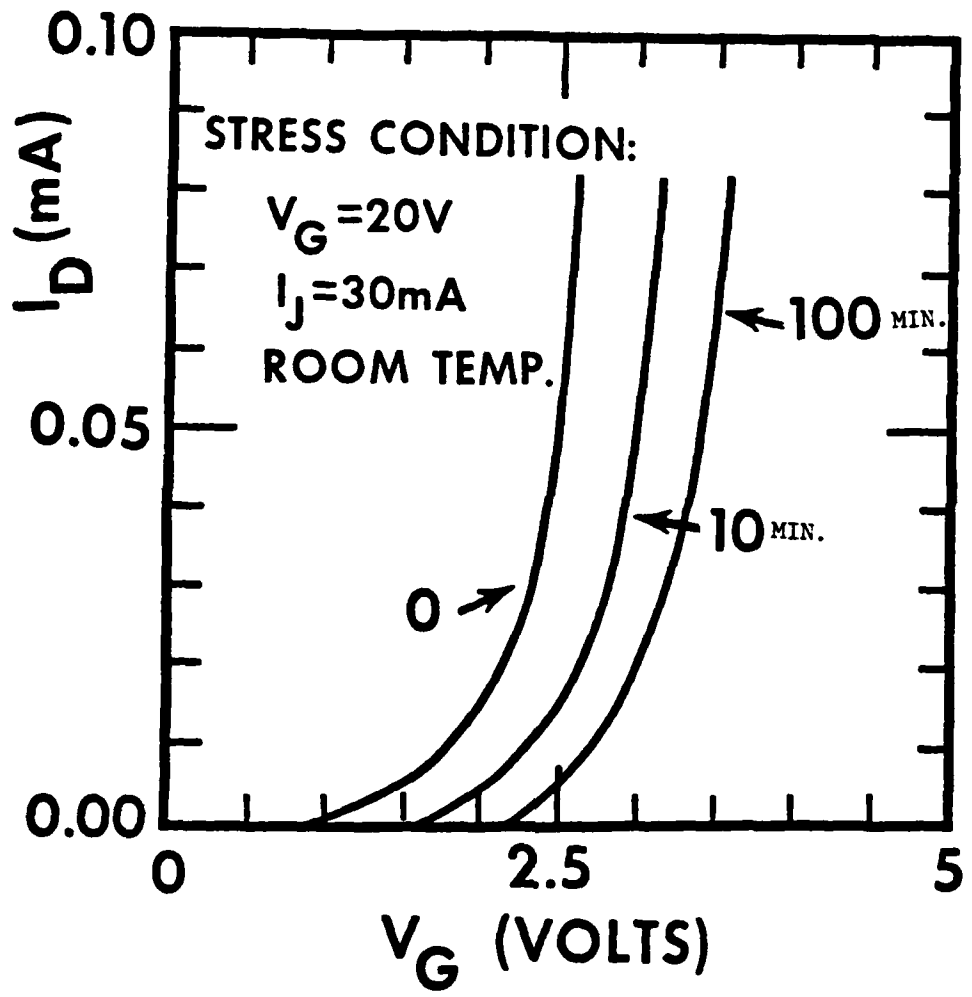


Fig. 2.8 (b) Shifts in transfer characteristics for an irradiated MOSFET after hot-electron injection for 0', 10', and 100', respectively.

with the results from the MOS capacitors.

## 2.6 CONCLUDING REMARKS : QUALITATIVE ANNEALING MODEL

In this chapter, we have shown the design and the operation of the parallel-plate RF plasma annealing system. Experimental results have been presented to demonstrate the effectiveness of this annealing technique. Its advantage over the conventional thermal annealing has been clearly brought out by the results in radiation-damaged MNOS structures and neutral traps where the latter technique has the most difficulty.

The results on the annealing of neutral traps are particularly interesting and are worth some discussion here. As shown in Fig. 2.7 and Table 2.1, the RF plasma annealing not only has completely removed the radiation-induced traps, but also has reduced some of the traps originally present in the sample prior to irradiation. These traps may have originated from the ion implantation and sputtering steps (see sample preparation in section 2.4.1), and were not completely removed by the subsequent heat treatments. The traps that are still remaining after the RF plasma annealing may be associated with the H<sub>2</sub>O related centers which have been reported to have similar capture cross-sections (Aitken et al. 1978, DiMaria 1978). It is not expected that RF plasma annealing would affect those traps that arise from chemical impurities.

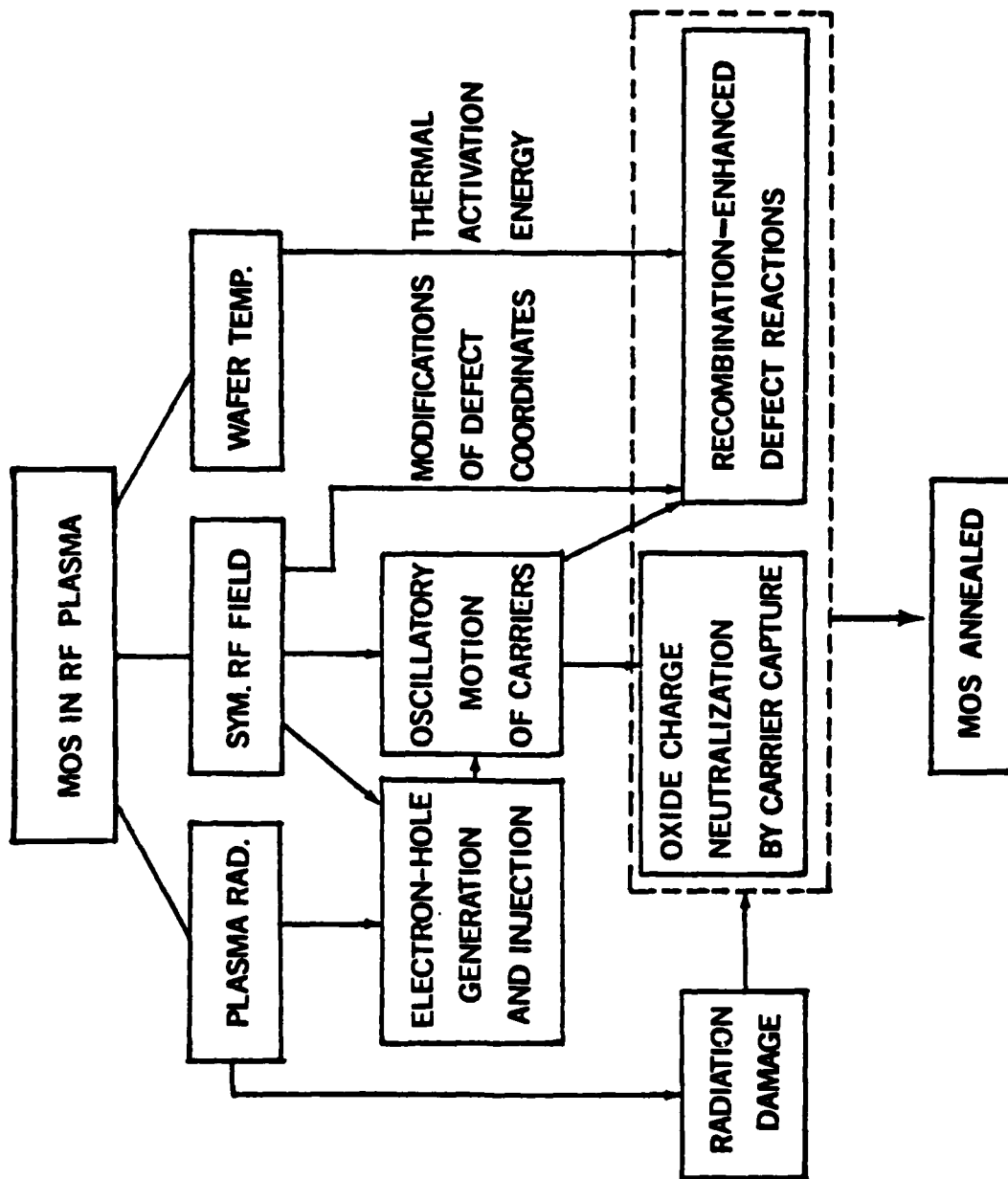
Without first analyzing the RF plasma and its detailed interactions

with the wafer, it is difficult to construct a meaningful model which can adequately describe the physics involved in the annealing process. However, based on the accumulated experimental evidence and some theoretical reasoning, Ma and Ma (1978) proposed a qualitative model which seems to have endured over the years. The essential features of this model will be presented here, and they will be reexamined in Chapters III and IV.

As shown in Fig. 2.9, the proposed annealing mechanism is qualitatively described in a block diagram. The MOS wafer in the RF plasma is subjected to the plasma radiation, a symmetric RF field across the oxide, and some induced wafer temperature, which are thought to be the three essential parameters that are responsible for the annealing process. The primary role of the plasma is to serve as an excitation source for the generation and injection of electrons and holes in the oxide. The RF field controls the motion and the recombination rate of these radiation-induced free carriers; it also modifies the defect reaction coordinates such that a more favorable reaction can be achieved (Ma and Ma 1978). Furthermore, the RF field along with the plasma-wafer interactions induces a moderate heating of the wafer, which provides the thermal activation energy and thus also contributes to the annealing.

The plasma-induced excess carriers could participate in two possible annealing processes. The first process involves the neutralization of the positive oxide charge centers through electron capture. The second process involves the more complicated recombination-enhanced-defect-

RF PLASMA ANNEALING MECHANISMS



Proposed RF plasma annealing mechanisms based on the plasma-wafer interaction, electron-hole generation, charge neutralization, and recombination-enhanced defect reactions.

Fig. 2.9

reactions (REDR), which have been observed in GaAs and some other semiconductors (Leamy and Kimerling 1977, Kimerling 1978), and could lead to the annihilation of the defects in  $\text{SiO}_2$ . The detailed theory of the REDR process and its significance in the RF annealing mechanism will be discussed in Chapter V.

The energetic plasma, although it plays a key role in the annealing process, is also a well known source of radiation damage (Zaininger 1967) if it acts alone. Therefore, the annealing process is in constant competition with the radiation damage process, and it is only through the proper cooperative interactions of all three essential annealing parameters that effective annealing is realized. This point will also be discussed in Chapter IV.

## CHAPTER III

### INTERACTION BETWEEN RF PLASMA AND MOS SAMPLE

#### 3.1 INTRODUCTION :

RF plasma has been widely used in various applications for quite a long time. Only recently has it become clear that one can take advantage of it for semiconductor fabrication, the most prominent example of which is plasma etching (or reactive ion etching). Another application, of course, is RF plasma annealing, which is the subject of interest here in this thesis.

In the previous Chapter, we proposed a qualitative annealing mechanism in which the annealing process was thought to be a result of the cooperative interactions involving plasma radiation, RF field across the wafer, and induced wafer temperature. In this Chapter, the RF plasma will be analyzed in more detail; in particular, the parameters that are relevant to the annealing process will be closely examined. In section 3.2, the various energetic species in an RF plasma will be reviewed. Their energy range and penetration depths through solids will be discussed. A separate section, section 3.3, is devoted to the discussion of UV and X-ray photons, because of their importance. The estimated photon flux absorbed by gate  $\text{SiO}_2$  will be calculated. In section 3.4, the induced wafer temperature in the RF plasma environment will be presented. In section 3.5, the RF voltage across the sample during RF plasma annealing will be estimated based on a theoretical calculation. Finally, we

conclude this Chapter with a brief comment on the interdependence of the plasma parameters.

### 3.2 THE NATURE OF THE RF PLASMA : IONS, ELECTRONS, NEUTRALS AND PHOTONS.

A plasma is a partially ionized gas which can be produced through the action of either very high temperatures or strong electric or magnetic fields. The present work focuses attention on the ionized gas produced by RF electric discharges. In a discharge, free electrons gain energy from an imposed electric field and lose this energy through collisions with neutral gas molecules. The transfer of the energy to the molecules leads to the formation of a variety of new active species including metastables, atoms, free radicals and ions.

Although the RF plasma is very complicated, the following parameters are reasonably common : the degree of ionization is usually about  $10^{-4}$ , the current densities are of the order of  $1 \text{ mA/cm}^2$ , and the electron velocity in the neutral plasma region where the electron density is equal to the positive ion density is much faster (three orders and corresponding to electron energy of  $\sim 2 \text{ eV}$ , Chapman 1980) than those of ions and neutrals.

In summary, a typical RF plasma contains :

- (1) charged particles, which include ions (positive and negative) and electrons with various kinetic energies; the Coulomb interaction between charges is both strong and long range,
- (2) neutral particles which include molecules, radicals, and atoms



either in their ground states or in various excited states, and  
(3) photons which include soft X-ray, ultraviolet, visible, and  
infrared light.

The glow associated with the RF plasma is mostly due to photons emitted during the radiative decay of the various excited neutral particles, sometimes due to the recombination of electrons and positive ions (Boley 1966, Chapman 1980). Soft X-ray and vacuum UV light is generated by the high energy electrons impinging upon an object, either the electrode plates, the chamber wall, or the sample.

The typical peak energies of these various species that exist in an RF plasma system have been summarized by McCaughan and Kushner (1974). The ions and neutrals usually do not exceed 200 eV, while the electrons and photons can have energies as high as the applied RF voltage (in the order of 1 - 2 KeV). Given their energies, the penetration depths of these various species can be obtained. For example, the mean free path of free electrons with 1 KeV energy in solid materials is approximately  $15 \text{ \AA}$  (C. C. Chang, 1975) which implies the penetration depth of these electrons is in the order of  $100 \text{ \AA}$ . The ions and neutrals have much larger masses and lower energies, and their penetration should be even shallower. Some experimental results have indicated that the bombardment of the ions in an RF plasma causes ion trapping within  $50 \text{ \AA}$  of the exposed sample surface (McCaughan et al. 1973, 1974, Deppe et al. 1977), which are consistent with the theoretical assessment.

From the above examination, one quickly reaches the conclusion

that the ions, neutrals, and electrons all have insufficient energy to penetrate through the gate aluminum and polysilicon of an MOS sample. The penetration of photons, however, is a different story, which will be presented in the next section.

### 3.3 ABSORPTION OF VUV AND X-RAY IN $\text{SiO}_2$

Fig. 3.1 shows the photon absorption coefficient as a function of photon energy for Al, Si and  $\text{SiO}_2$ . The data are collected from several publications (see references : Kane 1974, Samson 1967, Hovel 1975, and Oriel 1979). Here, the absorption coefficient,  $\mu$ , is defined by  $\Phi(x) = \Phi_0 e^{-\mu x}$ , where  $\Phi(x)$  is the photon flux at a distance from the sample surface and  $\Phi_0$  is the photon flux at the surface.

It can be seen that the aluminum film is semitransparent for photons with energies above 15.3 eV which is the plasma frequency of Al. Based on such data, the penetration depth of photons with different energies may be calculated. For example, the penetration depth in Al for a 1 KeV photon can be found to be approximately  $3\mu$ , which is considerably thicker than the Al gate used on our samples. Similarly, for a 350 eV photon, the penetration depth is approximately 4000 Å, which is very closed to the Al thickness. In the photon energy range  $h\nu \geq 15$  eV, the absorption spectrum for Si is very similar to that for Al, which is also shown in Fig. 3.1.

Due to the experimental limitations, we have not been able to measure the total photon flux in the plasma chamber. However, by

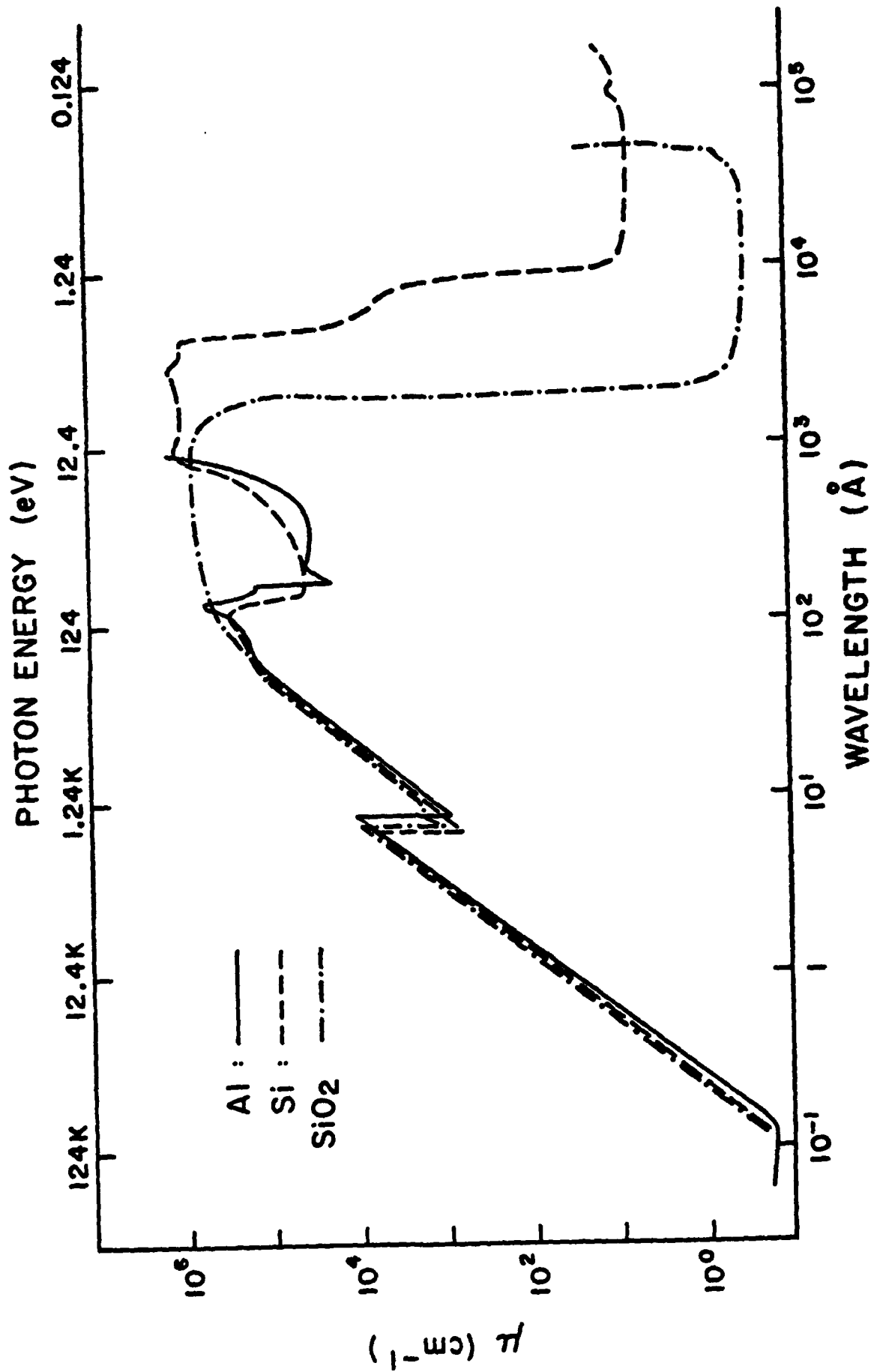


Fig. 3.1 Photon absorption coefficient as a function of photon energy. Solid curve corresponds to aluminum film, dashed curve corresponds to silicon film, and dash-dotted curve corresponds to SiO<sub>2</sub> film.

assuming that the deep UV and the soft X-ray photons are primarily generated by electrons impinging upon the RF plates (bremsstrahlung radiation), we can make an-order-of-magnitude estimate of the relevant photon flux.

From a theory given by Kirkpatrick (1946), the total bremsstrahlung energy  $U$  in MeV per absorbed electron, is given by

$$U = KZV^2 \quad (3.1)$$

where  $V$  is the total kinetic energy of electron in MeV,  $Z$  is the atomic number of the target material (for Al,  $Z = 13$ ), and  $K$  is a constant equal to  $0.7 \times 10^{-3} \text{ (MeV)}^{-1}$  for electron energy  $\ll 0.5$  MeV. If this bremsstrahlung energy is entirely converted to photons, then equation (3.1) can be used to calculate the photon flux generated in the RF plasma. The results are shown in Table 3.1 for RF powers in the range of 100 - 600 W.

Combining these results with the absorption coefficient data shown in Fig. 3.1, the total photon flux that penetrates through the Al gate and is absorbed by the  $\text{SiO}_2$  layer in an MOS sample can be calculated, and Table 3.2 shows the results for a sample with Al thickness ( $d_1$ ) of 3000 Å and  $\text{SiO}_2$  thickness ( $d_2$ ) of 500 Å.

It should be noted that the above results correspond to the maximum energy absorbed by gate  $\text{SiO}_2$ , and the procedure used for the calculation is the following :

Since in the photon range 0.3 - 2 KeV,  $\mu_1 = \mu_2 = \mu$ , where

RF POWER	MEASURED RF PEAK VOLTAGE	PLASMA CURRENT DENSITY	X-RAY ENERGY PER ELECTRON	AVAILABLE ELECTRON DENSITY	TOTAL AVAILABLE X-RAY FLUX
P (watts)	V (volts)	$J = 2P/(VA)$ (A/cm <sup>2</sup> )	$U = kZV^2$ (eV/e)	$N_e = J/q$ (e/cm <sup>2</sup> -sec)	$\Phi_0 = N_e U$ (eV/cm <sup>2</sup> -sec)
100	400	$1.54 \times 10^{-3}$	$1.46 \times 10^{-3}$	$9.60 \times 10^{15}$	$1.34 \times 10^{13}$
200	600	$2.06 \times 10^{-3}$	$3.28 \times 10^{-3}$	$1.29 \times 10^{16}$	$4.22 \times 10^{13}$
300	680	$2.72 \times 10^{-3}$	$4.20 \times 10^{-3}$	$1.70 \times 10^{16}$	$7.14 \times 10^{13}$
400	840	$2.93 \times 10^{-3}$	$6.42 \times 10^{-3}$	$1.83 \times 10^{16}$	$1.17 \times 10^{14}$
500	900	$3.42 \times 10^{-3}$	$7.37 \times 10^{-3}$	$2.14 \times 10^{16}$	$1.57 \times 10^{14}$
600	960	$3.85 \times 10^{-3}$	$8.39 \times 10^{-3}$	$2.40 \times 10^{16}$	$2.00 \times 10^{14}$

NOTE : "A" IS THE EFFECTIVE ELECTRODE AREA AND THE PLASMA CURRENT DENSITY (J), IN THE ORDER OF 1 mA/cm<sup>2</sup>, AGREES WITH B. CHAPMAN'S DATA (1980).

TABLE 3.1 Total available X-ray flux calculated using Eq. (3.1) for RF powers in the range of 100-600W.

P (W)	$\Phi_0$ (eV/cm <sup>2</sup> - sec)	$\Phi_1$ (eV/cm <sup>2</sup> - sec)	$\Phi_2$ (eV/cm <sup>2</sup> - sec)	$\Phi_{SiO_2}$ (eV/cm <sup>2</sup> - sec)	$N_{e-h}$ (#/cm <sup>2</sup> - sec)
100	$1.34 \times 10^{13}$	$5.36 \times 10^{12}$	$4.28 \times 10^{12}$	$1.08 \times 10^{12}$	$6.00 \times 10^{10}$
200	$4.22 \times 10^{13}$	$1.69 \times 10^{13}$	$1.35 \times 10^{13}$	$3.40 \times 10^{12}$	$1.89 \times 10^{11}$
300	$7.14 \times 10^{13}$	$2.86 \times 10^{13}$	$2.28 \times 10^{13}$	$5.80 \times 10^{12}$	$3.22 \times 10^{11}$
400	$1.17 \times 10^{14}$	$4.68 \times 10^{13}$	$3.74 \times 10^{13}$	$9.40 \times 10^{12}$	$5.22 \times 10^{11}$
500	$1.57 \times 10^{14}$	$6.28 \times 10^{13}$	$5.02 \times 10^{13}$	$1.26 \times 10^{13}$	$7.00 \times 10^{11}$
600	$2.00 \times 10^{14}$	$8.00 \times 10^{13}$	$6.40 \times 10^{13}$	$1.60 \times 10^{13}$	$8.90 \times 10^{11}$

Where  $\Phi_0$  is the total available photon flux from Table 3.1,

$\Phi_1$  is the photon flux right at the interface of Al and SiO<sub>2</sub>,

$\Phi_2$  is the photon flux at the interface of Si and SiO<sub>2</sub>,

$\Phi_{SiO_2} = \Phi_2 - \Phi_1$  is the energy absorbed by gate SiO<sub>2</sub>, and

$N_{e-h} = \Phi_{SiO_2} / 18$  eV is the free carrier generation rate with a pair generation energy of 18 eV.

TABLE 3.2

Procedure to calculate the total photon flux absorbed by the SiO<sub>2</sub> layer in an MOS sample with the data of TABLE 3.1.

$\mu_1$  = the absorption coefficient of Al and  $\mu_2$  = the absorption coefficient of  $\text{SiO}_2$ .

$$\Phi_1 = \Phi_0 e^{-\mu_1 d_1} = \Phi_0 e^{-\mu d_1}$$

$$\Phi_2 = \Phi_1 e^{-\mu_2 d_2} = \Phi_0 e^{-\mu d_1} e^{-\mu d_2} = \Phi_0 e^{-\mu(d_1 + d_2)}$$

$$\text{Hence, } \Phi_{\text{SiO}_2} = \Phi_1 - \Phi_2 = \Phi_0 \left[ e^{-\mu d_1} - e^{-\mu(d_1 + d_2)} \right]$$

Maximizing  $\Phi_{\text{SiO}_2}$ , one finds

$$\mu = \frac{1}{d_2} \ln \frac{d_1 + d_2}{d_1} \quad (3.2)$$

For the particular sample under consideration,

$$\mu = 2.3 \times 10^4 \text{ cm}^{-1}$$

From Fig. 3.1, the corresponding photon energy for this absorption coefficient is approximately 1 KeV. Therefore, the results in Table 3.2 are only accurate if the X-ray in the plasma has a monochromatic energy of 1 KeV. Since we do not know the exact energy distribution of the X-ray, what we have presented represents an upper limit.

#### 3.4 WAFER TEMPERATURE INDUCED IN THE RF PLASMA

Inside the RF plasma chamber, the sample is not intentionally

heated, but due to its interaction with the RF plasma, the wafer temperature does rise, and saturates within 10 minutes to a value between 50°C and 300°C, depending on the RF power used, 100 W to 600 W (Ma and Ma 1978). The wafer temperature has been monitored by a thermocouple attached to the wafer surface. The measurements are done in a "power-on" state using a high frequency L/C filter and an external temperature reference (Logan 1970, Kurylo 1978). Normally the wafer temperature rises within 10% of its final value in a period of 2 min or less. It is believed that the saturated temperature results from a rather delicate balance between heat input through plasma bombardment and induced eddy current, and heat loss through conduction and radiation.

Fig. 3.2 shows Logan's data (shaded area) for different types of substrates under 2 $\mu$  pressure. Kurylo's temperature results for a pressure range of 16 - 23 $\mu$  are also shown in the same graph for comparison. Therefore one can conclude that even at a very high RF power level ~800 Watts (~2.5 W/cm<sup>2</sup>), the wafer temperature does not exceed 400°C. These results strongly suggest that the dominant mechanism in RF plasma annealing is not thermal annealing in the conventional sense, because a temperature range of 550 - 700°C is required in the conventional thermal annealing to completely remove the radiation-induced neutral traps (Aitken et al. 1978, Gdula 1979, Aitken 1979).

### 3.5 RF VOLTAGE ACROSS MOS SAMPLE

Since it is conceptually easier to understand the voltage



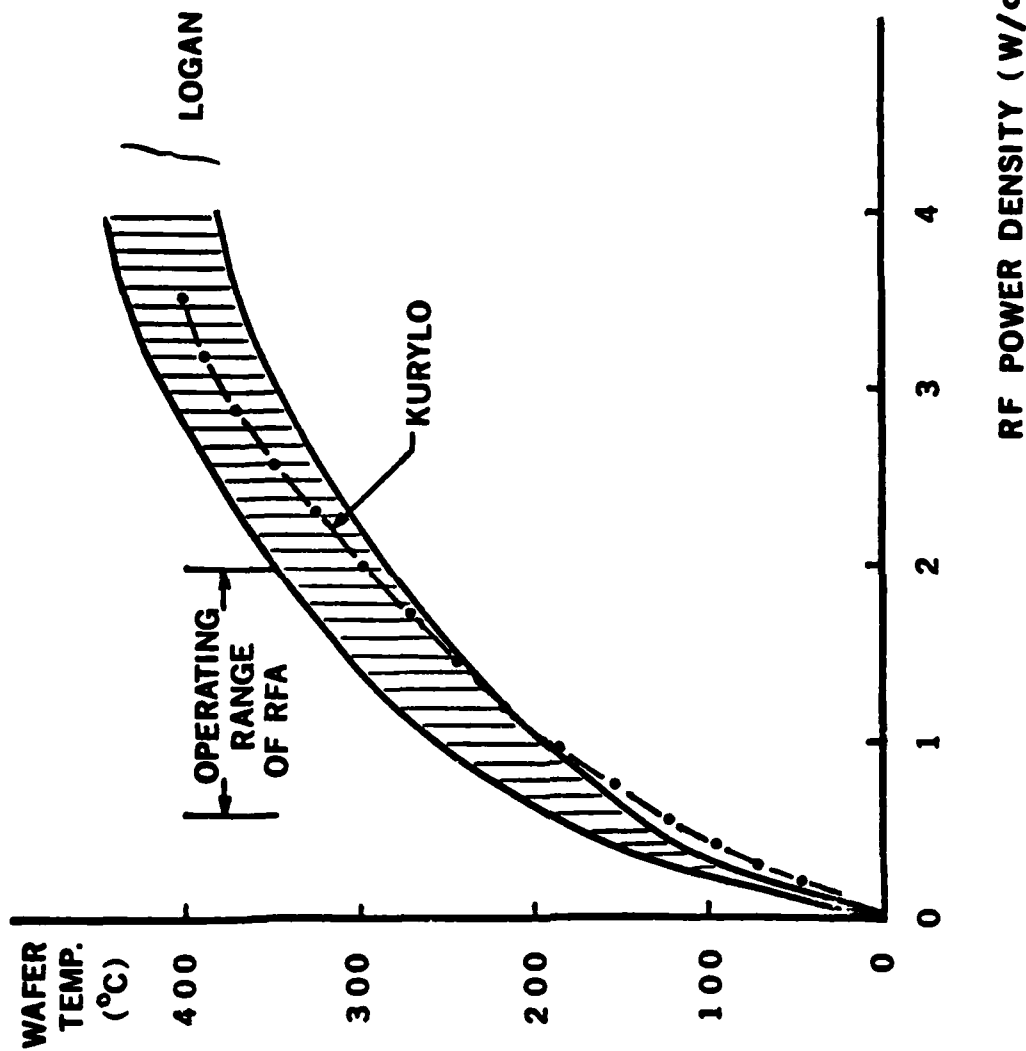


Fig. 3.2

Wafer temperature as a function of RF power density. Shaded area: Logan's data (1970) for different types of substrates under 2 $\mu$  pressure. Dash-dotted curve: Kurylo's data (1978) for pressures of 16-23 $\mu$ .

development across an MOS wafer in a dc plasma, we will examine the dc system first. It will be shown afterwards that the results can be readily modified for the ac system.

Consider an MOS device wafer suspended in a dc plasma. Initially the wafer will be struck by electrons and ions. Because of the much higher electron velocity, the sample surface immediately starts to buildup a negative charge (see section 3.2 and Chapman 1980) and hence a negative potential with respect to the plasma. As a result, the quasi-random motions of ions and electrons in the region of the wafer are disturbed. Since the sample surface charges negatively, electrons are repelled and positive ions are attracted. Thus the electron flux decreases, but the sample continues to charge negatively until the electron flux is reduced by repulsion just enough to balance the ion flux. Since electrons are repelled by the potential difference, it follows that the isolated sample will have a net negative charge surrounded by positive charges. This is generally known as a space charge, and in the context of glow discharge plasma, it forms a sheath and so the plasma potential,  $V_p$ , is always positive with respect to the floating potential,  $V_f$ , associated with the isolated sample (Chapman 1980).

Poisson's equation can be used to relate the variation of voltage with the distance across the space charge region (positive ions) and the Maxwell-Boltzmann distribution function gives the distribution of free electrons within the plasma. From the solution to the Poisson's equation, one obtains the potential distribution near the sample as :

$$V(x) = (V_f - V_p) e^{-x/\lambda_D} + V_p \quad (3.3)$$

where  $\lambda_D = \left( \frac{KT_e \epsilon_0}{n_e e^2} \right)^{1/2}$ ,  $n_e$  is the ionized charge density and  $V_f$  and  $V_p$  are as defined in Fig. 3.3. In Fig. 3.3, the steady-state voltage distribution is shown schematically with a sample floating in a 700 V dc glow discharge.

Now turn to the RF case. If the RF discharge system is symmetrical and the electron motion can readily respond and follow the ac frequency, the RF voltage distribution can be derived directly from the dc case, because the system can be simply viewed as a dc discharge with continuously varying amplitude and periodic switching in polarity.

Following this line of reasoning (Chapman 1980), the sheath potentials near the two electrodes and the sample can be expressed as a combination of dc and ac components as shown in Fig. 3.4(a). If the positive ions near the sample can be completely neutralized by the large electron flux from the electrode in each half RF cycle, then the amplitude of the RF voltage across the sample can be written as twice the sheath voltage between the plasma and the sample surface, and a symmetrical RF voltage having zero dc component will be developed across the sample. The voltage wave-forms near the electrodes and the sample are shown in Fig. 3.4(b).

The above discussion is a qualitative physical description. In order to estimate the amplitude of the RF voltage across the device, one

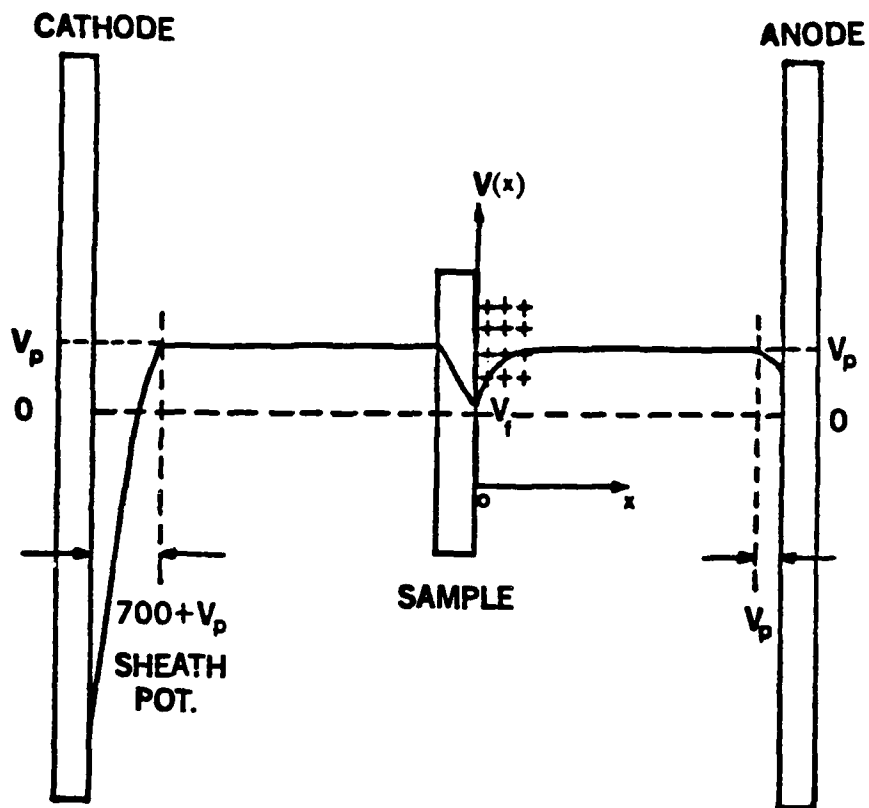


Fig. 3.3

Voltage distribution in a dc plasma system. Variations of the electrical potential are depicted in the vicinity of a floating sample.

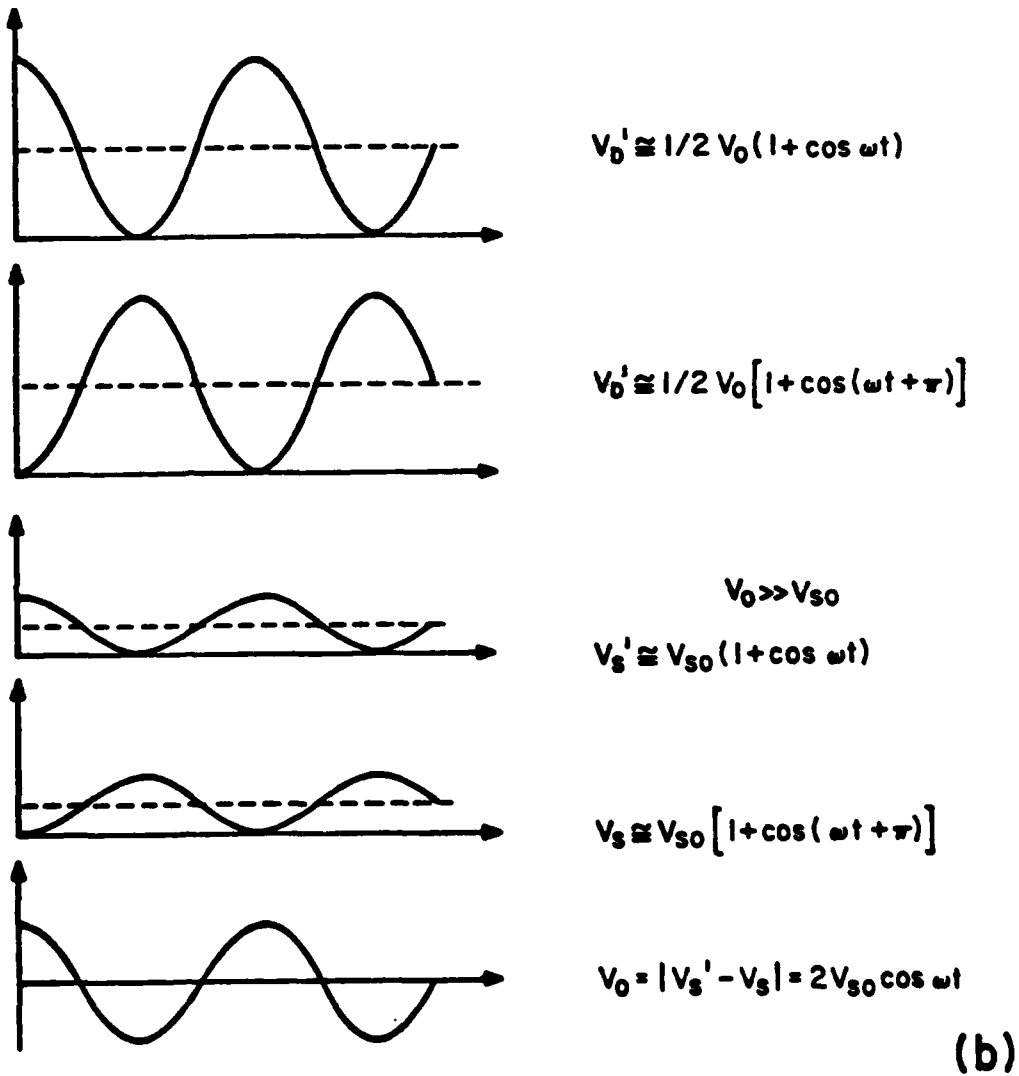
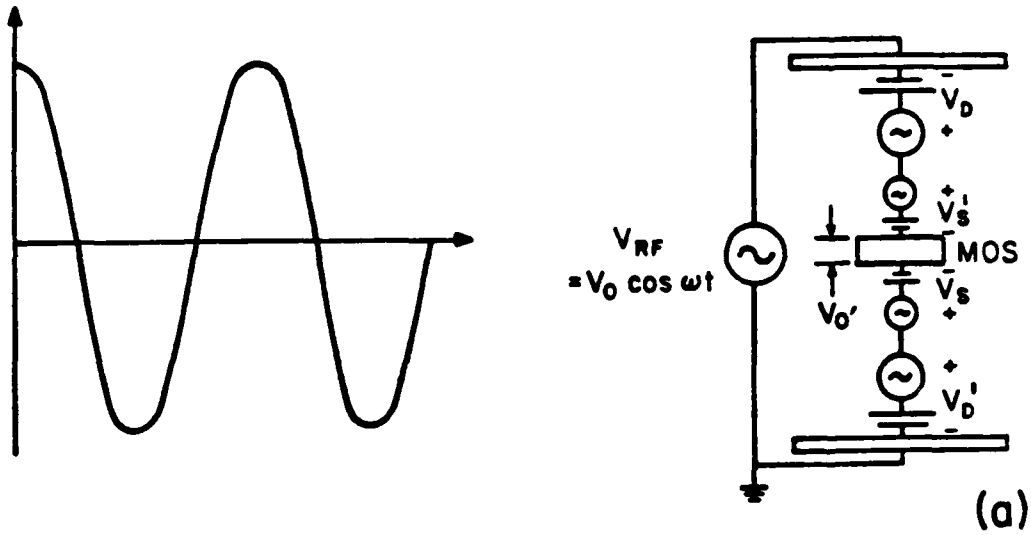


Fig. 3.4 (a) Schematic diagram showing the voltage distribution in a symmetrical RF plasma system.

(b) Possible waveforms of sheath voltages near electrodes and example

must do some numerical calculations based on an equivalent circuit model which is described next.

The RF plasma annealing system with an MOS sample in it is represented as a load impedance,  $Z_L$ , whose equivalent circuit is shown in Fig. 3.5(a) (Logan et al. 1969, Keller and Pennebaker 1979, Chapman 1980) where the  $r_s$ 's represent the lumped resistances in the space charge region,  $d_{se}$ 's are diodes representing the rectifying behavior of the electron flow across the space charge regions,  $C_{se}$ 's are the sheath capacitances of the space charge regions near the two electrodes,  $R_p$ 's are the lumped plasma resistances surrounding the MOS wafer,  $R_p/2$ 's are the lumped plasma resistances connecting the MOS sample to the sheath capacitances (Here the impedance of the MOS sample is negligible compared with  $R_p/2$ , as will be shown later in this section), and  $C_{st}$  is the stray capacitance.

The load impedance  $Z_L$  can be further simplified as an equivalent RC parallel network (Logan et al. 1969) shown in Fig. 3.5(b), where  $G_L$  is the total equivalent plasma conductance of the load, and  $C_L$  is the total equivalent capacitance of the load.

The equivalent load impedance,  $Z_L$ , can be calculated using the maximum power transfer theory (see Appendix B), from which the in-phase and quadrature components of the current,  $J_G$  and  $J_C$ , can be obtained. The stray capacitance,  $C_{st}$ , can be directly measured from the shield assembly of the main power line, and it has been found  $C_{st} = 125$  pf.

Following the procedure described in Appendix B, the following

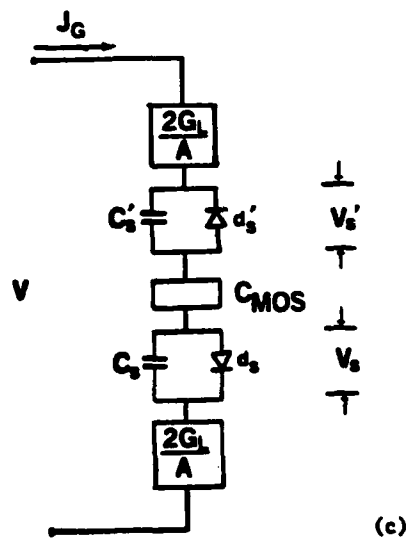
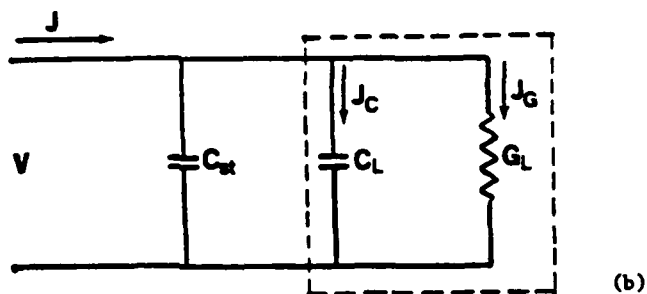
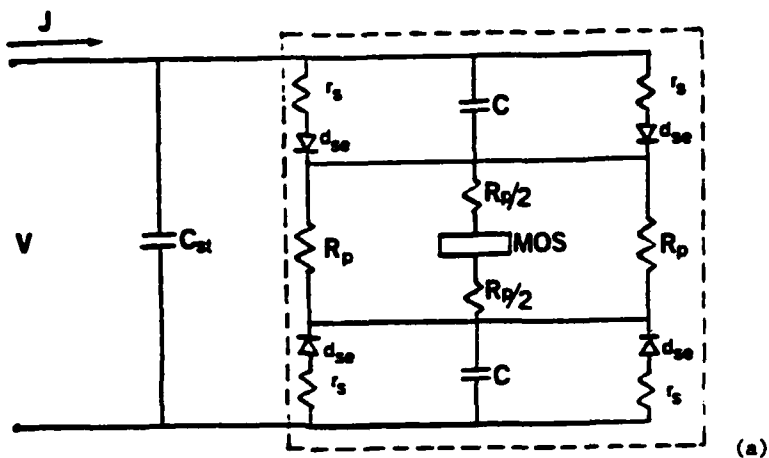


Fig. 3.5 (a) Equivalent circuit representation of an RF plasma an-nealing system with an MOS sample in it.  
 (b) Equivalent RC parallel network of load impedance  $Z_L$ .  
 (c) Equivalent circuit of the plasma conductive branch with appropriate sample impedance and its associated sheaths.

values have been determined for a 300 W RF power :

$$|J| = 2.95 \text{ mA/cm}^2,$$

$$|V| = 693 \text{ V (measured)}$$

$$Z_L = 3.7 - j 54 (\Omega)$$

Corresponding to  $G_L = 1.26 \times 10^{-3} \text{ } \Omega^{-1}$ , or  $G_L/A = 3.89 \times 10^{-6} \text{ } \Omega^{-1}/\text{cm}^2$ ,

$$C_L = 91 \text{ pf, or } C_L/A = 0.28 \text{ pf/cm}^2, \text{ and}$$

$$|J_G| = 2.68 \times 10^{-3} \text{ A/cm}^2 \quad (3.4)$$

$$|J_C| = 1.57 \times 10^{-4} \text{ A/cm}^2 \quad (3.5)$$

The above calculated conductance and capacitance values lie in the range of values published by Logan et al. (1969) for similar RF discharge systems. The calculated conductive current density,  $2.68 \times 10^{-3} \text{ A/cm}^2$ , is in excellent agreement with the measured value,  $2.72 \times 10^{-3} \text{ A/cm}^2$  (see Table 3.1), which is also not inconsistent with Chapman's general observation (of order of  $1 \text{ mA/cm}^2$ ).

Since  $|J_G| \gg |J_C|$  (see equations (3.4) and (3.5)), we can neglect the capacitive component, and redraw the equivalent circuit as having only the conductive component with an appropriate representation of the sample impedance and its associated sheaths. Here again the presence of the sample can be shown not to affect appreciably  $J_G$ . As shown in Fig. 3.5(c),  $2G_L/A$ 's are the lumped conductances per unit area connecting



the sheath capacitances,  $C_s$  and  $C_s'$ , to the electrodes, and  $d_s$  and  $d_s'$  represent the diodes across the sheaths of the MOS sample.

Once  $J_G$  has been determined, the RF voltage across the MOS device can be estimated as follows. Borrowing directly from the semiconductor device physics (Sze 1969, Grove 1967), the sheath region (space charge region) near the sample can be considered as a depletion layer capacitor obeying the following equation :

$$C_s(V_s) = \left( \frac{q\epsilon_0 n_i}{2} \right)^{1/2} V_s^{-1/2} = K V_s^{-1/2} \quad (3.6)$$

where  $V_s$  is the sheath potential,  $\epsilon_0$  is the permittivity of free space,  $n_i$  is the positive ion density in the space charge region, and

$K = \left( \frac{q\epsilon_0 n_i}{2} \right)^{1/2}$ . For a pressure of  $1\mu$  and  $10^{-4}$  degree of ionization, it has been reported that  $n_i \sim 10^9/\text{cm}^3$ , which corresponds to  $K = 2.66 \times 10^{-11} \text{ pf-V}^{1/2}/\text{cm}^2$ .

Chapman(1980) has suggested that the sheath potential  $V_s$  near an isolated object in the plasma is around 10 V. Using this value, the depletion capacitance of the sheath can be calculated from equation (3.6).

$$C_s(V_s) = K V_s^{-1/2} = 8.41 \times 10^{-12} \text{ pf/cm}^2 \quad (3.7)$$

From this the effective width of the space charge region,  $d_{\text{eff}}$ , can be calculated using the relation  $C_s = \frac{\epsilon_0}{d_{\text{eff}}}$ , and the result,  $d_{\text{eff}} = 1.05 \times 10^{-2} \text{ cm}$ , is in good agreement with Chapman's sheath width.

Due to current continuity, the current through the MOS device is equal to the current flowing across the space charge region. For each half cycle, one of the two rectifying diodes may be considered as a short circuit, and the other is open, and the current through the sheath capacitor associated with the open diode can be expressed as :

$$\begin{aligned} J_G &= C_s(V_s) \frac{dV_s}{dt} + V_s \frac{dC_s(V_s)}{dt} \\ &= \frac{1}{2} C_s(V_s) \frac{dV_s}{dt} = \frac{1}{2} \frac{K}{\sqrt{V_s}} \frac{dV_s}{dt} \end{aligned} \quad (3.8)$$

Let  $V_s = V_{so}(1 + \cos\omega t)$  (see Fig. 3.4(b)), the waveform of  $J_G$  can be calculated :

$$\begin{aligned} J_G &= \frac{1}{2} \frac{-KV_{so} \sin\omega t}{\omega V_{so}^{\frac{1}{2}} (1 + \cos\omega t)^{\frac{1}{2}}} = \frac{-KV_{so}^{\frac{1}{2}} 2\sin^{\frac{1}{2}}\omega t \cos^{\frac{1}{2}}\omega t}{2\omega 2^{\frac{1}{2}}(\cos^{\frac{1}{2}}\omega t)} \\ &= -\frac{K}{\omega} \left(\frac{V_{so}}{2}\right)^{\frac{1}{2}} \sin^{\frac{1}{2}}\omega t \\ &= |J_G| \sin^{\frac{1}{2}}\omega t \end{aligned}$$

thus, integrating equation (3.8) with  $|J_G| = 2.68 \times 10^{-3}$  and  $K = 2.66 \times 10^{-11}$ ,

$$\int 2.68 \times 10^{-3} \sin^{\frac{1}{2}}\omega t \, dt = \int \frac{1}{2} \frac{2.66 \times 10^{-11}}{V_s^{\frac{1}{2}}} dV_s$$

$$\frac{2.68 \times 10^{-3}}{\frac{1}{2}\omega} \cos^{\frac{1}{2}}\omega t = 2.66 \times 10^{-11} V_s^{\frac{1}{2}}$$

$$V_s^{1/2} = \left[ \frac{2.68 \times 10^{-3}}{\frac{1}{2} \times 8.52 \times 10^7 \times 2.66 \times 10^{-11}} \cos \frac{1}{2} \omega t \right]$$

$$V_s \approx 3 (1 + \cos \omega t)$$

Consequently, from Fig. 3.4(b),

$$V_s' = 3 \left[ 1 + \cos(\omega t + \pi) \right], \text{ and}$$

the voltage across the MOS sample

$$V_{O'} = |V_s - V_s'| = 6 \cos \omega t.$$

Therefore this calculation shows that for a RF input power of 300 W the RF voltage across the MOS device has a symmetrical waveform with an amplitude  $\sim 6$  V. This value serves as a guide for the selection of the RF voltages used in the simulation experiment (section 2.3).

The equivalent circuit shown in Fig. 3.5(c) is a good representation only if the presence of the MOS sample does not significantly affect the plasma current in the absence of this sample. In this equivalent circuit, the presence of the MOS sample is represented by an extra impedance,  $Z_{\text{MOS}}$  (which includes  $C_{\text{MOS}}$  and its sheath impedance), in series with the plasma conductance. The magnitude of  $Z_{\text{MOS}}$  for each half cycle is  $\frac{1}{\omega} \left( \frac{1}{C_{\text{MOS}}} + \frac{1}{C_s} \right)$ , where  $C_{\text{MOS}}$  (of order  $10^{-8} \text{ f/cm}^2$ )  $\gg C_s$  (of order  $10^{-11} \text{ f/cm}^2$ ). Therefore,  $Z_{\text{MOS}} \approx \frac{1}{\omega C_s} = 1.3 \times 10^3 \Omega/\text{cm}^2$  at  $f = 13.56 \text{ MHz}$ . On the other hand  $G_L/A = 3.89 \times 10^{-6} \text{ U/cm}^2$  as previously

calculated, suggesting that the impedance  $Z_{\text{MOS}}$  is negligible, and the presence of the MOS sample indeed does not significantly affect the plasma current.

The amplitude of the RF voltage developed across the MOS sample can also be estimated by the use of simple network theory. Again consider Fig. 3.5(c). For each half cycle,

$$|V_s'| = |V| \left| \frac{G_L/A + j\omega C_{\text{MOS}}}{G_L/A + j\omega C_{\text{MOS}} + j\omega C_s'} \right| \quad (3.9)$$

where  $V$  is the applied terminal RF voltage.

Since  $C_{\text{MOS}} \gg C_s'$ , and  $\omega C_s' \gg G_L/A$ , equation (3.9) can be simplified as

$$\begin{aligned} |V_s'| &\approx |V| \left| \frac{G_L/A}{\omega C_s'} \right| \\ &\approx 693 \frac{3.98 \times 10^{-6}}{7.54 \times 10^{-4}} \\ &\approx 4. \end{aligned}$$

This result is in satisfactory agreement with the one obtained from the previous approach.

Although a specific set of plasma parameters (13.56 MHz, 300 W, 10) has been used in the above calculations, the derivation can be easily extended to cover a wide range of plasma parameters. The RF power affects the terminal RF voltage, the plasma current, and the degree of

ionization. The electron density, the plasma current, and the sheath widths are related to the chamber pressure. The RF frequency not only influences the ionization efficiency, but also affects the impedance associated with the various capacitance components in the equivalent circuit.

It should be noted that the accuracy of the above results depends on the values selected for the electron density and the sheath voltages, which in our calculations were based on the typical published numbers (Chapman 1980) for similar RF discharge systems, and therefore some errors are expected. For future research, it is desirable to be able to measure directly the RF voltage across the wafer; or if this proves to be too difficult, it may be worth while to probe the electron density and the sheath voltages in the plasma so as to minimize the uncertainties concerning these parameters.

It will be shown in the next Chapter that the annealing rate is an increasing function of the RF voltage across the wafer, until saturation is reached. It is interesting to note that the experimentally observed saturation point occurs right around 4 - 6 V.

### 3.6 CONCLUSIONS

Although the RF plasma is very complicated, it is still possible to describe it at least qualitatively in terms of the parameters that are thought to be most relevant to the annealing process. According to the

proposed annealing mechanism (section 2.6), we believe that these parameters include X-ray photons, RF voltage across the wafer, and induced wafer temperature, and they have been discussed in some detail.

For a detailed understanding of the RF plasma annealing mechanisms, it is essential to understand the individual contribution of each of these parameters, and their cooperative effects. However, because of their interdependence in the RF plasma, it is very difficult to separate them out experimentally. For example, we have found that the annealing rate increases with input RF power (Fig. 2.5). Based on the properties of the RF plasma discussed in this Chapter, we know that the higher the RF power, the higher the displacement current through the device, and thus the RF voltage across the device. At the same time, the induced wafer temperature and the photon flux in the RF plasma will also increase. Obviously, the question still remains as to whether the increase in any one of these parameters has caused the improved annealing performance. Therefore it is desirable to find some means in which these annealing parameters can be independently controlled and their annealing effect separately studied. As it will be shown in the next Chapter, it is indeed possible to do so by simulating the annealing parameters without the RF plasma, and the results shed valuable light on the annealing mechanisms.

## CHAPTER IV

### EXPERIMENTAL SIMULATION OF RF PLASMA ANNEALING

#### 4.1 INTRODUCTION :

From the accumulated experimental data, and from the careful analysis of the various possible processes that may be taking place during RF annealing, a qualitative model to account for the qualitative annealing mechanisms (Ma and Ma 1978) has been proposed. In this model, three essential ingredients are required to take part in the annealing, which include the energetic gas plasma, the RF electric field, and the induced wafer temperature. The primary role of the plasma is to serve as an excitation source for the generation of electron-hole pairs in the oxide. The RF field controls the motion of these plasma-induced free carriers, and modifies the defect-reaction coordinates (Kimerling 1978) such that a more favorable annealing reaction can be achieved. Furthermore, this RF field along with the plasma-wafer interaction induces a moderate overall heating of the wafer, which also contributes to the defect annealing.

The plasma-induced excess carriers could participate in two possible annealing processes. The first process involves the neutralization of the positive oxide charge centers through electron capture. The second process involves the more complicated recombination-enhanced defect reactions (REDR), which have been observed

by Kimerling et al. (1977, 1978) in GaAs and other semiconductors, and could lead to the annihilation of these defects in the oxide. A more detailed review of the REDR process and its relevance in the RF annealing mechanisms will be presented in Chapter V.

As pointed out in the previous publications of Ma (1978), the energetic gas plasma, if it acts alone, is a source of radiation damage. It is only through the proper cooperative interactions of all three essential components that effective annealing is possible.

Due to the immense complexity of the RF plasma system, it is very difficult, if not impossible, to verify even the qualitative features of this annealing model directly from our experimental setup. The major difficulty arises from the fact that the plasma intensity depends strongly on the RF field, as does the wafer temperature. As a result, one cannot separate out the effect due to each of these three components. Therefore, we devised a simulated RF annealing experiment in which the RF field, the ionizing radiation, and the wafer temperature can be independently controlled, and the contribution of each component and their cooperative effect can be easily studied. The experimental results to be reported in this Chapter are consistent with the model we have proposed.

As mentioned in the previous Chapter, the only energetic species that can penetrate through the gate electrode and interact with the gate  $\text{SiO}_2$  layer are the soft X-ray photons, which are therefore selected as the excitation source in the experimental simulation.



## 4.2 EXPERIMENTAL DETAILS :

### 4.2.1 Sample Preparation

The MOS sample has a gate oxide of approximately 500 Å, thermally grown at 1000°C in dry O<sub>2</sub> on (100) p-type silicon with a resistivity of approximately 1 Ω-cm. A 30 min. dry N<sub>2</sub> annealing is done after the oxidation. Aluminum dots of 4000 Å thickness, thermally evaporated from a Ta boat, serve as the gate electrodes. High frequency and quasi-static C-V curves are measured to determine the initial oxide charge and surface states. For the sample used in this study, the oxide charge and surface state densities are in the low 10<sup>10</sup> /cm<sup>2</sup> range, with corresponding V<sub>FB</sub> and V<sub>MG</sub> values of approximately -0.9 V and -0.2 V, respectively.

The MOS sample is then irradiated with an X-ray beam to produce a large amount of oxide charge (approximately 4 x 10<sup>12</sup> /cm<sup>2</sup>, corresponding to V<sub>MG</sub> ~ -9.5 V), and surface states (approximately 10<sup>12</sup> /cm<sup>2</sup>), as reflected in the C-V curves. It is then kept at room temperature without bias for at least two hours before the annealing experiments. This step is necessary to ensure that no appreciable room temperature thermal annealing takes place during the period that RF annealing data are taken.

### 4.2.2 Setup and Procedure for Experimental Simulation

As shown in Fig. 4.1, an RF voltage is applied directly across the MOS sample, whose temperature can be adjusted using a heated chuck

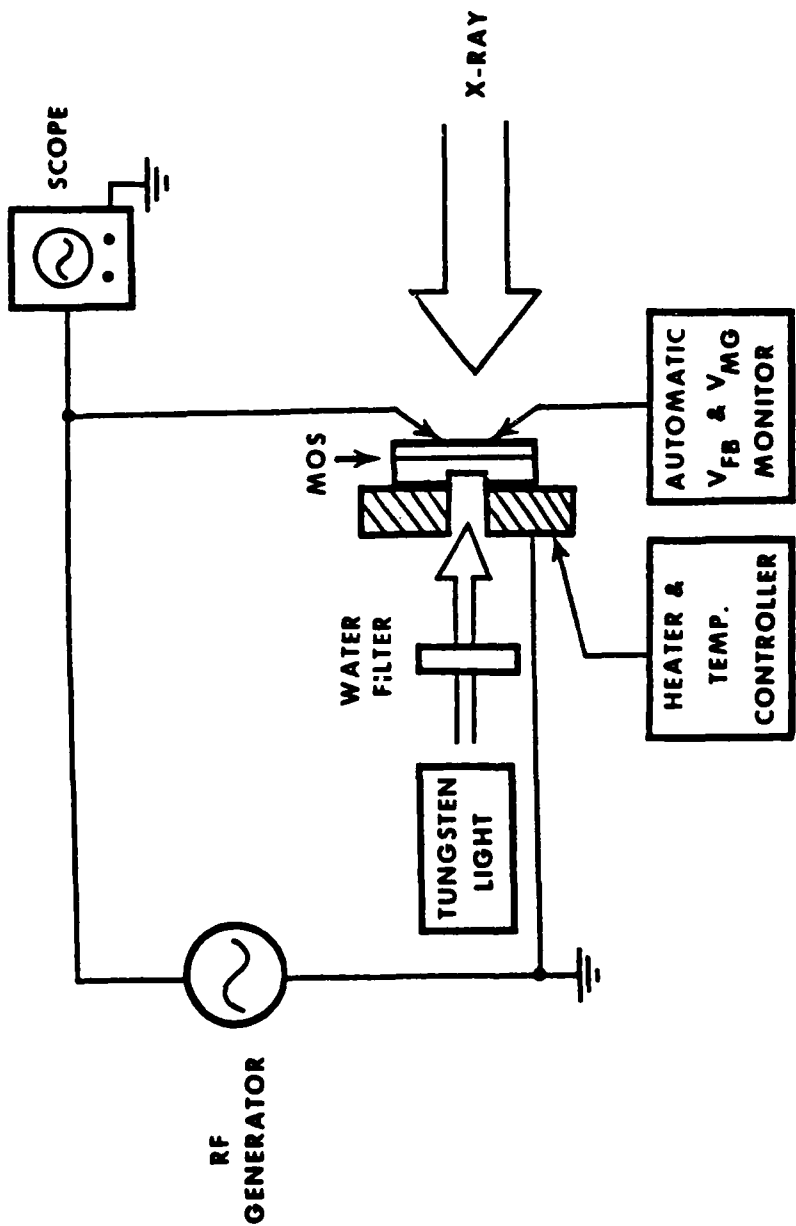


Fig. 4.1 Experimental setup for the simulated RF annealing process.

AD-A110 785

YALE UNIV NEW HAVEN CT DEPT OF ENGINEERING AND APPL--ETC F/S 20/12  
RF PLASMA ANNEALING ON MOS STRUCTURES.(U)

DEC 81 H CHIN

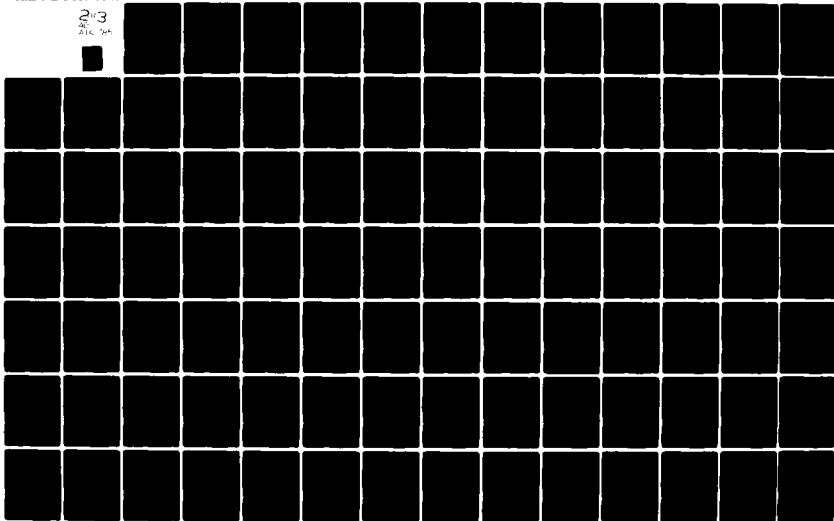
DAA829-79-C-0021

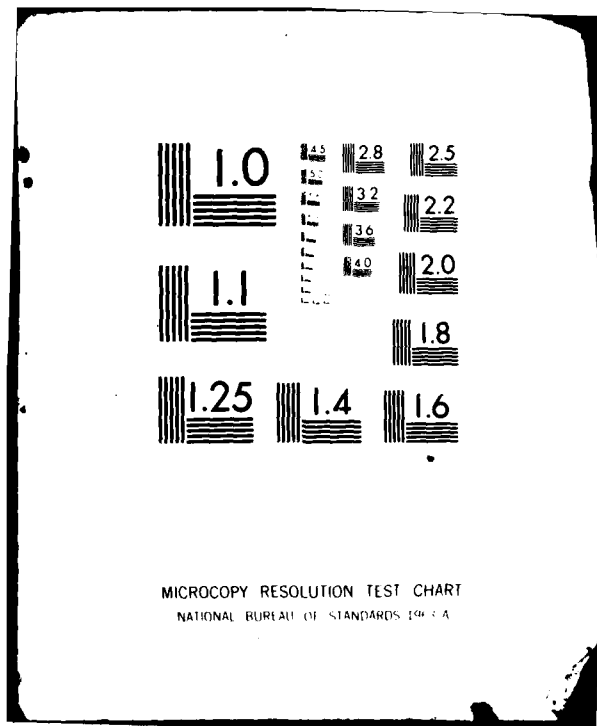
IMPACT ACCTY070

ARO-15835.6-EL

ML

100  
216 34





MICROCOPY RESOLUTION TEST CHART  
NATIONAL BUREAU OF STANDARDS 1963-A

with a temperature controller. An X-ray beam, from a commercial 35 kV tube with a W or Cu target, is used in place of RF plasma as the injection source of electrons and holes in this experimental simulation. Although the energy spectrum of this X-ray irradiation is different from the one in the RF plasma, it is believed that such a difference only contributes to a difference in the spatial distribution of the generated electrons and holes, and it does not alter the fundamental physics involved in the annealing process. Furthermore, a photon source which exactly duplicates the spectrum generated in our RF plasma is beyond our experimental capability at the present time.

The X-ray flux used in this study ranges from  $1.8 \times 10^{16}$  eV/cm<sup>2</sup>-sec to  $7.2 \times 10^{17}$  eV/cm<sup>2</sup>-sec. Using the absorption coefficients for Al and SiO<sub>2</sub> given in Fig. 3.1, the corresponding photon flux absorbed by gate SiO<sub>2</sub> layer has been calculated to range from  $2 \times 10^{12}$  eV/cm<sup>2</sup>-sec to  $9 \times 10^{13}$  eV/cm<sup>2</sup>-sec. The low end of the above values is comparable to the corresponding value in the RF plasma ( $\sim 5 \times 10^{12}$  eV/cm<sup>2</sup>-sec; see Table 3.2).

An ac voltage from a function generator (Wavetek Model 145 with variable frequencies from 0.0001 Hz to 20 MHz and variable peak voltages up to 15 V) is applied directly across the MOS sample. The voltage amplitude, which ranges from 0.4 V to 15 V, can be easily adjusted from the function generator for each frequency, and the frequency is varied over several decades from 10 MHz to 10 Hz.

Although the voltage and frequency dependences of the annealing

behavior have been studied (section 4.5), in most cases, however, the amplitude of the RF voltage used is fixed at 5 V. This value is selected based on the estimated RF voltage across the MOS sample in the RF plasma system (see Chapter III).

Sometimes (in the case of low wafer temperatures), illumination on the backside of the sample is provided by a tungsten lamp through an optical heat filter. This backside illumination simulates the visible and IR light which exists in the plasma. It also helps to maintain a symmetric ac field through the oxide, otherwise the field in the oxide will be much larger when the MOS sample is in accumulation than when it is in deep depletion, and a time averaged net dc field results. Since the RF annealing process is in competition with the X-ray radiation damage, the net annealing rate is reduced when the damage rate increases, and the presence of a dc bias during ionizing irradiation is known to produce more radiation damage in MOS structure. With the heat filter, the temperature rise of the sample due to the back illumination is less than  $5^{\circ}\text{C}$ , and no light with photon energies greater than the silicon band gap ( $\sim 1.12$  eV) will reach the Si-SiO<sub>2</sub> interface. Careful experimentation has verified that the back illumination does not contribute to the annealing other than to provide a symmetric ac field through the oxide.

An oscilloscope is used to monitor the RF waveform across the device during the experiment, from which we can determine if the probe is on the sample and whether the RF amplitude is in the desirable range. The sample holder is mounted along the X-ray beam track, and

the relative position of the probe on the vacuum chuck is kept fixed to ensure that the same radiation dose impinges upon the device for every experimental run. Rapid cooling of the device after each annealing is provided by compressed air which blows directly on the chip. It takes about 15 min. to cool down the device to room temperature from 100°C.

In order to find out the annealing rate as a function of time under various annealing conditions, numerous data points must be collected, and it becomes impractical to measure the entire C-V curve for each point. Therefore an automatic flat-band and midgap voltage monitor is used, which provides the necessary information that we need with a much reduced data collection time. Fig. 4.1.1 shows the circuit diagram of this monitor. The operation is as follows. First, following the initial C-V characterization, we obtain the  $C_{FB}$  and  $C_{MG}$  of the MOS sample. A capacitor with capacitance value corresponding to  $C_{FB}$  (or  $C_{MG}$ ) is then selected as a reference for the subsequent measurement. A Boonton 72B capacitance meter is used as a comparator, which measures the difference between the device capacitance (voltage dependent) and  $C_{FB}$  (or  $C_{MG}$ ), and produces an output voltage signal proportional to that difference. This output voltage is applied to a buffer (unity gain differential amplifier), an integrator, and then fed back to the sample. This loop proceeds many times in a very short period of time until finally the value of device capacitance is equal to  $C_{FB}$  (or  $C_{MG}$ ). Then the output of the Boonton meter is reduced to zero, integration stops, and the  $V_{FB}$  (or  $V_{MG}$ ) is recorded.

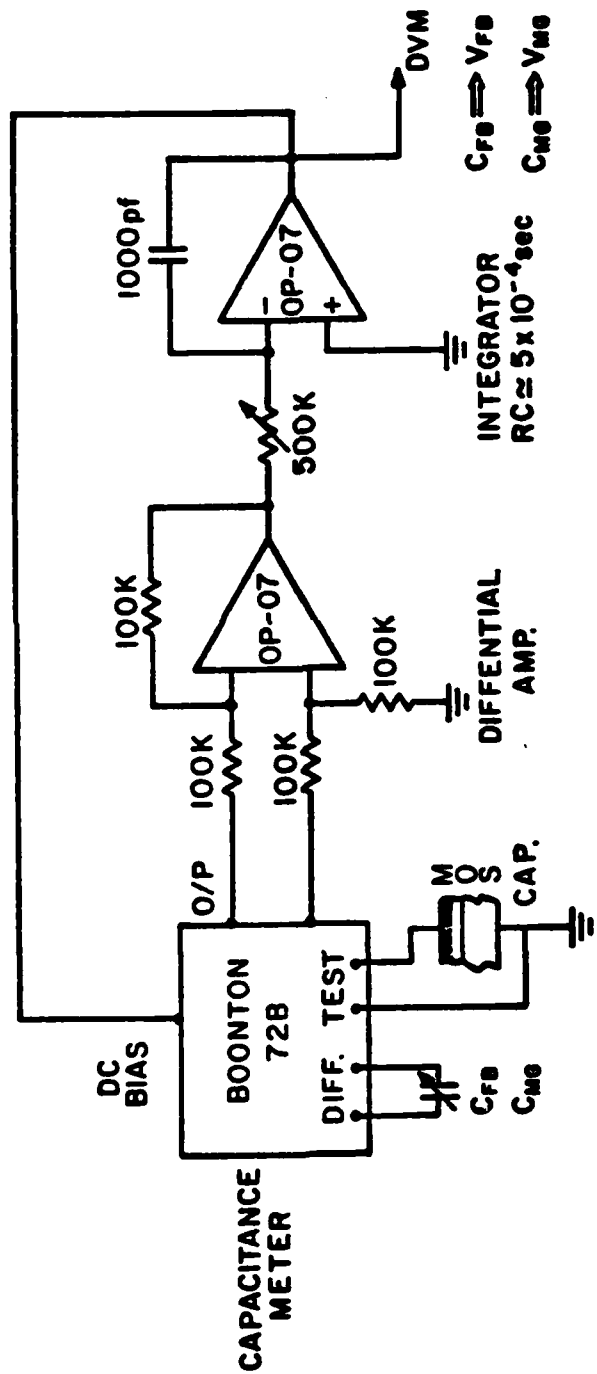


Fig. 4.1.1.1 Circuit diagram of the automatic flatband and midgap voltage monitor.



This monitor is used to continuously measure the changes in C-V shift of the MOS sample during the experiment. The reason that both  $\Delta V_{FB}$  and  $\Delta V_{MG}$  are monitored is the following. When the surface state density is high, as in the X-ray irradiated samples, the flatband voltage shift,  $\Delta V_{FB}$ , is no longer a good measure of the effective oxide charge, because of the charging effect of the surface states (Scoggan and Ma 1977). The midgap voltage shift,  $\Delta V_{MG}$ , however, is not influenced by the surface states and is directly proportional to the effective oxide charge. This conclusion has been reached through extensive studies of irradiated MOS capacitors having wide range of p-type and n-type doping concentrations (Scoggan and Ma 1977). The self-consistency of this conclusion has also been checked using the irradiated MOSFET samples. By measuring the distribution of the surface states, the difference in  $\Delta V_{FB}$  and  $\Delta V_T$  (threshold voltage shift) on the same device can be quantitatively explained by the charging of different portions of these states. Thus by monitoring  $\Delta V_{FB}$  and  $\Delta V_{MG}$  simultaneously, one can separate out the surface-state effect from the oxide charge effect.

In the case where annealing of the slow interface states is studied (section 4.5), the density of slow states is measured from the amount of the hysteresis,  $\Delta V_{SSS}$ , in the forward and the return traces of the high frequency C-V curves. Since this hysteresis is sensitive to the terminal voltages of the dc ramp, the applied ramp voltage range is kept fixed between -10 V and 5 V for both the forward and the return traces so that a meaningful comparison can be made.

#### 4.3 RESULTS AND RELATED DISCUSSIONS :

To quickly find out the effects of the RF field and X-ray irradiation, the first experimental simulation is conducted at room temperature with an X-ray flux of  $\sim 1.8 \times 10^{17}$  eV/cm<sup>2</sup>-sec, and C-V curves are recorded at several intervals. Using the absorption coefficient given in Fig. 3.1, the photon flux absorbed by the SiO<sub>2</sub> layer is calculated to be  $\sim 1 \times 10^{13}$  eV/cm<sup>2</sup>-sec, which is within the same order as the value obtained in the actual RF plasma (see Chapter III). The amplitude of the RF voltage used in all cases shown in this section is 5 V at a frequency of 1 MHz. We have found that for RF voltages above 5 V, the dependence on the voltage and frequency is rather weak (see section 4.4).

As shown in Fig. 4.2, the initial condition of the sample is represented by the solid C-V curve. By exposing this sample to the X-ray beam in the absence of the RF field, the C-V curve first shifts to X<sub>1</sub>, then to X<sub>2</sub>, indicating radiation damage by the X-ray, which is expected. On the other hand, if an RF field is coupled with the X-ray irradiation, one observes net annealing even at room temperature, as exhibited by curves XR<sub>1</sub> and XR<sub>2</sub>. This simple experiment serves to illustrate the importance of the RF field in the annealing process.

Fig. 4.3 shows the annealing of the effective oxide charge, depicted as the midgap voltage shift, as a function of time at several wafer temperatures. The starting V<sub>MG</sub> for all curves is approximately -9 V, although the same annealing behavior has been observed within a wide range

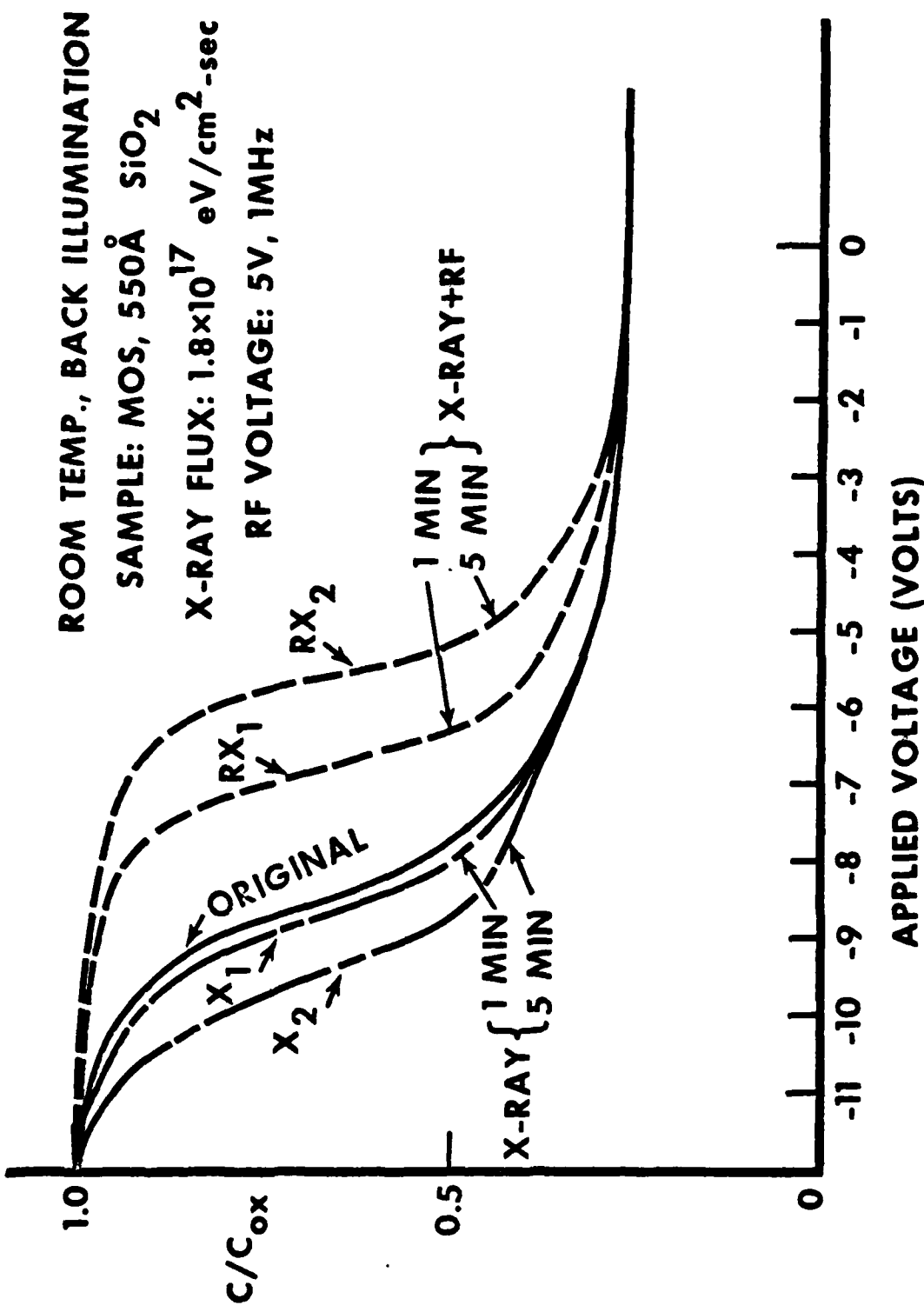


Fig. 4.2 High frequency C-V curves of an MOS capacitor showing the effects of X-ray irradiation and RF field at several time intervals. Solid curve corresponds to the initial state of the sample. Curves X<sub>1</sub> and X<sub>2</sub> correspond to X-ray irradiation only. Curves RX<sub>1</sub> and RX<sub>2</sub> correspond to X-ray irradiation coupled with an applied RF field. All experiments are done at room temperature.

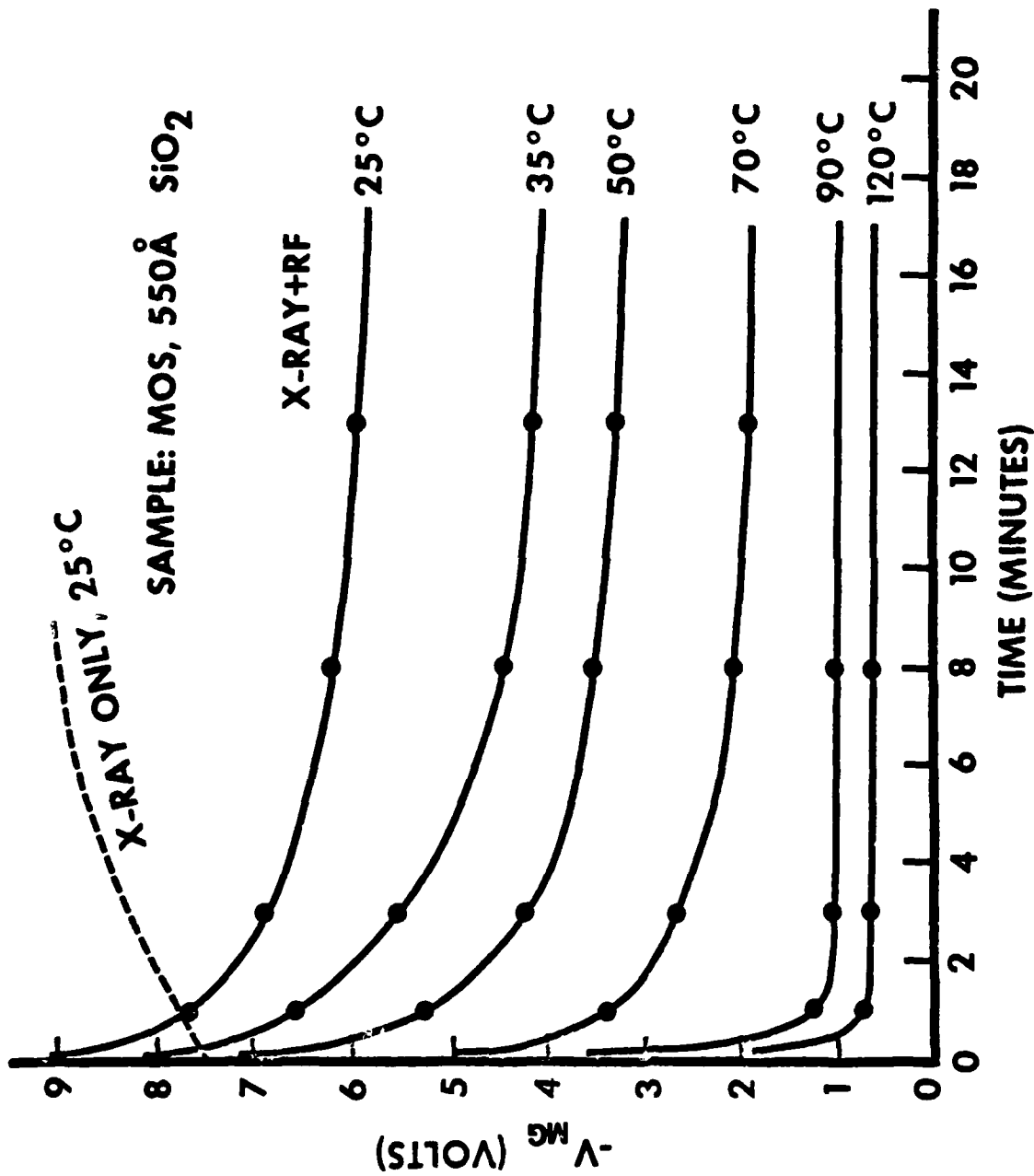


Fig. 4.3

C-V shift, measured at midgap, as a function of time under several different conditions. Solid curves correspond to the cases where X-ray irradiation and RF voltage are simultaneously applied. Dashed curve is taken with X-ray irradiation only. The X-ray and RF parameters are as specified in Fig. 4.2.

of the starting  $V_{MG}$ . The solid curves are taken at a temperature ranging from 25 to 120°C, with the X-ray irradiation and the RF voltage applied simultaneously. It is seen that significant annealing occurs even at room temperature. As a comparison, the dotted curve represents the case where only X-ray irradiation is applied without the RF voltage. In this case, further radiation damage, rather than annealing, is observed as expected. This result provides direct evidence that both the RF field and the wafer temperature play a significant role in the RF annealing process.

Fig. 4.4 serves to demonstrate the contribution of X-ray excitation in the annealing process. Although some annealing takes place at 65°C with RF voltage alone (upper curve), the rate of annealing increases significantly when X-ray radiation is coupled with the applied RF voltage (lower curve).

The above results were obtained with a modest level of X-ray flux. If the X-ray flux is increased substantially, the radiation damage effect starts to compete with the annealing, and the net annealing rate may decrease. As shown in Fig. 4.5, the annealing behavior for two different levels of X-ray flux is compared at room temperature and 70°C. The curves for the lower X-ray flux correspond to those in Fig. 4.3. At higher X-ray flux (a factor of 4 higher), the annealing rates at both temperatures are reduced. The 25°C curve even shows an upward trend after long annealing time, suggesting that the annealing cannot keep up with the radiation damage

ANNEALING TEMPERATURE : 65°C

RF VOLTAGE: 5V, 1MHz

X-RAY FLUX:  $1.8 \times 10^{17}$  eV/cm<sup>2</sup> -sec

SAMPLE: MOS, 550Å SiO<sub>2</sub>

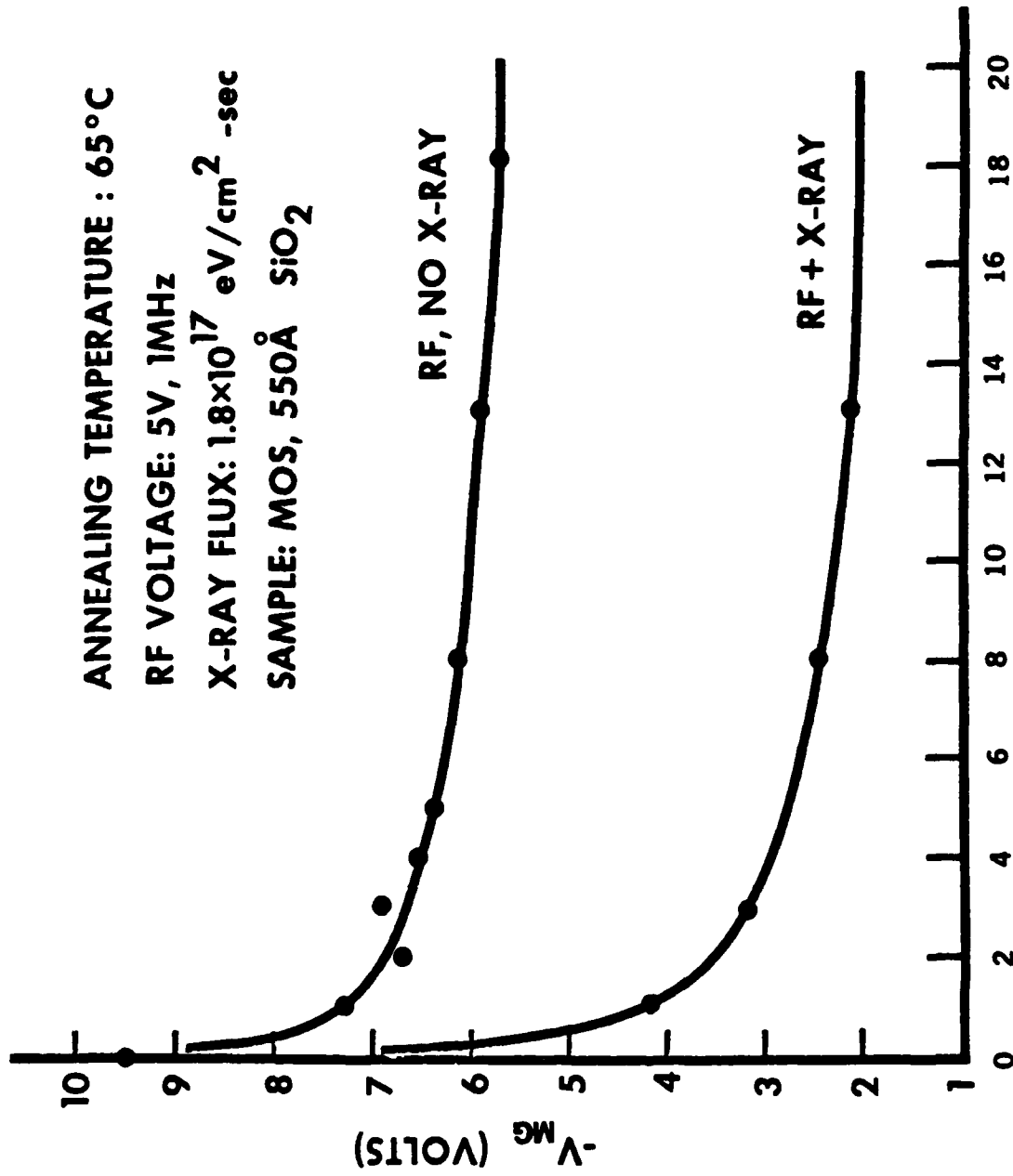


Fig. 4.4

Contribution of X-ray in the RF annealing process is exemplified. Curves correspond to C-V shifts, measured at midgap, as a function of time in a simulated RF annealing experiment at 65°C. Upper curve corresponds to the case where an RF voltage is applied in the absence of X-ray. Lower curve corresponds to the case where both X-ray and RF voltage are applied.

SOLID CURVES: HIGH X-RAY FLUX  
 DASHED CURVES: LOW X-RAY FLUX

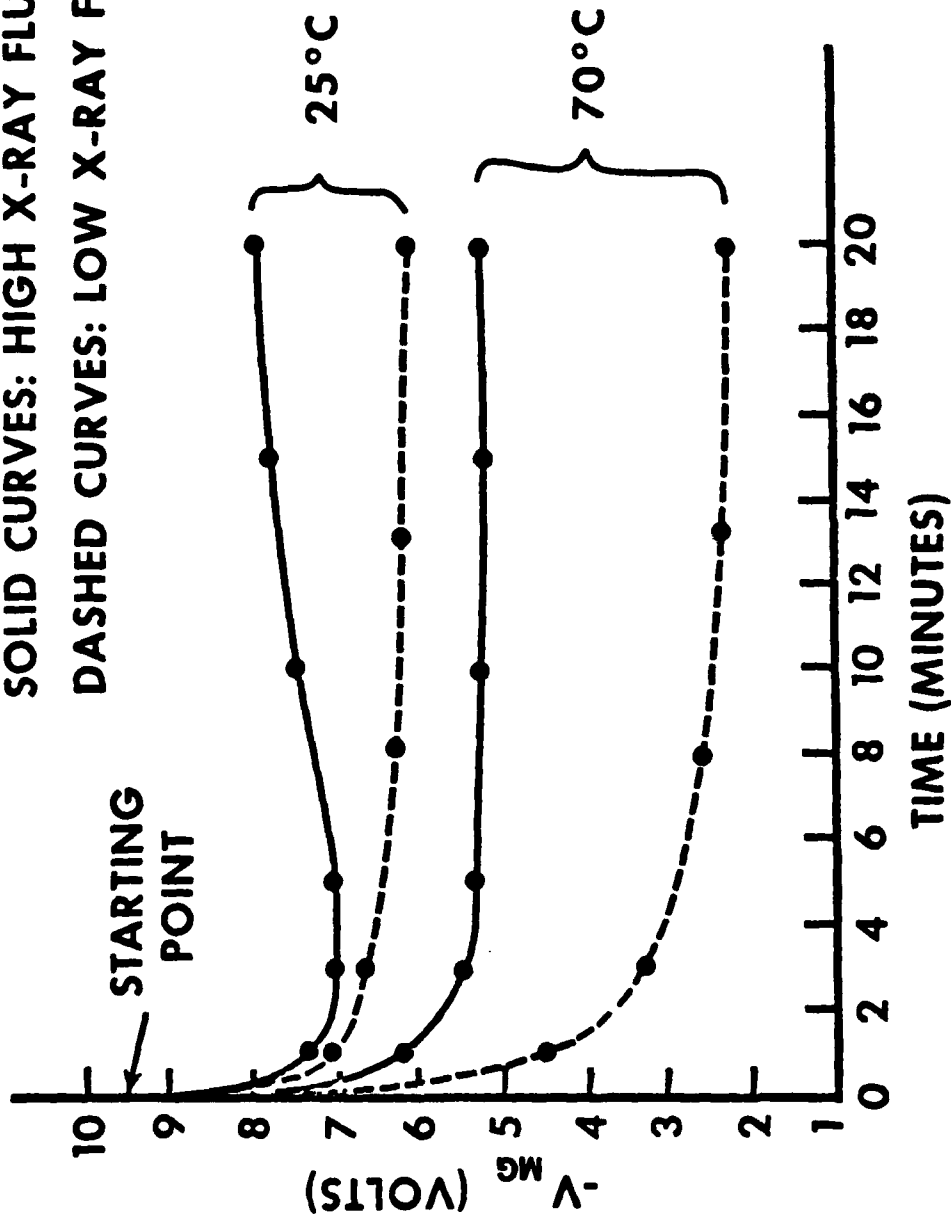


Fig. 4.5 Dependence of annealing on the X-ray flux at two different temperatures. Solid curves are taken with an X-ray flux of  $7.2 \times 10^{17}$  eV/cm<sup>2</sup>-sec. Dashed curves are taken with an X-ray flux of  $1.8 \times 10^{17}$  eV/cm<sup>2</sup>-sec.

effect in this case.

The fact that the X-ray irradiation, which is a well-known source of radiation damage in MOS structures, also contributes to the annealing in the presence of the RF field and temperature is very interesting. Since the primary function of the X-ray irradiation is to inject excess electrons and holes, their recombination through a defect site could then lead to the REDR process. Many of our recent results, in particular the annealing of radiation-induced neutral traps in  $\text{SiO}_2$ , also tend to support a mechanism through which certain structural defects are annihilated in the process. An annealing that would simply electrically neutralize a charged defect center would not remove the neutral traps.

Fig. 4.6 shows the annealing of the radiation-induced neutral traps in the simulation experiment. The annealing parameters are as specified in the figure. The quantitative trap parameters have been analyzed from these curves and are presented in Table 4.1. It is seen that both the control and the RF annealed samples exhibit only one trap with a relatively small capture cross section. This result indicates that, using this set of annealing parameters, the radiation-induced neutral traps can be completely annealed out. In contrast, it requires a temperature over  $550^\circ\text{C}$  to achieve the same result in the case of pure thermal annealing (Aitken et al. 1978, Gdula 1979). This experiment again demonstrates the importance of the X-ray radiation and RF field in the annealing process, and provides



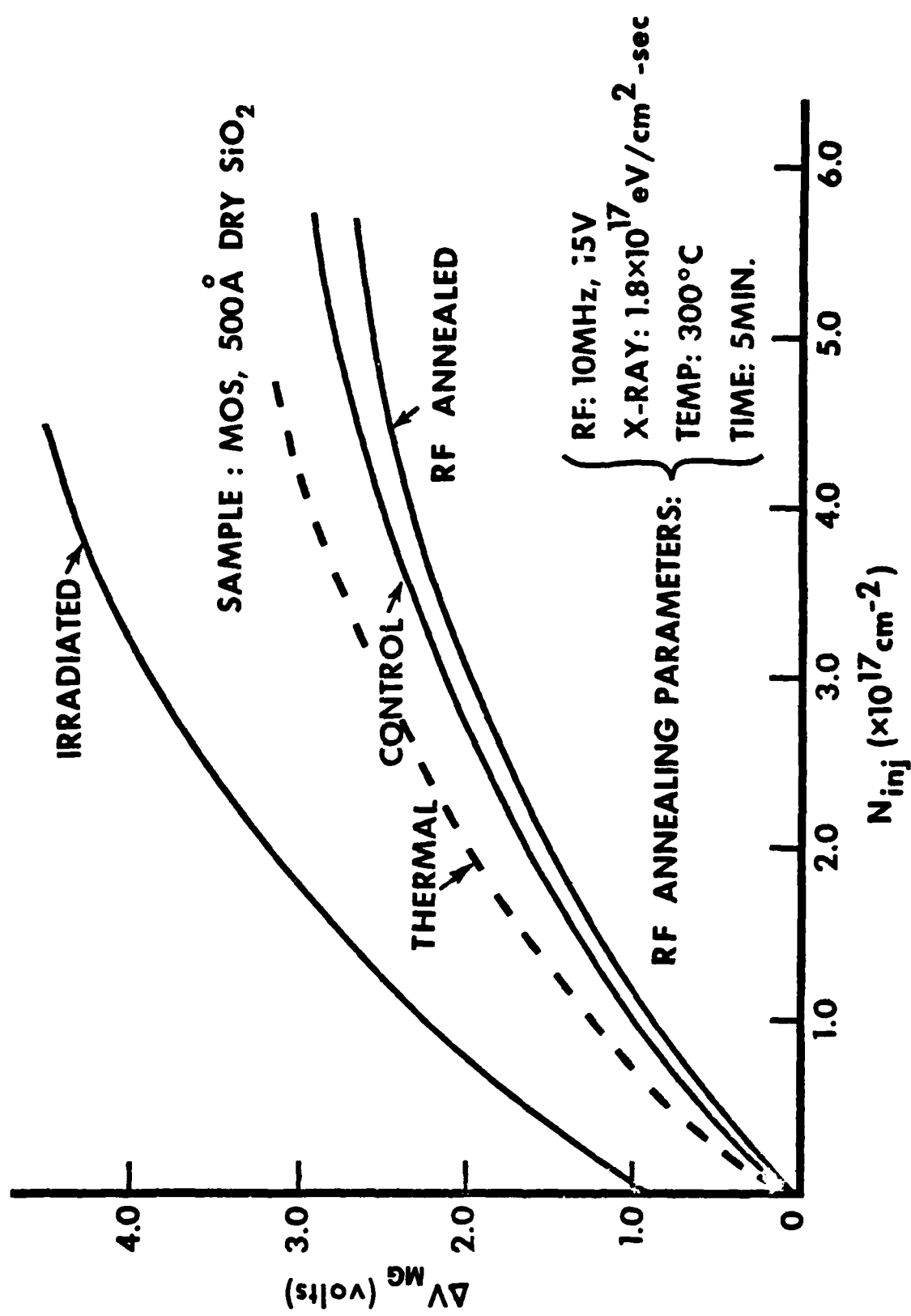


Fig. 4.6 Results of the avalanche injection measurement indicate that the radiation-induced neutral traps are completely removed by the (X-ray + RF field) annealing at 300°C.

TABLE 4.1 : Trap parameters obtained from Fig.4.6.  $\sigma$  : Capture cross section  
 $N_{\text{eff}}$  : Effective trap density

TRAP PARAMETER SAMPLE	$\sigma$ (cm <sup>2</sup> )	$N_{\text{eff}}$ (cm <sup>-2</sup> )
CONTROL	$3.91 \times 10^{-18}$	$1.38 \times 10^{12}$
SIMULATED RF ANNEALING AFTER IRRADIATION	$3.91 \times 10^{-18}$	$1.24 \times 10^{12}$
THERMAL ANNEALING AFTER IRRADIATION	$4.08 \times 10^{-18}$	$1.53 \times 10^{12}$
	$6.40 \times 10^{-17}$	$2.30 \times 10^{11}$

strong support for our annealing model.

Another convenient test of the REDR theory is the analysis of the activation energies associated with the annealing process. A reduction of the apparent defect reaction barriers is expected in the recombination-enhanced processes, which should be reflected in the measured activation energies (Kimerling 1978, Weeks et al. 1975).

In Fig. 4.7 we plot the annealing rate of positive oxide charge for a pure thermal process together with the recombination-enhanced processes at two different X-ray levels. These data are taken from an isochronal annealing experiment with a 2 minute annealing time, using the setup shown in Fig. 4.1. The annealing temperature ranges from 25°C to 125°C, the upper temperature being limited by the capability of our heated chuck at the present time. Although it is believed that more than one type of defects is involved in the annealing process with possibly different activation energies, the data in Fig. 4.7 does indicate that an average activation energy may be assigned for each process. From the slope of the best linear fit, the average activation energy for the pure thermal process is approximately 0.4eV, with a  $\pm 0.05$ eV spread among several different samples. This value is in good agreement with the one reported by Simons et al. (1968) for irradiated MOS samples. The other two curves (labeled recombination-enhanced process), however, both give rise to an average activation energy of approximately 0.13eV, corresponding to a factor of three reduction when compared to the pure thermal process. This significant reduction in the activation energy

$$N = \frac{V_{MG}(\text{POST-ANNEAL}) - V_{MG}(\text{PRE-ANNEAL})}{V_{MG}(\text{PRE-IRRAD.}) - V_{MG}(\text{POST-IRRAD.})} \times \frac{1}{\text{ANNEAL TIME}}$$

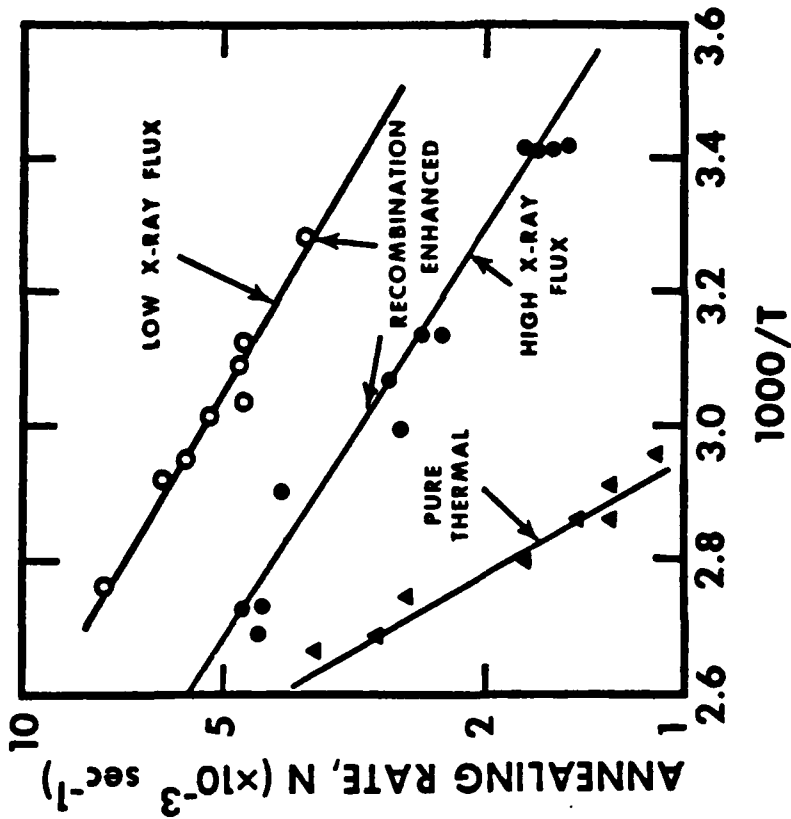


Fig. 4.7

Arrhenius plots of the oxide-charge annealing rate for pure thermal and recombination-enhanced processes. The X-ray fluxes are given in Fig. 4.5. The activation energies are 0.375 eV (pure thermal) and 0.128 eV (recombination-enhanced).

is consistent with the REDR model.

Notice in Fig. 4.7 that the difference in the X-ray flux for the two recombination-enhanced curves only affects the net annealing rates and does not affect the activation energies involved. This suggests that the recombination enhanced annealing process is a fundamental characteristic of certain defects, whose altered activation energy does not depend on the number of excess electrons and holes that are present. The net rate of annealing, however, does depend on the X-ray flux. Within the range of X-ray flux used in this study, the radiation damage component seems to play a significant role, which increases with the X-ray flux and negates the annealing rate.

The same observation goes for the surface states as well. Fig. 4.8 shows the Arrhenius plot for the annealing of surface states. Here the surface states correspond to the integrated number over the energy band between midgap and flatband due to the nature of the measurements described in section 4.2.2. Again the recombination-enhanced processes show lower activation energies and higher net annealing rates. For the pure thermal process, there exist two activation energies. In the temperature range of 25°C - 75°C, the average activation energy is approximately 0.32 eV, which is very close to the value reported by Jeppson and Svensson (1977). For higher temperatures, it is shown to be about 0.1 eV, in agreement with Nakagiri's data (1974) in the range 100°C - 500°C.

For the recombination-enhanced processes, some difference of

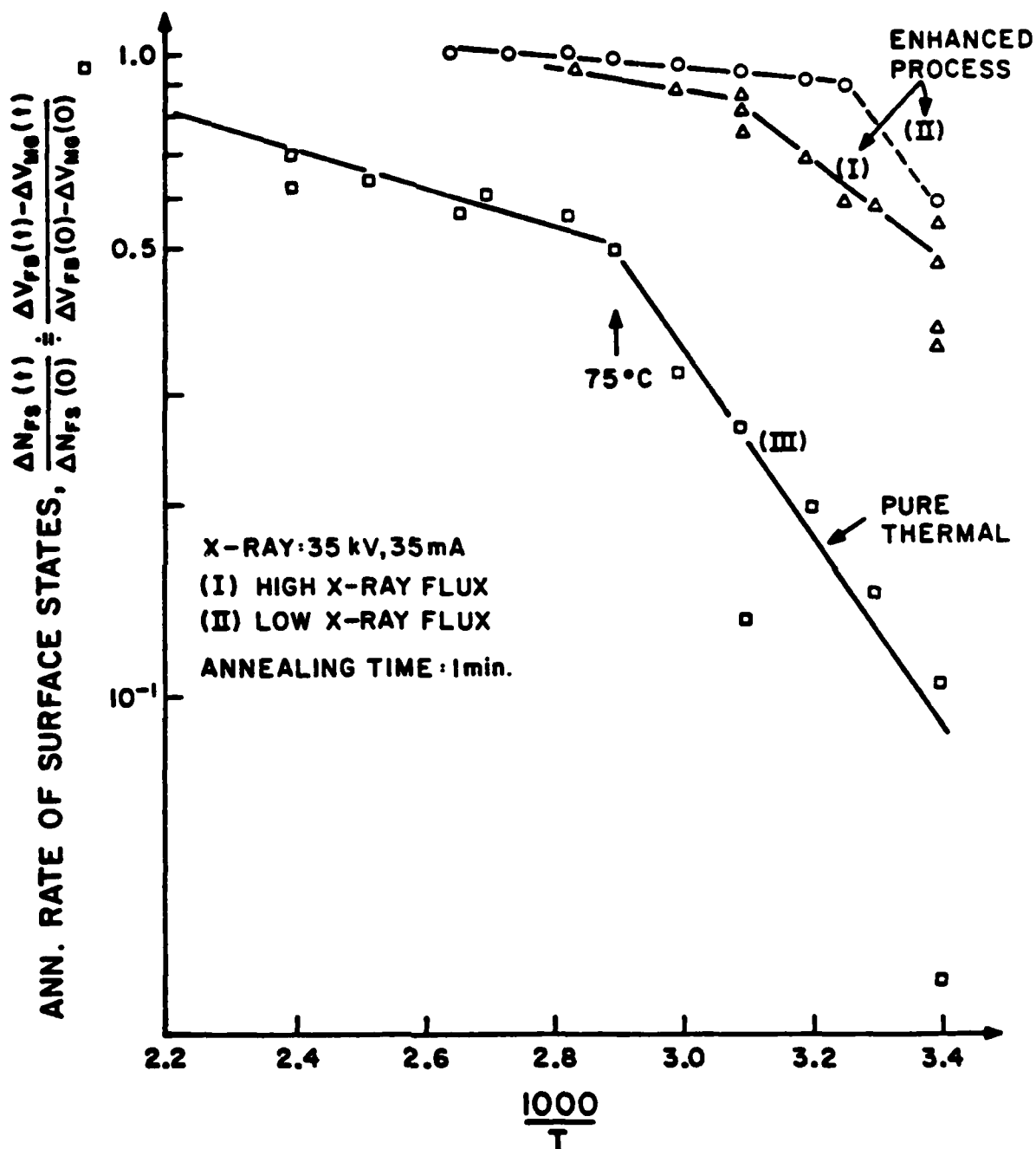


Fig. 4.8

Arrhenius plots for the annealing of surface states. The surface states correspond to the integrated number over the energy band between midgap and flatband. The X-ray fluxes are given in Fig. 4.5.

activation energy exists under different X-ray levels. These activation energies as presented here may be useful for qualitative comparison purposes, but they should not be taken too seriously in so far as the microscopic annealing mechanisms are concerned. As mentioned previously, these surface states are integrals over a continuous energy distribution, and the measured apparent activation energy thus corresponds to some average over this continuum. Although the exact atomic origin of these surface states is still not clearly understood, it is very unlikely that the states at different energy levels would all have the same activation energy upon annealing. For future studies, a more meaningful (but much more time consuming) experiment is to track the annealing rate of the surface state at a particular energy level, from which the activation energy associated with a particular interface defect may be accurately determined. This process can be continued to cover the entire range of the surface-state spectrum, and this information can then be used to analyze the surface-state annealing mechanisms.

The above activation energies have been obtained assuming the defect energy levels are discrete. As discussed in section 5.3 and 5.4, however, it is more appropriate to describe these defects as having a continuous distribution of activation energies around some mean values. Using a Gaussian distribution one can show that the mean values of the activation energies are raised to a level typically above 1 eV (sections 5.3 and 5.4). In both cases, however, a significant lower activation energy is obtained for the RF annealing process compared with the thermal annealing process. Since the essential physics involved is the same for both cases in as far

as the REDR model is concerned, we have elected to show only the simple discrete energy case here and to defer the more elaborate mathematical treatment for the distributed energy case until later in the next Chapter.

#### 4.4 FREQUENCY AND VOLTAGE DEPENDENCE OF RF ANNEALING

In the previous section, we have shown that it is possible to simulate the RF plasma annealing by applying a controlled amount of X-ray radiation, RF field, and wafer temperature. For convenience, however, we only showed results with a fixed RF frequency (1 MHz) and voltage (5 V peak). If the REDR model is indeed valid, then one expects the annealing rate to be a function of the RF voltage amplitude as well as its frequency, because the electron and hole transport and recombination processes depend strongly on these parameters (see Chapter VI).

In the following sections, we will show that these dependences have indeed been experimentally observed. Theoretical analysis indicated that the voltage dependence can be satisfactorily described by a first order recombination kinetics model, and the frequency dependence may be explained by the trapping kinetics of the holes.

##### 4.4.1 Annealing Results

As shown in Fig. 4.9, the annealing of the positive oxide charge is plotted as a function of the ac voltage for a wide range of frequencies. These data are taken from an isothermal (100°C) and isochronal (2 min) annealing experiment in the presence of the X-ray irradiation and the ac



voltage. In this Figure  $N_t^+$  is the effective density of the positive oxide charge prior to the annealing, and  $N_t^0(t)$  is the effective density of the positive oxide charge that has been annealed out after annealing time  $t$ . In this case  $t = 2$  min. Both densities are measured from the midgap voltage shifts of the high frequency C-V curves.

The data indicate that, within the range studied, the higher the amplitude and the frequency of the ac voltage, the better the annealing results. When the amplitude of the ac bias voltage is below 5 V, the annealed percentage is approximately linearly proportional to the voltage amplitude for a wide range of frequencies. For a voltage amplitude higher than 5 V, the annealed percentage reaches a saturation level. In Fig. 4.9, the shaded area below the level of the pure thermal annealing indicates the regime where the radiation damage rate exceeds the enhanced annealing rate.

The annealing results for the slow surface states ( $N_{SS}$ ) are shown in Fig. 4.10. It is apparent that a voltage and frequency dependence similar to that of the oxide charge has been observed.

To reveal the frequency dependence more clearly, we replot the results in Figs. 4.9 and 4.10 as a function of frequency using the ac voltage as a parameter. This is shown in Figs. 4.9.1 and 4.10.1. These curves indicate that the lower the ac voltage the stronger the frequency dependence.

It is interesting to note that, although higher frequency provides better annealing, enhanced annealing (compared with pure thermal annealing)

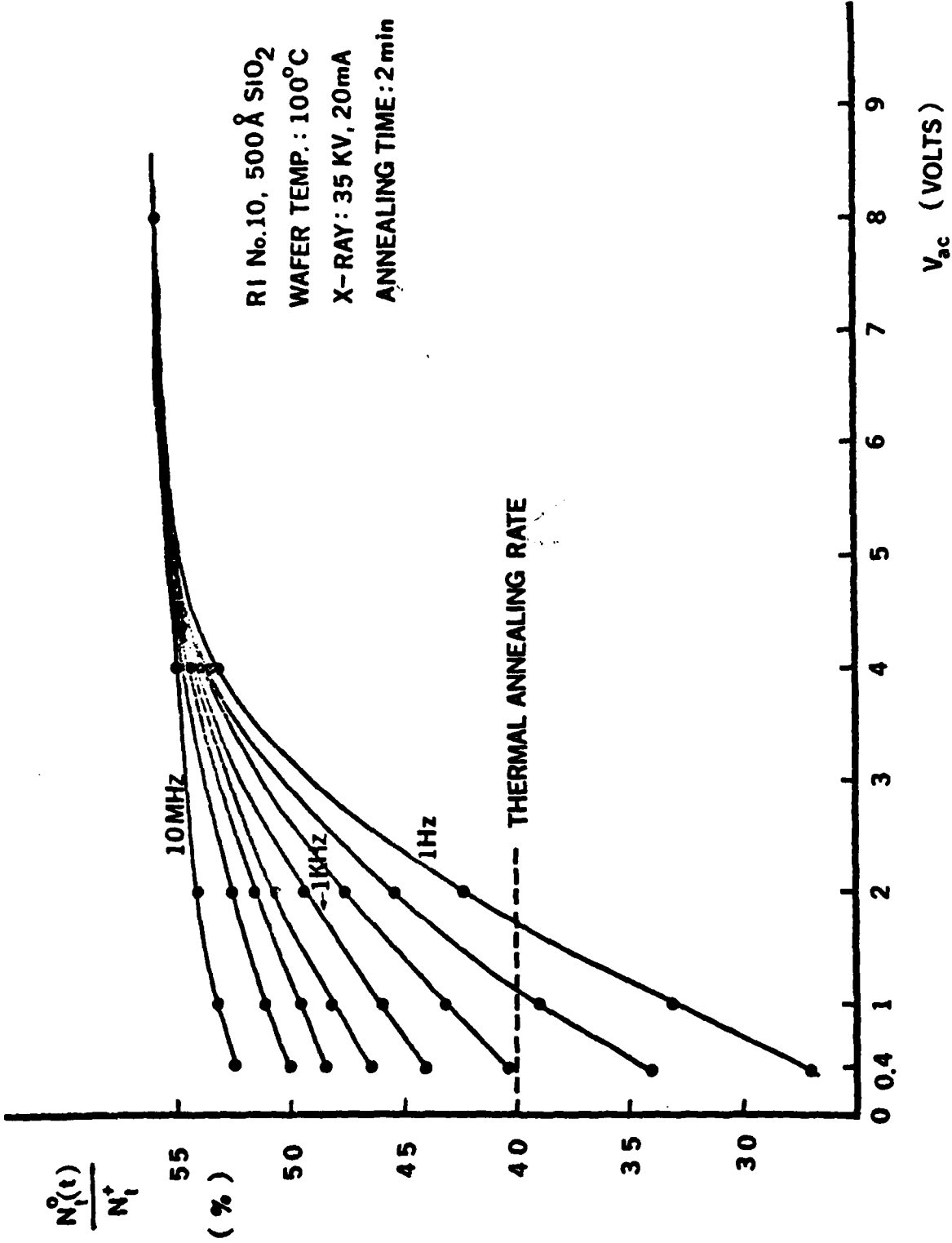


Fig. 4.9 Annealing of the positive oxide charge as a function of the ac voltage at 100°C for a wide range of frequencies.

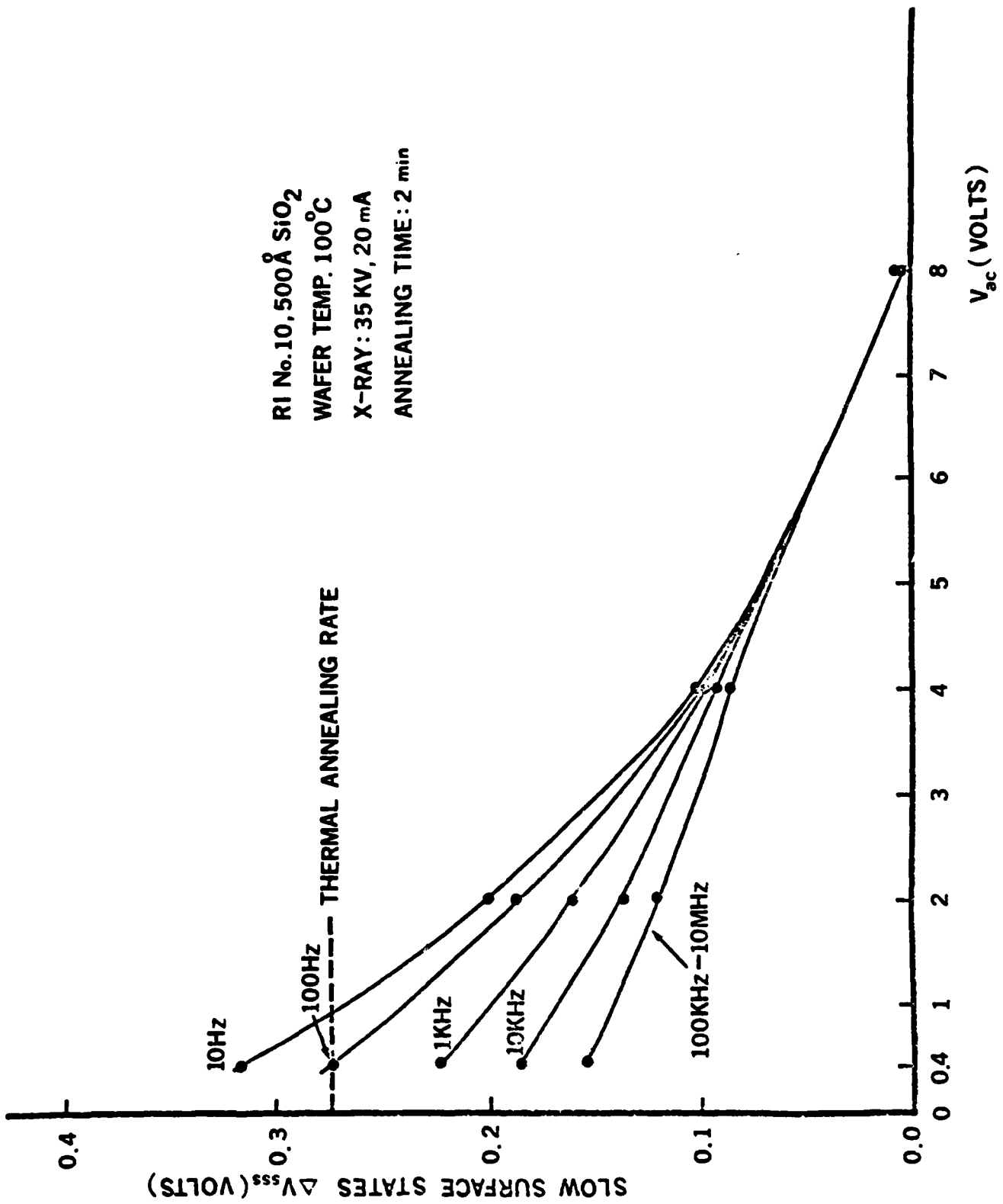


Fig. 4.10 Annealing of the slow surface states as a function of the ac voltage for a wide range of frequencies.

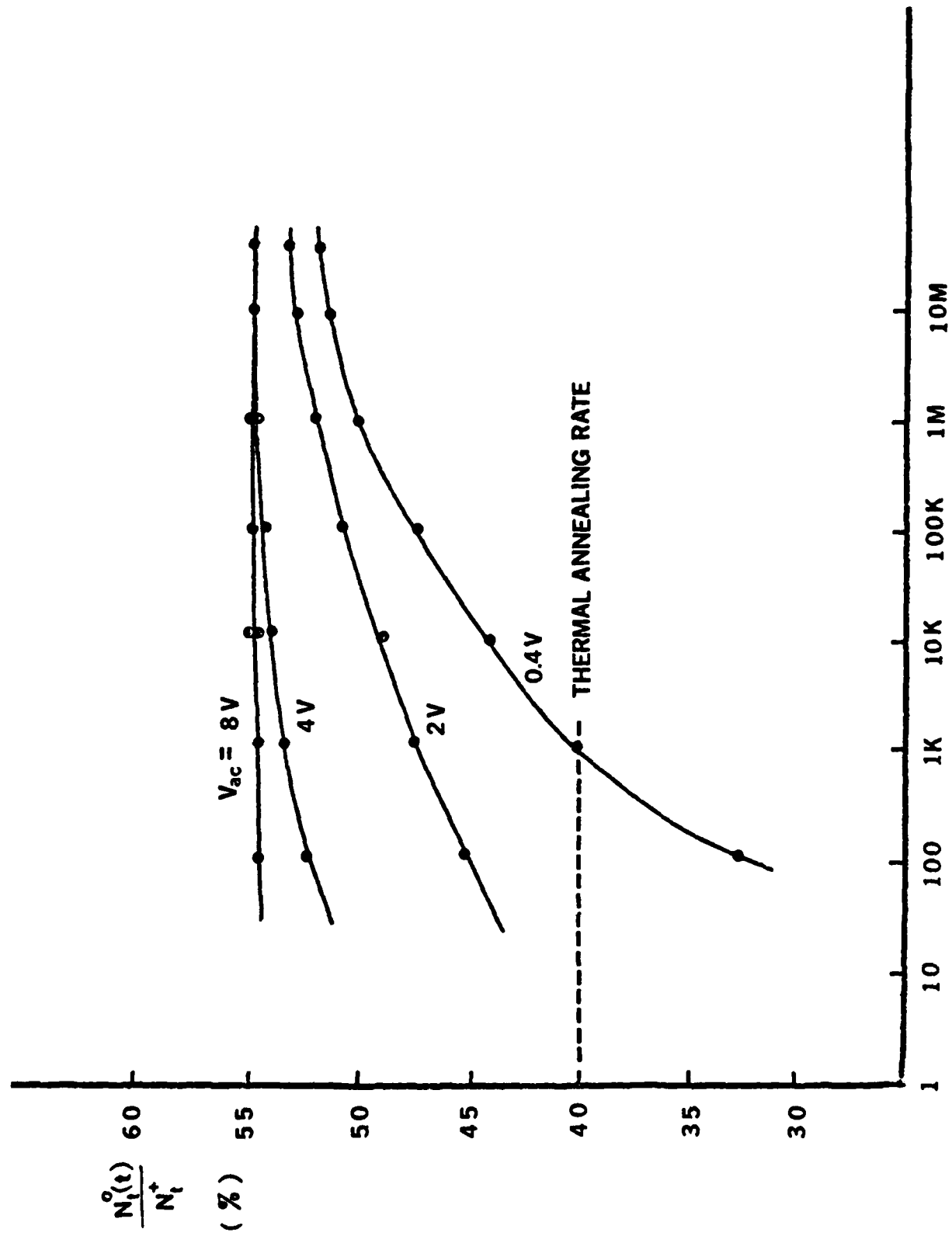


Fig. 4.9.1 Annealing of the positive oxide charge as a function of frequency using the ac voltage as a parameter. These curves are redrawn from Fig. 4.9.

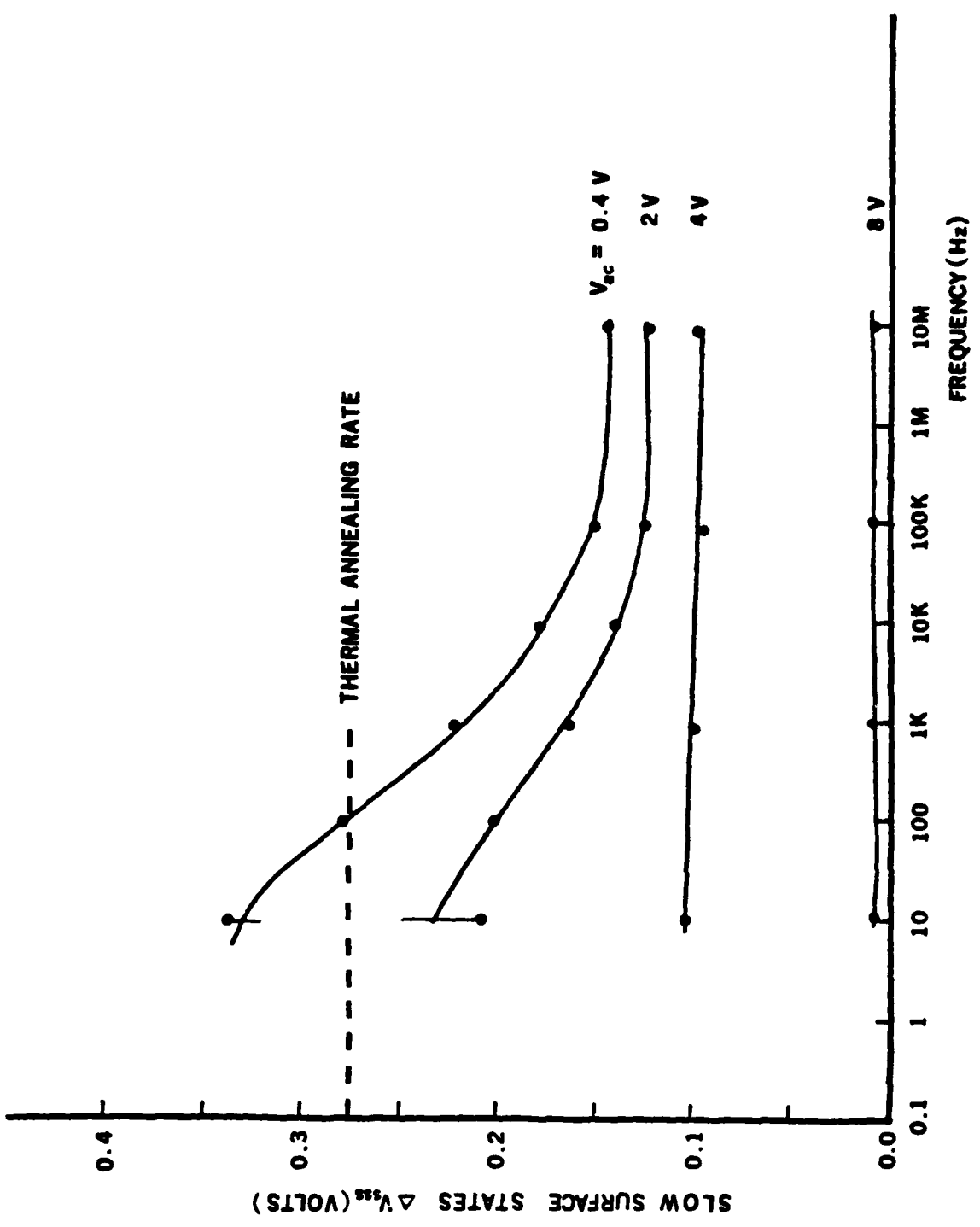


Fig. 4.10.1 Annealing of the slow surface states as a function of frequency using the ac voltage as a parameter. These curves are redrawn from Fig. 4.10.

is observed even at a frequency as low as 10 Hz as long as the ac voltage is above 2 V.

A theoretical model has been developed to account for the voltage and frequency dependences of the annealing results, which will be discussed in the next section.

#### 4.4.2 Theoretical Considerations and Data Analysis

##### A. Voltage Dependence

Under the X-ray irradiation, an excess density of electrons and holes is produced in the oxide, due to the combined effect of bulk generation and contact photoinjection as described in Chapter VI. These excess carriers undergo an oscillatory motion under the influence of the applied ac voltage, and electron-hole recombination continuously takes place. If the recombination event occurs through a defect center, then there is some probability that this defect can be annealed via the REDR mechanism discussed in section 2.6. According to this model, the annealing rate is directly proportional to the electron-hole recombination rate, and thus the experimentally observed voltage dependence of the annealing rate may be simply a manifestation of the same dependence of the recombination rate.

The process of electron-hole recombination in the  $\text{SiO}_2$  can be qualitatively described as follows. Due to the generally much larger capture cross-section of the hole traps (vs. electron traps) and the

much slower hole mobility, the probability of hole trapping is several orders of magnitude higher than electron trapping. Therefore, the recombination process can be viewed on average as a two-step process in series : first, a hole is trapped; then an electron is captured by this trapped hole through Coulombic interactions. The recombination rate is thus controlled by the second step, which makes the analysis simpler, because essentially one needs to deal with one type of carriers only.

Suppose the trapped hole density is  $N_t^+$  at  $t = 0$ . The rate equation for electron trapping is given by

$$\frac{dN_t^o(t)}{dt} = \frac{J\sigma}{q} \left[ N_t^+ - N_t^o(t) \right] \quad (4.1)$$

where  $N_t^o(t)$  is as defined in section 4.5.1,

$\sigma$  is the effective capture cross-section of positive charge center, and  $J$  is the total current flowing in the oxide under X-ray irradiation.

The solution of equation (4.1) with boundary conditions  $N_t^o(t = 0) = 0$ , and  $N_t^o(t = \infty) = N_t^+$  is

$$\frac{N_t^o(t)}{N_t^+} = 1 - \exp \left[ -\frac{J\sigma}{q} t \right] \quad (4.2)$$

When  $\frac{J\sigma}{q} t$  is very small, equation (4.2) can be rewritten as

$$\frac{N_t^o(t)}{N_t^+} \approx \frac{J\sigma}{q} t \quad (4.2.1)$$

The voltage dependence is implicit in the parameters  $J$  and  $\sigma$ , which will be discussed next.

The X-ray induced current,  $J$ , includes two components : the bulk generation,  $J_{ox}$ , and contact photoinjection,  $J_{inj}$ . These two components are functions of the oxide field,  $E_{ox}$ , and can be expressed as (see Chapter VI for details) :

$$J_{ox} = A E_{ox}, \quad (4.3)$$

$$J_{inj} = A' f(E_{ox}) e^{-(B/E_{ox})^{1/2}}, \quad (4.4)$$

$$\text{and} \quad J = J_{ox} + J_{inj} \quad (4.5)$$

where  $A$ ,  $A'$  and  $B$  are independent of  $E_{ox}$ , and  $f(E_{ox})$  is a weak function of oxide field. The functional forms of these parameters are defined in Chapter VI.

Combining equations (4.2), (4.3) and (4.4), the annealed percentage can be further expressed as :

$$\frac{N_t^o(t)}{N_t^+} = 1 - \exp\left[-\left(AE_{ox} + A'f(E_{ox}) e^{-(B/E_{ox})^{1/2}}\right) \frac{\sigma}{q} t\right] \quad (4.2.2)$$



In addition to  $J$ , the parameter  $\sigma$  is also a function of the oxide field, although the dependence is not as strong. Ning (1976) has shown experimentally that the field dependence of the capture cross-section of a positive charge center is proportional to  $E_{ox}^{-3}$  for oxide fields higher than 1 MV/cm. For lower oxide fields Ning's experimental data show considerable uncertainty about the exponent, but in general he has found that the higher the oxide field, the smaller the capture cross-section of a Coulombic trap due to the shrinkage of the capture volume with increasing field.

Preserving the form of Ning's field dependence with the exponent as an adjustable parameter, the capture cross-section can be written as

$$\sigma(E_{ox}) = C E_{ox}^{-a} \quad (4.6)$$

where  $C$  and  $a$  are independent of the oxide field. As will be shown later, the oxide field dependence of  $\sigma$  is quite weak for oxide-fields below 1 MV/cm in this study.

The parameter  $\sigma$  is also a function of temperature. When the wafer temperature gets higher, the capture radius decreases and the re-emission probability increases due to the increasing number of lattice phonons (DiMaria 1978). Lax (1960) has derived an expression for the temperature dependent capture cross-section of a positive charge center :

$$\sigma = \sigma_0 \lambda [1 - \exp(-\lambda)]^{-1} D(\lambda) \quad (4.7)$$

where  $\sigma_0$  has the unit of cross-section, and is independent of temperature,  $\lambda = h\nu_p/KT$  with  $h\nu_p$  the dominating LO phonon (60 meV for  $\text{SiO}_2$ ) (Hughes 1973, Lynch 1972, Spitzer and Kleinman 1961),

$$D(\lambda) = \int_0^\lambda p(\lambda-x) \left[1 - (x/\lambda)\right]^{-3/2} \exp(-x) dx$$
 with the sticking probability  $p(y) = 1 - (1 + y + \frac{1}{2}y^2) \exp(-y)$ .

In our experiments at a wafer temperature of  $100^\circ\text{C}$ ,  $\lambda \approx 0.2 < 1$ , and the cross-section  $\sigma$  varies as  $T^{-4}$  according to a calculation from equation (4.7). Therefore, the capture cross-section expressed in terms of its field and temperature dependence is

$$\sigma(E_{\text{ox}}, T) = C' E_{\text{ox}}^{-a} T^{-4} \quad (4.7.1)$$

where  $C'$  is a constant independent of  $E_{\text{ox}}$  and  $T$ . Substituting equation (4.7.1) back into equation (4.2.2), the voltage dependence of the annealing has the form.

$$\frac{N_t^0(t)}{N_t^+} = 1 - \exp\left[-\frac{t}{q} (AE_{\text{ox}} + A'f(E_{\text{ox}}) e^{-(B/E_{\text{ox}})^{1/2}}) (C'E_{\text{ox}}^{-a} T^{-4})\right] \quad (4.2.3)$$

So far we have discussed the case for a dc field. For an ac field, which is the case of interest here,  $E_{\text{ox}}$  is a harmonic function of time, and the analysis becomes much more complicated. Fortunately, the term representing the capture cross-section in equation (4.7.1) is a very weak

function of  $E_{ox}$ , and the term representing the photocurrent is approximately a linear function of  $E_{ox}$  in the field range of interest here (see Chapter VI). Therefore we can take  $E_{ox}$  in equation (4.2.3) to be the average magnitude of the field defined as

$$\bar{E}_{ox} = \frac{1}{T} \int_0^T |E_{ac} \sin 2\pi ft| dt = \frac{2}{\pi} E_{ac}.$$

Notice that the problem is independent of the polarity of the field.

Using equation (4.3.3) derived above, we have plotted a theoretical curve to fit the 1 KHz annealing data presented in Fig. 4.9. This is shown in Fig. 4.11. The values of the various parameters used in the numerical fitting procedure are listed in Table 4.2, where  $V_{ac}$  and  $J$  are experimentally determined quantities,  $\bar{V}_{ac}$ ,  $\bar{E}_{ox}$ , and  $J/q$  are calculated directly from the experimental data, and  $\sigma$  is the only adjustable parameter. Note also that a saturation level at 56% is set for the theoretical curve in order to allow quantitative comparison.

The values of  $\sigma$  listed in Table 4.2 correspond to the field-dependent capture cross-sections of the traps at 100°C. Numerically we have found that the field dependence goes as  $E_{ox}^{-0.214}$ . Using equation (4.7.1) the capture cross-sections at room temperature have been determined, and are listed in Table 4.3. Notice that the room temperature  $\sigma$  at  $E_{ox} = 1 \times 10^6$  V/cm in Table 4.3 is in excellent agreement with the value ( $\sim 1.2 \times 10^{-13}$  cm<sup>2</sup>) reported by Ning (1976).

Thus the field and temperature dependence of the traps in the field

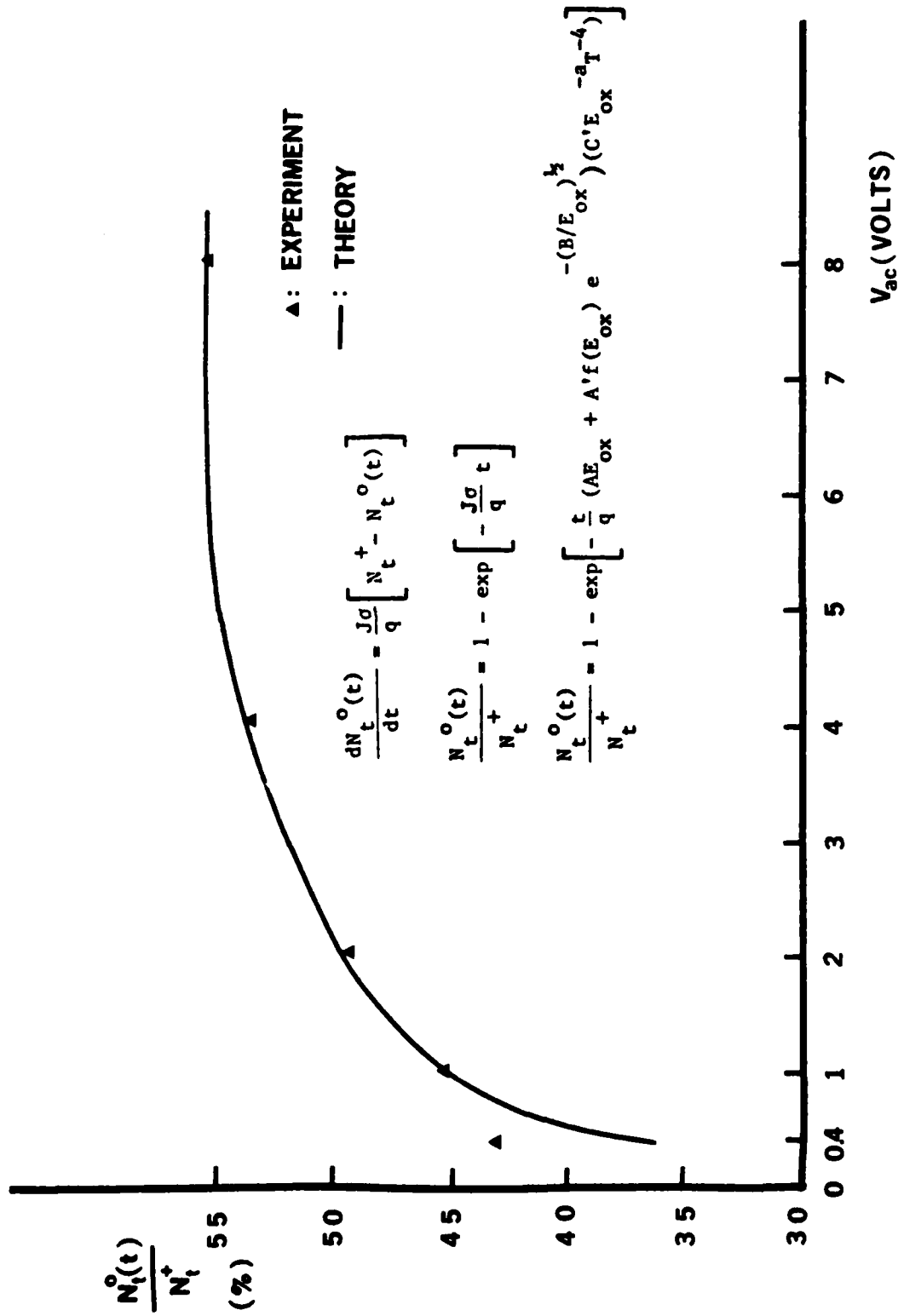


Fig. 4.11 Voltage dependence of the RF annealing behavior at 1 KHz. Solid triangles: experimental data obtained from Fig. 4.9. Solid curve: theoretical fit using Eq. (4.2.3).

TABLE 4.2 Values of the various parameters used in the numerical fitting procedure for the voltage dependence of RF annealing rate.

$V_{ac}$	$\overline{V}_{ac}$	$\overline{E}_{ox}$	$J = J_{ox} + J_{inj}$	$J/q$	$\sigma(\overline{E}_{ox}, 100^\circ C)$
0.4	0.254	$5.00 \times 10^4$	$0.189(0.0573 + 0.132) \times 10^{-7}$	$0.118 \times 10^{12}$	$1.44 \times 10^{-13}$
1.0	0.636	$1.27 \times 10^5$	$0.35(0.113 + 0.237) \times 10^{-7}$	$0.219 \times 10^{12}$	$9.72 \times 10^{-14}$
2.0	1.72	$2.54 \times 10^5$	$0.514(0.206 + 0.308) \times 10^{-7}$	$0.321 \times 10^{12}$	$6.81 \times 10^{-14}$
4.0	2.546	$5.1 \times 10^5$	$0.80(0.423 + 0.377) \times 10^{-7}$	$0.50 \times 10^{12}$	$6.52 \times 10^{-14}$
8.0	5.10	$1.0 \times 10^6$	$1.257(0.80 + 0.475) \times 10^{-7}$	$0.785 \times 10^{12}$	$5.62 \times 10^{-14}$
16	10.2	$2.1 \times 10^6$	$2.137(1.428 + 0.708) \times 10^{-7}$	$1.3357 \times 10^{12}$	$5.19 \times 10^{-14}$

TABLE 4.3 Trap capture cross-sections at room temperature obtained from Eq. (4.7.1).

$E_{ox} (V/cm)$	$1 \times 10^5$	$2 \times 10^5$	$5 \times 10^5$	$1 \times 10^6$	$2 \times 10^6$
$\sigma(E_{ox}, RT) (cm^2)$	$2.2 \times 10^{-13}$	$1.72 \times 10^{-13}$	$1.37 \times 10^{-13}$	$1.12 \times 10^{-13}$	$6.2 \times 10^{-14}$

range  $5 \times 10^4 - 2 \times 10^6$  V/cm may be expressed as

$$\sigma(E_{ox}, T) = 2.11 \times 10^{-2} T^{-4} E_{ox}^{-0.214}$$

This field dependence appears to be significantly weaker than that reported by Ning (1976) for fields above  $1 \times 10^6$  V/cm. In the lower field region, however, Ning's data show significant scattering, and a weaker field dependence is generally observed.

Comparing the theoretical curve with the experimental data in Fig. 4.11, it is apparent that the agreement is excellent for gate voltages above 1 V. The deviation in the low voltage region could be due to the fact that the present model is an oversimplification, which does not include the detailed hole trapping kinetics. It will be shown in the next section that the recombination process is in competition with the hole trapping process, and the latter becomes more important for low RF voltages and frequencies causing reduced net annealing rate. The uncertainties in the work function difference and the local charge effect may also contribute to this deviation.

According to the above analysis, therefore, the voltage dependence of the annealing behavior follows essentially the same trend as the voltage dependence of the recombination rate, as predicted by the REDR model. The experimentally observed frequency dependence (Figs. 4.9.1 and 4.10.1), however, is still to be resolved, and is the subject of discussion in the next section.

## B. Frequency Dependence

The frequency dependence of the annealing behavior is more difficult to understand. However, based on the fact that the annealing process is in constant competition with the radiation damage process, and that the latter is frequency dependent due to the low mobility of the holes, we have arrived at a model which can account for the experimental observation.

Consider first an MOS device under X-ray irradiation with a dc bias across the device. This might be viewed as the low frequency limit of the "RF" annealing experiment. For a positive bias on the gate electrode, the radiation-induced holes in  $\text{SiO}_2$  are driven toward the  $\text{SiO}_2$ -Si interface, and many of them are trapped by the hole traps distributed within a distance  $d$  from that interface. This distance  $d$  has been experimentally determined to be less than  $50 \text{ \AA}$  (DiMaria et al. 1976, Stivers and Sah 1980). The radiation-induced electrons to some extent recombine with the holes, but mostly are swept out of the oxide due to their much higher mobility. As a result, the well-known radiation-induced positive oxide charge is observed. For a negative bias, the radiation-induced holes in  $\text{SiO}_2$  are driven toward the gate electrode, and the hole trapping within the region  $d$  also occurs. But because of the closeness of the spatial distribution of the hole traps to the  $\text{SiO}_2$ -Si interface, the positive-bias case produces more trapped holes than the negative-bias case, due to their difference in the hole flux crossing the region  $d$ . In the positive-bias case the effective hole flux arises from the generation over the whole thickness of  $\text{SiO}_2$  plus a small contribution from the contact photoinjection (from the gate- $\text{SiO}_2$

interface), while in the negative bias case it is limited to the hole generation within the small region  $d$  plus the contribution from the contact injection (from Si-SiO<sub>2</sub> interface).

Thus under a dc bias, net radiation damage by X-ray irradiation is observed, with the damage being more severe for a positive bias. On the other hand, under a high frequency (13.56 MHz) RF voltage, the X-ray irradiation gives rise to net annealing as we have observed. Between these two limiting frequencies it is expected that the annealing process and the damage process occur simultaneously, and the net annealing rate is the difference of the two.

Consider now the frequency dependence of the hole trapping. Under an ac voltage, the radiation-induced holes are forced to move back and forth, and those that reach the region  $d$  will have some probability of being trapped. During each half cycle, the distance that a hole travels is

$$d_h = \int_0^{\frac{T}{2}} v_h(t) dt = \int_0^{\frac{T}{2}} \mu_h E_{ox} \sin 2\pi ft dt$$

$$= \frac{\mu_h E_{ox}}{\pi} \left(\frac{1}{f}\right) \quad (4.8)$$

where  $\mu_h$  = hole mobility in SiO<sub>2</sub>, and  $d_h \leq d_{ox}$ .

For the positive half cycle, the distance,  $d_h$ , from the SiO<sub>2</sub>-Si interface corresponds to an effective length within which the generated



holes can arrive at the hole traps, and therefore is proportional to the effective hole density available in the trapping process. For the negative half cycle, this effective length is essentially the constant  $d$  for  $d_h > d$ , and can be neglected in most cases where  $d_h \gg d$ .

From an analysis of the first-order hole trapping kinetics, the hole trapping can be described as

$$T_h = \alpha \left[ 1 - \exp(-n_h \sigma v_{th} t) \right] \quad (4.9)$$

where  $T_h$  is the trapped hole density,

$n_h$  is the effective hole density available for trapping,  $n_h \propto d_h$ ,

$\sigma$  is the capture cross-section of the hole traps,

$v_{th}$  is the thermal velocity of holes, and

$\alpha$  is a proportional constant.

Since  $n_h \propto d_h = \frac{\mu_h E_{ox}}{\pi} \left(\frac{1}{f}\right)$ , equation (4.9) can be re-expressed as

$$T_h = \alpha \left[ 1 - \exp(-\beta/f) \right] \quad (4.10)$$

where  $\beta \propto \frac{\mu_h E_{ox} \sigma v_{th} t}{\pi}$  is independent of frequency.

Equation (4.10) thus suggests that the amount of trapped holes within a given time period is a function of the frequency of the applied ac voltage. The relative net annealing is therefore given by

$$\begin{aligned} A &= 1 - T_h \\ &= 1 - \alpha \left[ 1 - e^{-\beta/f} \right] \end{aligned} \quad (4.11)$$

As shown in Fig. 4.12, the theoretical curve based on equation (4.12) is in reasonable agreement with the experimental data for the 0.4 V curve. This low-voltage curve has been selected here because it exhibits the strongest frequency dependence (see Fig. 4.9.1), and thus allows for a more meaningful comparison.

Both the theoretical curve and the experimental data indicate a saturation effect occurring around 1 MHz. The saturation occurs because as the frequency increases, the effective hole density available for trapping ( $\propto d_h$ ) decreases, as equation (4.8) indicates. As  $d_h$  becomes equal to or less than  $d$ , however, the effective length for the supply of hole flux to be trapped in region  $d$  becomes  $d$  itself and is independent of frequency. The saturation frequency for a given applied ac voltage can be estimated as follows. Suppose  $d = 50 \text{ \AA}$ , an upper limit determined by DiMaria et al. (1976). Then the saturation frequency corresponds to the frequency at which equation (4.8) yields  $d_h = 50 \text{ \AA}$ . Using  $V = 0.4 \text{ V}$  and  $\mu_h = 5 \times 10^{-5} \text{ cm}^2/\text{V-sec}$  (Hughes 1973, 1978), the calculated saturation frequency is  $f_s = 1.6 \text{ MHz}$ , in good agreement with the experimental result.

#### 4.5 CONCLUSION

In an experimental simulation to study the RF plasma annealing mechanisms, we have been able to independently control the flux of the ionizing radiation, the RF field, and the wafer temperature, and to observe their individual and cooperative effects. The presence of the

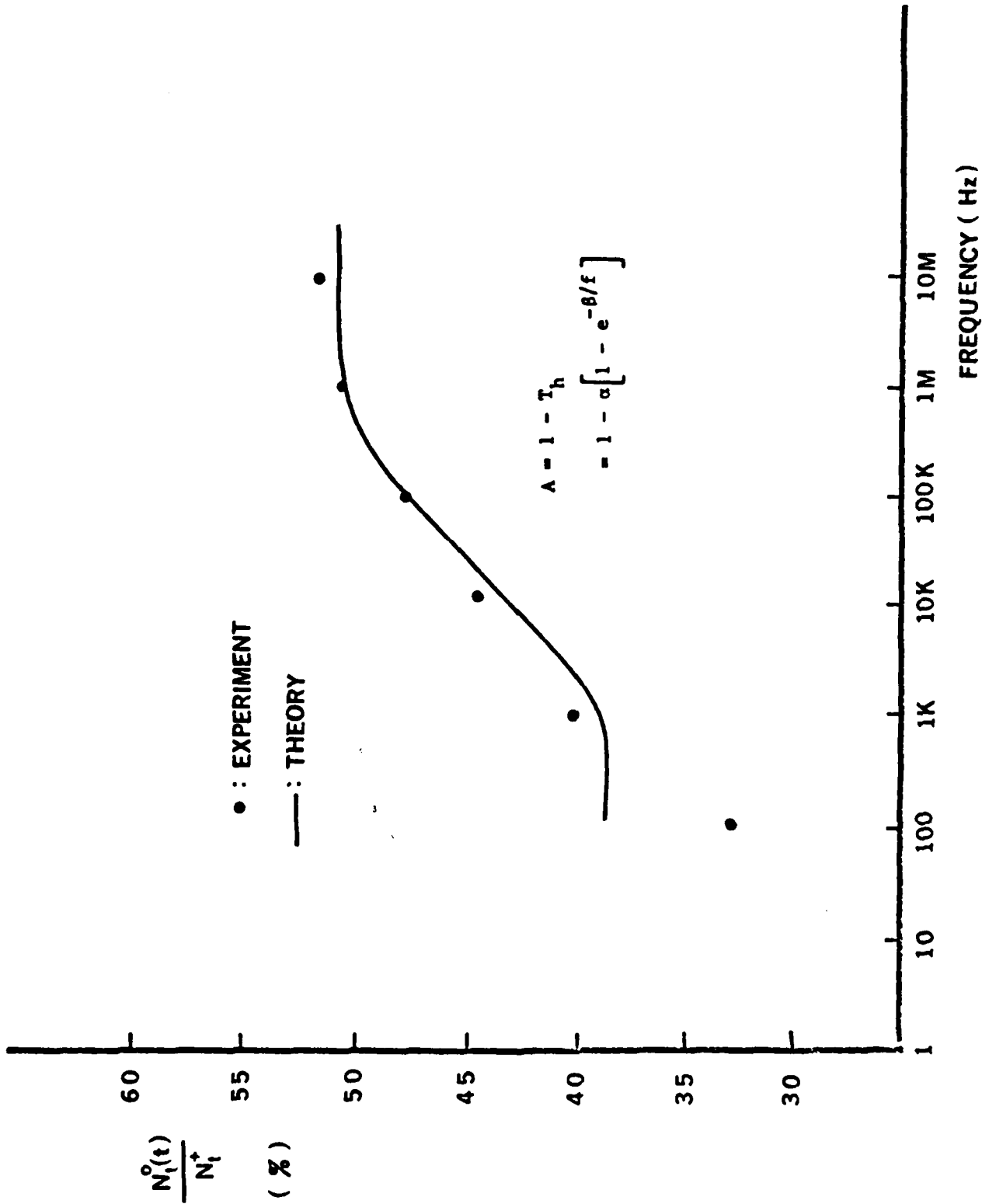


**Fig. 4.12** Frequency dependence of the RF annealing behavior at a peak ac voltage of 0.4 V. Solid dots: experimental data obtained from Fig. 4.9.1. Solid curve: theoretical fit using Eq. (4.11) with  $\alpha = 0.12$ ,  $\beta = 10984$ .

ionizing radiation and the RF field results in a reduction of the activation energy of the annealing process, which is consistent with a mechanism based on the REDR model.

The voltage and frequency dependence of RF annealing rate have been experimentally observed. The theoretical analysis indicates that the voltage dependence of the annealing behavior can be satisfactorily described by a first order recombination kinetics, and this dependence thus follows essentially the same trend as the voltage dependence of the recombination rate, as predicted by the REDR model. The frequency dependence of the annealing behavior is more difficult to understand. However, based on the fact that the annealing process is in constant competition with the radiation damage process, and that the latter is frequency dependent due to the low mobility of the holes, we have proposed a model taking into account the hole-trapping kinetics, which can account for the experimental observations.

Although the present study deals with the annealing of the oxide charge only, mainly because of the relative simplicity in the experimentation, we believe that the proposed REDR process must play an equally important role for the annealing of the neutral traps. A similar study on the neutral traps, however, is much more difficult because of the lengthy measurements and the tedious data analysis that are required to reveal these traps. To overcome this difficulty, the development of a computer interface for neutral trap measurements is necessary, and such results can be used to further clarify the REDR model.

## CHAPTER V

### MECHANISMS OF THERMAL ANNEALING AND RF ANNEALING

#### 5.1 INTRODUCTION

Thermal annealing has been widely used to remove the defects caused by ionizing radiation. Although it is certain that the thermal energy helps to promote the recovery of the deformed bonds, the detailed mechanisms involved are not yet clear. The reason that we are interested in the thermal annealing mechanism is that the Recombination-Enhanced Defect Reactions (REDR) model, which we believe is intimately related to the RF annealing process (Chapter II and IV), still requires thermal energy to activate the defect annealing process, although the activation energy is reduced by the recombination event.

In the first part of this Chapter, we will first discuss qualitatively the thermal annealing mechanism in which a configuration diagram is used to explain the difference in the defect energy levels determined by optical excitation and thermal activation. Then a mathematical model based on the first-order reaction kinetics is used to describe the annealing rate. It will be shown that a distributed activation energies, rather than a discrete level is physically more meaningful for the MOS system.

In the second part of this Chapter, the RF annealing mechanism is discussed. Three possible mechanisms for the electronic enhancement of defect reaction rate will be presented, of which the recombination

enhancement is shown to be the major effect in the RF annealing process. Finally, the quantitative REDR theory developed by Weeks, Tully and Kimerling (1975) will be used to examine our RF annealing results.

## 5.2 QUALITATIVE MODEL FOR THERMAL ANNEALING MECHANISM

It has been reported that the radiation-induced oxide charge and surface states in  $\text{SiO}_2$  can be completely annealed out in forming gas at a temperature between 300 - 450°C (Deal 1974, Balk 1965). The dependence of the atomic processes responsible for the annealing of radiation-induced defects upon the temperature in  $\text{SiO}_2$ , however, has not been explained.

The diagram in Fig. 5.1 illustrates a simple model of the electron-lattice interaction in which for simplicity the lattice is represented by a single coordinate. As the lattice vibrates, the trap level,  $E_t$ , moves up and down in the energy gap. Prior to the electron capture, the equilibrium position of the level is in the upper half of the gap. After capture of the electron the lattice near the defect relaxes in such a way as to lower the equilibrium position of the level in the energy gap. Consider the thermal excitation of an electron illustrated in Fig. 5.1. The thermal excitation energy,  $E_T$ , would be much smaller than the optical excitation energy,  $E_p$ , which is consistent with the experimental findings (DiMaria 1978, Mott and Davis 1979, Dekeersmaecker and DiMaria 1980).

The configuration diagram shown in Fig. 5.1(b) has been used by Gwyn (1966) to explain qualitatively the thermal annealing mechanism. In this diagram, the lower and upper curves correspond to the normal

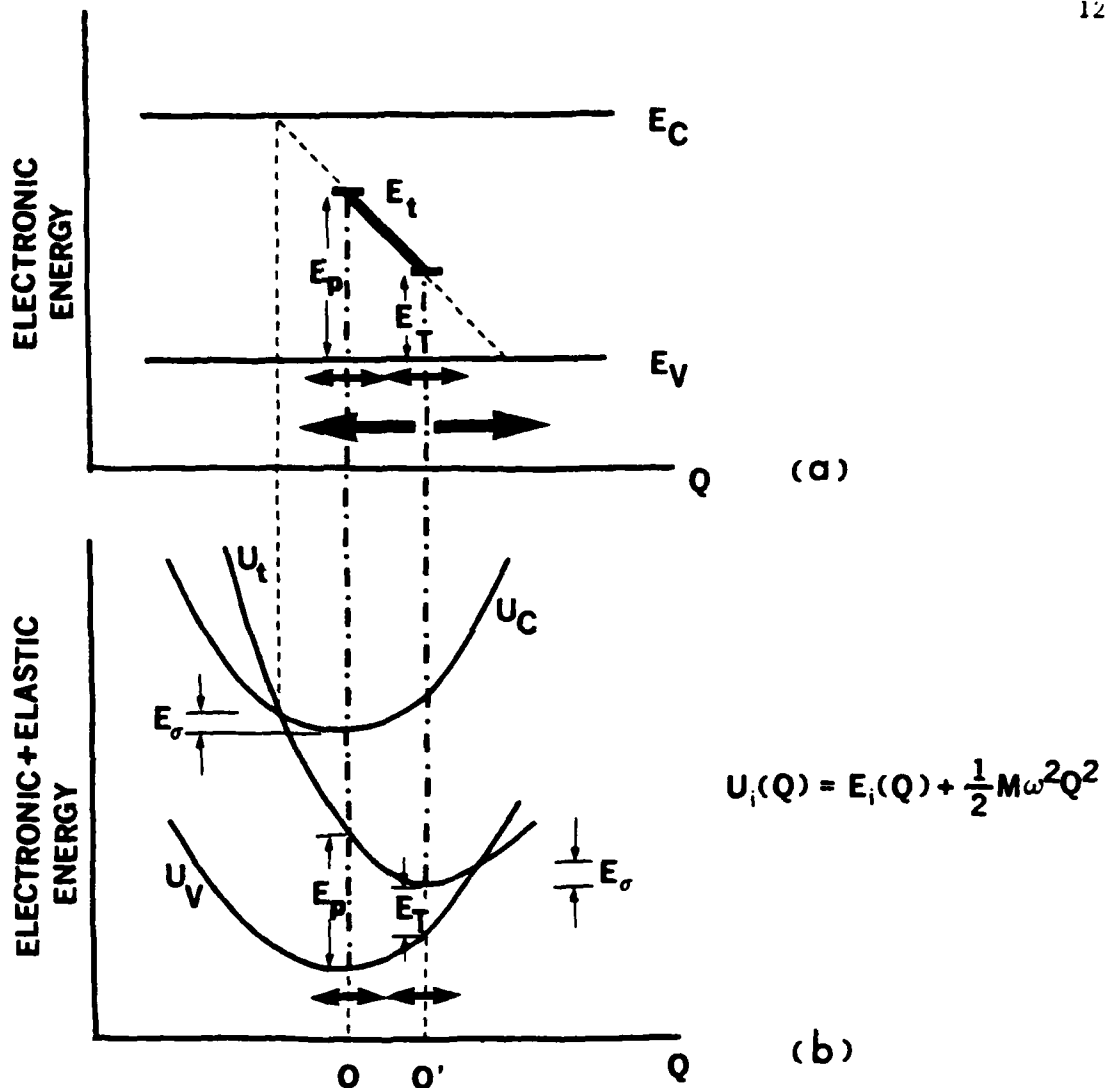


Fig. 5.1 (a)

Electronic energies vs lattice coordinate  $Q$ . The equilibrium positions of the lattice coordinates and the energy levels, before and after electron capture, are indicated by the dash-dotted lines. The short arrows represent the amplitudes of the thermal vibration. The long arrows represent the amplitude of the lattice vibrations about the new equilibrium position, immediately after capture.

(b)

The corresponding configuration coordinate diagram (electronic + elastic energies vs  $Q$ ). The optical excitation threshold  $E_p$  at lattice equilibrium and thermal excitation  $E_T$  are indicated.

conduction and valence potential wells ( $U_c$  and  $U_v$ ). The middle curve represents a trap energy level ( $U_t$ ) in the gap having a relaxed broken bond or trapped hole. With the presence of some thermal activation, the electron in the normal bond can be excited into the trap level with energy  $E_T$  instead of  $E_p$ . Following Gwyn's argument, once the electron has been excited from a normal bond to the trap level, a broken bond is formed. By repeating this process, the broken bond can be moved along the  $\text{SiO}_2$  lattice to the metal or silicon interface where recombination with an electron in the metal or silicon can occur.

The above annealing mechanism only qualitatively describes the possible motion of the defects, and is by no means complete; however, it does offer a plausible explanation whilst there is no other available accurate description of this subject. In the next section we will discuss a more detailed quantitative model using the first order rate equation for the thermal reactions.

### 5.3 QUANTITATIVE RATE EQUATION FOR THERMAL ANNEALING

#### 5.3.1 Single Activation Energy

Assuming that a first-order rate process with a single activation energy holds for short time intervals (Dekeersmaecker and DiMaria 1980), the thermal annealing rate for such a single level trap can be described by the following rate equation :

$$\frac{d}{dt} N(t) = R_T [N_0 - N(t)] \quad (5.1)$$



where  $N(t)$  = density of defects at time  $t$ ,

$N_0$  = density of defects before annealing,

$$R_T = \text{annealing rate} = \nu_T e^{-E_a/KT}, \quad (5.2)$$

$\nu_T$  = frequency factor, and

$E_a$  = single activation energy for thermal annealing.

The solution for equation (5.1) is

$$N(t) = N_0 \left[ 1 - \exp(-R_T t) \right] \quad (5.3)$$

and

$$R_T = \nu_T e^{-E_a/KT} = \frac{1}{t} \ln \left[ \frac{N_0}{N_0 - N(t)} \right], \text{ or}$$

$$R_T t = -\ln \left[ 1 - \frac{N(t)}{N_0} \right] \quad (5.4)$$

When  $N(t)/N_0 \ll 1$ , equation (5.4) can be simplified as

$R_T = \frac{1}{t} \cdot \frac{N(t)}{N_0}$  which corresponds to the annealing rate equation previously used in Chapter IV. Equation (5.4) suggests that, from an isochronal thermal annealing experiment, one may be able to obtain the activation energy,  $E_a$ , provided the Arrhenius plot yields a straight line.

Fig. 5.2 shows the Arrhenius plots of annealing rate for an X-ray irradiated MOS sample. Both the data for a pure thermal process and for the recombination-enhanced processes are plotted on the same graph for comparison. For the moment we are concerned with the thermal annealing

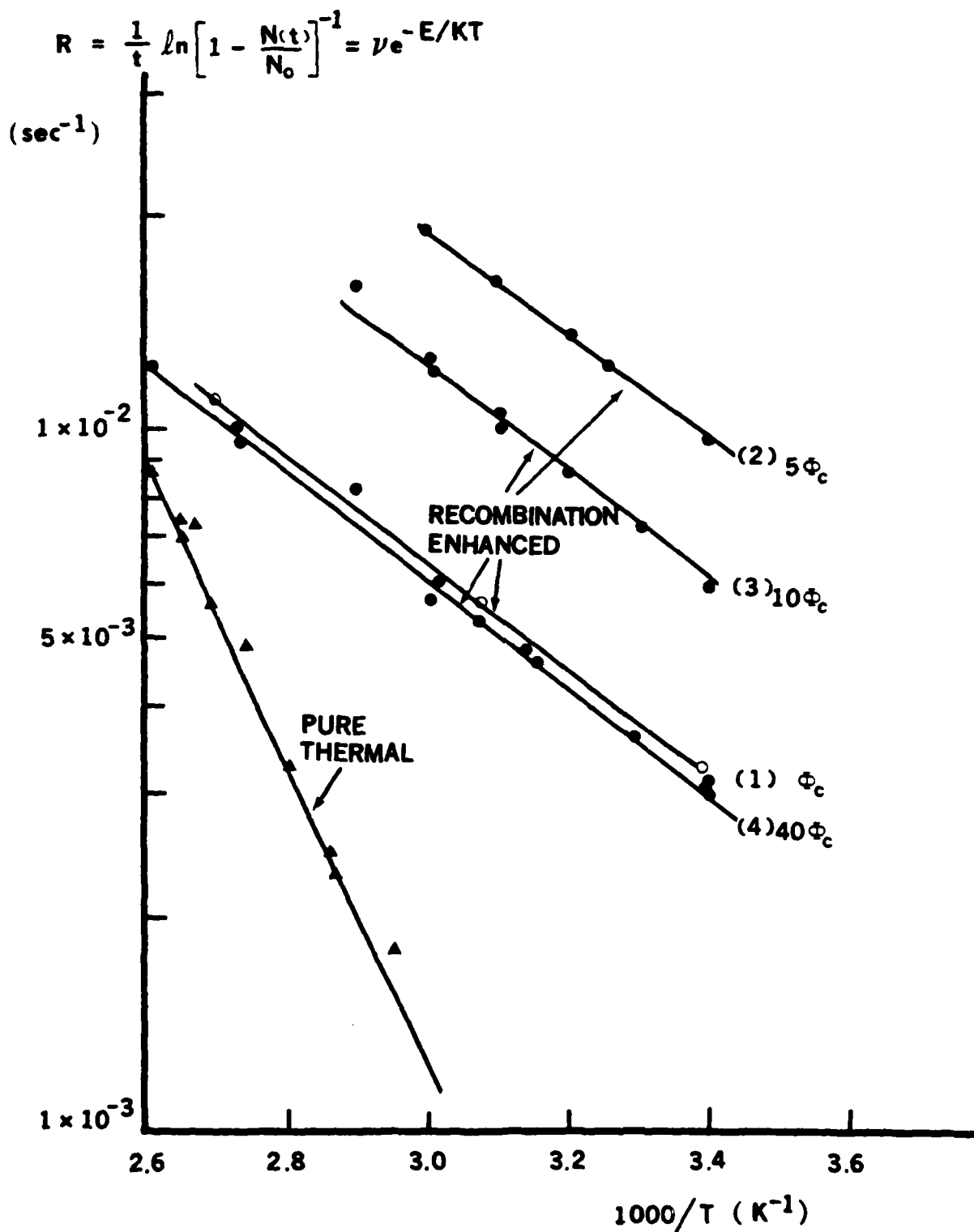


Fig. 5.2

Arrhenius plots of the annealing rate (Eq. (5.4)) for pure thermal and recombination-enhanced processes. Four X-ray fluxes are used where  $\Phi_c = 1.8 \times 10^{16}$  eV/cm<sup>2</sup>-sec. The activation energies are <sup>c</sup>0.413 eV (pure thermal) and 0.143 eV (recombination-enhanced).

process only; the recombination enhanced process will be discussed in the next section. These data are taken from an isochronal annealing experiment with one minute annealing time.

The data in Fig. 5.2 indeed show that an average activation energy may be assigned to each process. From the slope of the linear fit, the average activation energy for the pure thermal process is approximately 0.413 eV. The thermal annealing rate of Fig. 5.2 can be numerically expressed as :

$$R_T = 2.4 \times 10^3 e^{-0.413/KT} \quad (5.5)$$

Notice that a very low jump frequency factor  $\nu_T$  of  $2.4 \times 10^3 \text{ sec}^{-1}$  is required to fit the experimental results. This  $\nu_T$  differs wildly from the atomic vibration frequency,  $\nu_a \approx 10^{12} - 10^{14} \text{ sec}^{-1}$ . In addition, the activation energy,  $E_a$ , seems to be too small compared to the bonding energies of Si-Si (~2 eV) and Si-O (~4 eV) (Pauling 1960). A more reasonable activation energy for the bond reformation should be closer to the bonding energies. These discrepancies have led to some difficulties in the interpretation of the experimental results, and have cast some doubts on the validity of the single activation energy model.

It has been reported by Dekeersmaecker and DiMaria (1980) that the thermal detrapping of electrons in the MOS system can not, in general, be described by a single process with a uniquely defined activation energy. A similar conclusion has been reached in the study of the thermal kinetics associated with the release of mobile ions from traps (Hickmott

1975, Nauta and Hillen 1978, Boudry and Stagg 1979). On the other hand, if a distributed activation energies is assigned to the defects, more physically meaningful frequency factors and activation energies can be obtained (Dekeersmaecker and DiMaria 1980, Nauta and Hillen 1978, Boudry and Stagg 1979). This approach will be taken in the next section to examine the annealing behavior of the positive oxide charge in  $\text{SiO}_2$ .

### 5.3.2 Distributed Activation Energies

Although some of the radiation-induced defect centers in single crystalline materials can be adequately described as discrete energy levels (Kimerling 1976, 1978, Henry and Lang 1977), a distribution of levels is more probable for amorphous  $\text{SiO}_2$  inasmuch as the optical experiments do not yield a discrete line absorption spectrum, but rather a continuous distribution in energy (Brekhovskikh et al. 1971, Mitchell and Denure 1973, Koyama 1980). A similar energy distribution is likely to occur for the relaxed broken bonds where a wide variation of the bond distances and angles could exist.

Consider a Gaussian distribution of activation energies around a median energy,  $E_M$ , for the thermal annealing process as given by

$$f(E) = \frac{1}{\sqrt{2\pi} \Delta E} \exp \left[ -(E - E_M)^2 / 2(\Delta E)^2 \right] \quad (5.6)$$

where  $\Delta E$  is the standard deviation representing the broadening about  $E_M$ . Thus, the thermal annealing rate with the atomic vibration frequency

$v_a$  can be expressed as

$$\begin{aligned}
 R_T &= v_T e^{-E_a/KT} = v_a \int_{-\infty}^{\infty} e^{-E/KT} f(E) dE & (5.7) \\
 &= v_a \int_{-\infty}^{\infty} e^{-E/KT} \frac{1}{\sqrt{2\pi}(\Delta E)} e^{-(E - E_M)^2/2(\Delta E)^2} \\
 &= v_a e^{-E_M/KT} e^{(\Delta E)^2/2(KT)^2} \frac{1}{\sqrt{2\pi}} \int_{-\frac{E_M + \Delta E}{\sqrt{2}\Delta E\sqrt{2KT}}}^{\infty} e^{-y^2} dy
 \end{aligned}$$

Using the above equation with a range of possible  $v_a$ 's ( $\sim 10^8 - 10^{12} \text{ sec}^{-1}$ ), (Kekeermacker and DiMaria 1980) and a  $KT$  of 0.03 eV, more reasonable activation energies,  $E_M$ 's, can be obtained by adjusting the suitable  $\Delta E$ 's. Table 5.1 lists the calculated  $E_M$ 's for different  $\Delta E$ 's ranging from 0.03 to 0.3 eV and two different  $v_a$ 's ( $10^8$  and  $10^{12} \text{ sec}^{-1}$ ).

Table 5.1 Possible  $E_M$  (eV) : THE MEAN THERMAL ACTIVATION ENERGY

$\Delta E$ (eV) \ $v_a$ (sec <sup>-1</sup> )	0.03 = $KT$	0.1	0.15	0.2	0.25	0.3
$10^{12}$	1.1	1.2	1.4	1.68	2.0	$\geq 2.2$
$10^8$	0.8	0.9	1.15	1.45	1.78	$\approx 2.0$

The above table shows that the larger the  $\Delta E$  broadening, the larger the mean activation energy. In the above calculation the smallest broadening,  $\Delta E$ , is chosen to be approximately equal to  $KT (=0.03 \text{ eV})$  while the highest  $\Delta E$  is chosen according to the highest phonon energy of the silicon compounds which is close to  $0.25 \text{ eV}$  (Handbook of Chemistry and Physics 1979).

With  $\Delta E \approx 0.3 \text{ eV}$  and  $\nu_a = 10^{12} \text{ sec}^{-1}$ , the calculated mean activation energy  $E_M$  of  $2.2 \text{ eV}$  is in good agreement with the energy of the radiation-induced type-C trap ( $\sim 2.21 \text{ eV}$ ) measured from the cathodoluminescence spectra of thermal  $\text{SiO}_2$  (Koyama 1980). On the other hand, with  $\Delta E \approx 0.03 \text{ eV}$  and  $\nu_a = 10^{12} \text{ sec}^{-1}$ , the calculated  $E_M$  is  $1.1 \text{ eV}$ . As reported by many previous workers (Fanet and Poirier 1974, DiMaria 1978, Koyama 1980), the optical energy of the defect level  $E_p$  in thermal  $\text{SiO}_2$  could be in the range of  $5 - 7 \text{ eV}$  from the valence band edge. As shown in Fig. 5.1(b), the thermal motion of the lattice can change the excitation threshold from  $E_p$  to  $E_T$ , the thermal activation energy, which is smaller than  $E_p$ , but should still be of the order of  $1 \text{ eV}$  due to electron-phonon interactions.

Unfortunately, due to the lack of information on  $\Delta E$ , we have not been able to determine the exact values of the activation energies. However, by the use of distributed activation energies instead of the single energy, we have demonstrated that it is possible to bring the frequency factors and the activation energies closer to the physically meaningful values.

#### 5.4 MECHANISMS OF RF ANNEALING

As presented in Chapters II and IV, the RF annealing process has been shown to be much more effective than the thermal annealing process to remove the radiation-induced defects in thermal SiO<sub>2</sub>. Consider the RF annealing experiment once more. In addition to the heating, the wafer is exposed to the X-ray irradiation and an RF voltage. One direct consequence of the X-ray irradiation is the introduction of excess electrons and holes in the SiO<sub>2</sub> layer. Such an environment offers an excellent opportunity for the electronic enhancement of defect reactions in SiO<sub>2</sub>. As proposed by Kimerling (1978), there exists three possible mechanisms for the electronic enhancement of defect reaction rate: the electric field effect, the charge state effect, and the recombination-enhancement. It will be shown that the first two have negligible contributions in our system, and the recombination enhancement is the major effect in the RF annealing process.

##### 5.4.1 Possible Electronic Enhancement Processes in SiO<sub>2</sub>

###### A. Electric Field Effect

The electric field, when coupled with the defect potential, can lower the reaction barrier (DiMaria 1978, Kimerling 1976, 1978). The magnitude of this barrier lowering can be estimated from a simple electrostatic consideration (Kimerling 1978) as  $\Delta E = q a E_{ox}$ , where  $a$  is the defect size and  $E_{ox}$  is the average oxide field. For a typical defect in the SiO<sub>2</sub> system,  $\Delta E$  is of the order of 0.01 eV, which is

negligibly small compared to the activation energy, and therefore the electric field effect alone should not be a major contributor to the RF annealing process.

This may be easily verified experimentally. As shown in Fig. 5.3 the annealing of oxide charge at three different temperatures is plotted with and without the RF field. The data clearly indicate that the presence of the RF field does not enhance the annealing rate.

#### B. Charge State Effect

As suggested by Kimerling (1976, 1978), a change in the charge state (occupation) of a defect level may affect a reduction of the reaction barrier as the surrounding defect bonds relax. This effect has a strong dependence upon the "Fermi-level" in the material (Kimerling 1978), which could be changed by changes in temperature and carrier concentration. It has been argued that this is usually a small effect (Kimerling et al. 1971, 1975). Besides, Kimerling et al. (1971, 1975) have shown that the charge state effect is much stronger for the annealing of charged defects than neutral centers, while our experimental results indicate that the same enhancement factor has been observed for the annealing of oxide charge, surface states and neutral traps. This suggests that the charge state effect is also not important in the MOS system.

#### C. Recombination Enhanced Defect Reactions (REDR)

This process may be qualitatively described by the schematic diagram shown in Fig. 5.4. The excess electrons and holes (e.g. generated



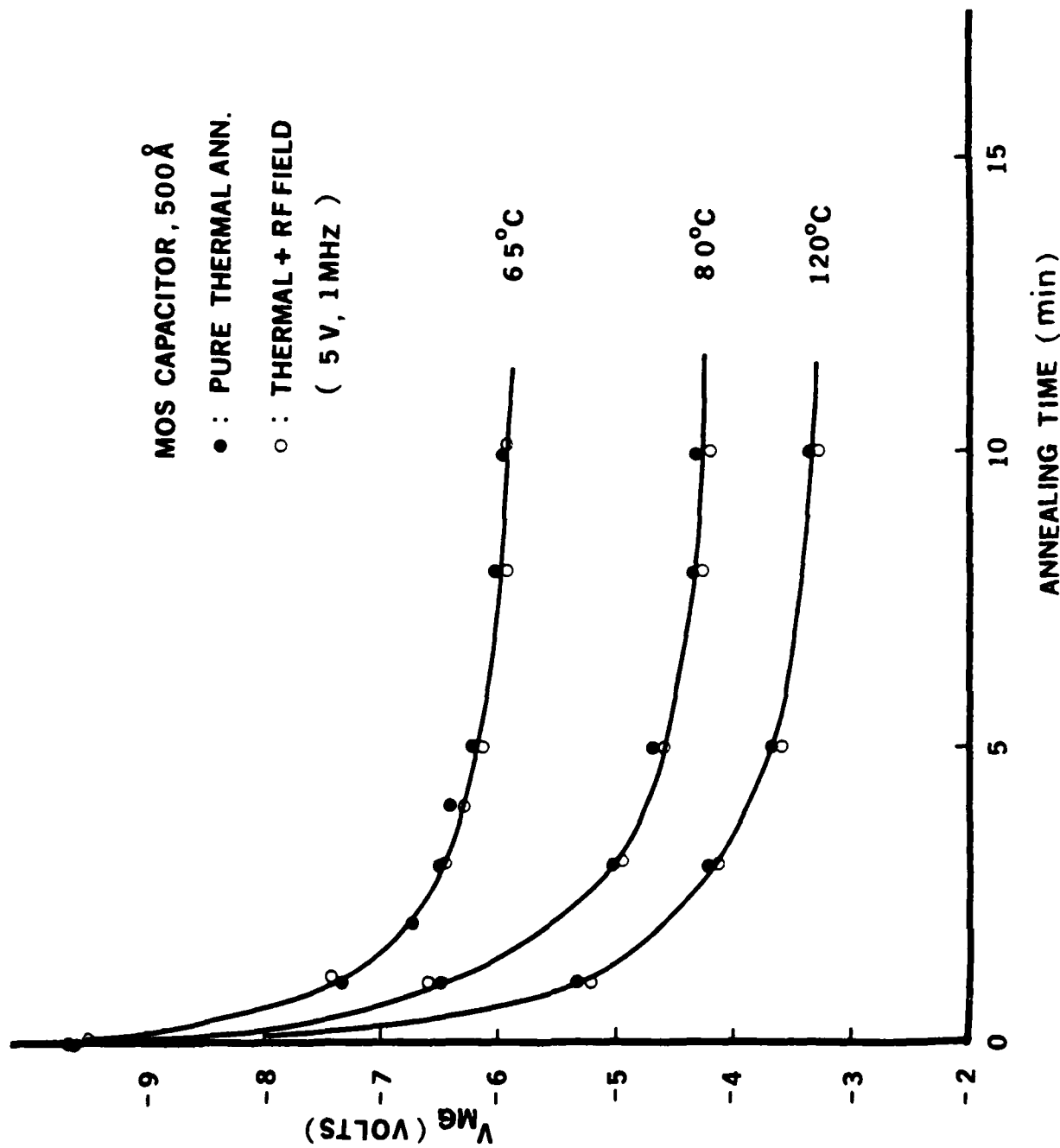


Fig. 5.3 The annealing of oxide charge at three different temperatures with and without RF field is compared.

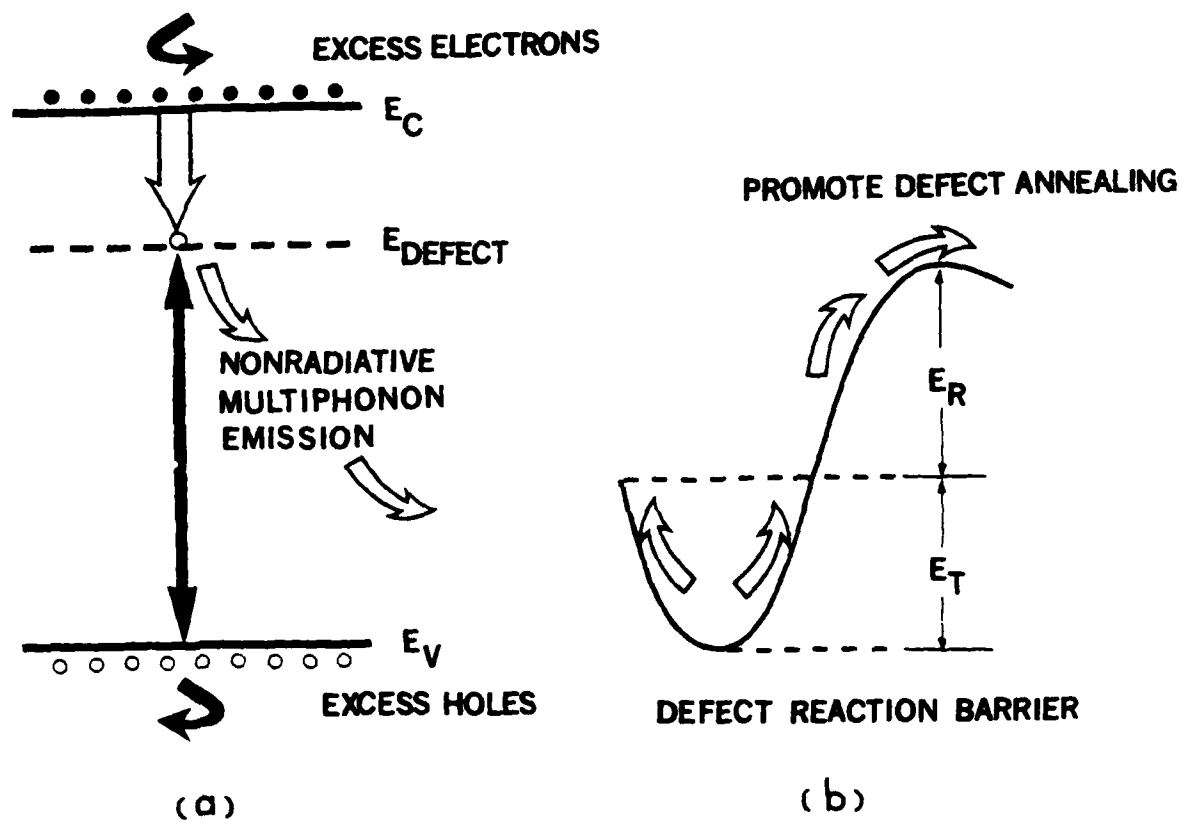


Fig. 5.4 (a) Schematic diagram showing the indirect recombination process followed by nonradiative multiphonon emission.

(b) Schematic diagram showing the recombination enhancement of defect reaction.

by X-ray irradiation) may recombine through a defect site. The transition energy released through non-radiative multiphonon emission can cause excitations of the vibrational states of the defect. If proper conditions are satisfied, this process could promote simple solid-state reactions involving the defect, such as diffusion, dissociation and annihilation (Kimerling 1976). We believe this is the most important electronic enhancement effect in the RF annealing process, which will be discussed in more detail next.

#### 5.4.2 REDR Theory and Its Mathematical Model

A mathematical model using unimolecular reactions to describe the recombination enhanced process has been formulated by Weeks, Tully and Kimerling in 1975. The fundamental physics of WTK theory is that the reaction rate constant is the sum of two terms : the usual thermally activated rate plus an additional term directly proportional to the recombination rate.

For a simple limiting case,  $E_T > E_R$ , the enhanced reaction rate may be written as :

$$R_{RE} = \eta R_R \exp \left[ \frac{E_T - E_R}{KT} \right] \quad (5.8)$$

where  $\eta$  is an efficiency factor,  $R_R$  is the recombination rate through the defect state,  $E_T$  is the pure thermal reaction barrier, and  $E_R$  is the

recombination energy that is channeled into the defect reaction process. In this case the electronic energy supplements the thermal energy already residing at the defect.

The physics behind  $\eta$  is complex, but it essentially describes the probability that the energy deposited at the defect site is directed along the reaction coordinates. Its mathematical form can be expressed as (Kimerling 1976, Weeks et al. 1975)

$$\eta = \frac{K_D}{K_L} \left[ \frac{E_T - E_R}{E_T} \right]^{S-1} \quad (5.9)$$

where  $K_D/K_L$  is the ratio of the rate of energy flow within the defect molecule to the rate of energy loss to the lattice, and the bracketed factor among  $S$  modes can find its way into the critical reaction mode.

As reported by Ballamy and Kimerling (1978) for the rate-limiting case, the recombination rate can be approximated by

$$R_R = \sigma v n = \sigma J/q \quad (5.10)$$

where  $\sigma$  is the capture cross-section of the defect site,  $v$  is the carrier velocity,  $n$  is the carrier concentration, and  $J$  is the externally collected current.

For the case where  $E_R > E_T$ , the reaction should be athermal, and equation (5.8) simplifies to

$$R_{ER} = \eta R_R \quad (5.11)$$

The efficiency factor in this case should be rewritten as (Weeks et al. 1975)

$$\eta = \frac{K_D}{K_L} \left[ \frac{E_R - E_T}{E_R} \right]^{S-1} \quad (5.12)$$

Whether the REDR process is likely or not in a given material is largely determined by the following factors (Weeks et al. 1975, Kimerling 1976, 1978). First, the defect must be a good recombination center and it should accommodate non-radiative electronic transitions, and hence should possess strong electron-phonon coupling. Thus most examples should be found in more ionic materials. Due to the large difference of the electronegativities between Si and O, the ionicity of amorphous  $\text{SiO}_2$  is approximately 50% (Pauling 1960), and therefore satisfies this requirement. Secondly, the energy involved in the electronic transition must be significant relative to the reaction barrier. Thus large bandgap materials are favored, and amorphous  $\text{SiO}_2$  with its 9 eV bandgap certainly falls in this category. Finally, the recombination rate must be high relative to the thermal excitation rate. Thus, high concentrations of free carriers (proportional to the X-ray flux in our experiment, see next section and Chapter VI) are preferred.

#### 5.4.3 Interpretation of RF Annealing Results by REDR Theory

The enhanced reaction rates at four different X-ray levels shown in Fig. 5.2 can be numerically expressed as :

$$R_{RE} = 1.0 e^{-0.143/KT} \quad \text{for curve 1 with } \Phi_c \text{ flux} \quad (5.13.1)$$

$$= 3.0 e^{-0.143/KT} \quad \text{for curve 2 with } 5\Phi_c \text{ flux} \quad (5.13.2)$$

$$= 1.9 e^{-0.143/KT} \quad \text{for curve 3 with } 10\Phi_c \text{ flux} \quad (5.13.3)$$

$$= 0.95 e^{-0.143/KT} \quad \text{for curve 4 with } 40\Phi_c \text{ flux} \quad (5.13.4)$$

where  $\Phi_c = 1.6 \times 10^{16} \text{ eV/cm}^2\text{-sec}$  is a unit of X-ray flux.

These curves show a strong flux dependence. According to equation (5.8), the net annealing rate,  $R_{RE}$ , should be proportional to the recombination rate,  $R_R$ , which is a linear function of X-ray induced current density,  $J$  (equation (5.10), Ballamy and Kimerling 1978). The experimental data in Fig. 5.2 show that, for low X-ray fluxes ( $\Phi_c - 5\Phi_c$ ), the annealing rate does increase with the flux. For higher fluxes ( $10\Phi_c - 40\Phi_c$ ), however, the annealing rate decreases with the flux. This can be explained by the X-ray damage process which competes with the annealing process. Apparently the radiation damage increases at a faster rate than the annealing as the X-ray flux increases, and at a certain flux level the two processes proceed at a comparable rate, and the net annealing rate is considerably reduced. The same behavior has been observed earlier as shown in Fig. 4.7.

The calculated enhancement factors, defined as  $R_{RE}/R_T$ , are in the

range of 14 - 45 at room temperature. It can be seen in Fig. 5.2 that the lower the temperature, the larger the enhancement, and beyond some critical temperature, the REDR process becomes insignificant and the thermally activated process dominates.

The results presented in Fig. 5.2 may be interpreted in terms of two possible REDR processes, depending on the relative magnitude of  $E_R$  and  $E_T$ .

Case 1 :  $E_R < E_T$

As discussed in the previous section, if  $E_R < E_T$  equation (5.8) can be used to describe the enhanced reaction rate. From an inspection of equation (5.13), our experimental results would yield  $E_T = 0.413$  eV and  $E_R = 0.27$  eV, provided a separate discrete energy can be assigned to the thermal activation energy and the recombination energy. Similarly equation (5.13) suggests a prefactor  $R_R \eta = 1 - 3$ , depending on the X-ray flux. Using the measured values of  $J/q = 10^{12} \text{ em}^{-2} \text{ sec}^{-1}$  (see Chapter VI), a reasonable value of  $\sigma = 10^{-13} \text{ cm}^2$  and from equations (5.8) and (5.9), one obtains  $R_R = 0.1 - 1 \text{ sec}^{-1}$ ,  $\eta = 0.1 - 3$ , and  $S = 2 - 5$ .

On the other hand, if instead of discrete energies, the distributed energies for  $E_R$  and  $E_T$  are more appropriate to describe the system, then the analysis of the experimental data becomes more involved.

Using the same procedure as described in section 5.3.2, the recombination-enhanced rate can be expressed as

$$\begin{aligned}
R_{RE} &= R_R \eta \int e^{-(E_1 - E_2)/KT} f(E_1) f(E_2) dE_1 dE_2 \\
&= R_R \eta \int e^{-E_1/KT} \frac{1}{\sqrt{2\pi} \Delta E_1} e^{-(E_1 - E_T)^2 / 2(\Delta E_1)^2} dE_1 \times \\
&\quad \int e^{-E_2/KT} \frac{1}{\sqrt{2\pi} \Delta E_2} e^{-(E_2 - E_R)^2 / 2(\Delta E_2)^2} dE_2 \quad (5.14)
\end{aligned}$$

where  $\Delta E_1$  and  $\Delta E_2$  are the standard deviations representing the broadening about  $E_T$  and  $E_R$ , respectively. Since both  $E_T$  and  $E_R$  are unknown, we may modify the above equation into one integral using  $\Delta E$  as the combined broadening about  $E_T - E_R$ . Equation (5.14) can then be simplified as

$$R_{RE} = R_R \eta \int e^{-E/KT} \frac{1}{\sqrt{2\pi} \Delta E} e^{-E - (E_T - E_R)^2 / 2(\Delta E)^2} dE \quad (5.14.1)$$

With previously calculated  $R_R$  ( $\approx 0.1 - 1 \text{ sec}^{-1}$ ) and  $\eta$  ( $\approx 0.1 - 3$ ), a range of modified activation energies ( $E_T - E_R$ ) can be obtained by adjusting the parameter  $\Delta E$ . Table 5.2 lists the calculated ( $E_T - E_R$ )'s for different  $\Delta E$ 's ranging from 0.03 eV to 0.3 eV.

Table 5.2 CALCULATED ( $E_T - E_R$ ) : THE MEAN ENHANCED ACTIVATION ENERGY

$\Delta E$ (eV)	0.03	0.1	0.15	0.2	0.25	0.3
$E_T - E_R$ (eV)	$\approx 0.2$	$\approx 0.35$	$\approx 0.55$	$\approx 0.71$	$\approx 1.22$	$\approx 1.53$



Once again we have shown that the effective activation energy for the recombination-enhanced process is significantly increased through the introduction of the broadening parameter  $\Delta E$ , just as in the case of the thermal annealing.

Case 2 :  $E_R > E_T$

In this case, the athermal enhanced reaction prevails, and

$$R_{RE} = R_R \eta = \frac{\sigma J}{q} \eta.$$

Although this process is defined as "athermal", there does exist some temperature dependence. As pointed out by Henry and Lang (1977), capture by multiphonon emission is often expressed in terms of an activated capture cross-section, which can be used to describe the temperature dependence of the enhanced rate ( $R_{RE}$ ) equation.

$$\sigma = \sigma_{\infty} e^{-E_{\sigma}/KT} \quad (5.15)$$

and 
$$R_{RE} = \frac{J}{q} \eta \sigma_{\infty} e^{-E_{\sigma}/KT} \quad (5.16)$$

where  $E_{\sigma}$  is the activation energy for MPE (of the order of 0.1 eV). The above enhancement and athermal behavior has been found by Lang and Kimerling (1976) for the E2 and E3 defect levels in GaP, and the same phenomenon could occur in amorphous SiO<sub>2</sub>.

Applying equation (5.16) to our data, one obtains  $E_{\sigma} = 0.143$  eV with

$\sigma = 3 \times 10^{-13} \text{ cm}^2$  at room temperature (Ning 1976),  $\sigma_{\infty} = 7.5 \times 10^{-11} \text{ cm}^2$  can be calculated using equation (5.15), which results in  $\eta = 10^{-2}$ .

Since we do not know the exact values of  $E_T$  and  $E_R$ , we can not say with any certainty which one of the two REDR processes is a more appropriate description of the RF annealing mechanism. It is possible that both processes exist simultaneously for different defects in  $\text{SiO}_2$ , and one or the other dominates under a given circumstance. Much more work is needed in order to resolve this problem.

#### 5.5 CONCLUSION

In an attempt to formulate a mathematical model for the RF annealing behavior, we found it necessary to examine the thermal annealing first, not only because of the similarity in the rate equations, but also because of the similarity in the physical mechanisms. Besides, the thermal annealing is much simpler, and is supposed to be much better understood. After a detailed analysis, however, we have found that, even for the thermal annealing, many questions remain to be resolved. For example, the activation energy involved in the annealing reactions has not been unequivocally determined, and its experimentally determined value depends strongly on whether the activation is discrete or distributed, and on the width of the distribution. From our analysis it appears that a distributed activation energy is a physically more meaningful description of the MOS system. To get quantitative information from such analysis, however, requires additional knowledge concerning the

actual energy distribution of the defect levels in  $\text{SiO}_2$ , which at the present time is not available.

Using the thermal annealing model as a guide, we then attempted to model the RF plasma annealing process based on the REDR theory. As expected, this problem is even more complicated, because it has all the difficulties possessed by the thermal annealing plus some additional uncertainties associated with the recombination-enhancement process. Nevertheless, we have analyzed the experimental results to the best of our ability using the two possible REDR models, and believe that we have at least laid the ground for the future development in this area.

## CHAPTER VI

### PHOTOCURRENT IN THERMAL $\text{SiO}_2$ UNDER X-RAY IRRADIATION : SIGNIFICANCE OF CONTACT INJECTION

#### 6.1 INTRODUCTION

Consider an MOS structure being irradiated by an X-ray beam. Under an applied dc bias, a current will flow in the external circuit. This current is, in general, composed of two components : (1) carrier injection from the metal/ $\text{SiO}_2$  or Si/ $\text{SiO}_2$  interface, and (2) generation current in the bulk  $\text{SiO}_2$ .

Although a significant amount of research has been done in the past on the ionizing radiation-induced currents in MOS systems (Curtis et al. 1974, Hughes 1973, 1978, Snow et al. 1967, Everhart and Hoff 1971, Farmer and Lee 1975), most authors addressed only the bulk generation component (Hughes 1973, 1978, Snow et al. 1967, Everhart and Hoff 1971), and the importance of the contact injection was either overlooked or thought to be negligible. Some workers (Curtis et al. 1974, Farmer and Lee 1975) did mention the possibility of photoinjection from the contacts, but no systematic experiments have been performed to find out how significant this current is relative to the total current.

If the current due to contact injection is indeed non-negligible, then some serious questions may be raised concerning the values of a number of important transport parameters such as the pair-generation

energy (Curtis et al. 1974, Ausman and McLean 1975), the mobility-lifetime product (Curtis et al. 1974, Snow et al. 1967, Hughes 1973, Everhart and Hoff 1971, Goodman 1966), and the field-dependent geminate recombination behavior (Curtis et al. 1974, Hughes 1978, Farmer and Lee 1975), many of which were obtained based on the measurements of radiation-induced current without taking into account the contribution from the contact injection.

Qualitatively, it is easy to understand that both current components should increase with the radiation flux and the applied electric field. In addition, it is reasonable to assume that for a given flux and field, the bulk generation current should scale with the oxide thickness (see section 6.2.2), while the contact injection component should be independent of the oxide thickness. Based on the simple argument, it is expected that the relative importance of the latter contribution will increase as the oxide gets thinner, and at or below some oxide thickness it will dominate. This principle thus offers an excellent possibility to separate out the two components using a series of samples having a range of oxide thicknesses and is the basis for the present experimental work.

It will be shown that for a 500 Å gate  $\text{SiO}_2$  both current components are approximately equal in magnitude for a wide range of electric fields ( $10^5 - 3 \times 10^6$  V/cm), and photoinjection from the contacts starts to dominate for oxides thinner than 300 Å. Since this is the thickness range most relevant to LSI and VLSI technologies, these findings are not only of scientific interest but also of practical importance. In

addition, the results to be presented are useful in the modeling of the RF plasma annealing rate as a function of applied RF voltage and frequency, which has been discussed in Chapter IV.

In section 6.2, the principles of photoinjection, bulk generation, and geminate recombination will be reviewed. The experimental details will be described in section 6.3. In section 6.4, the experimental results will be presented, followed by discussions on the significance of these findings; in particular, the importance of contact photoinjection will be substantiated, Onsager's theory of geminate recombination will be examined, and  $\mu\tau$  products of conduction electrons in  $\text{SiO}_2$  will be discussed.

## 6.2 THEORETICAL CONSIDERATIONS

### 6.2.1 Photoinjection

During X-ray irradiation, carriers (electrons and holes) in the electrodes of an MOS structure may be excited. Carriers with sufficient energy to surmount the potential barrier at either the metal-oxide or the oxide-silicon interface may be injected into the oxide to be collected at the other electrode, giving rise to a photocurrent. Such photocurrent induced by UV photons having energies less than the bandgap of  $\text{SiO}_2$  have been studied in considerable detail (Williams 1965, Goodman 1966, Powell and Berglund 1971). In particular, the field dependence of photoinjected current in  $\text{SiO}_2$  was of significant interest to several workers (Goodman 1966, Powell and Berglund 1971, DiMaria et al. 1977). The principal

physical mechanism for the observed field dependence has been proposed to be a result of the scattering of electrons in the region of oxide between the injection electrode and the image potential maximum. Due to the effect of the image force, the height and location of this maximum depends on the applied electric field, and the barrier lowering due to an increasing field results in an increase in the number of photoelectrons which have sufficient energy to escape.

Including the effects of the barrier lowering and scattering, Powell and Berglund (1971) have derived the photocurrent-field relationship which may be expressed as :

$$J_{inj} = J_o e^{-x_o/\ell} \quad (6.1)$$

where  $x_o = (q/16\pi\epsilon_i E_{ox})^{1/2}$  is the distance of the potential energy maximum from the injection interface,

$J_o = A(h\nu) (h\nu - \Phi_b + \Delta\Phi)^p$  is the current in the absence of scattering effect,

$\Phi_b$  is the zero-field barrier energy at the interface,

$\Delta\Phi$  is the field dependent barrier lowering,

$p$  : a parameter dependent on the excited electron energy distribution in the emitter,

$\ell$  : scattering mean free path,

$\epsilon_i$  : high frequency dielectric constant, and

$A$  : a constant for a given light intensity and photon energy  $h\nu$ .

It is worth noting that the above model predicts that the photocurrent vs oxide field characteristics are independent of oxide thickness. This property has very important implications in our current work, which allows us to separate experimentally the photoinjection component from the bulk generation component. Equation (6.1) has been established for monochromatic photons with energy less than the bandgap of  $\text{SiO}_2$ . In the case of broad band X-ray irradiation, as that used in our experiment, it is questionable whether the same field-dependence is applicable, especially when one considers the fact that hot electrons with much higher energies than the barrier are generated in this case. However, it is possible that a significant portion of these hot electrons, as they approach the interface, could lose substantial amount of their energy due to various relaxation processes (Ausman and McLean 1975, Rothwarf 1973), and the qualitative feature of equation (6.1) is preserved. As it will be shown in section 6.4.1, our experimental data tend to support this description.

There was one concern about the trapped-hole buildup during X-ray irradiation, which might adversely affect the measurements. An experiment performed by DiMaria et al. (1977), however, has shown that the location of the X-ray induced positive charge is so close to the interface that there is almost no change in the photo I-V curves before and after X-ray irradiation, even though the C-V curves do show shifts of several volts. Therefore, we believe that the slight buildup of positive charge at the Si-SiO<sub>2</sub> interface during our X-ray experiment should not significantly alter the photo I-V characteristics.



### 6.2.2 Generation Current in Oxide Bulk

When a  $\text{SiO}_2$  film is exposed to X-ray irradiation, electron-hole pairs are generated, and an additional photocurrent can be collected. The magnitude of this current,  $J_{\text{ox}}$ , depends on the electron-hole pair generation rate,  $G$ , carrier drift velocity,  $v_d$  and a time constant,  $\tau$ , and can be written (for one type of carriers) as

$$J_{\text{ox}} = q \cdot G \cdot \tau \cdot v_d \quad (6.2)$$

Since in  $\text{SiO}_2$  the electrons have a mobility several orders of magnitude higher than the holes (Hughes 1973), only electron current needs to be considered here. The time constant used in the above equation is either the carrier life time,  $\tau_\ell$ , or the electron transit time,  $\tau_t$ , depending on the relative magnitude of the two constants. For moderate or higher oxide fields ( $E_{\text{ox}} \geq 2 \times 10^5$  V/cm), the transit time  $\tau_t$  of an electron traversing through the  $\text{SiO}_2$  layer is of the order of a picosecond, and is much smaller than the electron lifetime  $\tau_\ell$  (Hughes 1973). In this case, the bulk generation current  $J_{\text{ox}}$  can be expressed as :

$$J_{\text{ox}} = q \cdot G \cdot \tau \cdot v_d = q \cdot G \cdot \tau_t \cdot v_d = q \cdot G \cdot d_{\text{ox}} \quad (6.2.1)$$

where  $d_{\text{ox}}$  is the oxide thickness. For very low field such that the transit time is longer than the lifetime,  $\tau = \tau_\ell$  in equation (6.2),

and

$$J_{\text{ox}} = q \cdot G \cdot \tau_\ell \cdot \mu \cdot E_{\text{ox}} \quad (6.2.2)$$

Since the recombination and trapping processes in  $\text{SiO}_2$  are likely to be complicated, a simple lifetime may not exist, but it is still a

useful concept with which to describe the bulk generation current under very low oxide field where the transit time becomes longer than the apparent lifetime.

From the energy deposited in the  $\text{SiO}_2$  and the pair creation energy, it is possible to estimate the carrier generation rate,  $G$ , and then the X-ray generated saturation current in the oxide bulk. The exact energy loss mechanisms of X-ray induced hot electrons in  $\text{SiO}_2$  are still not entirely clear. Ausman and McLean (1975) have proposed that the energy loss occurs primarily through plasma production and the subsequent decay of the plasmon into an electron-hole pair in  $\text{SiO}_2$  has been determined to be approximately 18 eV. The generation rate,  $G$ , is itself a function of the oxide field, most likely due to the geminate recombination process (Curtis et al. 1974, Hughes 1978, Farmer and Lee 1975), which will be described in the next section.

### 6.2.3 Geminate Recombination

The geminate recombination model (Curtis et al. 1974, Hughes 1978, Farmer and Lee 1975, Onsager 1938) of Onsager has been used to describe the quantitative field dependence of photoyield in the  $\text{SiO}_2$  film. The equations for calculating the photoyield as a function of field have been developed (Pai and Enck 1975, Mott 1977). The essential physics involved can be summarized as follows : when an electron-hole pair is created by ionizing irradiation, there exists a strong Coulomb attraction force between them until they get sufficiently far apart. This

attractive force is stronger especially in media with low dielectric constants. The geminate recombination becomes important when the photoexcited electrons and holes do not escape their mutual Coulomb attraction. For instance, in  $\text{SiO}_2$ , with a dielectric constant of 3.9, an electron and hole pair must be  $146 \text{ \AA}$  apart before the thermal energy at  $25^\circ\text{C}$  allows a reasonable chance for particles to overcome the Coulombic attraction and diffuse apart (Pai and Enck 1975, Mott 1977, Knights and Davis 1974).

The yield for two diffusing and oppositely charged particles under field is equal to (Pai and Enck 1975)

$$Y = \exp(-r_c/r_o) \left[ 1 + (e/KT) \frac{1}{2!} r_c E_{ox} + \dots \right] \quad (6.3)$$

where  $r_c = \frac{e^2}{4\pi\epsilon_1 KT} = 146 \text{ \AA}$  ( $T = 298\text{K}$  and  $\epsilon_1 = 3.9$ ) is the effective range of the Coulomb attraction between the pair, and  $r_o$  is another important parameter which represents the separation distance of the photo-excited electron moving away from hole before it thermalizes to an equilibrium situation. Following the argument of Knights and Davis (1974),  $r_o$  can be estimated numerically as follows. During the high energy photon ( $h\nu$ ) radiation, an electron may be excited to an energy,  $\Delta E = h\nu - E_g$  ( $E_g$  is the bandgap of the material) above the bottom of the conduction band. If the electron loses one phonon quantum  $h\nu_p$  per unit time of  $1/\nu_p$ , and the excess kinetic energy to be dissipated is now taken to be the excess over local potential (Coulomb) rather than the excess over the bandgap :

$$\text{K.E.} = (h\nu - E_g) + \frac{e^2}{4\pi\epsilon_i r}$$

The time required to dissipate this energy is then

$$t = \frac{(h\nu - E_g) + \frac{e^2}{4\pi\epsilon_i r}}{h\nu_p^2}$$

If the motion during this process is diffusive, then the separation distance  $r_0$  at the end of a thermalization time  $t$  will be given by

$r_0 = \sqrt{Dt}$ , where  $D$  is the diffusion coefficient of electron in  $\text{SiO}_2$ .

Therefore,

$$r_0 = \left\{ \frac{\left[ (h\nu - E_g) + \frac{e^2}{4\pi\epsilon_i r} \right] \cdot D}{h\nu_p^2} \right\}^{1/2} \quad (6.4)$$

In the above derivation for  $r_0$ , it is assumed that the only process involved is diffusion. The validity of this assumption is debatable. Hughes (1978) suggests that even when the carriers are hot, one cannot turn off the Coulomb attraction completely, so they must not be diffusing in the random thermalized fashion during the short time in which they are losing their excess kinetic energy. Therefore, a distribution of values for this adjustable parameter  $r_0$  is generally required to fit the experimental data with the geminate recombination theory. Even if there is no exact and accurate quantitative theory other than equation (6.4) with which to predict the  $r_0$  value for an insulator, this parameter is

still a very interesting physical quantity in which a significant amount of information about hot carrier relaxation.

As will be shown in section 6.4.3, the geminate recombination model can be used to describe the field-dependence of the bulk generation rate in our samples with excellent agreement between the theory and the experiment. Furthermore, when the data is extrapolated to the low field region, the  $\mu\tau_\ell$  product can be estimated.

#### 6.2.4 Total Collected Current

As discussed in sections 6.2.1 and 6.2.3, the total electron current induced by X-ray radiation collected in the external circuit consists of two components : (1) photoinjection from the contact, and (2) generation current in the bulk of  $\text{SiO}_2$ . Thus, the total electron current density,  $J$  can be expressed as (combining equations (6.1) and (6.2)) :

$$\begin{aligned} J &= J_{\text{inj}} + J_{\text{ox}} \\ &= J_0 e^{-x_0/\ell} + J_{\text{ox}} \end{aligned} \quad (6.5)$$

In the moderate and high field regime,  $\tau_\ell \gg \tau_t$ ,  $J_{\text{ox}} = q \cdot G \cdot d_{\text{ox}}$  (see equation (6.2.1)), and

$$J = J_0 e^{-x_0/\ell} + q \cdot G \cdot d_{\text{ox}} \quad (6.5.1)$$

As pointed out in section 6.2.1, for a given oxide field,  $J_{\text{inj}}$  is independent of oxide thickness. On the other hand, the bulk generation current,  $J_{\text{ox}}$ , is a linear function of the oxide thickness. Therefore, equation (6.5.1) predicts that a plot of  $J$  vs  $d_{\text{ox}}$  under

a constant field should be a straight line, whose slope is proportional to the bulk generation rate,  $G$ , and whose intercept at  $d_{ox} = 0$  is the injection current under that field. Using the oxide field as a variable parameter, a family of straight lines with different slopes and intercepts can be displayed on the  $J$  vs  $d_{ox}$  plot, from which the field-dependent  $J_{inj}$  and  $G$  can be extracted.

In the low field regime where  $\tau_l \ll \tau_t$ ,  $J_{ox} = q \cdot G \cdot \tau_l \cdot \mu \cdot E_{ox}$  (see equation (6.2.2)). Using the experimentally determined  $J_{ox}$  and  $G$  in this regime, the product  $\mu \tau_l$  can be determined.

### 6.3 EXPERIMENTAL DETAILS

#### 6.3.1 Sample Preparation

The devices used in this study are MOS capacitors fabricated on p-type 1  $\Omega$ -cm (100) silicon wafers. Dry oxides are thermally grown at 1000°C in  $O_2$  for various lengths of time to obtain five different oxide thicknesses (455 Å, 780 Å, 1200 Å, 2200 Å, and 3600 Å), which are then annealed in dry  $N_2$  gas at the growth temperature for 30 minutes. Aluminum is evaporated to serve as the gate as well as the back contact. No post-metallization annealing is done on these devices.

#### 6.3.2 Experimental Setup

As shown in Fig. 6.1, a dc voltage is directly applied to the gate of an MOS device, and a Keithley 602 current meter is used to

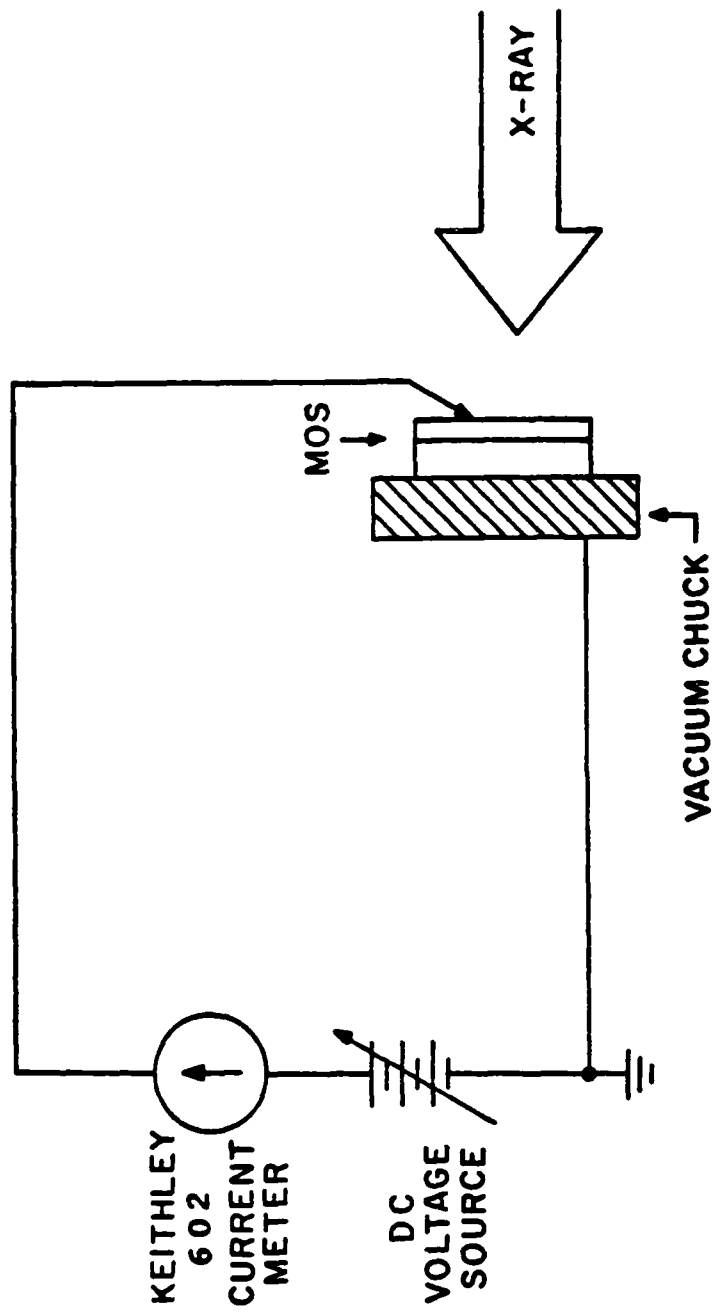


Fig. 6.1 Experimental setup for X-ray induced photocurrent measurement.

measure the current flowing through the device. An X-ray beam (35 kV, 35 mA) with a Cu-target is used as the radiation source to generate the photocurrent. Measurements of the photo I-V curves are completed within 3-5 minutes for each device to minimize the radiation damage. During the measurements, care has been taken to ensure that the current being measured is indeed the device photocurrent, and is not due to other spurious effect. After the I-V data are taken, C-V measurements are performed to examine the buildup of the positive charge and surface states in the device the buildup has been found to be insignificant in these experiments.

#### 6.4 RESULTS AND DISCUSSIONS

##### 6.4.1 Contact Photoinjection

Fig. 6.2 shows the experimental photocurrent as a function of oxide field (negative polarity on the gate) for MOS capacitors with different oxide thicknesses ranging from 455 Å to 3600 Å. The curves for positive gate voltages are qualitatively similar to these, and therefore are not shown here. It is obvious from these data that for a given device, the photocurrent increases with oxide field, and at a given field, it increases with the oxide thickness. These results are qualitatively consistent with the theory presented earlier.

To extract from the total current the contact injection component, we plot the total current as a function of oxide thickness



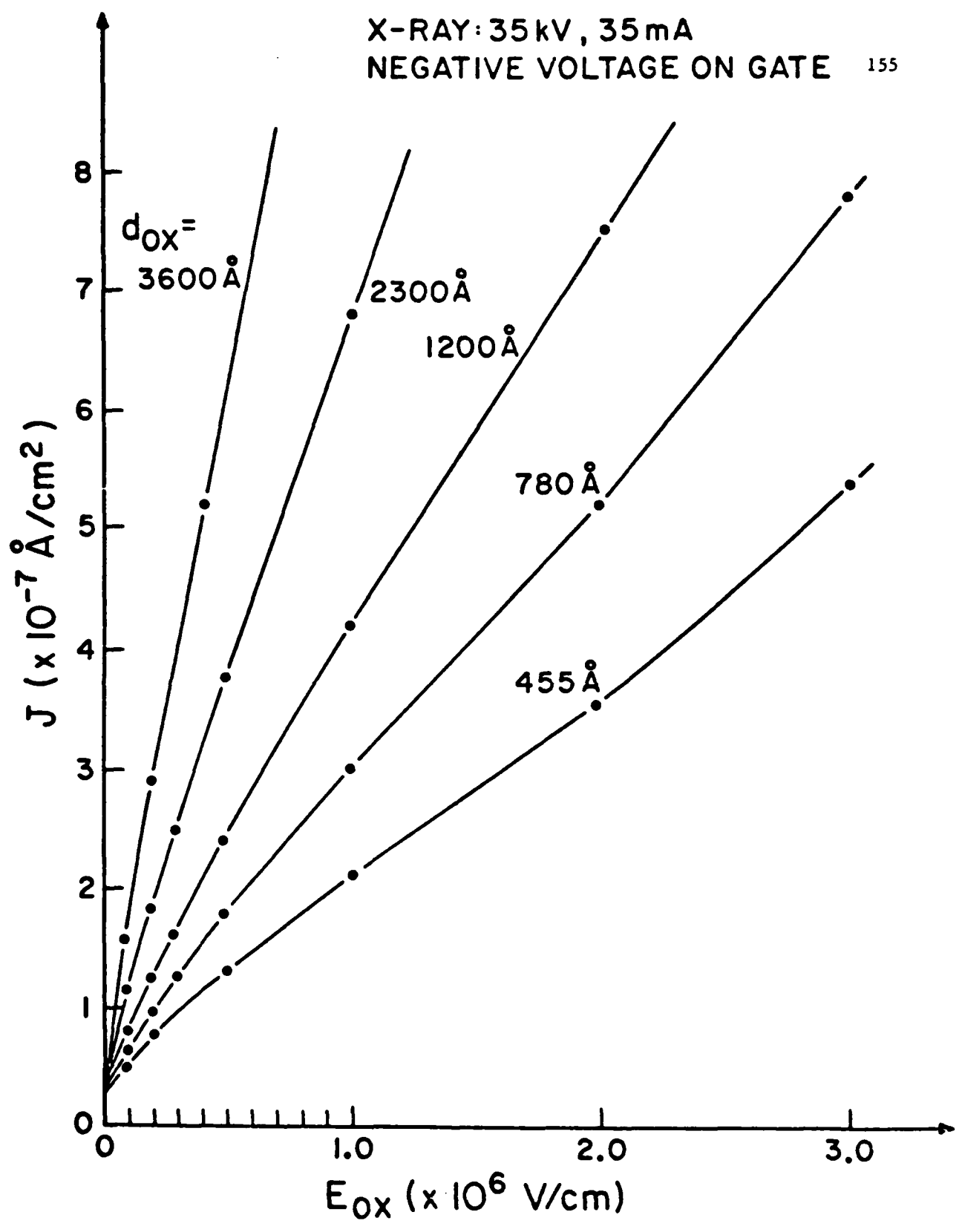


Fig. 6.2 Experimental X-ray induced photocurrent as a function of negative oxide field with oxide thickness as a parameter.

under a given oxide field, as shown in Figs. 6.3 and 6.4 for negative and positive gate voltages, respectively, with oxide field as a parameter. A salient feature in these figures is that a straight line can be used to describe very accurately the  $J$  vs  $d_{\text{ox}}$  characteristics over a wide range of oxide field ( $1 \times 10^5$  -  $3 \times 10^6$  V/cm), just as equation (6.5.1) would predict. These results further enhance our confidence in our measurements as well as the theory. In accordance with equation (6.5.1), extrapolations of the family of straight lines to  $d_{\text{ox}} = 0$  should give rise to the contact photoinjection currents,  $J_{\text{inj}}$ . This is shown in Fig. 6.5 plotted as a function of oxide field for both polarities. Solid circles (corresponding to negative polarity) are for injection from the Al-contact, while open circles are for injection from the Si-contact. The shapes of these curves are in good agreement with the photo I-V curves published by DiMaria et al. (1977) for  $\sim 5$ eV UV photons. Using Powell and Berglund's scattering potential model (equation(6.1)) we have also achieved a reasonable fit between the experimental data and the theory. These agreements strongly suggest that, although photons of energies far above the barrier height are used in our experiment, the hot electrons reaching the injection interface have been considerably de-energized, and their behavior can be essentially described by the same theory developed for lower energy excitations.

Figs. 6.3 and 6.4 also reveal the relative contribution of the contact injection current with respect to the total current. For an oxide thickness of  $500 \text{ \AA}$ , approximately 50% of the collected photo-

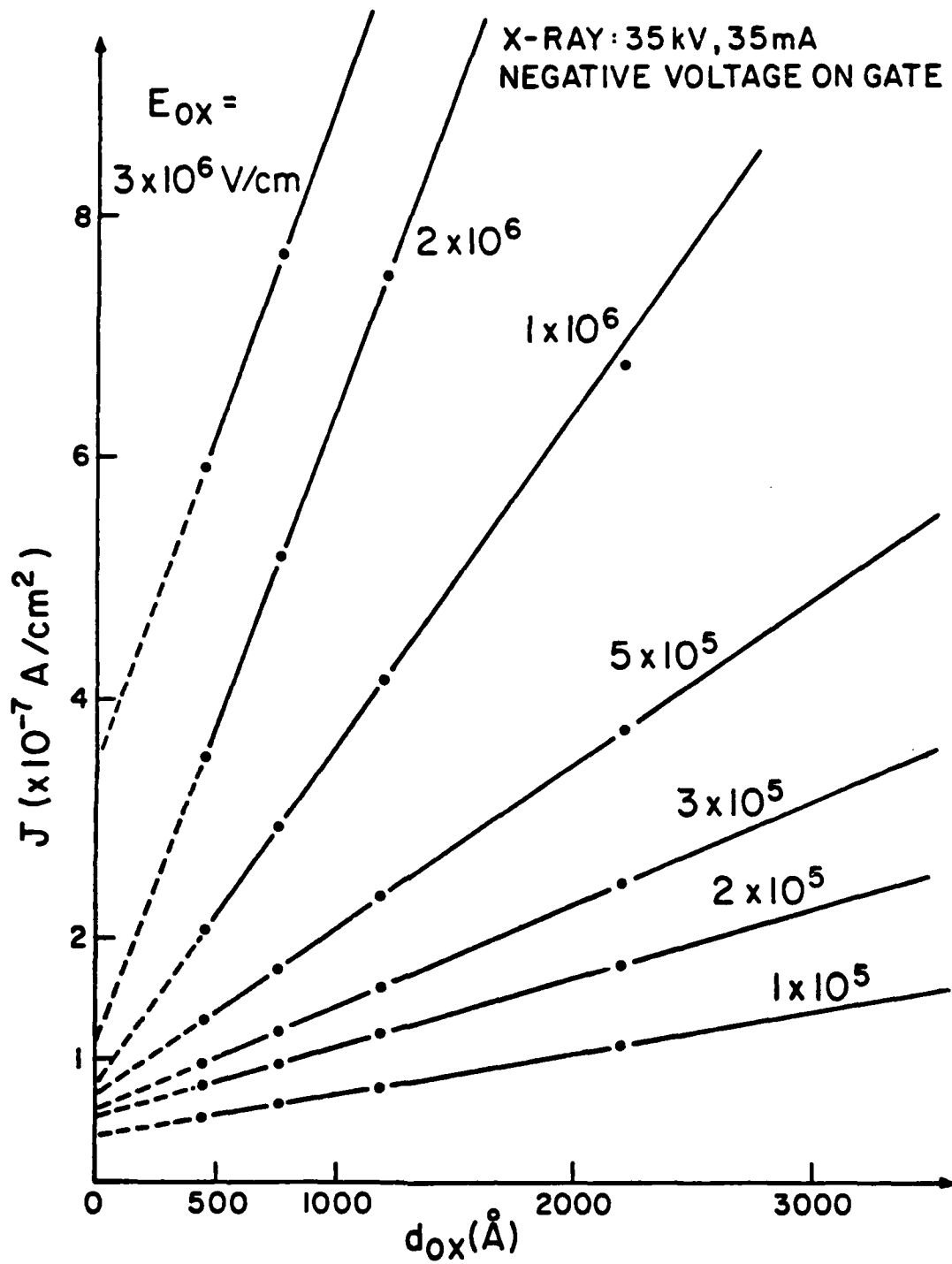


Fig. 6.3 Experimental X-ray induced photocurrent as a function of oxide thickness using negative oxide field as a parameter.

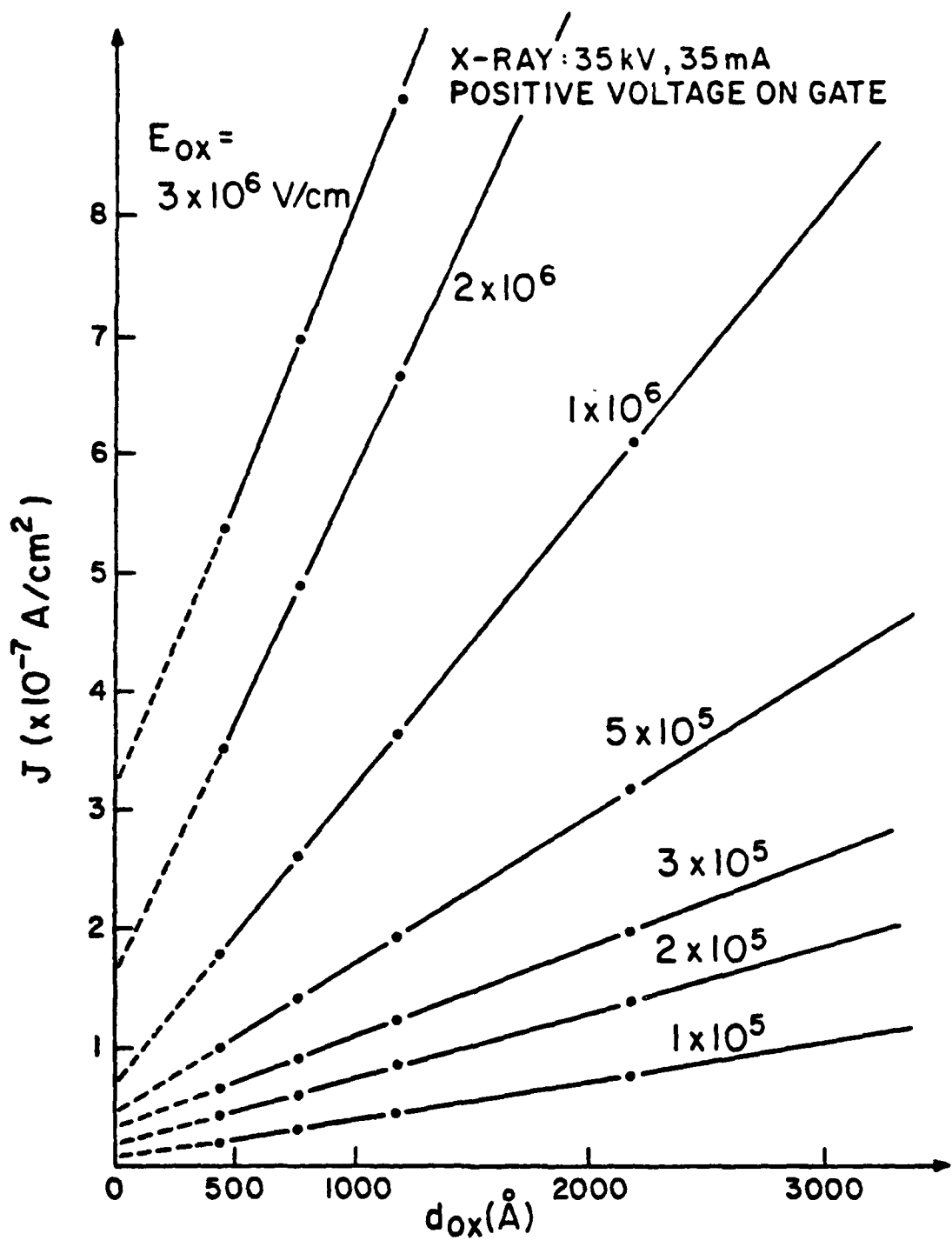


Fig. 6.4 Experimental X-ray induced photocurrent as a function of oxide thickness using positive oxide field as a parameter.

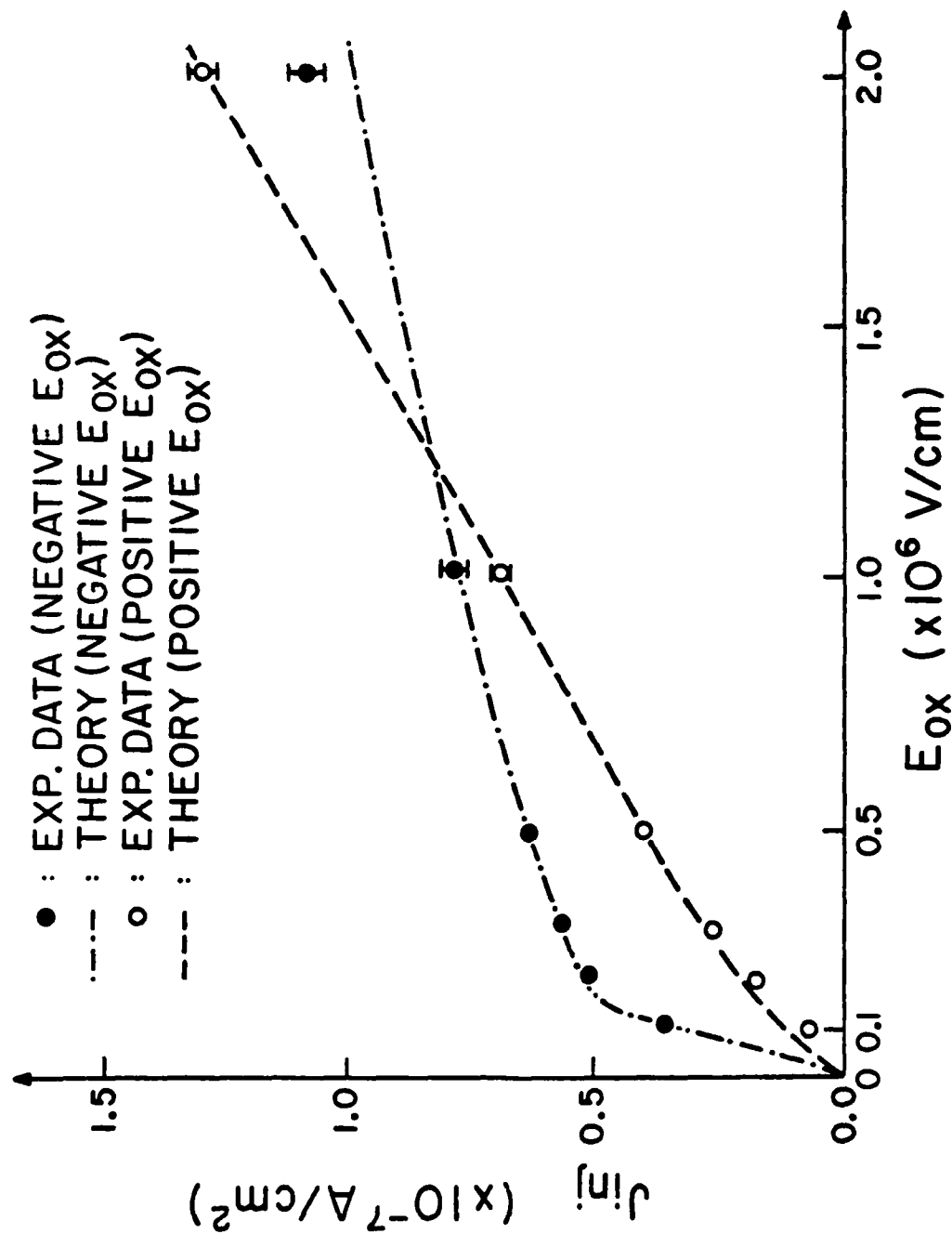


Fig. 6.5 Photoinjected currents as a function of oxide field.  
 Solid circles : experimental data under negative bias obtained from Fig. 6.3  
 Dash-dot curve: theoretical fit using equation (6.1) with  $\Lambda = 1.2 \times 10^{-7}$  and  $p = 2$   
 Open circles: experimental data under positive bias obtained from Fig. 6.4  
 Dashed curve: theoretical fit using equation (6.1) with  $\Lambda = 1.54 \times 10^{-7}$  and  $p = 3$

current is due to contact injection in the whole range of oxide fields studied here, and for thinner oxides, the contact injection component dominates. This points out the importance of not neglecting the contact photoinjection in problems related to the transport of electrons in MOS structures under ionizing radiation; especially for cases where the oxide thickness is comparable to or thinner than 500 Å.

#### 6.4.2 Generation in SiO<sub>2</sub>

Considering once again Figs. 6.3 and 6.4, if one subtracts the injection current from the total current, the generation current,  $J_{ox}$ , in the SiO<sub>2</sub> layer can be obtained. This current is a linear function of the oxide thickness in the field range being considered, as predicted by equation (6.2.1). According to equation (6.2.1), the slope of each straight line is proportional to the generation rate,  $G$ , at the specified field. Therefore, the generation rate as a function of oxide field is also implicit in these data, which will be discussed in the next section.

In fig. 6.6 a family of bulk generation currents as a function of oxide field (both polarities) is plotted for various oxide thickness. Two important features may be noted : (1) The curves for both polarities are essentially the same, as they should be given the symmetry of the problem. The slight difference between the two could be partly due to the difference in the trapping properties between the Al-SiO<sub>2</sub> interface, and partly due to the uncertainty in the assigned work function difference, and (2)  $J_{ox}$  is approximately linearly proportional

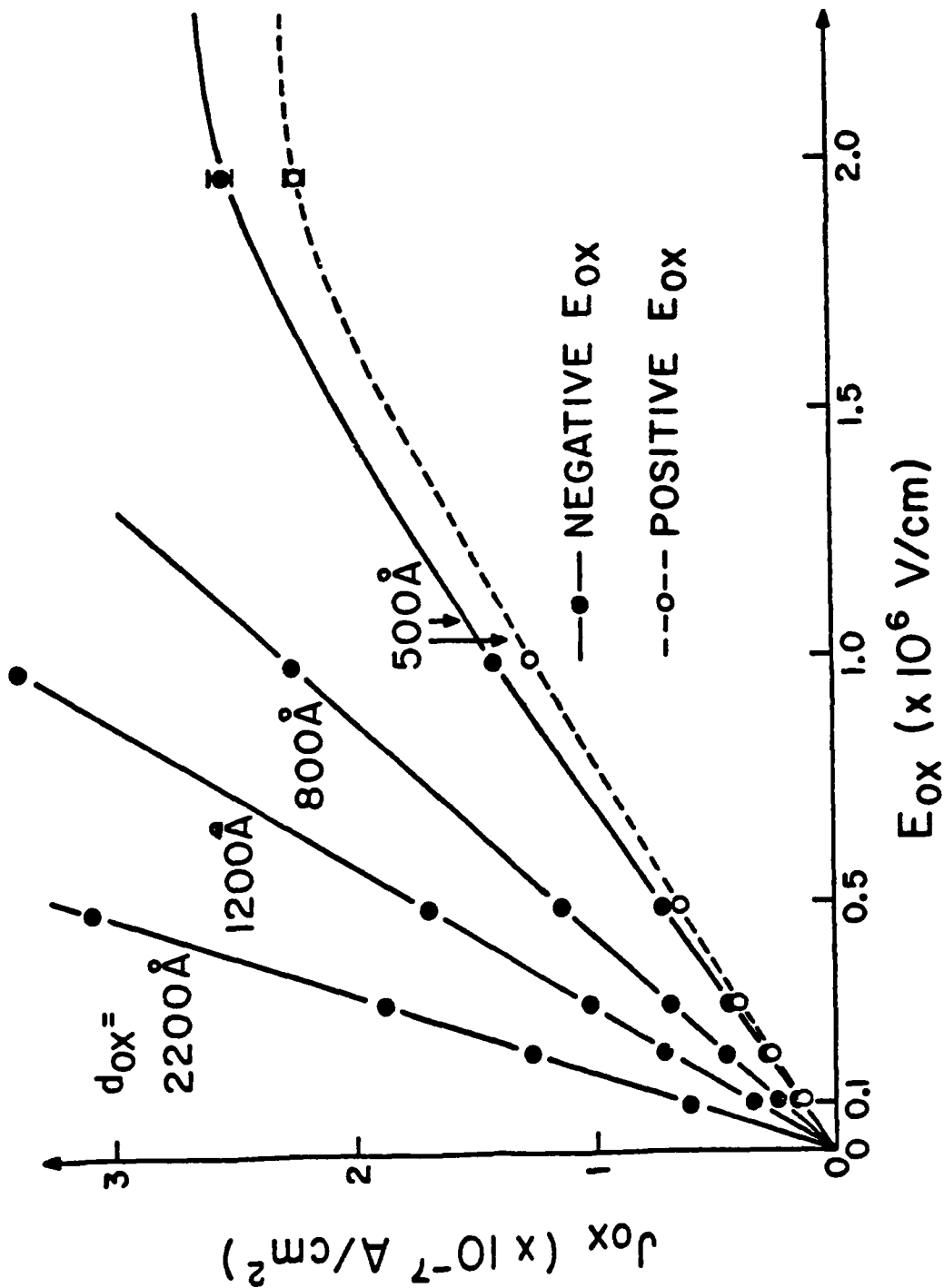


Fig. 6.6 Experimental photogeneration current in  $\text{SiO}_2$  as a function of oxide field. Currents under negative bias are shown for four different oxide thicknesses (solid curves). Current under positive bias is shown for the 500 Å oxide (dashed curve).

to  $E_{ox}$  in the range  $10^5 - 2 \times 10^6$  V/cm.

In this field range, an empirical formula which can be used to describe the oxide field and thickness dependences of  $J_{ox}$  is given as

$$J_{ox} = 2.8 \times 10^{-8} E_{ox}^3 d_{ox} \quad (6.6)$$

A more detailed discussion of  $G$  is now in order.

#### 6.4.3 Geminate Recombination

As discussed in section 6.2.3, a plausible model with which to describe the field-dependency of photogeneration rate in  $SiO_2$  is Onsager's theory of geminate recombination. As shown in equation (6.3), the yield is a function of field, and is proportional to the probability of the excited electron-hole pair escaping their coulombic attraction. This escape probability can be characterized by two range parameters,  $r_c$  and  $r_o$ , where  $r_c$  is the effective range of the coulombic attraction between the pair, and  $r_o$  represents the separation distance of the photo-excited electron moving away from the hole before it thermalizes to reach equilibrium.

In Fig. 6.7, solid and open circles show the experimentally determined generation rates as a function of negative and positive oxide fields in our MOS samples. These results have been obtained using equation (6.2.1) and Fig. 6.2 and 6.3. These curves indicate that, apart from small displacement, probably due to the experimental uncertainty stated earlier, both polarities give rise to essentially the same generation rate in  $SiO_2$ .



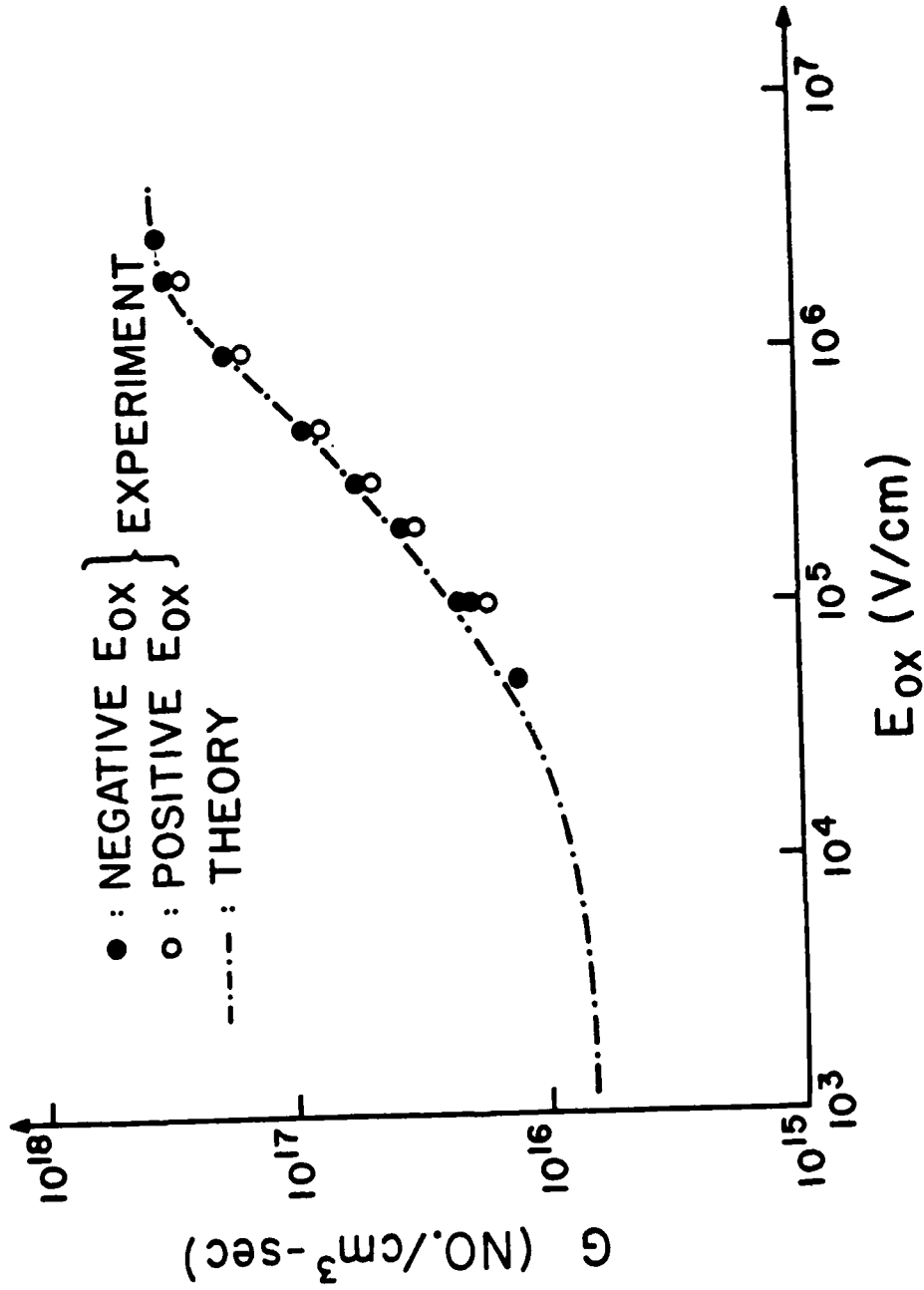


Fig. 6.7 Net pair generation rate in  $SiO_2$  as a function of oxide field.  
 Solid circles : experimental data under negative bias obtained from Fig. 6.6.  
 Open circles : experimental data under positive bias obtained from Fig. 6.6.  
 Dash-dot curve : theoretical fit using Onsager's geminate recombination with  $r_0 = 35 \text{ \AA}$ .

The theoretical generation rate based on Onsager's geminate recombination theory is also displayed in Fig. 6.7 for comparison. Here the generation rate is taken to be  $G = K Y$ , where  $K$  is a constant depending on the radiation flux, and equation (6.3) is used for the yield calculation with  $r_c = 142.5 \text{ \AA}$  ( $T = 300\text{K}$ ) and  $r_o = 35 \text{ \AA}$ . Notice that a single value, instead of a distribution, of  $r_o$  is selected for this calculation, and excellent fit has been achieved. This  $r_o$  value is close to the mean value  $40 \text{ \AA}$  of the Gaussian distribution selected by Hughes (1978) in his work. For field higher than  $2 \times 10^6 \text{ V/cm}$ , the curve begins to saturate, suggesting that the incident radiation is limiting the generation rate in this region.

Fig. 6.8 shows a comparison of the results reported by several authors (Curtis et al. 1974, Hughes 1978 and Powell 1975). Since we are only interested in their qualitative features, the data are normalized at  $2 \times 10^6 \text{ V/cm}$ , where the relative generation rate is taken to be 0.8 for all results.

It can be seen that Curtis' and Powell's results are in excellent agreement with ours in the field range up to  $2 \times 10^6 \text{ V/cm}$ , despite the fact that different radiation sources (X-ray, electron beam, and UV photons of  $10.2\text{eV}$ ) were used for the experiments. It should be noted that in Curtis' and Powell's experiments the energies of the radiation and the bias were such that injection from the contacts can be neglected, and in our experiment the contact injection component was subtracted out experimentally. Hughes' data, however,

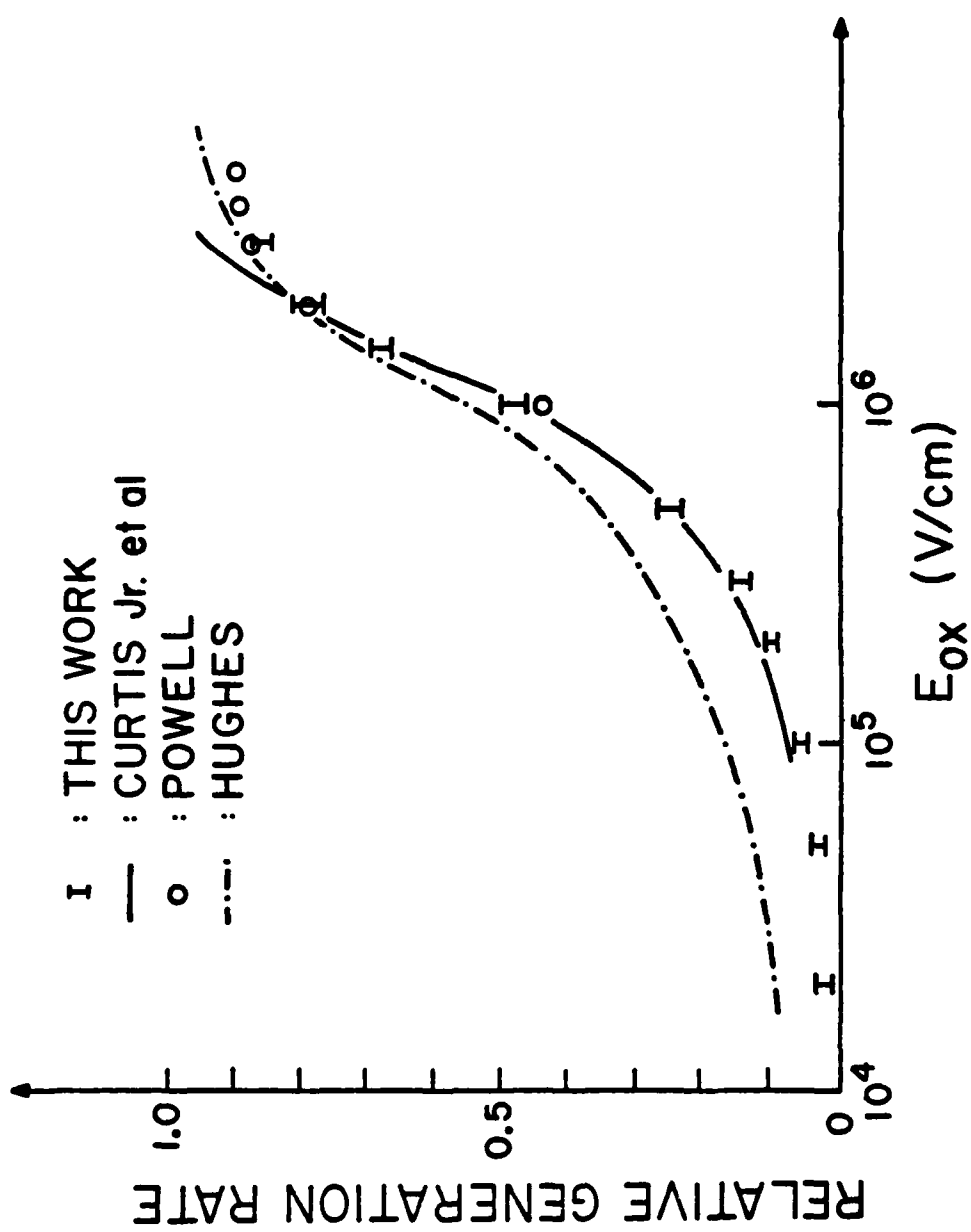


Fig. 6.8 Relative generation rate as a function of oxide field. Results from several different authors are compared. Data are normalized at a field of  $2 \times 10^6$  V/cm where generation rate is taken to be 0.8.

differs somewhat from ours, but the shapes of the curves are qualitatively similar.

From equation (6.3), it is expected that in the very low field region, where  $e r_c E_{ox} / 2KT \ll 1$ , the yield is independent of field, and can be expressed as :

$$Y = e^{-r_c/r_o} \quad (6.3.1)$$

$$\text{which implies } G = K e^{-r_c/r_o} \quad (6.7)$$

On the other hand, the oxide current in this low field region is, from equation (6.2.2)

$$J_{ox} = q \cdot G \cdot \tau_{\ell} \cdot \mu \cdot E_{ox} = 2.8 \times 10^{-8} d_{ox} E_{ox}$$

From the above equation and equation (6.7.1) and Fig. 6.7, K may be estimated, and the  $\mu \tau_{\ell}$  products in our samples can be calculated.

$$\text{Numerically, we found } \mu \tau_{\ell} = 2.74 \times 10^{-5} d_{ox} \text{ (cm}^2/\text{V)} \quad (6.8)$$

This suggests that  $\mu \tau_{\ell}$  is linearly proportional to the oxide thickness, a result in reasonable agreement with many others (Curtis et al. 1974, Hughes 1978, Snow et al. 1967, Everhart and Hoff 1971, and Goodman 1966). This linear dependence may be a consequence of the fact that coulombic traps are concentrated near the Si-SiO<sub>2</sub> interface (DiMaria et al. 1977, Stivers and Sah 1980), and therefore the probability of trapping averaged over the volume of the oxide increases with thinner oxide. For an oxide of 1000 Å thickness,  $\mu \tau_{\ell} = 2.74 \times 10^{-10} \text{ cm}^2/\text{V}$ . If we take  $\mu = 20 \text{ cm}^2/\text{V-sec}$  (Hughes 1975), the carrier lifetime is

calculated to be approximately  $1 \times 10^{-11}$  sec for the 1000 Å sample.

## 6.5 CONCLUSIONS

From a systematic experiment, we have found that, under X-ray irradiation, the photoinjected current from the contact can be a significant part of the total photocurrent in an MOS capacitor. For a 500 Å  $\text{SiO}_2$ , the contact photoinjection is approximately equal to the bulk generation and starts to dominate for oxides thinner than 300 Å. These results are of particular importance to VLSI technologies in which the understanding of process-induced radiation effects is essential for the further development of advanced lithography and dry etching processes, and to the development of radiation-hard MOS devices in which the device operation in an ionizing radiation environment must be understood.

Onsager's theory of geminate recombination has been shown to be able to satisfactorily explain the field-dependent generation rate in  $\text{SiO}_2$  over the field range of  $1 \times 10^5 - 2 \times 10^6$  V/cm. In the lower field region where the electron transit time is longer than its lifetime, the mobility-lifetime product has been found to be linearly proportional to the oxide thickness, a result not inconsistent with the fact that coulombic traps tend to concentrate near the  $\text{SiO}_2$ -Si interface. For a 1000 Å  $\text{SiO}_2$ , this product has been estimated to be approximately  $3 \times 10^{-10}$   $\text{cm}^2/\text{V}$ .

These findings are useful for the understanding of radiation-induced charge buildup in MOS structures. In addition, these results are being applied in our laboratory to model the kinetics of RF plasma

annealing, in which the X-ray induced carrier transport and recombination processes play an essential role (see Chapters IV and V).

## CHAPTER VII

### CONCLUSION

The RF plasma annealing process is a very interesting subject to study, not only because of its potential importance in the VLSI technology arena, but also because of the intriguing physics involved. Given an MOS wafer in a low pressure RF plasma environment, one would normally expect to find the wafer damaged by the plasma radiation, as one typically observes in an RIE (reactive ion etching) experiment. However, by properly selecting the relevant RF plasma parameters one not only can avoid the radiation damage effect, but also can even anneal out the damage introduced prior to the RF plasma treatment. Why does the RF plasma do such drastically different things under different conditions? What makes the RF plasma annealing work? Can one identify the most important parameters that are essential to the annealing process? If so, what are their roles in the fundamental annealing mechanisms? To sum it up, what are the annealing mechanisms? The objective of this thesis research was thus to try to answer these questions to a sufficient degree so as to lay a solid foundation for future researchers.

To start with, we needed an RF plasma annealing system in our laboratory. Based on Professor Ma's earlier experience with the first generation annealing apparatus, we designed and constructed a parallel-plate system, which was then subsequently used to anneal a variety of MOS device samples. In the process of the design, construction, and operation of the system, We learned a few important

things about the RF plasma generation, impedance matching, and RF plasma itself, and this experience has proved beneficial for the overall research project.

Having built the RF plasma annealing system, we then started to do the annealing experiments. We have found that not only the radiation-induced oxide charge and surface states can be readily removed, as previously reported by Ma and Ma in their earlier work, but also the radiation-induced neutral traps have disappeared after the annealing treatment. The results on neutral traps provided strong support for the idea that the dominant annealing process cannot be just thermal effect, because it would require a temperature over 550°C for thermal annealing to be as effective, a temperature high enough to destroy the device.

To understand the RF plasma annealing mechanisms, which was our primary objective, we felt it necessary to first study the RF plasma. Although the RF plasma is a complicated system containing various energetic electrons, ions, neutrals, and photons, we soon realized that the only energetic species that can penetrate through the gate electrode and interact with the SiO<sub>2</sub> layer is the deep UV and soft X-ray photons. This finding considerably simplified our task in modeling the annealing process. In addition, we were able to calculate the photon flux absorbed by the SiO<sub>2</sub> layer, the RF voltage across the MOS system, and the induced wafer temperature during the annealing. These parameters later served as a guide for the design of our simulation experiments.



The experimental simulation was the key to our modeling effort, and was central to my entire thesis. Without it, we would not have been able to separate the contribution from the photon radiation, the RF field, and the wafer temperature. It not only allowed us to verify that the annealing process depends on the cooperative interactions of these three parameters, but also provided us the valuable information on the activation energies, and revealed the frequency and voltage dependences of the annealing rate, all of which are consistent with the REDR model, a model which we have proposed as the most important microscopic mechanism that leads to the annealing process.

The REDR model was introduced prior to this work to explain the enhanced annealing rate in GaAs, InP, and many other wide bandgap semiconductors. The essence of this model is that the indirect recombination of excess electrons and holes through a defect site could result in a reduction of the activation energy involved in the defect annealing reaction, and thus an increase in the annealing rate at a given temperature. This recombination-enhancement effect was indeed experimentally observed by the Bell Lab group in which the excess carriers were injected either by forward-biasing a pn junction or by external excitation with an electron-beam. In the case of RF plasma annealing, the excess carriers in  $\text{SiO}_2$  are generated by the photon radiation, and this system is therefore a natural candidate for the REDR process to take place. Our experimental data indeed provided strong support for this model.

In order to model the voltage and frequency dependences of the RF annealing rate, we found that a detailed understanding of the X-ray induced photocurrent in an MOS structure was necessary, in particular the question whether the contact photoinjection current plays a significant role in the overall photocurrent and its voltage dependence must be answered. In view of the fact that such information is not available in the literature, we decided to find out for our own. Based on the principle that the photoinjection current is independent of the oxide thickness, while the bulk generation current is linearly proportional to the thickness, we designed and conducted a systematic experiment to separate out these two components. The results of this experiment, as it turned out, not only provided us the necessary information originally looked for, but also revealed several interesting fundamental phenomena. For example, we found that for an MOS structure with a  $\text{SiO}_2$  thickness of 500 Å or less, which is the typical thickness range used for the modern integrated circuits, the X-ray induced contact photoinjection current makes up more than 50% of the total current, and its voltage dependence follows that predicted by the internal photoemission theory developed earlier for UV photons. We also found that the voltage dependence of the X-ray induced bulk generation current in  $\text{SiO}_2$  was in excellent agreement with Onsager's theory of geminate recombination. These findings are of particular importance for the studies of ionizing radiation effects in which the carrier generation and transport must be better understood.

We expected the annealing rate to be a function of the RF voltage amplitude and frequency, but the actual experimental results were still somewhat a surprise to us, especially the fact that the enhanced annealing behavior could be observed at a frequency as low as 10 Hz (for  $V_{ac} > 2V$ ) and at a voltage as low as 0.4V (for  $f \geq 10$  KHz). This finding again demonstrated the virtue of our experimental simulation, because we would never have been able to reveal such behavior with a real RF plasma annealing setup. Although we were able to develop a simple theory based on the recombination kinetics to explain the results, we do not feel that we have achieved a complete understanding of this complicated problem. This is one area that deserves further investigation.

The REDR model itself is a fascinating subject which should be on the priority list for future studies. Although the existing theory appears to provide satisfactory explanation of our results, there still remain some fundamental questions. For example, one key element in the REDR model is the indirect recombination of the excess electrons and holes through a defect site, and the recombination energy released through this process is said to lower the defect reaction barrier and to enhance the annealing rate. But why this recombination acts as a constructive force rather than as a destructive force to create more defect centers is not understood. In fact Ballamy and Kimerling (1979) did observe a degradation of the device performance due to prolonged recombination of the excess electrons and holes in GaAsP material. The only basic difference between their experiment and the RF plasma annealing experiment is the absence and the presence of the

RF field. Therefore, the RF field must be playing an additional role besides controlling the transport of the electrons and holes. How does the RF field influence the direction of the defect reactions should be addressed in order to fully understand the RF annealing mechanisms.

One question that has frequently been raised is the effect of the gas species in the plasma on the annealing behavior, in particular the role that the hydrogen plays. Although we can not completely rule out the possibility that the hydrogen species in the RF plasma may contribute somewhat to the annealing process, the results of our experimental simulation strongly suggest that one does not need hydrogen to achieve an effective annealing rate for thermal  $\text{SiO}_2$ . For CVD deposited  $\text{SiO}_2$ , however, we do have some experimental evidence which shows (Appendix C.2) that the incorporation of hydrogen in the RF plasma can further improve the annealing rate. The reason that the effect of hydrogen is more significant in CVD  $\text{SiO}_2$  than in thermal  $\text{SiO}_2$  has been suggested in Appendix C.2. In any case, further study is necessary to determine the extent the chemical reactions involving hydrogen and other gas species contribute to the overall annealing rate in thermal  $\text{SiO}_2$ .

The preliminary results from the X-ray luminescence study (Appendix D) are also worth noting, because this experiment may reveal the annealing mechanism from a different perspective. Due to the equipment limitations, we were not able to detect any signal from an MOS sample, but we did find that the intensity of a luminescence peak, presumably due to certain defect center, from a coverglass slide could be either increased by exposure to

AD-A110 785

YALE UNIV NEW HAVEN CT DEPT OF ENGINEERING AND APPL--ETC F/G 20/12  
RF PLASMA ANNEALING ON MOS STRUCTURES.(U)  
DEC 81 H CHIN

DAA629-79-C-0021

ML

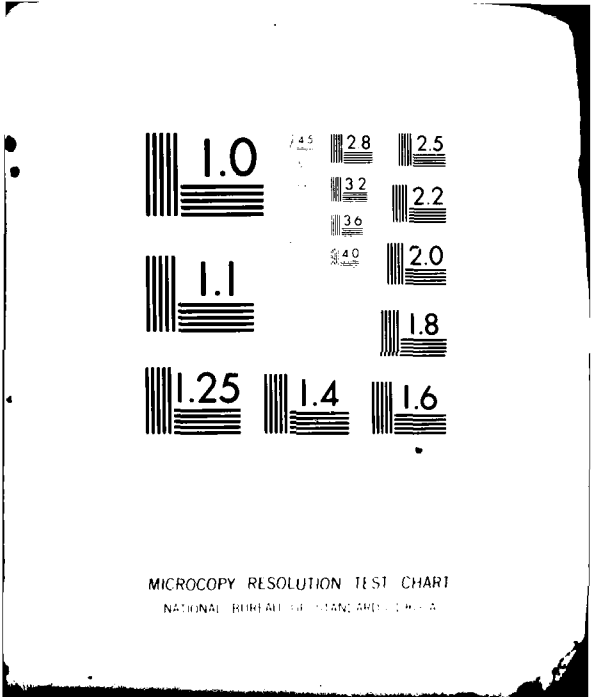
IMPACT COPY

ARO-15835.6-EL

3  
2  
4

■


END  
DATE  
SERIAL  
3-82  
DTIC



MICROCOPY RESOLUTION TEST CHART  
NATIONAL BUREAU OF STANDARDS-1963-A

X-ray, or decreased by RF annealing, and the annealing behavior was very similar to that of thermal SiO<sub>2</sub>. Given a more sensitive photon detector, it is conceivable that the annealing of the defects in thermal SiO<sub>2</sub> could be studied by observing its luminescence spectra, thus would add a new dimension to our understanding of the annealing mechanisms. This is another area worth further investigation.

In addition to the annealing of the radiation effects in MOS structures, we have used the RF plasma annealing technique for a number of other applications. Among them, the radiation hardening of MOS devices (Appendix C.1) has a promising potential to make a major impact on the defense and space electronic industry. What needs to be done is to tailor the annealing parameters so that a 3-5 times more radiation-hard MOS devices can be obtained. Substantial amount of experimental as well as theoretical work is expected to achieve this goal. It may prove that the present system is not adequate to do what is required, and a third generation RF plasma annealing system needs to be designed and constructed. Given the present knowledge and experience as a result of this study, whoever is going to undertake that task will be in a far better position than when I started to make it happen.

In summary, this thesis has made a step towards a better understanding of the RF plasma annealing mechanisms. Many questions remain unresolved, but it is hoped that the present study has laid a solid foundation for those who continue to investigate this subject.

## APPENDIX A

### CONTAMINATION PROBLEMS IN RF PLASMA CHAMBERS

Device contamination in the RF plasma chamber can be easily detected using steady-state C-V measurements : (1) the quasi-static C-V characteristic of the MOS capacitor indicates that the device becomes very leaky at a higher bias voltage; and (2) the high frequency C-V trace shows a rising capacitance in the inversion region. These phenomena can be attributed to contamination caused by surface impurities (Sze 1969, Grove 1967).

In some cases, if the surface impurities reside on the sample surface without penetrating into the bulk  $\text{SiO}_2$ , these problems can be eliminated by performing a second RF plasma annealing without exposing the device to the plasma, by soaking the devices in diluted HF solution (10% HF + 90% DI water) for a very short time, or by agitating the devices in an acetone or methanol solution.

In order to get rid of all the possible kinds of contamination, several factors must be considered :

- (1) The Bell Jar, the inner chamber cylinder, and the sample holder must be constructed from a high purity grade material, preferably fused silica quartz.
- (2) The electrode plates should be made of high purity metal to prevent the sputtering of undesired impurities which could exist in the metal. Metal gaskets should be used instead of ordinary rubber or Viton O-rings (plasma reacts more easily with organic materials).



- (3) Due to the strong back-streaming at pressures below  $10\mu$ , the pump oil vapor can dissolve into active species in the plasma and then be deposited onto the sample surface. As a result, an oil-free pumping system is required. For example, using a Vac-Sorb system for roughing and a cryo-pump for the high-vacuum regime would be appropriate.
- (4) Finally, the sample and the system should be cleaned thoroughly. It has been found that sputtering cleaning of the whole system using oxygen plasma is suitable. The procedure is as follows: 1 torr oxygen pressure is used to generate high pressure plasma and this pressure is maintained for 10 min. Then in the "power on" state of the plasma, the whole system is pumped down to the required pressure ( $\leq 10^{-5}$  torr).

In addition to the above considerations, if higher power ( $\geq 700$  W) RF annealing must be performed, a water cooling system surrounding the main RF cable and its feedthrough (the connection between the atmosphere and the vacuum) is necessary to avoid cable burning caused by heat dissipation and arc discharge across the cable insulator. Such phenomena are mainly due to the low heat conduction inside the vacuum chamber.

APPENDIX B

INDUCTION COIL DESIGN AND MATCHING NETWORK

Fig. B.1 shows the RF plasma annealing system with the RF generator, the matching network, and the effective impedance  $Z_L$  which represents the plasma load. This plasma load impedance  $Z_L$  can be viewed as consisting of a resistance  $R_L$  and a capacitance  $C_L$ . From the maximum power transfer theorem, both the load resistance and capacitance can be expressed as functions of the capacitors,  $C_1$  and  $C_2$ , the inductor  $L$ , and the source resistor  $R_s$ .

At the maximum power transfer condition, we have

$$Z_o = Z_L^*$$

where  $Z_L^*$  is the complex conjugate of  $Z_L$  and  $Z_o$  is defined as the total impedance looking into the dashed line of Fig. B.1.

$$\frac{\frac{1}{j\omega C_1} R_s}{R_s + \frac{1}{j\omega C_1}} + j\omega L + \frac{1}{j\omega C_2} = R_L - \frac{1}{j\omega C_L}$$

$$\frac{R_s - j\omega C_1 R_s^2}{1 + \omega^2 C_1^2 R_s^2} + j\omega L + \frac{1}{j\omega C_2} = R_L + j\frac{1}{\omega C_L}$$

$$\text{Therefore, } R_L = \frac{R_s}{1 + \omega^2 C_1^2 R_s^2} \tag{B.1}$$

$$\frac{1}{\omega C_L} = \omega L - \frac{1}{\omega C_2} - \frac{\omega C_1 R_s^2}{1 + \omega^2 C_1^2 R_s^2} \tag{B.2}$$

$C_1 = 10 - 1000 \text{ pf}$   
 $C_2 = 25 - 500 \text{ pf}$

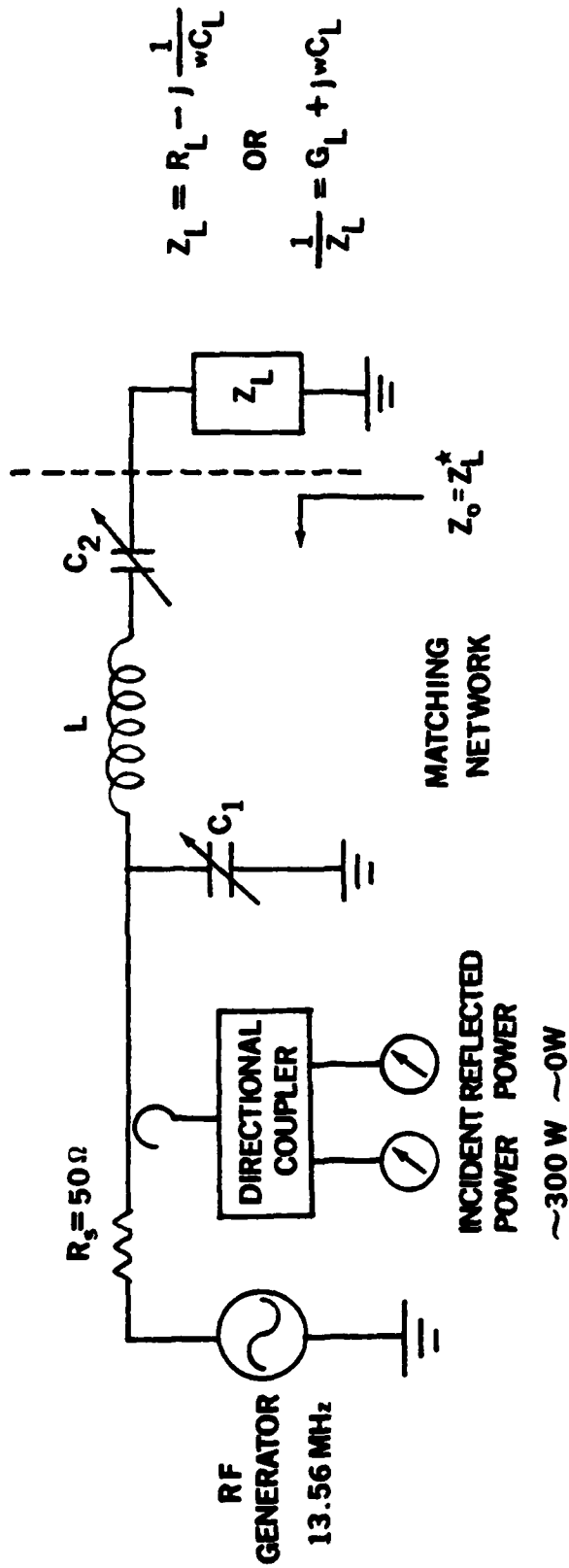


Fig. B.1 Equivalent circuit diagram for an RF system. The RF generator, directional coupler and matching network are included to show the condition for the maximum power transfer.

By varying  $C_1$  and  $C_2$  in the equations (B.1) and (B.2), the tunable range can be determined. As shown in Fig. B.2, with the original  $L$  of  $1 \mu\text{H}$ , the tunable reactance range ( $\frac{1}{\omega C_L} = 0-50\Omega$ ) is suitable only for an ordinary RF sputtering system with small spacing ( $\sim 1$  inch) between two electrodes. For the RF plasma annealing system, the much larger spacing ( $> 7$  inches) between two electrodes will give rise to a much larger reactive component. This load reactance component is not within the tunable range, and therefore a coil with an inductor of  $\sim 5 \mu\text{H}$  is used to meet the requirement. Fig. B.2 also shows this new adjustable range.

The coil design rule which follows, is taken from The Radio Amateur's Handbook (2-11, 1979). The approximate inductance of a single layer air-core coil may be calculated from the simplified formula:

$$L(\mu\text{H}) = \frac{a^2 n^2}{9a + 10b} \quad (\text{B.3})$$

where  $L$  = inductance in microhenrys,  
 $a$  = coil radius in inches,  
 $b$  = coil length in inches,  
 $n$  = number of turns.

The notation is explained in Fig. B.3.

This formula yields a good approximation for coils having a length equal to or greater than  $0.8 a$ .

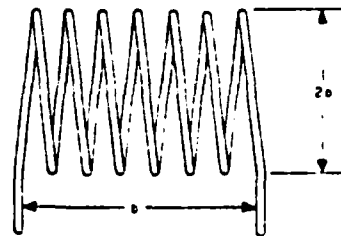


Fig. B.3 Coil dimensions used in the inductance formula. The wire diameter does not enter into the formula.

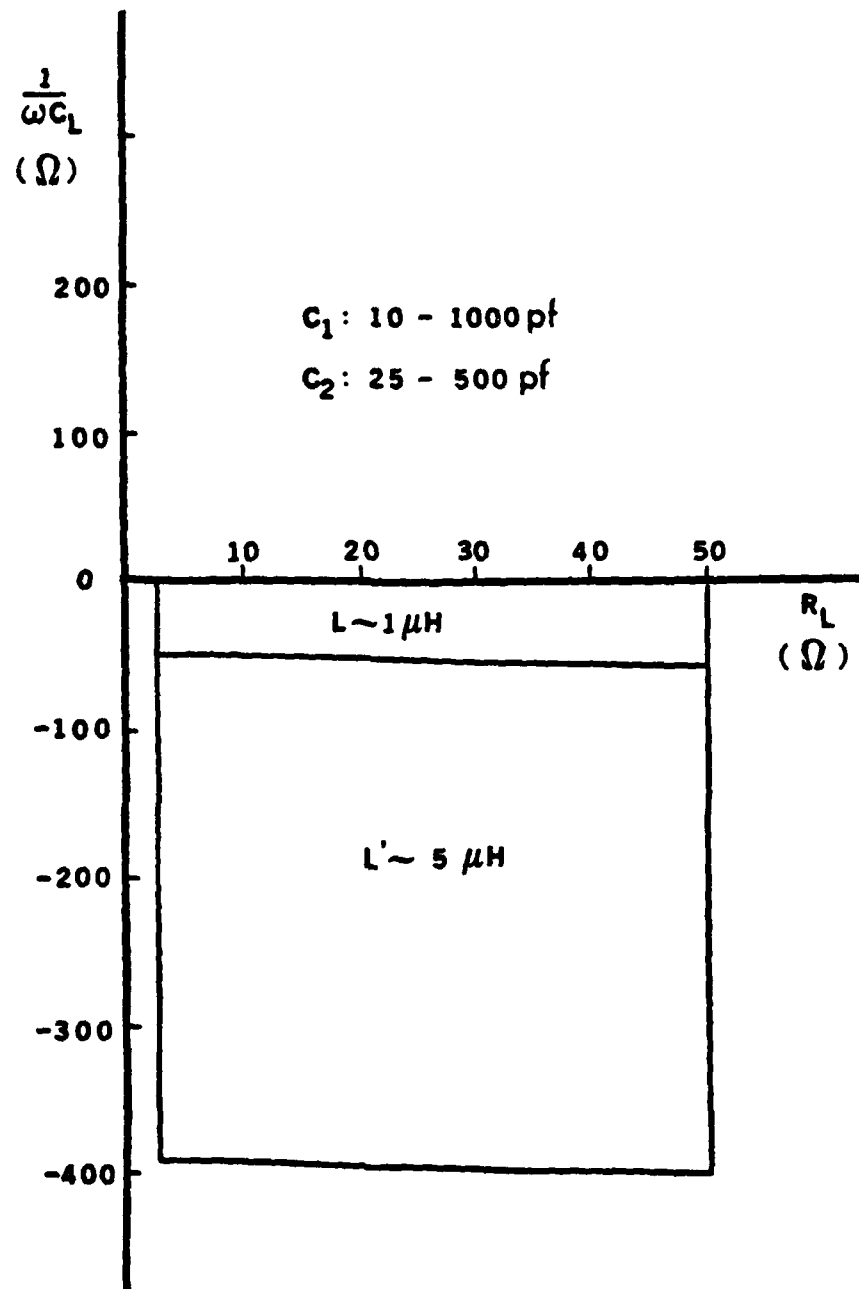


Fig. B.2

Under optimal (maximum power transfer) condition the tunable load impedance range obtained from Eqs. (B.1) and (B.2) by varying  $C_1$  and  $C_2$ . The small area is for  $L = 1 \mu\text{H}$  and the large area is for  $L = 5 \mu\text{H}$ .

With a quarter-inch copper tube an inductance of 5  $\mu\text{H}$  can easily be obtained by winding a coil with 8 turns and adjusting a and b. This value has also been verified using a vector impedance meter. With this inductance value in the matching network, the tuning capability increases and maximum power transfer can be easily achieved without any reflected power.

Furthermore, the coil size limits the usable frequency range for the RF plasma system. The inductance required to use the same form of matching network at a frequency below 0.5 MHz is so large that the coil dimension tends to become unwieldy. In addition, at a frequency above  $\sim 150$  MHz, the coil becomes too small to be effectively coupled to a discharge apparatus. Consequently, commercially available RF plasma systems always operate within the above frequency range.

## APPENDIX C

### OTHER APPLICATIONS OF RF PLASMA ANNEALING

RF plasma annealing has been proven to be an effective technique for removing all the known radiation-induced defect centers in MOS device structures (Chapter II). The proposed mechanism involves the interaction of the energetic plasma excitation with defective  $\text{SiO}_2$  bonds, assisted by the RF field and induced wafer heating. RF plasma annealing is believed to lead to a more ordered  $\text{SiO}_2$  structure; i.e. less defective bonds in the bulk  $\text{SiO}_2$  and better bonding structures at the interface, both of which are reflected in the improved MOS electrical properties.

Due to the above effect, many device structures involving an insulator layer and an associated interface region can be expected to exhibit improved electrical properties after proper RF plasma annealing. Other areas in which RF plasma annealing has been demonstrated to be effective are as follows :

- (1) "Radiation Hardening": As mentioned in the proposed model, RF plasma annealing can lead to a more ordered Si-O structure, and thus it is not unreasonable to expect a more radiation-hard MOS device structure following this treatment. The preliminary experimental results have indicated improvement in radiation-induced shifts by a factor of RF plasma annealing in radiation hardening technology for either soft or hardened devices (see Appendix C.1 for details).
- (2) "Infrared Detectors" :  $\text{InSb}$  and  $\text{Hg}_x\text{Cd}_{1-x}\text{Te}$  MOS structures have been

widely used for infrared detection purposes. However, due to the low melting temperature, the material degradation of InSb takes place at temperatures above 200°C -- for  $\text{Hg}_x\text{Cd}_{1-x}\text{Te}$ , the degradation begins as low as 100°C. The requirement of low temperature processes introduces a large amount of oxide charge and surface states into these MOS capacitors. For an effective, conventional thermal annealing, a temperature higher than 300°C is needed. Hence this high temperature annealing cannot be applied to these materials. In contrast, RF plasma annealing is a low temperature process in which the wafer temperature can be maintained below 200°C for RF powers less than 300 W and below 100°C for powers less than 150 W. A comprehensive set of experiments has been performed to show that RF plasma annealing with hydrogen can achieve excellent annealing results under the above conditions. We believe that RF plasma annealing is a potentially powerful process when added to the fabrication of infrared detectors (see Appendix C.2 for details).

- (3) "Solar Cells" -- Schottky Diode : Due to their simple structure Schottky type Solar Cells are likely to become very popular in industry. The devices are prepared by depositing thin metal films on silicon wafers to form Schottky barriers. RF plasma annealing has been tested for its effectiveness on this particular structure. The Schottky diodes for the tests (with 95 Å Al on  $n/n^+$  (100) silicon substrate) were provided by Columbia University. The I-V characteristics of these devices measured before RF plasma annealing indicate an ohmic behavior with a low resistance. In contrast, a



good rectifying junction is formed after 400 W RF plasma annealing. The result is shown in Fig. C. It is believed that the enormous density of surface states between Al and Si has been substantially reduced thus achieving the intended Schottky behavior. The annealing results on MIS solar cells are also promising as explained below.

- (4) MTOS (Metal-Tunneling-Oxide-Semiconductor) Memory Device : This device, invented by Lai et al. (1978), has been demonstrated to function as an optical memory unit. Teng (1981) has further studied this structure and identified some important parameters to control the threshold behavior. Thus, several possible applications using MTOSFET structure have been pointed out (Teng et al. 1981). After RF plasma annealing, the dark current of the device can be reduced by three orders of magnitude (less leaky), and the "on-current" increases by more than one order (less surface states) compared with the original device without RF plasma treatment. At the same time, the holding voltage (memory effect) has been reduced to the theoretical value, i.e. approximately the predicted value without the effect of fixed charge and surface states.
- (5) An MOS capacitor with GaAs substrate. It has been shown that the devices can have improved interface properties after an RF plasma annealing following the spin-on silicon dioxide deposition (Ma and Miyauchi 1979).

The other potential applications of this technique may be :

- (1) SOS (silicon on sapphire) and SOI (silicon on insulator) structures

SCHOTTKY DIODE  
 $135 \text{ \AA Si} / 95 \text{ \AA Al} / n/n^+$   
 AREA =  $0.25 \text{ cm}^2$

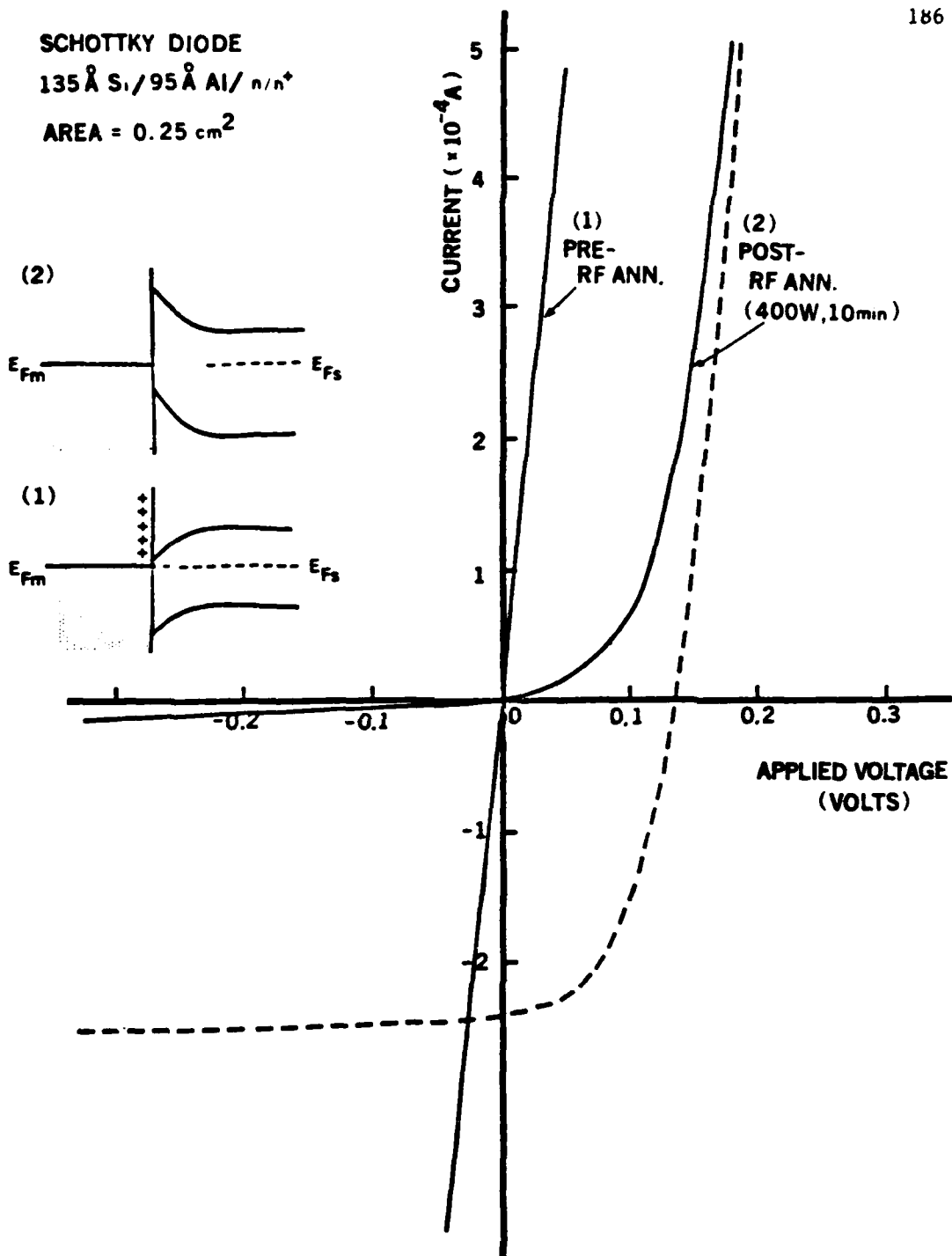


Fig. C

Current-voltage characteristics of Schottky diode:  
 (1) before RF plasma annealing (ohmic contact), and  
 (2) after 400W RF plasma annealing for 10 min. (rectifying behavior).

with high quality oxide and good interface properties cannot easily be obtained. High annealing power is required for these thick insulator configurations.

- (2) Poly-silicon gate devices which have two  $\text{SiO}_2$ -Si interfaces that are easily subject to damage.
- (3) Devices with polysilicon and amorphous silicon substrates.

## APPENDIX C.1

### RADIATION HARDENING OF MOS DEVICES BY RF PLASMA ANNEALING

The consequence of RF plasma annealing is believed to be a more ordered SiO<sub>2</sub> structure which is reflected in the electrical properties of MOS devices. Based on the proposed annealing model (section 2.6), it is not unreasonable to expect more radiation-hard MOS devices following proper RF plasma annealing. Also, an improvement in the radiation hardness resulting from RF plasma annealing could serve as indirect evidence that microscopic structural modifications of the SiO<sub>2</sub> layer have taken place. Therefore a series of experiments has been conducted to investigate the effects of RF plasma annealing on the radiation hardness of MOS structures. The preliminary results are very encouraging, and some of these will be presented.

The first set of experiments is done on simple MOS capacitors. These p-type MOS capacitors are exactly the same as the one with the low doping concentration (1-3 Ω-cm) mentioned in section 2.4. The sample irradiation is performed in a Co<sup>60</sup> γ-ray source of 2.1 x 10<sup>4</sup> rad/hour flux. No external voltage bias is applied during the irradiation for this set of experiments. Prior to irradiation, some samples have been treated in a parallel-plate RF plasma annealing chamber at a pressure of less than 10 μ and an RF power of 400 W.

High frequency and quasi-static C-V curves are used to determine the flatband voltage,  $V_{FB}$ , midgap voltage  $V_{MG}$ , surface state density  $N_{FS}$ , and inversion voltage  $V_I$ , before and after irradiation (see section 2.4

for details).

The preliminary results from this set of experiments can be summarized as follows. Table C represents the effects of RF plasma annealing on the radiation-induced C-V shifts. Fig. C.1 shows the radiation hardening results in terms of the surface state density in the Si bandgap at two different dose levels. The dashed curves represent the energy distributions of the radiation-induced surface states for the control device, and the solid curves are for the RF plasma annealed devices.

These results indicate that a simple RF plasma annealing treatment provides improvement by at least a factor of two as far as radiation-induced C-V shifts are concerned. Since the oxide growth process for this set of experiments was not intended to provide radiation-hard devices, we are not discouraged by the fact that these results are still inferior to the state-of-the-art radiation-hard MOS devices.

We have also investigated the effects of RF plasma annealing on some qualified radiation-hard samples obtained from Sandia Lab. Using the same RF annealing condition of 400 W for 15 min., the results show that under  $10^5$  Rad(Si) irradiation, the flatband and midgap shifts have improved slightly ( $\sim 0.2$  V), but the improvement of the surface state density is almost negligible. From these preliminary experiments, we believe that a longer annealing time and a higher annealing power ( $\geq 600$  W) are required for the desired improvements. These results, however, do serve to demonstrate the potential of RF plasma annealing in radiation hardening technology.

TABLE C

## EFFECTS OF RF PLASMA ANNEALING ON RADIATION-INDUCED SHIFTS

SHIFTS	- $\Delta V_{FB}$ (Volts)			- $\Delta V_{MG}$ (Volts)			$\Delta N_{FS}$ ( $\text{cm}^{-2}$ )			$\Delta V_I$ (Volts)		
	0.2	0.5	1.0	0.2	0.5	1.0	0.2	0.5	1.0	0.2	0.5	1.0
DOSAGE (MRAD)												
PROCESS:												
NO RF	2.2	3.4	4.5	1.6	2.3	3.55	$1.3 \times 10^{12}$	$3.6 \times 10^{12}$	$\approx 10^{13}$	0.9	$\geq 4.$	$\geq 6.$
PLASMA ANNEALING												
RF PLASMA ANNEALING	1.1	1.7	2.5	0.6	1.05	1.65	$5 \times 10^{11}$	$9.8 \times 10^{11}$	$1.95 \times 10^{12}$	0.1	0.9	2.4

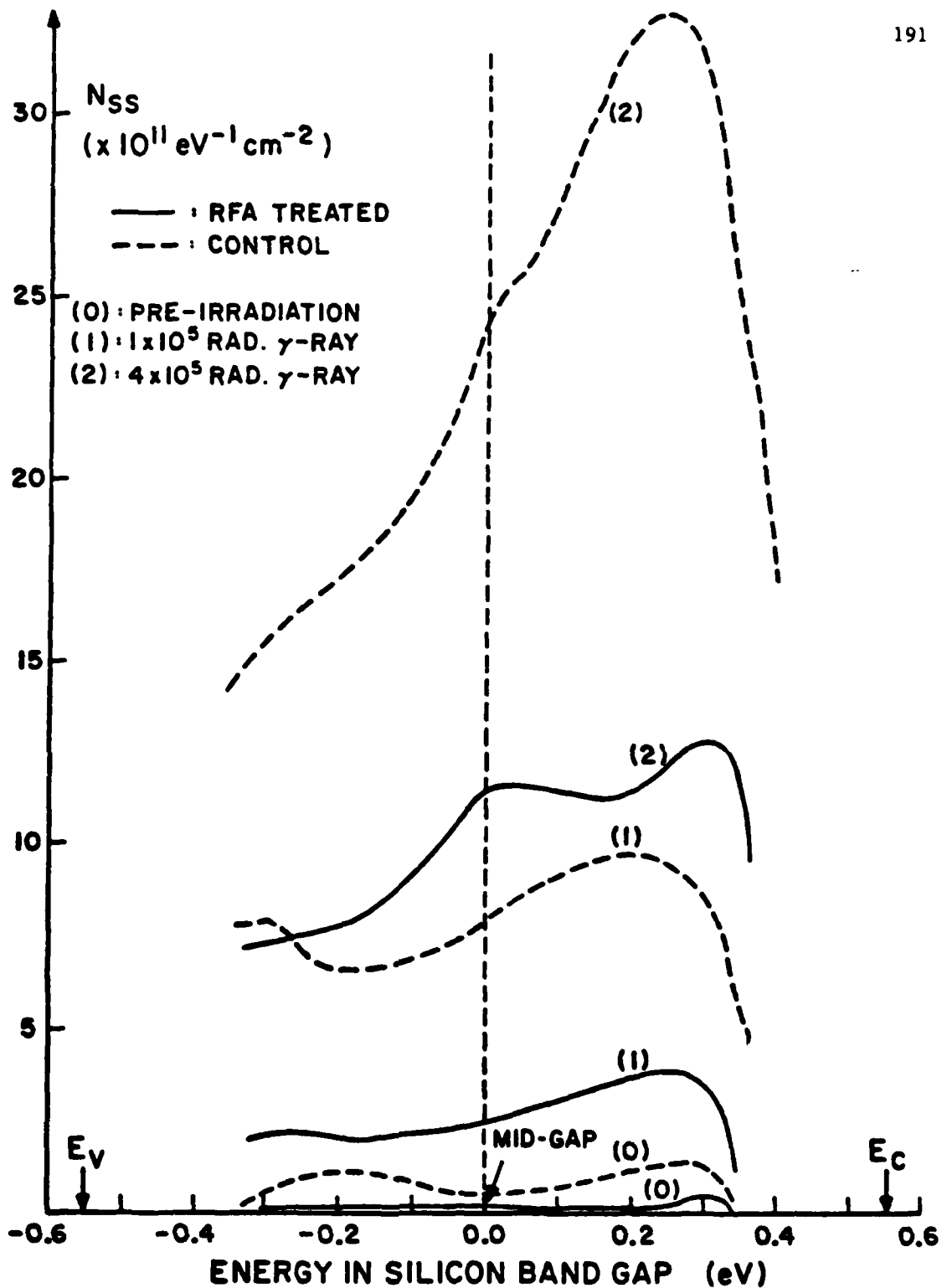


Fig. C.1

Radiation hardening results on surface state distribution after RF annealing. For high-dosage irradiation, a broad peak develops in the upper half of the silicon bandgap.

Future experiments should also include studies of the hardening effect of the threshold shifts on actual MOSFET devices, the effects of the biased radiation bombardment, and the effects of various RF annealing conditions : especially high RF power ( $\geq 700$  W) and different gas species (without any hydrogen content).



## APPENDIX C.2

### RF PLASMA ANNEALING ON MOS CAPACITORS WITH InSb SUBSTRATE

#### INTRODUCTION

Based on the high frequency C-V measurement, there exists a large amount of oxide charges and surface states in the InSb - substrate MOS capacitors supplied by the Santa Barbara Research Center Laboratory. In order to make the devices function will, some annealing process is necessary. For an effective conventional thermal annealing, a temperature higher than 300°C is needed. But a wafer temperature higher than 200°C could cause degradation of the InSb material. In contrast, RF annealing is a low temperature process in which the wafer temperature is never above 200°C for RF power less than 300 W. This technique has been applied successfully to remove fixed charges and surface states in Si-based MOS devices. Therefore, a comprehensive set of experiments has been performed to define the possible optimum RF annealing parameters for InSb MOS structures. During the course of the investigation, RF annealing in the presence and absence of hydrogen has been studied, and it has been found that RFA with hydrogen can achieve better annealing results than that without hydrogen. Judging from the results of the annealing, we have demonstrated experimentally that RFA is a potentially powerful process to be added to the fabrication of infrared detectors.

#### EXPERIMENTAL DETAILS

Initially, purified air (20% O<sub>2</sub> + 80% N<sub>2</sub>) is used as the gas species.

RF power is maintained in a range from 200 W to 400 W, annealing time from 5 min. to 20 min., and the wafer either facing up or down. These conditions, provided some improvements but are judged insufficient. (see Annealing Mechanism)

Later, forming gas ( $H_2/N_2$  mixture with varying amounts of hydrogen content from 2% to 10%) is used as the plasma gas species. The experimental results indicate that the existence of hydrogen is very helpful for the annealing although the exact  $H_2$  content is not important. The simple mechanism involved will be explained later.

After several trial and error experiments, it has been found that if the continuous anneal time is longer than 10 min. at an RF power level of 300 W, some of the devices are either damaged or destroyed. The reason for that is believed to be due to the high wafer temperature which rises to a level exceeding  $200^{\circ}C$ . This is the limiting temperature for InSb, above which degradation of the material starts to occur.

As discussed in Chapter III, at an RF power of 300 W the temperature of the wafer continuously increases within the first 15 min. and reaches  $200^{\circ}C$  at about 10 min. A lower temperature can be maintained at this power level if one can keep the annealing time shorter than 10 min. Therefore, a 5 min. continuous anneal is tried. Although some devices with larger  $V_{FB}$  are not annealed back completely, no damage is observed even for power as high as 300 watts. To further improve the  $V_{FB}$ , an additional 5 minute run is performed after which the samples are allowed to cool down following the first 5 min. RFA. Finally, one possible

optimal condition has been reached:

- (1) RF power : 300 W.
- (2) Annealing time : 5'+5'+5' (Three times five minutes)  
The last 5 min. was used for stabilization.
- (3) Pressure of the inner chamber : around 10 microns.
- (4) Gas species : ~~low~~ gas (10% H<sub>2</sub> + 90% N<sub>2</sub>)
- (5) The wafer ~~was~~ ~~put~~ up in all the annealing runs.

#### RESULTS AND DISCUSSIONS

More than 200 devices have been measured. These samples are all InSb-MOS devices with an oxide thickness about 1500 Å and have plasma deposited SiO<sub>2</sub> on the vertical system. The high frequency C-V curves after RF plasma annealing are shown in Fig. C.2. It can easily be seen that V<sub>FB</sub> shifts back from either -2.0 V or +2.0 V to ~0 V after RF plasma annealing and that the inversion parts of the C-V curves show significant improvement indicating the reduction of fast surface states. Hysteresis stays roughly the same indicating some mismatch between InSb and the oxide which could not be improved with the RF annealing conditions mentioned above. Experimental results also show that the uniformity of the V<sub>FB</sub> distribution is slightly better after RF annealing. Furthermore the promising results on the multiplexor test chip strongly suggest that this technique is also suitable for fully fabricated InSb integrated circuit wafers (e.g. C C D).

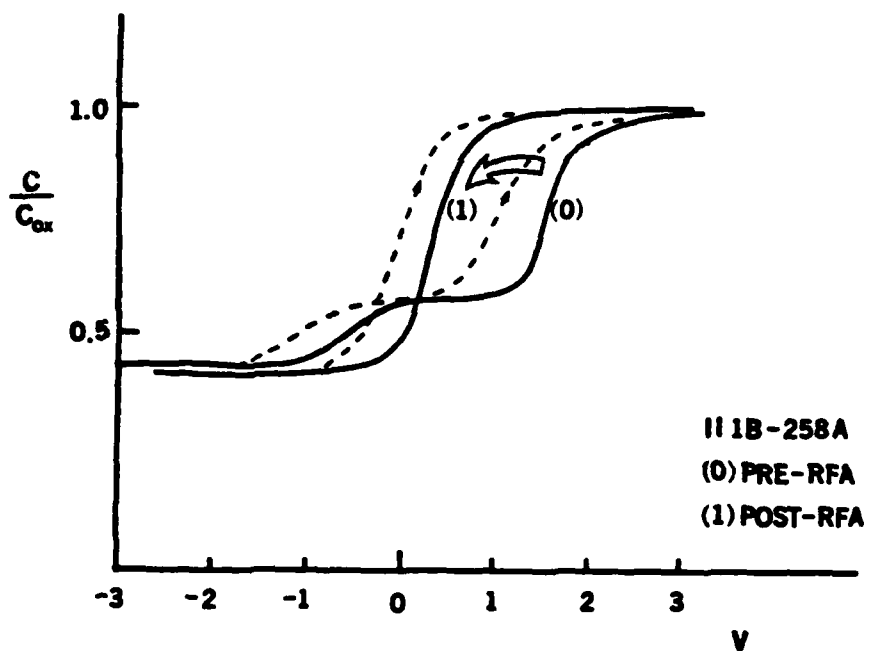
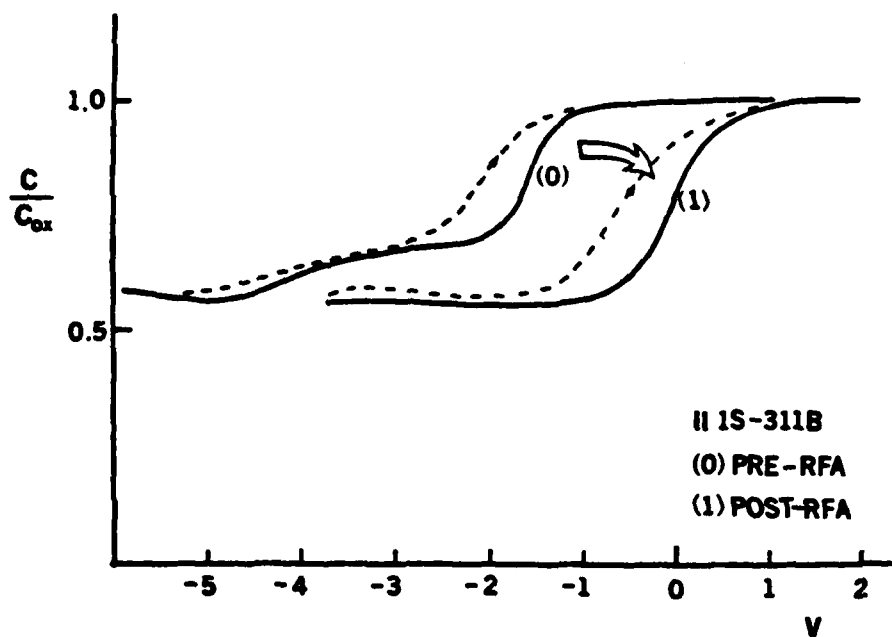


Fig. C.2

RF plasma annealing results of InSb MOS capacitors. The upper high frequency C-V curves show  $V_{FB}$  shifts from -2V to 0V, and the lower ones show  $V_{FB}$  from +2V to 0V.

## ANNEALING MECHANISM WITH HYDROGEN

The oxides on the top of InSb substrates are all grown in a relatively low temperature environment. There must exist many bonding defects due to incomplete chemical reactions. To complete the chemical reactions, a large amount of energy higher than the reaction barrier is needed. In the absence of hydrogen, typical RF plasma annealing provides a reduction of the activation energy by approximately 0.25 eV (see Chapters IV and V), and those defects with a reaction barrier of this magnitude may be annealed. For some of the defect centers with higher activation energy, however, a large RF power is needed. Since the allowable wafer temperature limits the RF power that we can use, some of the more persistent defects will remain. The inclusion of hydrogen is helpful in this case.

The effect of hydrogen in the annealing process is believed to be due to the chemical reaction between the active hydrogen species and the defective bonds such as  $\equiv \text{Si} \cdot + \text{H} \rightarrow \equiv \text{Si} - \text{H}$ . Such reaction is exothermic and can take place at low temperature. In the RF plasma, the hydrogen molecules may be dissociated to form hydrogen atoms, a very reactive species. These hydrogen atoms can easily diffuse through the gate and form Si - H and Si - OH bonds with the defects, leading to the reduction of the oxide charge and surface states.

Some of the devices which could not be improved could have been impurity-contaminated during the original fabrication and/or some other processes. We have evidence showing that a strong chemical reaction occurs between the plasma and some wafer surfaces. Another possibility is the

existence of excess In and Sb at the interfacial layer which may have come from the oxidation of the surface during processing, and it is not expected that the RF annealing process can change the chemical profile of the material.

#### CONCLUSION

The experimental results suggest that the low temperature process induced defect centers (oxide charge and surface states) can be removed by RF plasma annealing, and it is a promising fabrication process for infrared detectors.

Those samples which did not improve are most likely due to improper sample preparation, and I believe that RF annealing should work for the properly prepared InSb-based samples.

Based on the experience with Si-MOS devices, the optimal conditions are not obtained until a large number of annealing parameters are tested. Therefore, my feeling is that we are still far from reaching the optimized annealing conditions for InSb devices.

APPENDIX D  
X-RAY LUMINESCENCE SPECTRA  
(XLS)

INTRODUCTION

Trap characterization by luminescence emission has been proposed in the past using cathodoluminescence (Mitchell and Denure 1973, Jones and Embree 1978, Koyama 1980) and high field electroluminescence (Solomon and Klein 1976). In this Appendix, we will show that under X-ray irradiation, the light emission through the defect levels in amorphous  $\text{SiO}_2$  can provide useful information about the traps.

As reported by Koyama (1980), there exist two bands (5600 Å and 2900 Å wavelengths) whose intensities increase with the radiation dose and which originate from radiation-induced defects. By using the same setup as for the experimental simulation, the peak intensities of these two bands can be monitored at different temperatures as the annealing time elapses. Thus an accurate activation energy can be assigned to each band, allowing the origins of these defects and their correlation with the oxide charge, surface states and neutral trap to be clarified. This also helps to understand the RF plasma annealing mechanism.

EXPERIMENTAL DETAILS

Both MOS and MOM samples are used in this study.  $\text{In}_2\text{O}_3$  is evaporated to a thickness of ~2000 Å (Pan and Ma 1980) as a transparent metal electrode. For MOS samples, a dry oxide is thermally grown on (100) p-type Si for

various time periods to obtain thicknesses ranging from 500 Å to 5000 Å. For MOM samples, a No. 1 cover glass (which contains 64% SiO<sub>2</sub> and 36% other oxide and has thickness  $1 \times 10^{-2}$  cm) is coated with In<sub>2</sub>O<sub>3</sub> on both sides.

The experimental setup is similar to the one shown in Fig. 4.1 with some modifications in order to detect the luminescence spectra. As shown in Fig. D.1 the modifications include :

- (1) A Heath Photomultiplier (model EU-701-30), sensitive in the visible range, is used for light detection. The photocurrent is sensed by a current meter which is connected to the output of the photomultiplier.
- (2) A optical fiber pipe serving as a light guide is used to transfer the emitted light from the sample surface to the phototube.
- (3) A series of precision filters (with 100 Å bandwidth and central wavelengths ranging from 4000 Å to 6000 Å) is inserted in front of the photomultiplier to obtain a low-resolution spectral distribution of the luminescence emission.

## RESULTS AND DISCUSSIONS

### A. MOS Samples with Thermal SiO<sub>2</sub>

No detectable X-ray induced luminescence signal is obtained when the oxide thickness is varied from 500 Å to 5000 Å. It is believed that due to strong electron-phonon interaction in SiO<sub>2</sub> and low density of defect centers, the light emission probability is very small, and the low-sensitivity phototube we have in our laboratory is not suitable for



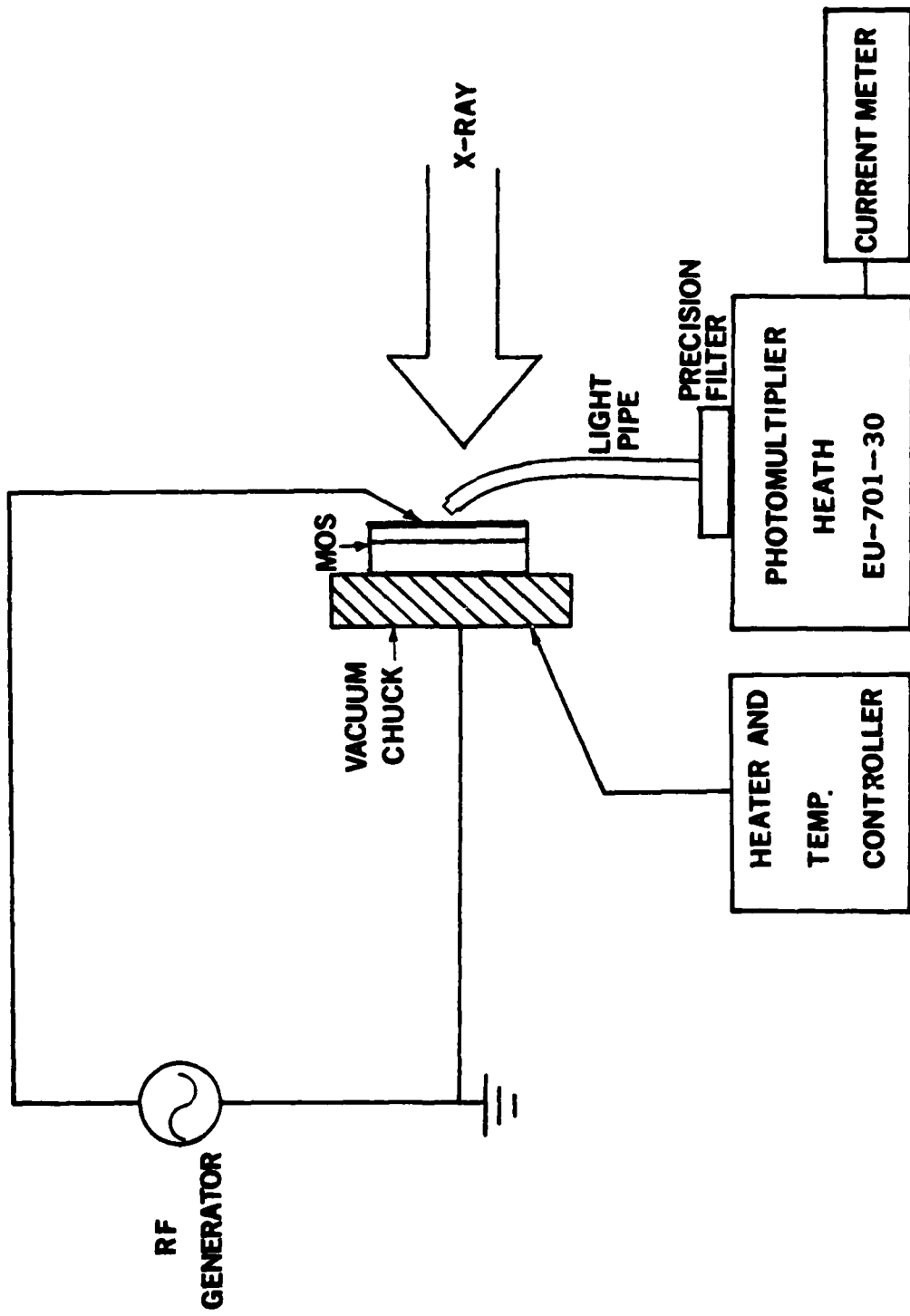


Fig. D.1 Experimental setup for X-ray luminescence measurement.

detecting such weak signals. Based on my calculation, a photon counting system with an ability of detecting about 50 photons per second would probably be needed for this purpose.

During the above mentioned experiment, we have found that the background signal which arises from the X-ray luminescence spectra (XLS) of the optical fiber (made of fused silica) is similar to the one published by H. Koyama (1980) under electron beam irradiation. As shown in Fig. D.2, the XLS peak appears exactly at  $5600 \text{ \AA}$ , a level corresponding to Koyama's band C which increases substantially with increasing irradiation.

#### B. MOM Samples with Coverglass as Oxide

Having decided that we do not have enough sensitivity to study by MOS samples we then used a No.1 coverglass to perform the same experiment. In this case, the X-ray luminescence signal from the coverglass is very clear (one order higher intensity than the background noise), mainly because the coverglass is three orders of magnitude thicker than the thermal  $\text{SiO}_2$ . When the measured luminescence intensity is correlated to the effective defect density, the same experimental simulation as shown in section 4.3 can be performed to observe the annealing behavior of the defect.

Fig. D.3 shows the X-ray luminescence signal vs temperature at a wavelength of  $5400 \text{ \AA}$ . The signal reduction with increasing sample temperature could be due to the increase of the lattice vibrations causing stronger non-radiative phonon emission. For easy comparison, all the

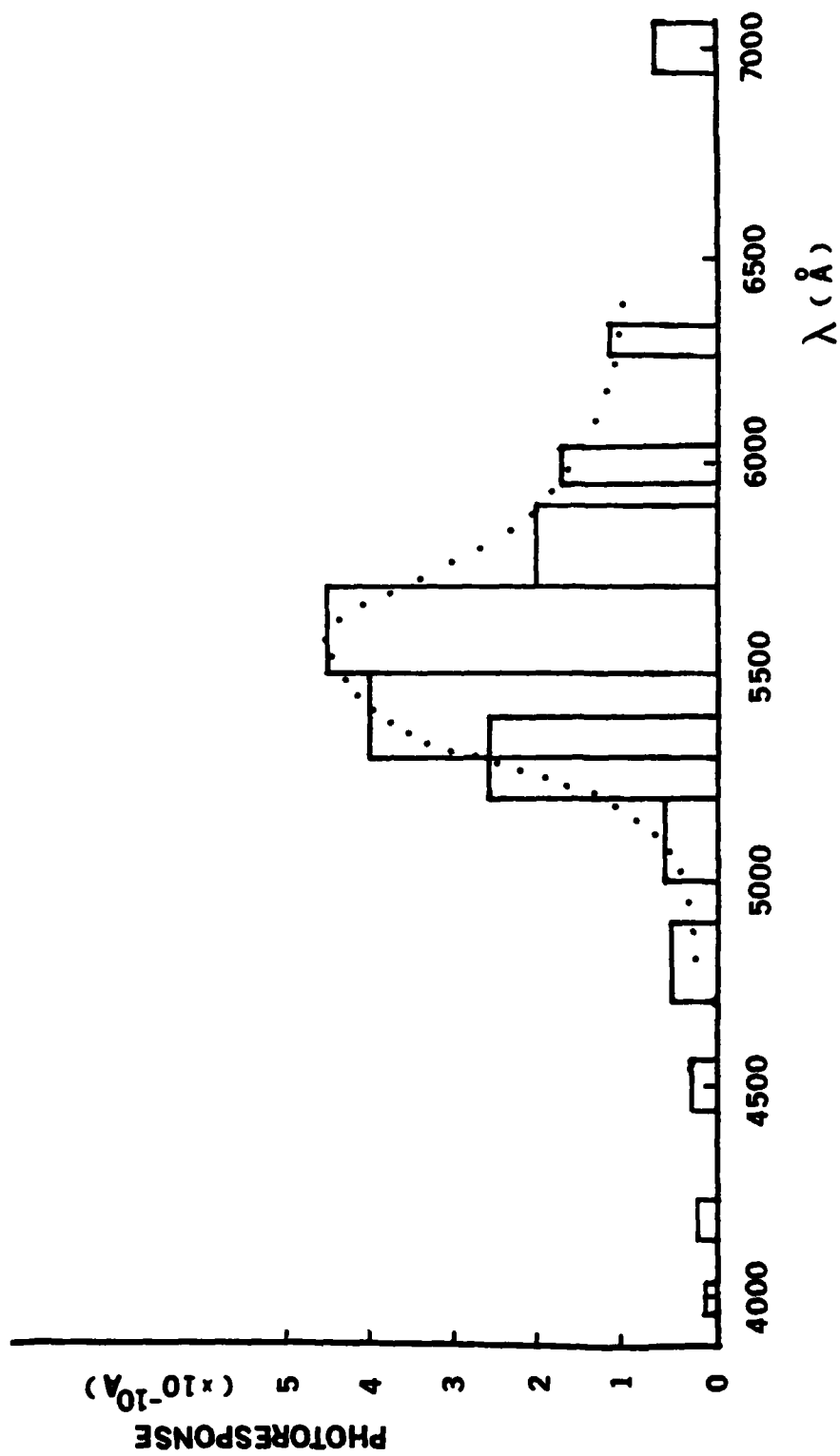


Fig. D.2 X-ray luminescence spectra for a typical optical fiber at room temperature.

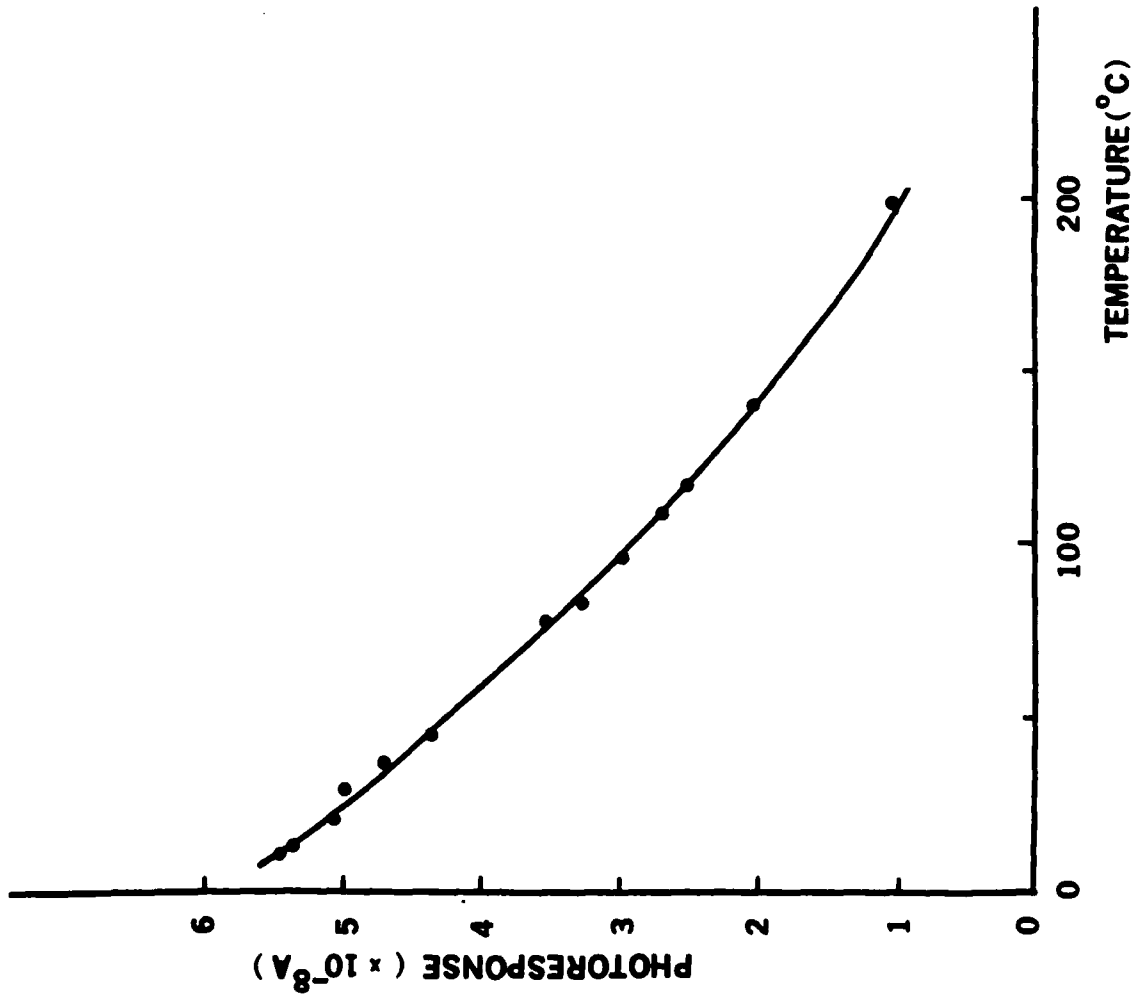


Fig. D.3 X-ray luminescence at 4500 Å as a function of ambient temperature for a No. 1 coverglass.

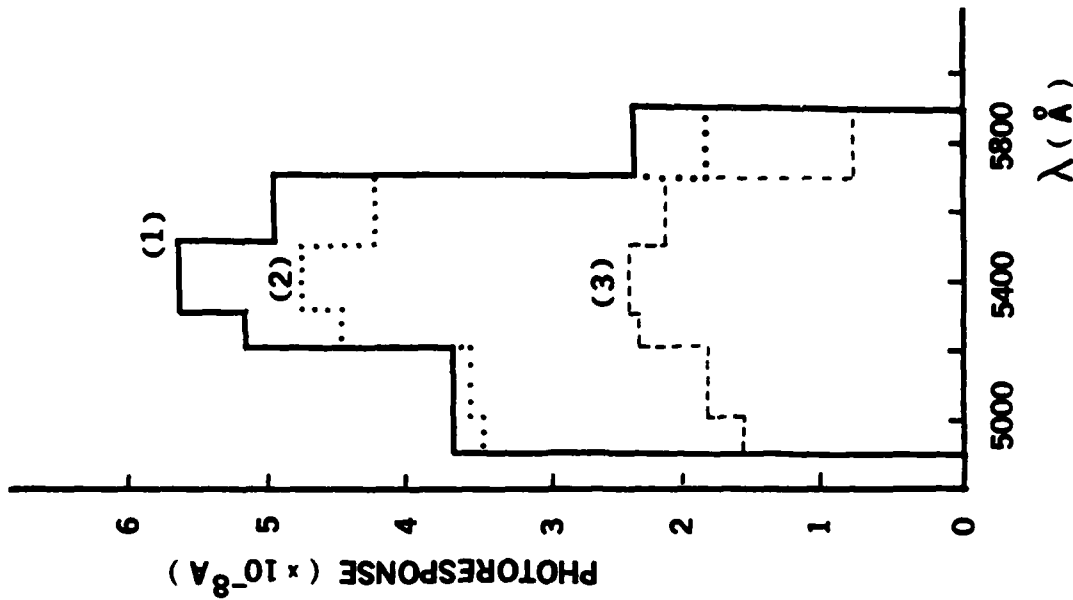


Fig. D.4 X-ray luminescence spectra for a No. 1 coverglass :  
 (1) after heavy irradiation,  
 (2) RF annealed at 50°C after irradiation and (3) RF annealed at 100°C after irradiation.

experimental luminescence signals in this study are measured at room temperature.

Due to equipment limitations, only the luminescence spectra between 5000 Å and 6000 Å could be investigated. As shown in Fig. D.4, curve 1 is the X-ray luminescence signal after heavy X-ray radiation damage before simulated RF annealing. Curves 2 and 3 show the data after the X-ray (35 KV, 35 mA, Cu) and the RF field (15 V at 10 MHz) are applied simultaneously at two different temperatures, 50°C and 100°C respectively for 10 min.

Fig. D.5 shows the annealing rates of the 5400 Å peak for a pure thermal process and for the RF enhanced process. These data are taken from the X-ray luminescence signal at 5400 Å after an isochronal annealing experiment with a 10 min. annealing time. The X-ray exposure time for obtaining luminescence signal is very short (approximately 30 seconds) during which the radiation damage has been experimentally proven to be negligible. The annealing temperature ranges from 25°C to 100°C. The average activation energy for the pure thermal process is approximately 0.36 eV, very close to the value for the effective oxide charge annealing in SiO<sub>2</sub> (see Fig. 4.7). The enhanced process has an activation energy of about 0.12 eV, which differs from that of the pure thermal process by a factor of 3.

The mechanisms which lead to the similarity between the activation energies for the annealing processes of the effective oxide charge in thermal SiO<sub>2</sub>, and those of the 5400 Å luminescence peak in a No.1 coverglass

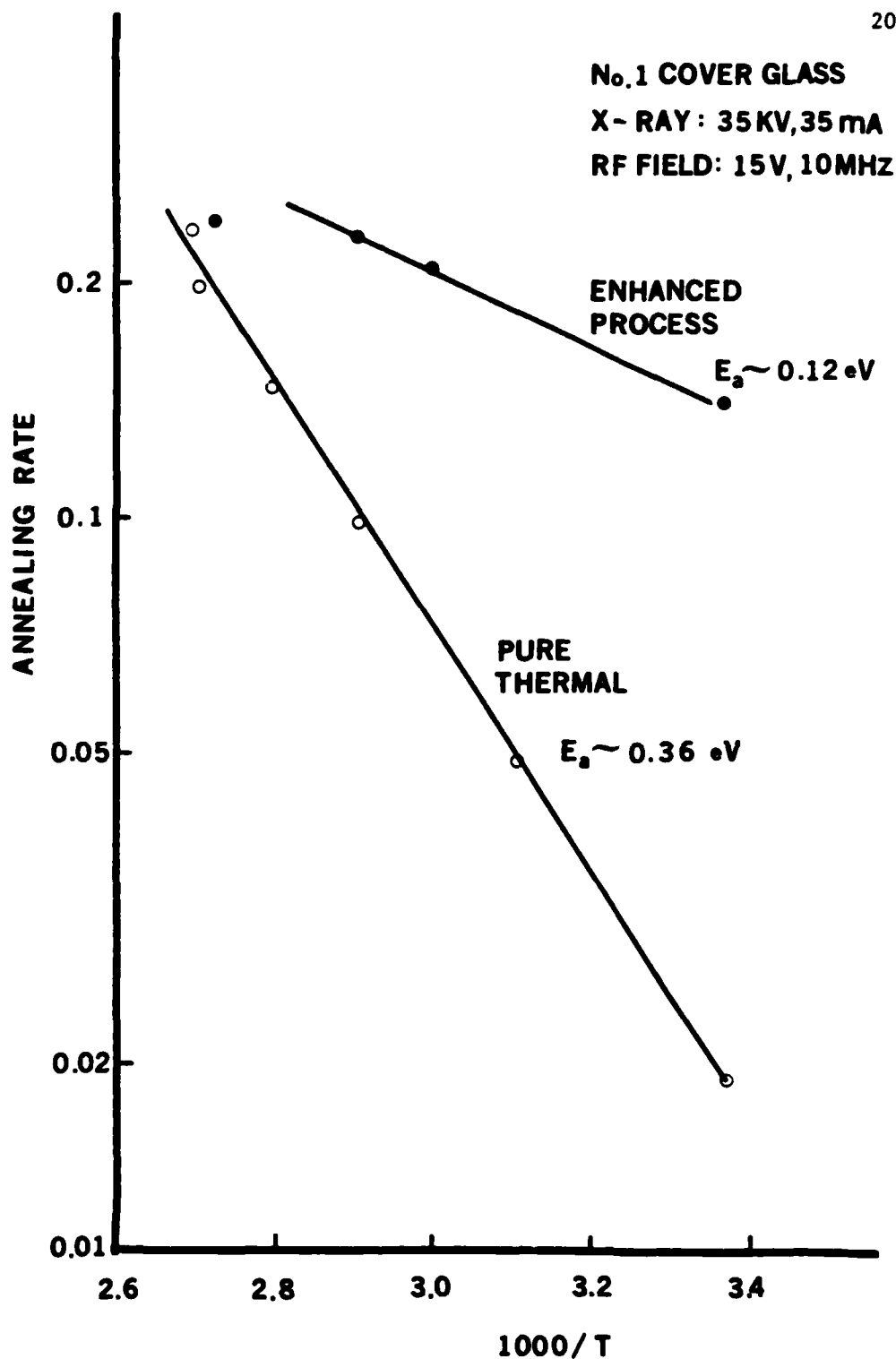


Fig. D.5

Arrhenius plot of the annealing rate for pure thermal and enhanced processes. The experiment is done by examining the X-ray luminescence peak at  $4500 \text{ \AA}$  from a No. 1 cover-glass.

are not completely understood. But it is probable that the 5400 Å peak in the XLS of the coverglass could originate from the radiation-induced oxide charge centers.

Due to the high impurity content in a No.1 coverglass which is much different from thermal SiO<sub>2</sub>, one can not reach the conclusion that the radiation-induced oxide charge center can produce a 5400 Å luminescence peak in any form of SiO<sub>2</sub>. But we believe that this experiment can provide more information about the origins of these defect centers and their correlation with the radiation-induced oxide charge, surface states, and neutral traps. Further investigations using thermal SiO<sub>2</sub> with a photon counting system are required to clarify the mechanisms for both the radiation damage and RF annealing.

## REFERENCES

- J. M. Aitken, "1  $\mu$ m MOSFET VLSI Technology : Part VIII--Radiation Effects." IEEE, ED-26(4), 372-378 (1979).
- J. M. Aitken, D. R. Young, and K. Pan, "Electron Trapping in Electron-Beam Irradiated SiO<sub>2</sub>." J. Appl. Phys., 29, 3386-3391 (1978).
- G. A. Ausman Jr. and F. B. McLean, "Electron-Hole Pair Creation Energy in SiO<sub>2</sub>." Appl. Phys. Lett., 26(4), 173-175 (1975).
- P. Balk, J. Electrochem. Soc., 112, 185C (1965).
- W. L. Ballamy and L. C. Kimerling, "Premature Failure in Pt-GaAs IMPATT'S - Recombination-Assisted Diffusion as a Failure Mechanism." IEEE, ED-25(6), 746-752 (1978).
- C. N. Berglund and R. J. Powell, "Photoinjection into SiO<sub>2</sub> : Electron Scattering in the Image Force Potential Well." J. Appl. Phys. 42(2), 573-579 (1971).
- J. S. Best and J. O. McCaldin, "Interfacial Impurities and the Reaction between Si and Evaporated Al." J. Appl. Phys., 46(9), 4071-4072 (1975).
- Forrest I. Boley, "Plasmas - Laboratory and Cosmic." D. Van Nostrand Co., New Jersey (1966).
- M. R. Boudry and J. P. Stagg, "The Kinetic Behavior of Mobile Ions in the Al - SiO<sub>2</sub> - Si System." J. Appl. Phys., 50(2), 942-950 (1979).
- S. M. Brekhovskikh, I. K. Vitol et al., "Effect of Impurities and Structural Defects on Electronic Processes in Quartz Glass." Optics and Spectroscopies (U.S.S.R.), 30, 60-62 (1971).



- C. C. Chang, "General Formalism for Quantitative Auger Analysis."  
Surface Science, 48, 9-21 (1975).
- Brian Chapman, "Glow Discharge Processes - Sputtering and Plasma Etching."  
John Wiley and Sons. Chapter 1-5 (1980).
- M. R. Chin and T. P. Ma, "Photocurrent in Thermal SiO<sub>2</sub> under X-ray  
Irradiation : Significance of Contact Injection." Submitted for  
Publication in J. Appl. Phys. (1991).
- M. R. Chin and T. P. Ma, "Voltage and Frequency Dependence of RF Annealing."  
to be published.
- M. R. Chin and T. P. Ma, "Radiation Hardening of MOS Devices by RF Plasma  
Annealing." to be published.
- E. V. Condon, Chapter 8 of "Handbook of Physics." edited by E. V. Condon  
and H. Odishaw, McGraw Hill, New York, 1967.
- O. L. Curtis Jr., J. R. Srour, and K. Y. Chiu, "Hole and Electron  
Transport in SiO<sub>2</sub> Films." J. Appl. Phys. 45(10) 4506-4513 (1974).
- B. E. Deal, "The Current Understanding of Charges in the Thermally  
Oxidized Silicon Structure." J. Electrochem. Soc., 121, 198C-205C  
(1974).
- R. F. DeKeersmaecker and D. J. DiMaria, "Electron Trapping and Detrapping  
Characteristics of Arsenic - Implanted SiO<sub>2</sub> Layers." J. Appl. Phys.  
51(2), 1085-1101 (1980).
- H. R. Deppe, B. Hasler, and J. Hopfner, "Investigations on the Damage  
Caused by Ion Etching of SiO<sub>2</sub> Layers at Low Energy and High Dose."  
Solid State Electron., 20, 51-55 (1977).

- D. J. DiMaria, Z. A. Weinberg, and J. M. Aitken, "Location of Positive Charges in SiO<sub>2</sub> Films on Si Generated by VUV Photons, X-ray, and High-Field Stressing." J. Appl. Phys., 48(3), 898-906 (1977).
- D. J. DiMaria, Proc. Intl. Conf. on Physics of SiO<sub>2</sub> and Its Interfaces, 160-178, S. T. Pantelides, Ed., Yorktown Height N.Y., (1978).
- P. V. Dressendorfer, Ph. D. Thesis, Yale University. (1978).
- E. P. EerNisse and G. F. Derbenwick, "Viscous Shear Flow Model for MOS Device Radiation Sensitivity." IEEE NS-23(6), 1534-1539 (1976).
- R. D. Evans, Chapter 21 of "Atomic Nucleus", McGraw Hill, N.Y. (1965).
- T. E. Everhart and P. H. Hoff, "Determination of Kilovolt Electron Energy Dissipation vs Penetration Distance in Solid Materials." J. Appl. Phys., 42(13), 5837-5846 (1971).
- C. Falcony-Guajardo, F. J. Feigl and S. R. Butler, "Charge Trapping and Associated Luminescence in MOS Oxide Layers." Leigh University (1980).
- J. M. Fanet and R. Poirier, "Charge Storage in SiO<sub>2</sub> under Low-Energy Electron Bombardment." Appl. Phys. Lett. 25(4), 183-185 (1974).
- J. W. Farmer and R. S. Lee, "Photocurrents and Photoconductive Yield in MOS Structures during X-ray Irradiation." J. Appl. Phys., 46(6), 2710-2715 (1975).
- D. Frohman-Bentchkowsky, "FAMOS - A New Semiconductor Charge Storage Device." Solid State Electronics, 17, 517-529 (1974).
- R. A. Gdula, "The Effects of Processing on Radiation Damage in SiO<sub>2</sub>." IEEE, ED - 26(4), 644-646 (1979).

- A. Goetzberger and E. H. Nicollian, "Temperature Dependence of Inversion-Layer Frequency Response in Silicon." The Bell System Technical Journal, 513-522 (1967).
- A. Goetzberger, E. Klausmann, and M. Schulz, "Interface States on Semiconductor/Insulator Surfaces." CRC Critical Rev. Solid State Sci. 6(1), 1 (1976).
- A. M. Goodman, "Photoemission of Electrons from Si and Au into SiO<sub>2</sub>." Phys. Rev. 144(2), 588 (1966), and "Photoemission of Holes from Si into SiO<sub>2</sub>." Phys. Rev. 152(2), 780 (1966).
- Peter V. Gray and D. M. Brown, "Density of SiO<sub>2</sub> - Si Interface States." Appl. Phys. Lett. 8(2), 31-33 (1966).
- A. S. Grove, "Physics and Technology of Semiconductor Devices." John Wiley and Sons, Inc. New York (1967).
- A. S. Grove, B. E. Deal, E. H. Snow, and C. T. Sah, "Investigation of Thermally Oxidized Si Surfaces Using MOS Structures." Solid State Electronics, 8, 145 (1965).
- C. W. Gwyn, "Model for Radiation-Induced Charge Trapping and Annealing in Oxide-Layer of MOS Devices." J. Appl. Phys. 40, 4886-4892 (1969), and Ph.D. Dissertation "An Analysis of the Effects of Ionizing Radiation in One-Dimensional MOS Structures." Xerox University Microfilms, Ann Arbor, Michigan (1968).
- C. H. Henry and D. V. Lang, "Nonradiative Capture and Recombination by Multiphonon Emission in GaAs and GaP." Phys. Rev. B. 15(2), 989 (1977).

- T. W. Hickmott, "Thermally Stimulated Ionic Conductivity of Sodium in Thermal SiO<sub>2</sub>." J. Appl. Phys. 46(6), 2583-2598 (1975).
- Harold J. Hovel, "Solar Cell", Thomas J. Watson Research Center, IBM. Absorption Coefficient of Si in 1.0 - 5.0 eV Photon Energy range. (1975).
- G. Hu and W. C. Johnson, "Relationship between Trapped Holes and Interface States in MOS Capacitors." Appl. Phys. Lett. 36(7), 590-592 (1980).
- G. W. Hughes, "Interface-State Effects in Irradiated MOS Structures." J. Appl. Phys. 48(12), 5357-5359 (1977).
- G. W. Hughes and G. J. Brucker, "Radiation Hardened MOS Technology." Solid State Technology 70-76 July (1979).
- H. L. Hughes, "Radiation-Induced Perturbations of the Electrical Properties of the Si - SiO<sub>2</sub> Interface." IEEE NS-16(6), 195-200 (1969).
- R. C. Hughes, "Charge-Carrier Transport Phenomena in Amorphous SiO<sub>2</sub> : Direct Measurement of the Drift Mobility and Lifetime." Phys. Rev. Lett. 30, 1333 (1973).
- R. C. Hughes, "Hot Electrons in SiO<sub>2</sub>." Phys. Rev. Lett. 35(7), 449 (1975), and "Time-Resolved Hole Transport in a - SiO<sub>2</sub>." Phys. Rev. B. 15(4), 2012-2020 (1977).
- R. C. Hughes, "High Field Electronic Properties of SiO<sub>2</sub>." Solid State Electronics, 21, 251-258 (1978).
- K. O. Jeppson and C. M. Svensson, "Negative Bias Stress of MOS Devices at High Electric Fields and Degradation of MNOS Devices." J. Appl. Phys. 48(5), 2004-2014 (1977).

- Colin. E. Jones and D. Embree, "Correlation of the 4.77 - 4.28 eV Luminescence Band in SiO<sub>2</sub> with Oxygen Vacancy." J. Appl. Phys., 47(12), 5365-5371 (1976).
- P. F. Kane and G. B. Larrabee, "Characterization of Solid Surface." Plenum, New York, Absorption Coefficient of Al in 1 Å - 100 Å Wavelength Range (1974).
- J. H. Keller and W. B. Pennebaker, "Electrical Properties of RF Sputtering Systems." IBM j. Res. Develop., 23(1), 3-15 (1979).
- L. C. Kimerling, "New Developments in Defect Studies in Semiconductors." IEEE NS-23(6), 1501 (1976).
- L. C. Kimerling, "Recombination Enhanced Defect Reactions." Solid State Electronics, 21, 1391-1401 (1978).
- P. Kirkpatrick, "Theory of Continuous X-ray Spectra from Thick Targets." Phys. Rev. 70, 446A (1946).
- J. C. Knights and E. A. Davis, "Photogeneration of Charge Carriers in Amorphous Selenium." Phys. Chem. Solid, 35, 543-554 (1974).
- H. Koyama, "Cathodoluminescence Study of SiO<sub>2</sub>." J. Appl. Phys., 51(4), 2228-2235 (1980).
- H. Koyama, K. Matsubara and M. Mouri, "Cathodoluminescence Study of a SiO<sub>2</sub> Layer on Si with the Aid of Auger Electron Spectroscopy." J. Appl. Phys., 48(12), 5380-5381 (1977).
- A. Kurylo, Private Communication (1978).
- S. K. Lai, Ph.D. Thesis, Yale University (1979).
- S. K. Lai, "Two Carrier Nature of Interface State Generation in Hole Trapping and Radiation Damage." Appl. Phys. Lett. 39(1), 56-60 (1981).

- S. K. Lai and D. R. Young, "Effects of Avalanche Injection of Electrons in  $\text{SiO}_2$  - Generation of Fast and Slow Surface State." to be published (1981).
- R. B. Laughlin, J. D. Joannopoulos, and D. J. Chadi, Proc. of Intl. Conf. on the Physics of  $\text{SiO}_2$  and Its Interface. 321, Pergamon Press, N.Y. (1978).
- M. Lax, "Cascade Capture of Electron in Solids." Phys. Rev. 119(5), 1502-1523 (1960).
- H. J. Leamy and L. C. Kimerling, "Electron-Beam Induced Annealing of Defects in GaAs." J. Appl. Phys. 48(7), 2795-2803 (1977).
- J. S. Logan, N. M. Mazza, and P. D. Davidse, "Electrical Characterization of Radio Frequency Sputtering Gas Discharge." J. of Vacuum Science and Technology, 6(1), 120-123 (1969).
- J. S. Logan, F.S. Maddocks, and P. K. Davidse, "Metal Edge Coverage and Control of Charge Accumulation in RF Sputtered Insulators." IBM J. Res. Develop 182-191, March (1970).
- G. Lucovsky, "Spectroscopic Evidence for Valence-Alternation-Pair Defect States in Vitreous  $\text{SiO}_2$ ." Phil. Mag. B 39(6), 513-530 (1979).
- G. Lucovsky, "Paramagnetic Centers Associated with Bonding Defects in V- $\text{SiO}_2$ ." Phil. Mag. 41(4), 457-467 (1980).
- W. T. Lynch, "Calculation of Electric Field Breakdown in Quartz as Determined by Dielectric Dispersion Analysis." J. Appl. Phys. 43(8), 3274-3278 (1972).
- T. P. Ma and R. C. Barker, "Effect of Gamma-Ray Irradiation on the Surface States of MOS Tunnel Junctions." J. Appl. Phys. 45, 317-321 (1974).

- T. P. Ma, "Oxide Thickness Dependence of Electron-Induced Surface States in MOS Structures." *Appl. Phys. Lett.*, 27, 615-616 (1975).
- T. P. Ma, G. Scoggan, and R. Leone, "Comparison of Interface State Generation by 25-KeV Electron-Beam Irradiation of P-Type and N-Type MOS Capacitors." *Appl. Phys. Lett.*, 27, 61-63 (1975).
- T. P. Ma, B. H. Yun, D. J. DiMaria and G. A. Scoggan, "Effects of Electron-Beam Irradiation on the Properties of CVD  $\text{Si}_3\text{N}_4$  Films in MNOS Structures." *J. Appl. Phys.* 47, 1599-1604 (1976).
- T. P. Ma and W. H-L. Ma, "Low Pressure RF Annealing : A New Technique to Remove Charge Centers in MIS Dielectrics." *Appl. Phys. Lett.*, 32(7), 441-444 (1978).
- T. P. Ma and W. H-L. Ma, "Effects of RF Annealing on Excess Charge Centers in MIS Dielectrics." *IEEE*, 5C-13, 445-454 (1978).
- T. P. Ma and K. Miyauchi, "MIS Structures Based on Spin-on  $\text{SiO}_2$  on GaAs." *Appl. Phys. Lett.*, 34(1), 88-90 (1979).
- T. P. Ma and M. R. Chin, "Removal of Radiation-Induced Electron Traps in MOS Structures by RF Annealing." *Appl. Phys. Lett.*, 36(1), 81 (1980). *IEDM Technical Digest*, 224-228 (1979).
- T. P. Ma and M. R. Chin, "RF Annealing Mechanisms in Metal-Oxide-Semiconductor Structures - an Experimental Simulation." *J. Appl. Phys.*, 51(10), 5458-5463 (1980).
- W. H-L. Ma and T. P. Ma, "The Effect of RF Annealing upon Electron-Beam Irradiated MIS Structures." *Solid State Electronics*, 22, 663-666 (1979).

- D. V. McCaughan and V. T. Murphy, "Low Energy Ion Bombardment Effects in  $\text{SiO}_2$ ." IEEE, NS-19, 249-255 (1972).
- D. V. McCaughan, R. A. Kushner and V. T. Murphy, "Ion Neutralization Processes at Insulator Surfaces and Consequent Impurity Migration Effects in  $\text{SiO}_2$  films." Phys. Rev. Lett. 30, 614 (1973).
- D. V. McCaughan and Richard A. Kushner, "Degradation of Oxide Films due to Radiation Effects in Exposure to Plasmas in Sputter Deposition and Backsputtering." Proc. IEEE 62(9), 1236-1241 (1974).
- F. B. McLean, "A Framework for Understanding Radiation-Induced Interface States in  $\text{SiO}_2$  MOS Structures." IEEE, NS-27, 1651 (1980).
- N. F. Mott, "Photogeneration of Charge Carriers and Recombination in Amorphous Semiconductors." Phil. Mag., 36(2), 413-420 (1977).
- N. F. Mott and E. A. Davis (1979) Electronic Processes in Non-crystalline Material, second edition, Clarendon Press, Oxford.
- Masaru Nakagiri, "Surface State Generation in MOS Structure by Applying High Field to the  $\text{SiO}_2$  Film." Japanese J. Appl. Phys., 13(10), 1610-1617 (1974).
- P. K. Nauta and M. W. Hillen, "Investigation of Mobile Ions in MOS Structure Using the TSIC Method." J. Appl. Phys., 49(5), 2862-2875 (1978).
- E. H. Nicollian and C. N. Berglund, "Avalanche Injection of Electrons into Insulating  $\text{SiO}_2$  Using MOS Structures." J. Appl. Phys., 41(7), 3052-3057 (1970).
- E. H. Nicollian, C. N. Berglund, P. F. Schmidt, and J. M. Andrews, "Electrochemical Charging of Thermal  $\text{SiO}_2$  Films by Injected Electron Currents." J. Appl. Phys. 42(12), 5654-5664 (1971).



- T. H. Ning and H. N. Yu, "Optical Induced Injection of Hot Electrons in  $\text{SiO}_2$ ." J. Appl. Phys. 45(12), 5373-5378 (1974).
- C. B. Norris and E. P. Eernisse, "Ionization Dilation Effects in Fused Silica from a to 18-KeV Electron Irradiation." J. Appl. Phys. 45(9), 3876-3882 (1974).
- L. Onsager, "Initial Recombination of Ions." Phys. Rev. 54, 554 (1938).
- Oriel Corporation, data sheet of absorption coefficient from visible to IR light. (1979).
- D. M. Pai and R. C. Enck, "Onsager Mechanism of Photogeneration in Amorphous Selenium." Phys. Rev. B 11(12), 5163-5174 (1975).
- C. A. Pan and T. P. Ma, "Highly Transparent Conductive Films of Thermally Evaporated  $\text{In}_2\text{O}_3$ ." J. of Electronic Materials 10(1), 43-57 (1981).
- L. Pauling, "The Nature of Chemical Bond." Third-Edition, 85 (1960).
- R. J. Powell and G. F. Derbenwick, "Vacuum Ultraviolet Radiation Effects in  $\text{SiO}_2$ ." IEEE, NS-18, 99-105 (1971).
- R. J. Powell and C. N. Berglund, "Photoinjection Studies of Charge Distributions in Oxides of MOS Structures." J. Appl. Phys. 42(1), 4390-4397 (1971).
- R. J. Powell, "Radiation-Induced Hole Transport and Electron Tunnel Injection in  $\text{SiO}_2$  Films." IEEE, NS-22(6), 2240-2246 (1975).
- A. G. Revesz, "The Defect Structure of Grown Silicon Dioxide Films." IEEE, ED-12, 97-102 (1965).
- A. G. Revesz, K. H. Zaininger, and R. J. Evans, "Interface States and Interface Disorder in the Si- $\text{SiO}_2$  System." J. Phys. Chem. Solids, 28, 197-204 (1967).

- A. Rothwarf, "Plasmon Theory of Electron-Hole Pair Production : Efficiency of Cathode Ray Phosphors." J. Appl. Phys. 44(2), 752-756 (1973).
- C. T. Sah, "Origin of Interface States and Oxide Charges Generated by Ionizing Radiation." IEEE, NS-23, 1563-1568 (1976).
- J. A. R. Samson, "Techniques of Vacuum Ultraviolet Spectroscopy." John Wiley, New York (1967).
- G. A. Scoggan and T. P. Ma, "Effects of Electron-Beam Radiation on MOS Structures as Influenced by the Silicon Dopant." J. Appl. Phys., 48, 249-300 (1977).
- M. C. Shine, "A Simplified Technique for Measuring Fast Surface States." Solid State Electronics, 18, 1135-1140 (1975).
- R. A. Sigsbee and R. H. Wilson, "Electron Irradiation Dilation in SiO<sub>2</sub>." Appl. Phys. Lett. 23(10), 541-542 (1973).
- M. Simons Jr., L. K. Monteith, and J. R. Hanster, "Some Observations on Charge Buildup and Release in SiO<sub>2</sub> Irradiated with Low Energy Electrons." IEEE, ED-15, 966-973 (1968).
- E. H. Snow, A. S. Grove and D. J. Fitzgerald, "Effects of Ionizing Radiation on Oxidized Silicon Surfaces and Planar Devices." Proc. IEEE, 55(7), 1168-1185 (1967).
- P. Solomon and N. Klein, "Electroluminescence at High Fields in SiO<sub>2</sub>." J. Appl. Phys. 47(3), 1023-1026 (1976).
- W. G. Spitzer and D. A. Kleinman, "Infrared Lattice Bands of Quartz." Phys. Rev. 121(5), 1324-1335 (1961).

- A. R. Stivers and C. T. Sah, "A Study of Oxide Traps and Interface States of Si-SiO<sub>2</sub> Interface." J. Appl. Phys. 51(12), 6292-6304 (1980).
- S. M. Sze, "Physics of Semiconductor Devices." John Wiley and Sons, Inc., New York (1969).
- C. W. Teng, T. P. Ma, and R. C. Barker, "Signal Amplification and Threshold Control of MTOS Junction." (to be published).
- K. K. Thornber and R. P. Feynman, "Velocity Acquired by an Electron in a Finite Electric Field in a Polar Crystal." Phys. Rev. B1, 4099-4114 (1970).
- J. D. Weeks, J. C. Tully, and L. C. Kimerling, "Theory of REDR in Semiconductors." Phys. Rev. B 12(8), 3286-3292 (1975).
- Z. A. Weinberg, D. R. Young, D. J. DiMaria, and G. W. Rubloff, "Exciton or Hydrogen Diffusion in SiO<sub>2</sub>?" J. Appl. Phys. 50(9), 5757 (1979).
- R. Williams, "Photoemission of Electrons from Silicon into Silicon Dioxide." Phys. Rev. 140(2A), A 569 (1965).
- P. S. Winokur, J. M. McGarrity, and H. E. Boesch, Jr., "Dependence of Interface-State Buildup on Hole Generation and Transport in Irradiated MOS Capacitors." IEEE, NS-23, 1580-1585 (1976).
- P. S. Winokur and M. M. Sokoloski, "Comparison of Interface-State Buildup in MOS Capacitors Subjected to Penetrating and Nonpenetrating Radiation." Appl. Phys. Lett., 28(10), 627-630 (1976).
- P. S. Winokur and H. E. Boesch, Jr., "Interface-State Generation in Radiation-Hard Oxides." IEEE, NS-27, 1647 (1980).
- K. H. Zaininger and A. G. Holmes-Siedle, "A Survey of Radiation Effects in MIS Devices." RCA Rev. 28, 208-240 (1967).

FILMED  
3-8